UAB
Universitat Autònoma de Barcelona

Advancing in the treatment of transthyretin amyloidosis: Utilizing structure-driven approaches to develop kinetic stabilizers

Universitat Autònoma de Barcelona

Departament de Bioquímica i Biologia Molecular

Institut de Biotecnologia i Biomedicina

Doctoral thesis submitted by Francisca Garcia de Carvalho Pinheiro as candidate for the degree of Ph.D. in Biotechnology from the Autonomous University of Barcelona.

The present thesis has been performed at the Department of Biochemistry and Molecular Biology and at the Institute of Biotechnology and Biomedicine, under the supervision of Dr. Irantzu Pallarès Goitiz and Prof. Salvador Ventura Zamora.

Francisca Garcia de Carvalho Pinheiro

Dr. Irantzu Pallarès Goitiz   Prof. Salvador Ventura Zamora

Bellaterra, May 2023

Table of contents

Summary

Transthyretin (TTR) misfolding and amyloid aggregation is associated with a group of fatal disorders known as TTR amyloidosis (ATTR). Most of these diseases are hereditary, being caused by mutations that destabilize TTR's native state. Noteworthy, *wild-type* protein deposition also occurs and is considered a common cause of heart failure in the elderly. Small molecules that bind TTR can act as kinetic stabilizers, preventing tetramer dissociation and thus aggregation. In this context, our group repurposed tolcapone, an FDA-approved molecule for Parkinson's Disease, as a potent TTR aggregation inhibitor. Importantly, tolcapone's unique ability to cross the blood-brain barrier suggests that it could be an option for leptomeningeal amyloidosis, a rare type of ATTR that cannot be addressed with any of the current therapies.

In the present thesis, we demonstrated that tolcapone binds to and inhibits the aggregation of TR variants associated with leptomeningeal amyloidosis, suggesting that it can become the first broad-spectrum drug to treat all manifestations of the disease. Despite the excellent performance of tolcapone, the structures of TTR:tolcapone complexes revealed that it could be redesigned to establish more contacts with the protein, which could improve its potency. By combining rational design and molecular dynamics simulations we discovered M-23, a molecule that presents one of the highest affinities for TTR reported thus far. The crystal structure confirmed that, as intended, M-23 forms new and strong contacts with the protein, leading to a higher tetramer stabilization both *in vitro* and in serum relative to tolcapone. These results encouraged us to further develop M-23 into a drug for ATTR, yet its poor pharmacokinetic profile could compromise its therapeutic use. In this context, we developed PITB, a M-23 derivative that keeps the interactions it establishes with TTR while improving its pharmacokinetics. The structural and biophysical characterization of PITB interaction with TTR revealed that it binds with high affinity to both the wild-type protein and the two most clinically significant TTR variants, stabilizes them, and inhibits their aggregation. Most importantly, PITB exerted a higher tetramer stabilizing effect in plasma from patients than tolcapone, which together with its remarkable pharmacokinetics make of PITB a very promising candidate to treat ATTR and at an affordable cost for all patients. While much insight has been gained in these studies through three-dimensional structures, they do not shed light into the dynamics of the conformational alterations involved in the amyloidogenicity of disease-related TTR variants or assess the effect of molecular binders. To address this gap, in this thesis we exploited the potential of two mass spectrometry-based footprinting methods, hydrogen deuterium exchange (HDX) and fast photochemical oxidation of proteins (FPOP). The data obtained provided valuable insights into the effect of pathogenic mutations and kinetic stabilizers on TTR structure, opening a new avenue for the personalized screening of TTR kinetic stabilizers targeting specific variants.

All in all, the results obtained in this thesis provide significant understanding of the structural-determinants of TTR kinetic stabilization, and support the development of the molecules presented here as drugs to treat ATTR.

Resumen

El mal plegamiento y la agregación amiloide de la transtiretina (TTR) se asocian a un grupo de trastornos de pronóstico fatal conocidos como amiloidosis por TTR (ATTR). Estas enfermedades son mayoritariamente hereditarias y están causadas por mutaciones que desestabilizan el estado nativo de la TTR. Hay que indicar que la deposición de la variante natural de la proteína parece ser una causa frecuente de insuficiencia cardíaca en las personas mayores. Ciertas moléculas pequeñas que se unen a la TTR pueden actuar como estabilizadores cinéticos, impidiendo la disociación del tetrámero y, por tanto, la agregación. En este contexto, nuestro grupo reposicionó tolcapone, una molécula aprobada por la FDA para la enfermedad de Parkinson, como un potente inhibidor de la agregación de TTR. Además, al ser capaz de atravesar la barrera hematoencefálica podría suponer una opción para la amiloidosis leptomeníngea, intratable a fecha de hoy.

En la presente tesis, demostramos que tolcapone se une e inhibe la agregación de las variantes de TTR asociadas con la amiloidosis leptomeníngea, lo que sugiere que puede convertirse en el primer fármaco de amplio espectro para tratar todas las manifestaciones de la enfermedad. Las estructuras de los complejos cristalográficos (TTR:tolcapone) revelaron la posibilidad de mejorar su potencia estableciendo contactos adicionales con la proteína. Combinando el diseño racional y las simulaciones de dinámica molecular diseñamos M-23, una molécula que presenta una de las mayores afinidades por la TTR descritas hasta la fecha. La estructura cristalina confirmó que, como se pretendía, M-23 forma nuevos y fuertes contactos con la TTR, lo que conduce a una mayor estabilización del tetrámero tanto in vitro como en suero en relación con tolcapone. Estos resultados nos animaron a seguir avanzando M-23 como fármaco para la ATTR, aunque su deficiente perfil farmacocinético podría comprometer su uso terapéutico. En este contexto, desarrollamos PITB, un derivado de M-23 que mantiene las interacciones que establece con TTR al tiempo que mejora su farmacocinética. La caracterización estructural y biofísica de la interacción de PITB con TTR reveló que se une con alta afinidad tanto a la proteína de tipo salvaje como a las dos variantes de TTR más significativas clínicamente, las estabiliza e inhibe su agregación. Y lo que es más importante, el PITB ejerce un mayor efecto estabilizador del tetrámero en plasma de pacientes que tolcapone, lo que unido a su destacable farmacocinética hacen de PITB un candidato muy prometedor para tratar la ATTR y a un coste asequible para todos los pacientes. Aunque se han obtenido muchos conocimientos en estos estudios a través de estructuras tridimensionales, estos no arrojan luz sobre la dinámica de las alteraciones conformacionales implicadas en la amiloidogenicidad de las variantes de TTR ni para evaluar el efecto de ligandos estabilizantes. Con el objetivo de cubrir esta necesidad, en el presente trabajo explotamos el potencial de dos técnicas analíticas de huella peptídica basadas en la espectrometría de masas como son el intercambio de deuterio por hidrógeno (HDX) y la oxidación fotoquímica rápida de proteínas (FPOP). Los datos obtenidos nos han proporcionado información relevante tanto sobre el efecto de las mutaciones patogénicas de la TTR como de los agentes estabilizantes analizados. Por todo ello, estas técnicas nos permiten establecer una alternativa muy prometedora y que no ha sido explorada previamente para el cribado personalizado de estabilizadores cinéticos de TTR dirigidos a variantes específicas.

En conjunto, los resultados obtenidos en esta tesis proporcionan una comprensión significativa de los determinantes estructurales de la estabilización cinética de TTR, y apoyan el desarrollo de los estabilizadores cinéticos como fármacos prometedores para el tratamiento de la ATTR.

Resum

El mal plegament i l'agregació amiloide de la transtiretina (TTR) s'associa amb un grup de trastorns de pronòstic fatal coneguts com a amiloïdosi per TTR (ATTR). Aquestes malalties són majoritàriament hereditàries i són causades per mutacions que desestabilitzen l'estat natiu de la TTR. Cal indicar que la deposició de la variant natural de la proteïna sembla ser una causa freqüent d'insuficiència cardíaca en les persones majors. Unes certes molècules petites que s'uneixen a la TTR poden actuar com a estabilitzadors cinètics, impedint la dissociació del tetràmer i, per tant, l'agregació. En aquest context, el nostre grup va reposicionar tolcapone, una molècula aprovada per la FDA per a la malaltia de Parkinson, com un potent inhibidor de l'agregació de TTR. A més, en ser capaç de travessar la barrera hematoencefàlica podria suposar una opció per a l'amiloïdosi leptomeníngia, intractable en data d'avui.

En la present tesi, demostrem que tolcapone s'uneix i inhibeix l'agregació de les variants de TTR associades amb l'amiloïdosi leptomeníngia, evidencies que suggereixen que podríem estar davant del primer fàrmac d'ampli espectre pel tractament de totes les manifestacions de la malaltia. Les estructures dels complexos cristal.logràfics (TTR:tolcapone) van revelar la possibilitat de millorar la seva potència mitjançant l'establiment de contactes addicionals amb la proteïna. Combinant el disseny racional i les simulacions de dinàmica molecular hem dissenyat el M-23, una molècula que presenta una de les majors afinitats per la TTR descrites actualment. L'estructura cristal·lina confirma que, com es pretenia, M-23 forma nous i forts contactes amb la TTR, la qual cosa condueix a una major estabilització del tetràmer tant *in vitro* com en sèrum en compració amb tolcapone. Aquests resultats ens van animar a continuar avançant el M-23 com a fàrmac per a l'ATTR, malgrat que el seu deficient perfil farmacocinètic en compromet el seu ús terapèutic. En aquest context, vam desenvolupar el PITB, un derivat de M-23 que manté les interaccions que estableix amb la TTR al mateix temps que millora la seva farmacocinètica. La caracterització estructural i biofísica de la interacció de PITB amb TTR va revelar que s'uneix amb alta afinitat tant a la proteïna de tipus salvatge com a les dues variants de TTR més significatives clínicament, les estabilitza i n'inhibeix la seva agregació. A més a més, cal remarcar que el PITB exerceix un major efecte estabilitzador del tetràmer en plasma de pacients que tolcapone, la qual cosa unit a la seva destacable farmacocinètica fan del PITB un candidat molt prometedor per al tractament de l'ATTR i a un cost assequible per als pacients. Malgrat que s'han obtingut molts coneixements en base a l'estudi de les estructures tridimensionals, aquestes no aporten llum sobre la dinàmica de les alteracions conformacionals implicades en l'amiloidogenicidad de les variants de TTR ni quan volem avaluar l'efecte de lligands estabilitzadors. Amb l'objectiu de cobrir aquesta necessitat, en el present treball explotem el potencial de dues tècniques analítiques de petjada peptídica basades en l'espectrometria de masses com són l'intercanvi de deuteri per hidrogen (HDX) i l'oxidació fotoquímica ràpida de proteïnes (FPOP). Les dades obtingudes ens han proporcionat informació rellevant a nivell de residu tant de l'efecte de les mutacions patogèniques de la TTR com de la unió dels agents estabilitzants analitzats. En consequència, destacar que aquestes tècniques ens permeten establir una alternativa molt prometedora i que no ha estat explorada prèviament per al cribatge personalitzat d'estabilitzadors cinètics de TTR dirigits a variants específiques. En conjunt, els resultats obtinguts en aquesta tesi proporcionen una comprensió significativa dels determinants estructurals de l'estabilització cinètica de TTR, i donen suport al desenvolupament dels estabilitzadors cinètics com a fàrmacs prometedors per al tractament de l'ATTR.

List of publications

This thesis is in the format of a compendium of the following published works:

1. **Pinheiro, F.**; Pallarès, I.; Peccati, F.; Sánchez-Morales, A.; Varejão, N.; Bezerra, F.; Ortega-Alarcon, D.; Gonzalez, D.; Osorio, M.; Velázquez-Campoy, A.; Rosário Almeida, M.; Reverter, D.; Busqué, F.; Alibés, R.; Sodupe, M.; Ventura, S. Development of a Highly Potent Transthyretin Amyloidogenesis inhibitor. Design, synthesis and evaluation. J. Med. Chem. (2022) 65: 14673-14691.
2. **Pinheiro, F**.; Varejão, N.; Esperante, S.; Santos, J.; Velázquez-Campoy, A.; Reverter, D.; Pallarès, I.; Ventura, S. Tolcapone, a potent aggregation inhibitor for the treatment of familial leptomeningeal amyloidosis. FEBS J. (2021) 228: 310-324.

Other co-authored articles not included in this thesis:

1. Peña-Díaz, S.; Pujols, J.; Vasili, E.; **Pinheiro, F.**; Santos, J.; Manglano-Artuñedo, Z.; Outeiro, T.; Ventura, S. The small aromatic compound SynuClean-D inhibits aggregation and seeded polymerization of multiple α-Synuclein strains. J. Biol. Chem. (2022) 298: 101902.
2. Esperante, S.; Varejão, N.; **Pinheiro, F.**; Sant'Anna, R.; Luque-Ortega, J.; Alfonso, C.; Sora, V.; Papaleo, E.; Rivas, G.; Reverter, D.; Ventura, S. Disease-associated mutations impacting BC-loop flexibility trigger long-range transthyretin tetramer destabilization and aggregation. J. Biol. Chem. (2021) 297: 101039.
3. **Pinheiro, F.***; Santos, J.; Ventura, S.* AlphaFold and the amyloid landscape. J. Mol. Biol. (2021) 233: 167059. * co-corresponding authorship
4. Martins, P.; Navarro, S.; Silva, A.; Pinto, M.; Sárkany, Z.; Figueiredo, F.; Pereira, P.; **Pinheiro, F.**; Bednarijova, Z.; Burdukiewicz, M.; Galzitskaya, O.; Gazova, Z.; Gomes, C.; Pastore, A.; Serpell, L.; Skrabana, R.; Smirnovas, V.; Ziaunys, M.; Otzen, D.; Ventura, S.; Macedo-Ribeiro, S. MIRRAGGE – Minimum Information Required for Reproducible AGGregation Experiments. Front. Mol. Neurosci. (2020) 13: 582488.
5. Peña-Díaz, S.; Pujols, J.; **Pinheiro, F.**; Santos, J.; Pallares, I.; Navarro, S.; Conde-Gimenéz, M.; García, J.; Salvatella, X.; Dalfo, E.; Sancho, J.; Ventura, S. Inhibition of α-Synuclein Aggregation and Mature Fibril Disassembling With a Minimalistic Compound, ZPDm. Front. Bioeng. Biotechnol. (2020) 8: 588947.
6. Peña-Díaz, S.; Pujols, J.; Conde-Gimenéz, M.; Carija, A.; Dalfo, E.; García, J.; Navarro, S.; **Pinheiro, F.**; Santos, J.; Salvatella, X.; Sancho, J.; Ventura, S. ZPD-2, a Small Compound That Inhibits alpha-Synuclein Amyloid Aggregation and Its Seeded Polymerization. Front. Mol. Neurosci. (2019) 12: 306.
7. Carija, A.; **Pinheiro, F.**; Iglesias, V.; Ventura, S. Computational Assessment of Bacterial Protein Structures Indicates a Selection Against Aggregation. Cells (2019) 8: 856.
8. **Pinheiro, F.**; Ventura, S. Inducing α-Synuclein compaction: a new strategy for inhibiting α-Synuclein aggregation? Neural Regen. Res. (2019) 14: 1897-1898.
9. Carija, A.; **Pinheiro, F.**; Pujols, J.; Brás, I.; Lázaro, D.; Santambrogio, C.; Grandori, R.; Outeiro, T.; Navarro, S.; Ventura, S. Biasing the native α-Synuclein conformational

ensemble towards compact states abolishes aggregation and neurotoxicity. Redox Biol. (2019) 22: 101135.

10. Pujols, J.; Peña-Díaz, S.; Lázaro, D. F.; Peccati, F.; **Pinheiro, F.**; Gonzaléz, D.; Carija, A.; Navarro, S.; Conde-Gimenéz, M.; García, J.; Guardiola, S.; Giralt, E.; Salvatella, X.; Sancho, J.; Sodupe, M.; Outeiro, T. F.; Dalfo, E.; Ventura, S. Small molecule inhibits α-Synuclein aggregation, disrupts amyloid fibrils, and prevents degeneration of dopaminergic neurons. Proc. Natl. Acad. Sci. U.S.A. (2018) 115: 10481-10486.

11. Pujols, J.; Peña-Díaz, S.; Conde-Gimenéz, M.; **Pinheiro, F.**; Navarro, S.; Sancho, J.; Ventura, S. High-Throughput Screening Methodology to Identify Alpha-Synuclein Aggregation Inhibitors. Int. J. Mol. Sci. (2017) 18: 478.

12. Sant'Anna, R.; Gallego, P.; Robinson, L.Z.; Pereira-Henriques, A.; Ferreira, N.; **Pinheiro, F.**; Esperante, S.; Pallarès, I.; Huertas, O.; Rosário Almeida, M.; Reixach, N.; Insa, R.; Velazquez-Campoy, A.; Reverter, D.; Reig, N.; Ventura S. Repositioning tolcapone as a potent inhibitor of transthyretin amyloidogenesis and associated cellular toxicity. Nat. Commun. (2016) 7: 10787-10800.

List of abbreviations

α-syn	α-synuclein
Aβ	Amyloid-β peptide
AD	Alzheimer's Disease
AO	Age at onset
ASO	Antisense oligonucleotide
ATTR	Transthyretin amyloidosis
CSF	Cerebrospinal fluid
CTS	Carpal tunnel syndrome
ERK	Extracellular signal-regulated kinases
FAC	Familial amyloid cardiomyopathy
FAP	Familial amyloid polyneuropathy
FDA	Food and Drug Administration
FPOP	Fast photochemical oxidation of proteins
hATTR	Hereditary transthyretin amyloidosis
HBPs	Halogen binding pockets
HDX	Hydrogen deuterium exchange
IDPs	Intrinsically disordered proteins
IEF	Isoelectric focusing
iNOS	Inducible form of nitric oxide synthase
ITC	Isothermal titration calorimetry
IV	Intravenous
KO	Knockout
LA	Leptomeningeal amyloidosis
LT	Liver transplantation
MS	Mass spectrometry
PD	Parkinson's Disease
PK	Pharmacokinetic
PO	Per oral
RAGE	Receptor for advanced glycation end products
RBP	Retinol-binding protein
siRNA	Small interfering RNA
SSA	Senile systemic amyloidosis

T$_4$	Thyroxine
THAOS	Transthyretin amyloidosis outcome survey
TTR	Transthyretin
WT	Wild-type

INTRODUCTION

1. Protein folding versus aggregation

Proteins are biomolecules formed by hundreds or even thousands of small units called aminoacids covalently linked by peptide bonds. These macromolecules are highly abundant, constituting most of the dry weight of cells, and diverse, reflecting its relevance in a multitude of functions, including transport, immune response, signaling, catalysis or structural support[1]. In order to perform their biological functions, the majority of proteins must attain a defined three-dimensional structure, known as the native state[2].

The process through which a protein acquires its native state, from an initially unstructured conformation, is called protein folding[3]. In addition to the native conformation, it is now recognized that proteins can adopt an alternative structure, known as amyloid, which can be accessed through a process named protein aggregation. Of note, protein folding and aggregation are competing pathways that a protein can undergo depending on the conditions[4,5]. Importantly, protein aggregation is associated with numerous human diseases, including Alzheimer's and Parkinson's disease, type II diabetes and systemic amyloidosis as transthyretin amyloidosis (ATTR), drawing attention to this phenomenon[6].

1.1 The fundamentals of protein folding

Understanding how a protein transitions from an unfolded state to a unique conformation has been a major problem in the field of biology.

The first insights into the folding process came from the studies performed by Christian B. Anfinsen and colleagues in the 1960s' and 1970s'. These studies, which were focused on the unfolding and refolding of ribonuclease A, demonstrated that all the information needed to acquire the native state is encoded in the aminoacid sequence of a protein and that losing the native state leads to a loss of function[7]. Moreover, Anfinsen observed that protein folding was a spontaneous process, which led him to hypothesize that a protein's native state in its physiological milieu corresponds to the one with the lowest Gibbs free energy of the whole system[2]. These works settled the basis for the sequence-structure-function paradigm, which states that the amino acid sequence of a protein dictates its three-dimensional structure, which, in turn, determines its function[8].

After the pioneering studies of Anfinsen and coworkers, Cyrus Levinthal shed additional light on the mechanism of protein folding. The work of Levinthal showed that there is a huge discrepancy between the calculated time required for a protein to fold by randomly trying out all the possible conformations (1.6×10^{27} years for a protein with 100 residues) and the actual time a protein takes to fold (μs-ms). This discrepancy is known as the Levinthal's paradox and suggested that protein folding must be at least partially guided by the formation of intermediates[9]. Afterwards, several models have been proposed to explain how folding occurs inside cells. These include the nucleation-propagation[10], the framework model[11] and the hydrophobic collapse model[12]. Although the last two models were largely accepted, it was believed that they could both play a role in the folding process. Thus, a unifying model, named nucleation-condensation model, was proposed. This model states that hydrophobic interactions drive the compaction of the entire polypeptide chain and, then, secondary and tertiary structural elements are formed, generating

partially folded structures (molten globules) that are further refined to achieve the native structure[13,14].

Noteworthy, instead of following a single folding pathway, there is likely a variety of routes that a protein can follow to reach the native state. The different conformations that a protein can adopt during this process are typically represented by theoretical bidimensional diagrams called energy landscapes. The folding funnel model is the most common way to illustrate the process of protein folding (**Figure 1**). The wider part of the funnel is occupied by an ensemble of unfolded states, which correspond to the highest energetic species. As folding progresses, the number of conformations accessible to the protein decreases and it moves into narrower and more stable regions of the funnel until it reaches the native state[15,16]. While this process appears smooth for short proteins, allowing them to fold rapidly, it is much more complex for large proteins, which exhibit rougher landscapes with numerous partially folded intermediates. Additionally, the shape of an energy landscape is highly influenced by the environmental conditions, such as temperature[4,17,18].

Importantly, the discovery of proteins that do not fold into defined three-dimensional structures and, yet are functional, defied the structure-function paradigm. Instead of acquiring a unique structure, the so-called intrinsically disordered proteins (IDPs) can acquire a variety of functional conformations, introducing the concept of disorder-function paradigm. Remarkably, 15-45% of eukaryotic proteins contain at least one disordered region with more than 30 consecutive residues[19-21]. In addition to IDPs, the existence of sequences, named chameleon sequences, that can adopt different structures in the same protein or in different proteins has shaken the idea that one aminoacid sequence encodes for one specific structure[22,23]. Due to their conformational plasticity, chameleon sequences and, especially, IDPs, have been found in protein aggregates related with disease[24-26]. Classical examples of IDPs linked to protein aggregation disorders include the amyloid-β peptide (Aβ), α-synuclein (α-syn) and tau, which are associated with Alzheimer's Disease (AD), Parkinson's Disease (PD) and Pick's disease, respectively. Of note, globular proteins, such as β_2-microglobulin and transthyretin (TTR), are also found aggregated in dialysis related amyloidosis and ATTR, respectively[6]. In this case, however, aggregation might be triggered by partial unfolding with concomitant exposure of aggregation prone regions, which are normally buried in the core of the protein, to the solvent[27].
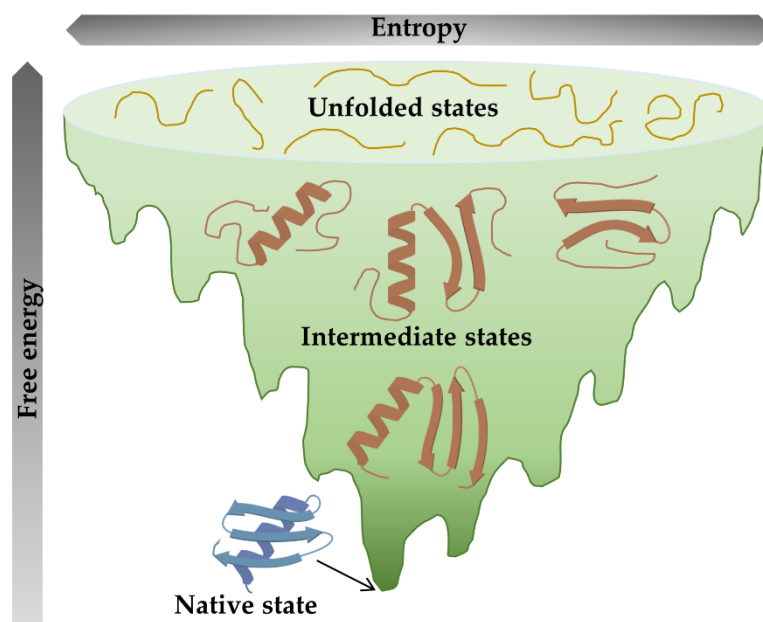
Figure 1. Schematic representation of the folding funnel. According to the folding funnel hypothesis, the ensemble of unfolded states might navigate numerous routes in is path to the native state, populating different intermediate states. As the polypeptide chain moves down the funnel, both the entropy (represented by the width of the funnel) and the Gibbs free energy (denoted by the depth of the funnel) decrease. The lowest entropy and energy species corresponds to the native state. The rugged appearance of the energy landscape illustrates the existence of energy barriers, which trap the protein intermediates, slowing the folding process.

1.2 Exploring the energy landscape of protein folding and aggregation

Protein aggregation is driven by hydrophobic interactions and hydrogen bond formation, similarly to protein folding, although the first involves contacts between different molecules, i.e., intermolecular rather than intramolecular interactions. In the living cell, protein folding and aggregation are competing pathways, both of which are potentially accessible to a polypeptide chain. As a result, a combined energy landscape for protein folding and aggregation was created (**Figure 2**). Within the aggregation landscape, prefibrillar species, like oligomers, populate poorly defined energy minima, whereas amorphous aggregates and amyloid fibrils occupy sharper and deeper minima[4,28]. In fact, the observation that any protein sequence can form amyloid fibrils, even chains comprising only one type of amino acid or single amino acid residues, led to the suggestion that the amyloid fold corresponds to the global free energy minimum of all polypeptide chains[6,29,30]. Noteworthy, the energy minimum corresponding to amyloid fibrils can be occupied by a multitude of fibril morphologies, known as polymorphs, even under the same solution conditions[5,31].
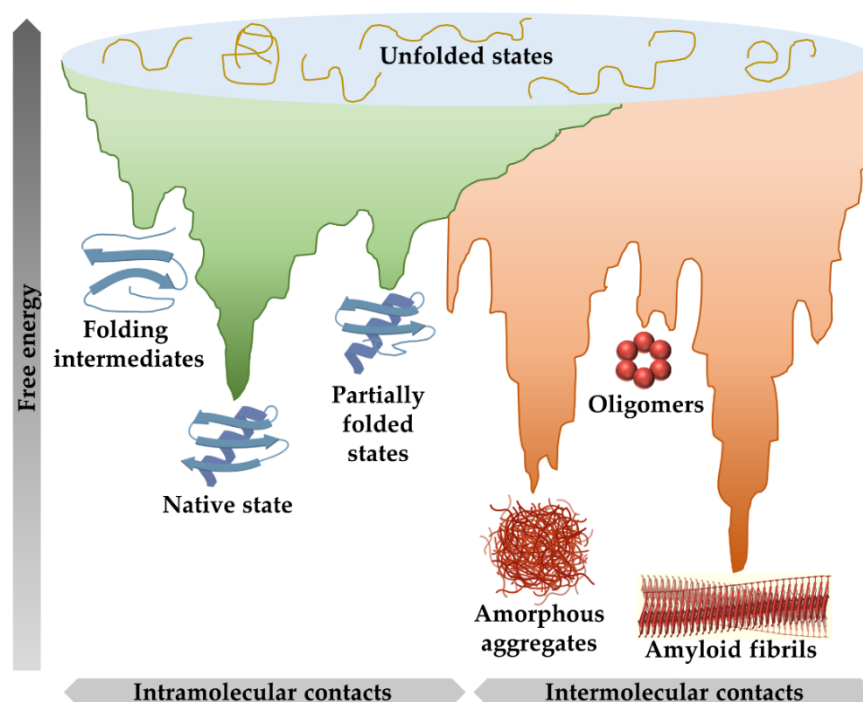
Figure 2. Illustration of the energy landscape of protein folding and aggregation. The surface shows the multitude of conformational states accessible to a polypeptide chain during folding (green surface) and aggregation (red surface). While the formation of intramolecular contacts guides the conformational search for the protein's native state, the establishment of intermolecular interactions can lead to the formation of amyloid fibrils. Partially folded states, which can be populated either during folding or from the native state (e.g., due to local unfolding events), are thermodynamically favored in comparison to the unfolded state, but display a higher energy than the native conformation. These species have a high tendency to establish intermolecular interactions and can drag the protein into the aggregation sub-funnel.

In the combined energy landscape of protein folding and aggregation, both parts of the funnel overlap, reflecting the idea that aggregation can be triggered from species populated during the folding process. Partially folded intermediates, for example, can be on- or off-pathway to the native state. Kinetically trapped off-pathway intermediates have a high tendency to engage in intermolecular interactions, leading to aggregate formation[4,5,32]. Additionally, the partial unfolding of the native state might expose hydrophobic regions, which are prone to establish contacts with other molecules, prompting aggregation. Remarkably, these local unfolding events can occur even under highly native conditions, for example, via thermal fluctuations or small movements that are related with protein function as catalysis or ligand binding[27,33,34]. Moreover, the presence of mutations can increase the frequency of these unfolding events, raising the population of partially unfolded species, as it was described for lysozyme[35,36] or TTR[37,38]. In addition, a change in solution conditions (e.g., pH, temperature and pressure) or in protein concentration can favor the formation of these species[27]. On the other hand, for IDPs, partial structuring of the natively unfolded structure can originate aggregation-competent conformations, i.e., partial folding instead of partial unfolding[39,40]. As for globular proteins, the aggregation propensity of IDPs is highly modulated by the occurrence of mutations and environmental factors such as pH, ionic strength or temperature[39].

Although it has been typically considered as detrimental, amyloids that play specific functional roles have been described in the last decades. The so-called functional amyloids were discovered for the first time in bacteria, but are now recognized in all kingdoms of life, including in humans[41-43]. One of the most well-known examples in bacteria are the extracellular curli amyloid fibrils, which are involved in biofilm formation and integrity[44]. In yeast, Sup35, Ure2p and HET-s can assemble into self-propagating amyloid fibrils (a prion), which modulate translation termination at stop codons, nitrogen catabolism and heterokaryon compatibility, respectively[45-47]. In humans, the first known functional amyloid was Pmel17, which plays a key role in melanin synthesis inside the melanosomes[48]. Additionally, the formation of reversible amyloid fibrils by protein and peptide hormones was proposed to underlie the mechanism of hormone storage in humans[49]. All in all, these examples evidence that the amyloid fold has been used by nature to perform a variety of cellular tasks, similarly to what happens with globular proteins. This idea drove the emergence of a new goal in the amyloid field, the development of functional nanomaterials based on artificial amyloids, i.e., amyloid fibrils synthesized *in vitro* from non-toxic proteins and peptides. These biomaterials have been applied for different biomedical and biotechnological purposes, such as optoelectronic, biosensing, drug delivery, or tissue engineering[50,51].

1.3 The molecular and mesoscopic structure of amyloid fibrils

The amyloid fold is a generic protein fold, thus being accessible to most protein sequences[6]. Although amyloid fibrils can be formed by different, unrelated, sequences, they share a common, highly ordered, architecture known as cross-β. In this structure, parallel or anti parallel β-strands that are oriented perpendicularly to the fibril axis assemble into β-sheets that run the fibril length[6,28] (**Figure 3A**). The cross-β spine was initially identified using X-ray fiber diffraction. The diffraction pattern produced by amyloid fibrils exhibits two sharp diffraction signals, at 4.7-4.8 Å and 8-12 Å, which are thought to arise from the spacing between the β-strands and adjacent β-sheets, respectively[52] (**Figure 3B**). This unique configuration can be further detected by Fourier transform infrared spectroscopy, producing a band at 1625 cm^{-1}, and circular dichroism, exhibiting a minimum at 217 nm[53]. A more detailed structural analysis of amyloid fibrils was brought by the advent of solid-state state NMR and cryo-electron microscopy. The structures obtained from these techniques revealed that the β-strands generally form β-sheets with a parallel in-register arrangement, i.e., the strands have the same orientation and each residue in one molecule is aligned with the equivalent residue in the neighboring molecule (**Figure 3C**)[54-57].

On a mesoscopic scale, amyloid fibrils are typically composed by 2-8 protofilaments that twist around each other rendering unbranched fibrils with 7-13 nm diameter and up to several microns in length, as observed by electron microscopy or atomic force microscopy techniques [6,28]. In an amyloid fibril, the number of protofilaments and their orientation is a major source of fibril polymorphism, although different arrangements of β-strands and β-sheets can further contribute to this phenomenon[28,31]. Remarkably, fibril polymorphism has been described in fibrils generated *in vitro* under the same conditions[58] and even in fibrils extracted from the same patient[59]. The fact that amino acid sequences were not shaped by evolution to adopt the amyloid fold, unlike it happens with the native structure, was proposed to underlie the existence of polymorphism[6,60]. Functional amyloids, on the other hand, were suggested to have a lower

degree of polymorphism as, in this case, the amyloid architecture is required to perform a physiologically relevant function[60].

To conclude, amyloid fibrils can also be detected by the binding of dyes, like Thioflavin-T and Congo-Red, which suffer a change in fluorescence and absorbance, respectively, upon binding to fibrils[61]. The tinctorial properties of amyloid fibrils, together with the fibrillar morphology and the cross-β structure are considered the hallmarks of amyloid structure[6].
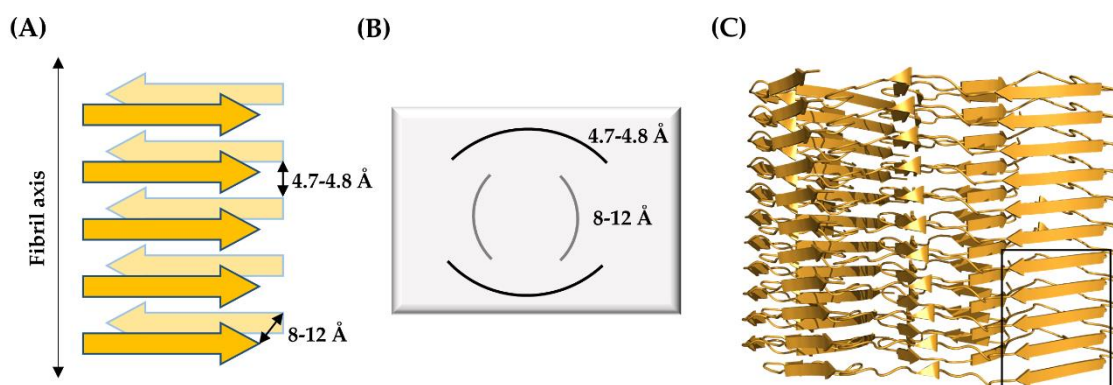
Figure 3. Common architecture of amyloid fibrils. (A) Schematic representation of the cross-β structure. In each β-sheet, the strands run perpendicular to the fibril axis with a spacing of 4.7-4.8 Å. The separation between two β-sheets in the cross-β structure is between 8 and 12 Å. (B) Illustration of the X-ray diffraction pattern of amyloid fibrils. The reflections at 4.7-4.8 Å and 8-12 correspond to the molecular spacing between β-strands and β-sheets, respectively, as shown in (A). (C) Cartoon representation of the cryo-electron microscopy structure of a transthyretin fibril evidencing the parallel in-register alignment of β-sheets (solid line). Figure prepared from PDB file 6SDZ.

1.4 Cell- and protein-specific strategies to counteract protein aggregation

The increasing awareness that the tendency to undergo aggregation is not specific to some proteins, but rather an intrinsic property of polypeptide chains, suggested the existence of mechanisms that prevent this process[62].

In cells, a set of sophisticated quality control mechanisms serves this purpose. The ability of proteins to achieve their native structure, with concomitant burial of aggregation-prone regions in the hydrophobic core, is a fundamental strategy to avoid protein aggregation[62,63]. To assure the correct folding of proteins and minimize nonnative interactions, cells mostly rely on molecular chaperones. Molecular chaperones, most of which are heat shock proteins (e.g., Hsp40s, Hsp70s and Hsp90s), enhance the rate of folding, decreasing the population of intermediates that can enter in the aggregation landscape, and protect the aggregation-prone regions from intermolecular interactions. Moreover, they participate in the refolding of misfolded and/or aggregated structures and in protein degradation via the ubiquitin-proteasome system or autophagy[64-66]. When the protein repair mechanisms do not work, proteins are targeted for protein degradation. Whereas the ubiquitin-proteasome system is responsible for the degradation of individual proteins that did not fold properly, autophagy is behind the removal of protein aggregates[67,68]. Accumulating evidence shows that there is a decline in the activity of these mechanisms with aging, especially due to a decrease in the levels of key proteins in these systems, as chaperones. Remarkably, this can be a result of

transcriptional downregulation, but also of protein sequestration by the increasing number of aggregates[69-71]. Furthermore, it is thought that the progressive failure of the quality control machinery leads to an increase in protein aggregation, which, in turn, contributes to its collapse, exerting positive feedback. Overall, these observations might explain why aging is the major risk factor for protein aggregation diseases[6,72].

In addition to quality control mechanisms existing in cells, proteins themselves have evolved protective strategies to escape from aggregation[62]. For example, it was shown that highly conserved proline and glycine residues, which are known β-breakers, inhibit aggregation in some proteins[73,74]. Moreover, proline, lysine, arginine, glutamate and aspartate, were found to be enriched in the positions flanking aggregation prone regions, or hot spots, which are short stretches with a high content of hydrophobic residues able to drive the aggregation process[75,76]. The presence of β-breakers and charged residues at the flanks of aggregation prone regions reduces their intrinsic aggregation propensity, thus being named as gatekeepers[75,77]. Other sequence adaptations to prevent protein aggregation consist in avoiding long stretches of consecutive hydrophobic residues[78] and maintaining an overall high net charge[79]. The importance of charge in protein aggregation explains the impact of pH and ionic strength in modulating the aggregation tendency of a protein[80,81]. All these sequence-specific strategies are especially important in IDPs since, in this case, the primary mechanism to fight aggregation, folding, cannot be applied[82,83]. Finally, since protein aggregation is highly modulated by protein concentration, protein sequences have been finely regulated, probably by several of the aforementioned strategies, so that their aggregation propensity does not exceed their solubility limit *in vivo*. In agreement, protein expression levels are inversely correlated with their aggregation propensity[62,84].

Despite dedicated efforts to prevent protein aggregation, it can still occur, especially due to aging, but also genetics, environmental risk factors (e.g., pesticide exposure) and lifestyle habits (e.g., lack of physical activity). Protein aggregation underlies a group of diseases named amyloidosis[6].

2. Transthyretin amyloidosis

TTR is one of the >30 proteins involved in the generation of amyloidosis, a group that also includes Aβ and α-syn, which are related with AD and PD, respectively[6]. The extracellular deposition of TTR fibrils in various organs and tissues underlies the onset of a progressive, life-threatening, disease named ATTR[85]. ATTR was first described in Portugal[86] and subsequently in Japan[87] and Sweden[88] and is currently reported in at least 32 countries[89]. ATTR comprises wild-type ATTR, which arises from genetically unaltered TTR and hereditary ATTR (hATTR), which is caused by the deposition of one of more than 130 genetic variants of TTR[90].

2.1 Clinical spectrum

Nonhereditary wild-type ATTR, typically known as senile systemic amyloidosis (SSA), is a late onset disease characterized by the deposition of TTR fibrils in the myocardium, leading to congestive heart failure and, ultimately, death, which usually occurs 3-4 years after the diagnosis [91-94] (**Figure 4**). Most patients with SSA are elderly men, with a mean age of 75 years[93,95].

Common signs and symptoms include shortness of breath, exercise intolerance, fatigue, dizziness, peripheral edema and arrhythmias[93]. Additionally, patients with SSA may present features of carpal tunnel syndrome (CTS), which is frequently the first manifestation of the disease[96], spinal canal stenosis[97] and spontaneous biceps tendon rupture[98].

In contrast, hereditary ATTR is an autosomal dominant inherited disease that has been associated with more than 130 mutations[99] and is currently regarded as the most frequent form of familial amyloidosis[100]. This high genetic heterogeneity contributes to an extremely variable phenotypic presentation that can be primarily polyneuropathic (known as familial amyloid polyneuropathy, FAP), cardiac (named familial amyloid cardiomyopathy, FAC), or a mix of both. Moreover, the central nervous system can also be affected, giving rise to phenotype know as familial leptomeningeal amyloidosis (LA)[99,101] (**Figure 4**). Importantly, the phenotype is not uniform and can vary with the TTR mutation, age at onset (AO), geographical area, and even among family members who share the same mutation[101].

Regarding FAP, it is a severe systemic disease with predominant destruction of the somatic and autonomic peripheral nervous system. In most endemic regions (Portugal, Cyprus and Majorca), FAP presents an early-onset, occurring before the age of 40 years, while in endemic regions of Sweden and nonendemic areas the AO tends to be higher (age > 50 years)[102]. In Japan, individuals related with the endemic foci exhibit an earlier onset than the ones outside these areas[103]. Life expectancy is ~11 years from disease onset in early-onset FAP, while the late-onset variant presents a more rapid course (survival is ~7 years from onset)[104,105]. In early-onset FAP, small nerve fibers are typically affected first, causing neuropathic pain, paresthesia (sense of burning) and hypoesthesia (numbness). As larger nerve fibers become involved, motor deficit appears, as does the loss of light touch and deep sensations. This sensory and motor neuropathy usually follows a distal-to-proximal progression, first affecting the feet and then the upper limbs. Autonomic symptoms, including orthostatic hypotension, bladder abnormalities, and gastrointestinal and erectile disfunction, are severe and may be the first manifestation of the condition. Heart involvement is frequent in these patients and is mainly characterized by conduction disturbance (e.g., arrhythmias) that requires pacemaker implementation. A positive family history of FAP is considered a hallmark of early-onset disease[106,107]. On the contrary, in late-onset FAP, there is early involvement of both small and large nerve fibers, with deep sensory loss, muscle wasting, weakness, and balance abnormalities. Sensorimotor symptoms may start in the lower extremities, in the upper limbs, or simultaneously in all four limbs. Autonomic symptoms are relatively mild, while heart dysfunction may be severe, especially in male patients. Moreover, there is a marked male preponderance in the late-onset type and a lower incidence of family history, hampering the diagnosis[104,105]. A positive history of CTS is common in FAP and can be an early disease manifestation, especially in late-onset patients[108,109]. Ocular involvement (e.g. vitreous opacities, glaucoma, dry eye) and/or CNS manifestations (e.g. episodes of focal neurological deficits, brain hemorrhage, dementia) are frequently seen in the advanced stage of the disease, both in early- and late-onset FAP[110,111]. Patients with FAP usually die of cachexia, infections, or cardiac failure[112].

In resemblance to SSA, patients with FAC experience debilitating physical symptoms related to heart failure, although the symptoms tend to appear earlier (between 40 and 70 years of age)[94,113]. Bilateral CTS is also a common clinical feature in this disorder[114,115]. Additionally, signs

of neuropathy have been frequently observed in patients diagnosed with FAC, further evidencing the multisystemic nature of ATTR[115,116]. As for SSA, subjects with FAC are primarily men and have a low life expectancy (2 to 6 years after diagnosis)[94,117].

Finally, LA is characterized by amyloid deposition in brain and spinal cord leptomeninges, as well as in the walls of subarachnoid vessels. The build-up of amyloid fibrils in these regions is manifested with seizures, progressive cognitive impairment with dementia, ataxia and hemorrhagic strokes[118]. Visual deterioration often occurs, due to amyloid accumulation in the vitreous humor, in which case it is known as familial oculoleptomeningeal amyloidosis[119]. Additionally, affected individuals may present autonomic and peripheral neuropathy and cardiac dysfunction[120]. In patients with LA, the AO ranges from 26 to 69 years, and average disease duration corresponds to corresponds to 9.3 ± 7.1 years[120,121].
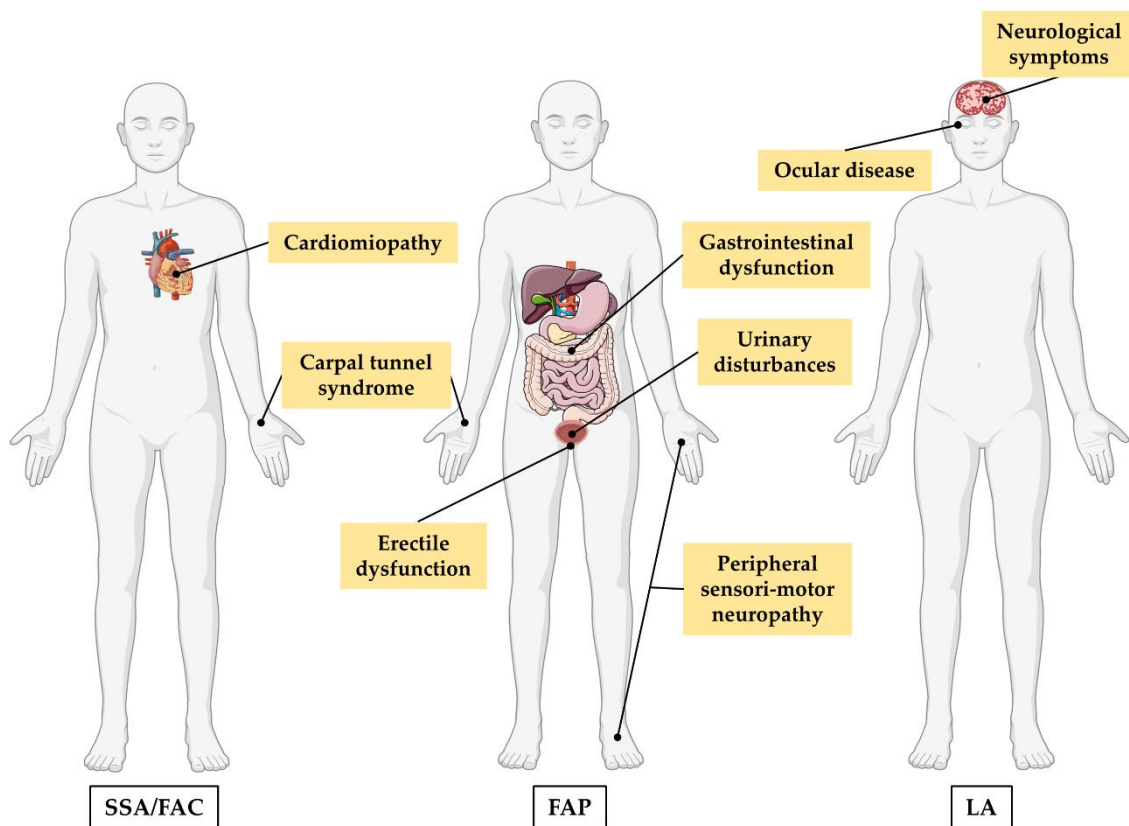
Figure 4. Clinical features of ATTR. Simplified view of the main manifestations of the four forms of ATTR.

2.2 Genetics

hATTR is a worldwide disease that arises from mutations on the TTR gene. To date, more than 130 mutations in the TTR gene have been detected and, except for one micro deletion, they are all missense point mutations[99]. Although most affected individuals are heterozygous for one TTR pathogenic variant, patients who are homozygous have been described[122,123]. Interestingly, few non-pathogenic mutations have also been identified, as have patients carrying one pathogenic and one non-pathogenic mutation[124,125].

2.2.1 Genotype-phenotype correlation

Despite the broad phenotypic heterogeneity of hATTR, some mutations have been associated with particular phenotypes. For example, the V30M mutation, which is the most common pathogenic mutation worldwide[101], is predominantly related with FAP[126]. This variant is responsible for a large endemic focus in northern Portugal, where the disease was first described by Corino de Andrade[86], as well as other endemic areas in Sweden, Japan, Majorca and Cyprus[85]. In fact, it is the only mutation identified thus far in endemic regions of Cyprus and Majorca[127,128]. On the other hand, the V122I mutation is the most frequent cause of FAC[129]. Since its discovery in fibrils extracted from the heart of a 68-year-old black man with late-onset cardiac amyloidosis[130], it has become clear that this mutation is almost exclusively encountered in patients from West Africa or identifiable West African descent[115,131]. Up to 4% of African Americans may carry this mutation in the TTR gene[132,133], a number that is even higher in African Americans with heart failure who are over 60 years of age[134]. Apart from V30M and V122I, several mutations have been related with these phenotypes. Other mutations that mainly present as a neuropathy or cardiomyopathy include V28M, L58H and S77Y, or T60A, I68L and L111M, respectively[118,135]. On the contrary, only 15 mutations causing LA have been described thus far, including D18G, A25T, V30G, Y69H and Y114C[120].

Importantly, the clinical presentation of hATTR is not solely determined by the disease-causing mutation as the same mutation may manifest differently, even within the same family[136]. The V30M mutation provides a clear example of this disparity. Individuals carrying the V30M mutation may have early- or late-onset FAP[108]. Although the division between these two subtypes was established in different clusters worldwide[102], early- and late-onset cases are often found in the same geographical region and in the same family. In fact, the children of an affected adult frequently show an earlier AO than their parent, a difference that could be higher than 10 years. This phenomenon, known as anticipation, is more pronounced when the disease is inherited from the mother and when the child is male[137]. Although the mechanisms behind the distinct AO in V30M carriers are still not fully elucidated, several genetic factors have been proposed to play a role. For example, single nucleotide haplotype polymorphisms at the TTR locus transmitted by the non-carrier parent (trans-acting factor) have been associated with early-onset disease[138]. Additionally, polymorphisms in other genes, such as androgen receptor genes[139], and the mitochondrial copy number[140], have been shown to influence the AO. Overall, these studies indicate that other genetic factors apart from the TTR mutation might impact the clinical presentation of the disease, further complicating the establishment of genotype-phenotype correlations.

2.2.2 Penetrance

Penetrance refers to the proportion of people carrying a particular genetic mutation that also express the associated disease phenotype. Generally, hATTR is considered to have incomplete penetrance, which means that individuals carrying the mutation can remain asymptomatic for their whole life but may see their children become affected[136]. Of note, the penetrance of hATTR is highly variable, depending on the age, geographical region, and even the gender of the transmitting parent[85,136].

The V30M mutation has a high penetrance in Portugal, around 80% by age 50 and 91% by 70 years, whereas in Sweden is much lower, 11% at 50 years of age and 30% at 70 years[141,142]. A lower penetrance is typical of late onset phenotypes, as the ones presented in endemic regions of Sweden and nonendemic regions of Japan, explaining why a positive family history is less frequent in these cases[103,117]. Importantly, some studies suggest that the penetrance is significantly higher when the mutation is inherited from the mother than from the father[137,142].

Although the phenotypic penetrance of other TTR mutations has not been adequately determined, age-dependent penetrance has also been suggested for the FAC related mutation V122I, mainly affecting carriers over 65 years of age[143].

2.3 Geographical distribution

The heterogeneity of ATTR, together with a low disease awareness, makes it difficult to diagnose this disorder. Understanding the geographic distribution of ATTR genotypes and phenotypes can facilitate an earlier diagnosis and treatment engagement. In this context, the Transthyretin Amyloidosis Outcomes Survey (THAOS) has become a valuable tool. Founded in 2007, THAOS is the largest ongoing, worldwide, longitudinal, observational survey of patients with ATTR (both SSA and hATTR), including asymptomatic carriers of pathogenic mutations (NCT00628745)[144].

Among all patients enrolled in THAOS, the V30M mutation is the most frequent genotype (49.6%), followed by wild-type (WT) TTR (23.5%) and V122I (6.0%). V30M is the most common mutation in Europe, Asia and South America, while most patients in North America have the WT protein or the V122I variant. Accordingly, most patients in Europe, Asia and South America present a predominantly neurologic phenotype at enrollment, whereas predominantly cardiac is the most common phenotype in North America (**Figure 5A**). Although V30M is mostly associated with neuropathy, some patients exhibit a predominantly cardiac phenotype, especially patients with late-onset disease. Signs of neuropathy in patients with SSA and cardiac mutations are not uncommon, despite being mainly associated with cardiomyopathy. Indeed, 16.7% of patients with cardiac mutations display a predominantly neurologic phenotype. Besides predominantly neurologic and cardiac, a substantial proportion of patients carrying the WT protein, the V30M variant, or cardiac mutations, present a mixed phenotype, further underscoring the multisystemic nature of ATTR[101,114].
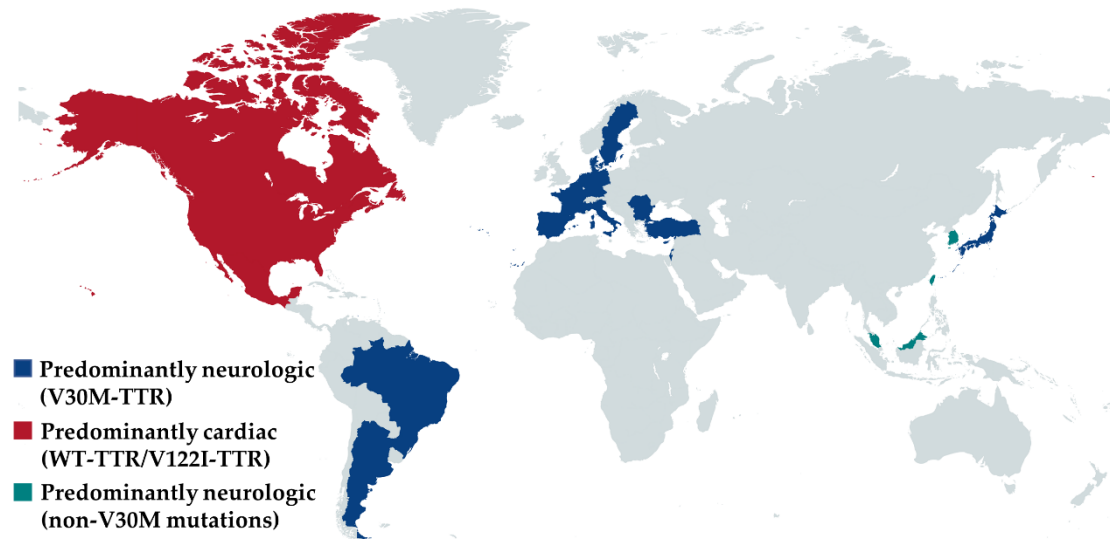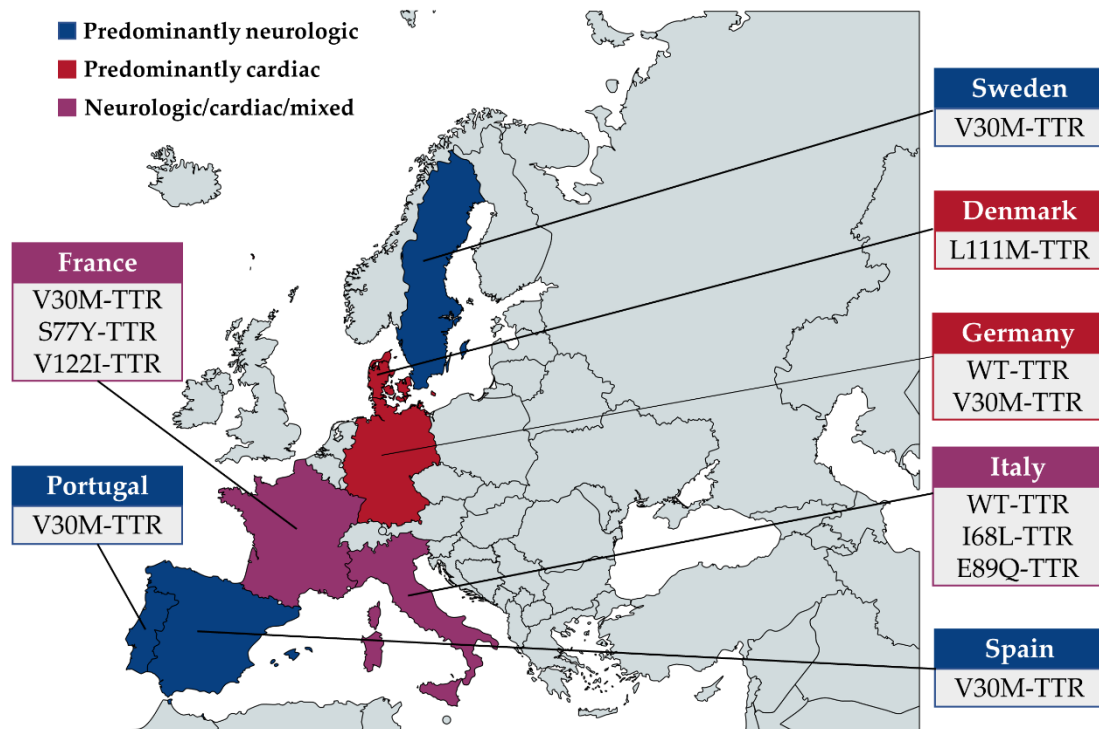
Figure 5. Geographic distribution of ATTR genotype and phenotype across the world. (A) Most common phenotype and genotype among all THAOS patients from North and South America, Europe, and Asia (data cutoff: August 2021)[101]. (B) Subject phenotypes and most frequent TTR mutations observed in patients enrolled in THAOS from six continental Western Europe countries (data from January 2016)[116].

In the Western Europe countries in THAOS registry, subjects from Portugal, Sweden and Spain, mainly manifest a neurologic phenotype, essentially due to the V30M variant[116,145]. In other countries, such as France, Italy, Germany and Denmark, most patients have a cardiac or mixed phenotype and there is greater genetic heterogeneity[102,116] (**Figure 5B**). In France, for example, as many as 29 different mutations have been identified[146], including variants predominantly associated with polyneuropathy (e.g., S77Y[104]) and cardiomyopathy (e.g., V122I[115]). In Italy,

Germany and Denmark, the cardiac phenotype prevails and is mainly associated with WT or cardiac mutations genotype. In Italy and Denmark, the most frequent mutations are I68L and L111M, respectively. In fact, I68L is the most common mutation in Western Europe, after V30M. Other mutation with a primarily cardiac phenotype is T60A[147]. This variant is the most common in the UK[148] and the second most common in the United States[114]; it is frequently encountered in northwest Ireland and populations with Irish ancestry[149]. Regarding SSA, it is observed in all continental Western European countries enrolled in THAOS, except in Portugal, Belgium and Cyprus. Noteworthy, SSA is the most frequent form of ATTR in Germany and Italy[116].

2.4 Prevalence

ATTR is considered a rare disease worldwide. The global prevalence of FAP has been estimated to be around 10,000 persons, although this number could be much higher, ranging from 5,526 to 38,468 persons. The highest prevalence estimates were reported in areas of northern Portugal and northern Sweden, where the disease is endemic[116]. A nationwide epidemiological study in Portugal reported a prevalence of 22.93/100,000 inhabitants with FAP in 2016, corresponding to 1,865 individuals. Moreover, the authors estimated that in the period from 2010 to 2016 there were on average 71 new patients diagnosed with FAP each year, corresponding to an incidence of 0.87/100,000 people[150]. Interestingly, in endemic areas of Sweden the prevalence is lower than expected given the estimated V30M carrier frequency of 2%[151,152]. The lower penetrance of the genetic trait and the higher proportion of late onset cases in Sweden could underlie this difference[142]. In the endemic region of Majorca, in Spain, a prevalence of 5/100,000 inhabitants has been reported[153].

Regarding FAC, there are not many epidemiological studies in the literature. In a prospective study performed in France, the authors found that up to 5% of the persons diagnosed with hypertrophic cardiomyopathy have TTR-FAC related mutations[115]. In the African American population, the frequency of the V122I mutation is 3% to 3.9%[131] and, indeed, one study showed that 10% African Americans with severe heart failure aged 60 years or older carry this mutation[134]. As for FAC, the true prevalence of SSA remains unclear, although it could be higher than the one of hereditary ATTR. In an autopsy study done in Finland, SSA was detected in the autopsy of 25% of subjects 80 years of age or older[154]. Similarly, the prevalence of SSA in autopsied subjects from Japan over 60 years of age was 5.8%, a number that was even higher among individuals older than 90 (34.9%)[155].

Noteworthy, although ATTR is typically considered a rare disease, its prevalence is likely higher than reported. A low disease awareness, especially in non-endemic regions, together with a clinical presentation that overlaps with other pathologies, can result in underdiagnosis and misdiagnosis and bias the prevalence estimates towards lower values[117,151].

3. Transthyretin

TTR is a 55 kDa protein, which is mainly synthesized in the liver and choroid plexus, being secreted into the blood and cerebrospinal fluid (CSF), respectively[156,157]. During adulthood, TTR plasma levels range from 20 to 40 mg/dL[158]. These levels are decreased in newborns and begin to decline after 50 years of age[159]. In the CSF, TTR concentration is lower (5 to 20 mg/L) than in

plasma[160], but it accounts for approximately 25% of the total CSF protein concentration[161]. In addition to the liver and choroid plexus, TTR synthesis has been described in several other tissues[162], such as the retinal pigment epithelium[163] and the pancreatic islets of Langerhans[156].

3.1 Functional roles

TTR has been associated with a wide range of functions in humans. Nevertheless, the most relevant and prominent role of TTR is the transport of the thyroid hormone thyroxine (T_4) and retinol (vitamin A), which is, in fact, reflected in its name (*trans*porter of *thy*roxin and *retin*ol)[164]. In plasma, T_4 circulates bound to thyroid hormone binding proteins, which include, besides TTR, the thyroid-binding globulin and albumin. The higher affinity of thyroid-binding globulin for T_4, in comparison to TTR, together with the high abundance of albumin in plasma, make that TTR carries only about 15% of the total T_4[165]. On the contrary, T_4 transport in the CSF is mainly mediated by TTR, which distributes up to 80% of the hormone[166]. While TTR binds directly to T_4, its function as retinol transporter relies on the formation of a complex with the retinol-binding protein (RBP). The association of TTR with the RBP-retinol complex occurs in the liver, before it is secreted into the plasma, and is thought to prevent the renal filtration of RBP[167,168]. Of note, binding to RBP does not preclude T_4 binding to TTR[169]. According to its role as a T_4 and retinol carrier, adult knockout (KO) TTR mice showed decreased levels of T_4, RBP and retinol in plasma, yet there were no signs of altered thyroid hormone function or vitamin A deficiency. This suggests that TTR's transporter role could be compensated through other mechanisms [170-172]. On the other hand, developing TTR KO mice presented a delayed bone growth, CNS maturation and intestine and muscle development, supporting a crucial role for TTR in post-natal stages of development. The fact that there are no humans reported that lack TTR further supports this idea[173].

Besides its function as a transport protein, novel activities for TTR have been described in the last years. For example, it was shown that TTR has proteolytic activity, being able to cleave apolipoprotein A-I[174], Aβ[175] and neuropeptide Y[176]. This proteolytic activity has been shown to have beneficial, but also detrimental effects. As an example, apolipoprotein A-I cleavage by TTR decreased its ability to induce cholesterol efflux and increased its amyloidogenicity, both factors contributing to the development of atherosclerosis[174]. On the contrary, the peptides originated from Aβ proteolytic cleavage were shown to have lower amyloidogenicity than the full peptide. Remarkably, TTR was also able to degrade aggregated forms of Aβ, lowering their toxicity, suggesting a neuroprotective effect on AD[175]. This neuroprotective role of TTR in AD has been described in detail in several studies. One of the first evidences relating TTR with Aβ came from the observation that TTR is the most abundant Aβ-binding protein in the CSF[177]. Moreover, TTR concentration in the CSF was shown to be significantly diminished in the brain of AD patients, turning TTR levels into a possible biomarker of the disease[178]. In agreement, the overexpression of human WT-TTR in a transgenic mouse model of AD reduced Aβ deposition and improved the cognitive function and behavioral performance of the animals[179]. Recently, TTR tetramer stability has been proposed to be associated with its neuroprotective effect and, accordingly, the administration of iododiflunisal, a TTR tetrameric stabilizer, to a transgenic mouse model of AD resulted in a smaller pathological phenotype[180]. TTR has been found to have neuroprotective properties in cases of cerebral ischemia as well. When TTR KO mice were subjected to permanent middle cerebral artery occlusion, which is a commonly used model of cerebral

ischemia, they displayed larger infarct areas compared to WT mice. Interestingly, TTR was also shown to promote neurite outgrowth in mice hippocampal neurons in physiological conditions[181]. Thus, the acceleration of memory deficits with aging in TTR KO mice might be explained by the lack of TTR in the hippocampus, as this region plays a key role in learning and memory[182]. This neuritogenic activity of TTR has also been described in the peripheral nervous system, as TTR KO mice presented slower nerve regeneration after sciatic nerve crush compared with WT littermates[183]. Noteworthy, besides TTR's role in proteolysis and its neuroprotective effects in the nervous system, new roles for TTR have been described, including its impact on cellular fate, proliferation and metabolism, and its role in immune system regulation[162].

Overall, new functions are being assigned to TTR, apart from its well-known role as a carrier protein. An extensive comprehension of the physiological functions of TTR is especially relevant since therapies targeting TTR mainly rely on protein stabilization or reduction of protein levels, affecting its activity.

3.2 Structural features

The X-ray crystal structure of human TTR was determined for the first time in 1971[184] by Blake and coworkers and later refined to 1.8 Å resolution[185]. Native TTR was shown to be a homotetramer formed by two identical dimers that are related by a two-fold crystallographic axis (**Figure 6A**). Each monomer is composed of 127 residues that are organized into eight β-strands, named from A to H, forming an inner (DAGH) and outer (CBEF) β-sheets that stack with each other constituting a β-sandwich structure (**Figure 6B**). With the exception of strands A and G, which are parallel, all the other strand interactions are anti-parallel. Additionally, there is a short helix of nine residues between the E and F strands known as the EF helix. The tetrameric structure of TTR is maintained by two interfaces, one between the subunits A(C) and B(D) and other between the subunits A(B) and C(D). The first interface involves the H and F strands from neighboring subunits and is stabilized by numerous hydrogen bonds and by the insertion of residue F87 into a hydrophobic pocket in the opposing subunit. These contacts, known as monomer-monomer contacts, originate a strong dimer interface. On the other hand, the dimer-dimer contacts that form the native tetramer are weaker and mainly consist of hydrophobic interactions between pairs of AB and GH loops (**Figure 6C**). This interface creates two identical hourglass-shaped T_4-binding sites located in opposite sides of the molecule (**Figure 7A**)[185,186]. Noteworthy, the two-fold TTR crystallographic axis runs through the center of the T_4-binding sites, creating a two-fold symmetry in the channel itself. This implies that the ligands either possess molecular symmetry or bind in two-fold related orientations[187].
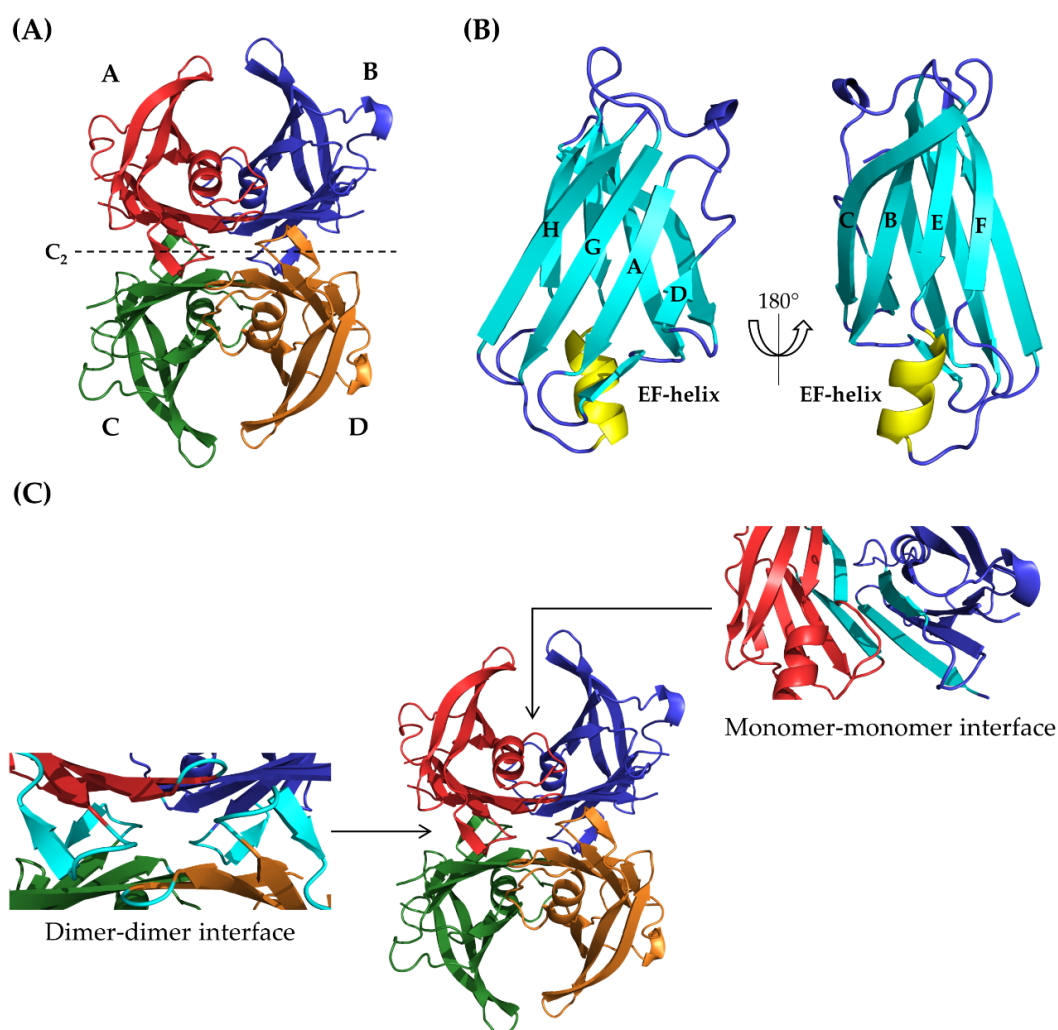
Figure 6. TTR structure. (A) Cartoon representation of the TTR tetramer with its four identical subunits (labeled A, B, C and D) depicted in different colors. The dashed line represents the crystallographic C_2 axis of symmetry that relates the AB and CD dimer. (B) Close-up view of a TTR monomer showing the eight β-strands (in cyan) and the α-helix (in yellow) that form the TTR tertiary structure. (C) TTR tetramer indicating the interface between subunits A and B (monomer-monomer interface) and between the AB and CD dimers (dimer-dimer interface). The regions highlighted in cyan correspond to the β-strands F and H of subunits A and B, as well as the AB and GH loops of the four subunits. These areas play a crucial role in stabilizing the monomer-monomer and the dimer-dimer interface, respectively. Figure prepared using the PDB structure 1F41.

The crystal structure of the TTR-T_4 complex revealed that the T_4-binding pockets are formed by three pairs of symmetric depressions which were termed halogen binding pockets (HBPs) due to the position of the iodine atoms of T_4 (**Figure 7B**). HBP1/1' is located at the entrance of the channel and is mainly formed by the residues K15, L17, T106 and V121 from both subunits. HBP2/2' is placed at the center of the channel and is highly hydrophobic, comprising residues L17, A108, A109 and L110 of both subunits. Finally, HBP3/3' lies in the inner part of the binding pocket and is established by the side chains of A108, L110, Ser117 and T119 of both subunits (**Figure 7C**)[188]. The side chains of L110, S115 and S117 cause a marked local constriction of the T_4 channel near the center, which defines an inner and outer binding cavity[187]. Each binding pocket binds one T_4 molecule in two symmetry related orientations with a 50% occupancy. The hormone binds deep in the pocket, with the phenolic group interacting with S117 and T119 in

the inner binding cavity and the α-carboxylate and α-amino groups interacting with K15 and E54 at the entrance of the channel. Moreover, the 3',5'-iodines contact with the side chains of L17 and L110 and the 3,5-iodines fit within a pocket formed by the methyl groups of T106, A108 and V121 and the methylene of K15[187,188].
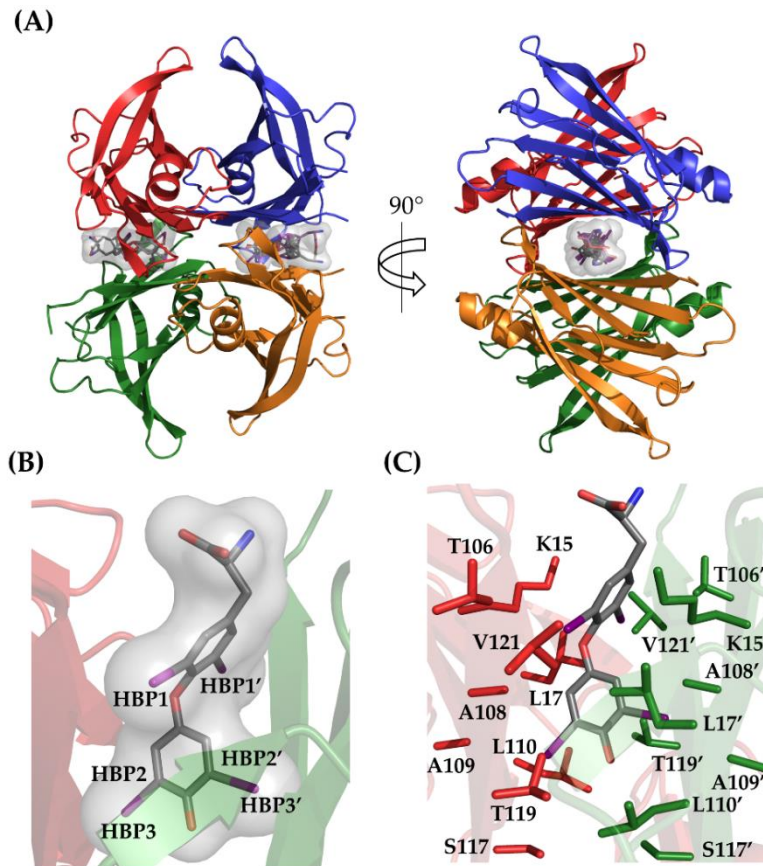
Figure 7. X-ray crystal structure of TTR bound to T₄. (A) Structure of TTR tetramer with two T$_4$ molecules bound in the central hydrophobic channel. The T$_4$ molecules are shown as sticks enclosed in a transparent surface. As a result of the two-fold crystallographic axis, each hormone molecule is found in two symmetry-related conformations in the T$_4$-binding site. (B) Enlarged view of a T$_4$-binding pocket depicting the position of the six HBPs (three from each subunit forming the cavity). To simplify the representation, only one of the two T$_4$ binding orientations is displayed. (C) TTR residues that constitute the HBPs are represented as sticks colored according to the TTR subunit (red for subunit A and green for subunit B). Structural data obtained from PDB file 2ROX.

3.3 Misfolding and amyloid formation

Since the link between TTR amyloid fibril formation and disease was established, many studies have been conducted to try to decipher how TTR amyloidogenesis occurs.

The most accepted theory for TTR aggregation was developed by Jefferey Kelly and coworkers and defends that TTR amyloidogenesis is initiated by rate-limiting tetramer dissociation into monomers, which partially unfold into an amyloidogenic intermediate, and, subsequently, aggregate[189,190] (**Figure 8**). This hypothesis arose from the observation that TTR fibrils could be formed, *in vitro*, at a pH below 5, a condition in which tetrameric TTR dissociates into monomers[189,190]. Moreover, by studying the self-assembly pathway of an engineered TTR monomer (M-TTR), the authors concluded that the amyloidogenic intermediate is not the native

monomer, but one with a defined, yet altered, tertiary structure. Importantly, at a pH lower than 3.9, M-TTR significantly loses its tertiary structure, which is accompanied by an increase in β-sheet content and hydrophobic exposure. This alternative conformation is consistent with a molten globule-like state and is significantly less amyloidogenic than the one formed at higher pH [189,191]. Other question addressed by Kelly's group was how TTR tetramer dissociation occurs. For that purpose, two constructs were used, one tethering the A(C) and B(D) subunits and another tethering the A(B) and C(D) subunits. The observation that the second construct is unable to undergo dissociation led the authors to hypothesize that TTR tetramer dissociation occurs by scission of the weaker AB/CD dimer-dimer interface[192].
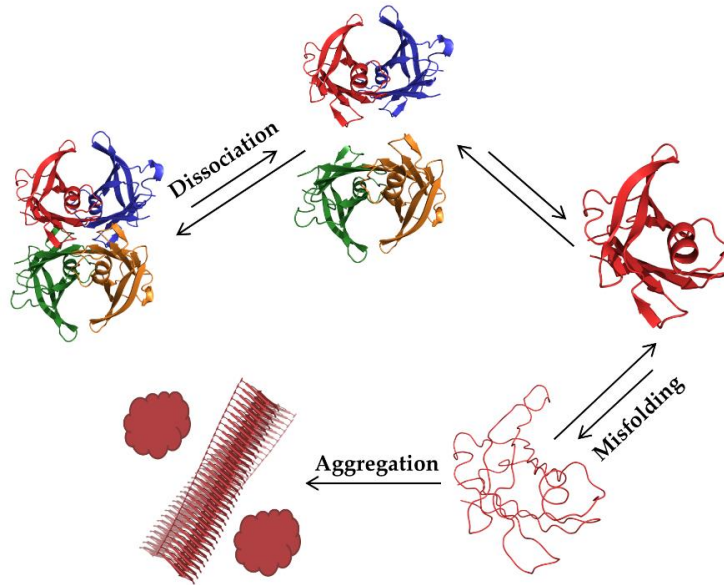
Figure 8. The mechanism of TTR aggregation. TTR aggregation is thought to be initiated by rate-limiting tetramer dissociation at the AB/CD dimer-dimer interface, originating a pair of dimers that rapidly convert into monomers. These monomers are highly prone to misfold, forming an amyloidogenic intermediate, which ultimately leads to the production of amyloid fibrils and amorphous aggregates.

After studying the first steps of TTR aggregation, researchers investigated how the monomeric amyloidogenic intermediate is converted into amyloid fibrils[193]. The aggregation kinetics of most amyloid forming proteins follows a nucleation-dependent polymerization (**Figure 9A**)[6]. In this case, the rate-limiting step is the generation of a nucleus, often composed by several subunits, which takes place during the lag phase. After nuclei formation, fibril growth occurs rapidly through the constant addition of monomers, until the amount of monomers in solution decreases, leading to a rate decline and, ultimately, to the saturation phase[194]. In this model, the existence of an oligomeric nucleus, which is the highest energy specie along the pathway, has two important consequences: (1) the rate of polymerization shows a high-order dependence on the concentration of the monomeric precursor, and (2) the reaction is significantly accelerated upon the addition of preformed aggregates, named seeds[195]. On the contrary, the rate of TTR aggregation does not show a high-order dependence on M-TTR concentration and is not increased by seeding. These observations suggested that TTR aggregation under partially denaturing conditions follows a downhill polymerization in which the amyloidogenic monomer is the highest energy specie (**Figure 9B**). In other words, after the amyloidogenic intermediate is

formed, all the steps along the pathway are thermodynamically favorable and essentially irreversible[193]. Of note, the mechanism here explained assumes that a low pH medium is required for TTR aggregation, which was proposed to be produced *in vivo* by the lysosomes[196]. On the contrary, Quintas et al., showed that TTR tetramer dissociates into non-native monomeric species at pH 7.0 and nearly physiological ionic strengths, suggesting TTR amyloidogenesis can occur under natural conditions[197].

(A)

(B)
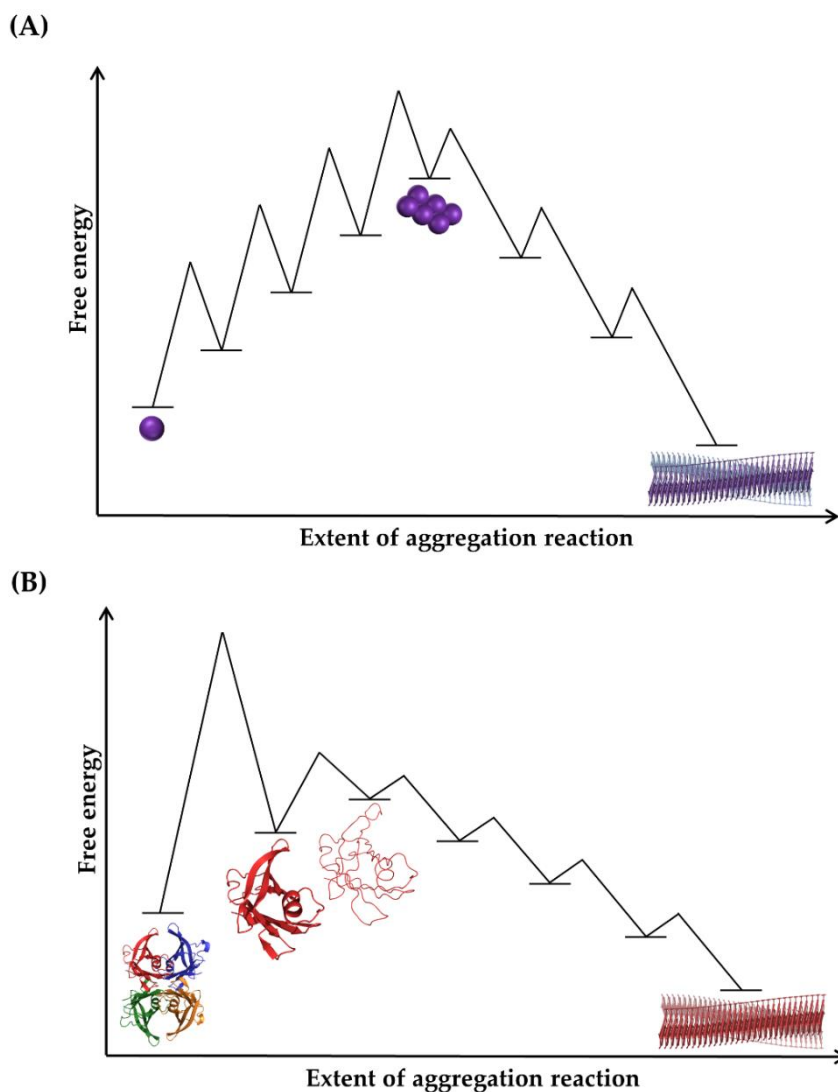
Figure 9. Nucleation-dependent and downhill polymerization models. (A) The classic model of nucleated polymerization involves the initial formation of an oligomeric nucleus from the unstructured monomer through a series of unfavorable equilibria. After the nucleus is created, the polymer can growth by the favorable addition of monomers. (B) On the contrary, TTR aggregation is thought to be a downhill polymerization. In this case, the rate-limiting step is the dissociation of the TTR tetramer, after which an amyloidogenic monomer is produced. Once this intermediate is formed, all the association steps that lead to aggregation are energetically favorable.

More recently, a new mechanism for TTR amyloidogenesis was proposed, which defends that TTR aggregation *in vivo* is triggered by proteolytic cleavage[198]. The idea of a role for proteolysis in TTR amyloidogenesis came from the observation that the TTR residue 49-127 fragment is a major component of *ex vivo* TTR amyloid fibrils, regardless the presence of mutations or their

position[199]. Interestingly, fibrils mainly composed of C-terminal fragments, named type A fibrils, have been associated with cardiac deposition and later age at onset, being especially common in patients with SSA[200,201]. Compelling evidence for the pathological role of TTR proteolytic cleavage came from the studies of Bellotti and coworkers. The authors showed that trypsin cleavage of WT-TTR and pathogenic variants induces fibril formation[198,202]. The TTR S52P variant, which produces a very aggressive clinical phenotype, is highly susceptible to cleavage of the peptide bond K48-T49. The X-ray crystal structure of S52P revealed that proline incorporation at this position leads to the loss of a hydrogen-bond network that is important for the stability of the β-turn that connects strands C and D. The destabilization of this loop likely perturbs the adjacent strands, increasing the susceptibility to proteolysis. Importantly, after cleavage of the peptide bond, the fragment must be released from the native tetramer to cause aggregation, which, *in vitro*, was done by fluid agitation[202]. On the other hand, the WT protein and TTR variants L55P, V122I and V30M were not cleaved by proteolysis unless exposed to shear forces[198]. All in all, Bellotti and collaborators hypothesized that TTR fibrillogenesis involves two phases, a preliminary phase in which the K48-T49 peptide bond is cleaved, without necessarily releasing the 49-127 fragment, and another one in which the fragment is released from the protein followed by fibril formation. Additionally, both phases are enhanced by the presence of shear forces, which could be generated *in vivo* by fluid flow and are particularly high in the heart. This mechanism could provide a basis for selective TTR amyloid deposition in the heart[198,202]. Noteworthy, the fact that trypsin is exclusively located in the duodenum made it highly unlikely that this enzyme could participate in systemic TTR amyloid deposition *in vivo*, thus triggering a search for tryptic proteases with wider tissue distribution. This search led to the identification of plasmin as a leading candidate for TTR proteolytic cleavage *in vivo*. In resemblance to trypsin, plasmin is able to cleave WT-TTR and pathogenic TTR variants, inducing fibrillogenesis, *in vitro*. *In vivo*, plasmin is ubiquitously activated due to its key role on fibrinolysis on the vascular wall, but also on the extracellular matrix. Therefore, the authors hypothesized that, when tetrameric TTR enters in contact with activated plasmin, either in the extracellular matrix or in the fibril clot, it can undergo proteolysis, releasing a mixture of truncated fragments and full-length protomers. Moreover, physiological fibrinolysis is stimulated by physical activity, which was proposed to explain TTR amyloid deposition in the heart and carpal tunnel, which are sites of repetitive and vigorous movement[203]. In agreement, increased plasmin activity was found in cardiac and lingual amyloid deposits of a transgenic mouse model expressing TTR S52P. Furthermore, KO of α_2-antiplasmin, which is the physiological inhibitor of plasmin, enhanced TTR amyloid deposition, supporting the role of plasmin in TTR fibrillogenesis, *in vivo*[204].

Despite enormous efforts, the exact mechanism by which TTR converts into amyloid fibrils *in vivo* is not known. Understanding the molecular mechanism by which TTR aggregates is essential to establish risk factors and for developing new therapies for the treatment of ATTR.

3.4 The amyloidogenic potential of TTR variants

Although the mechanism by which TTR forms amyloid fibrils *in vivo* remains unclear, it is widely accepted that protein stability plays a crucial role. In agreement, most TTR pathogenic variants described to date present a lower stability than the WT protein[197,205-207]. Importantly, TTR mutations can affect its quaternary stability, tertiary stability, or both[38,208]. Pathogenic TTR mutations that decrease tetramer stability are generally believed to lower the kinetic barrier for

TTR tetramer dissociation, shifting the equilibrium towards the monomer, and thus promoting aggregation[207]. This is the case of the FAC-related variant V122I. The V122I-TTR tetramers were reported to have a stability of 25.6 kcal/mol, which is ~ 7 kcal/mol less than the one of WT tetramers[208]. Accordingly, V122I-TTR was shown to dissociate 2 to 3-fold faster than the WT protein, which was translated into a higher rate of fibril formation[38,207]. On the other hand, this mutation does not seem to affect, at least significantly, the tertiary stability of the protein[208]. In this sense, the behavior exhibited by V122I-TTR diverges from the one presented by V30M-TTR, the most common variant associated with FAP. The V30M mutation has been proposed to have a higher impact in TTR tertiary stability than quaternary stability and, indeed, V30M-TTR tetramers were shown to dissociate slightly slower than WT tetramers[38,208]. Additionally, V30M-TTR was reported to form fibrils at a lower rate than V122I-TTR and, especially, L55P-TTR, which is related to a very aggressive form of FAP that manifests around the second decade of life[38,209]. The dissociation half-life ($t_{1/2}$) of L55P-TTR was calculated to be 4.4 hours, which means that it dissociates 10-fold faster than the WT protein[38]. This, together with its reduced tertiary stability, renders the L55P variant extremely aggregation prone, even at physiological pH[38,209]. All in all, it appears that the rate of TTR fibril formation is mainly dictated by the rate of tetramer dissociation[38].

While most TTR mutations reduce its stability, increasing its amyloidogenic potential, some mutations, as T119M, seem to enhance the stability of the protein, hindering aggregation[125]. The T119M variant presents an extremely slow tetramer dissociation rate ($t_{1/2}$ for T119M = 1534 hours; $t_{1/2}$ for WT = 42 hours) and, accordingly, it forms fibrils 3000-fold slower than the WT protein[38]. The incorporation of one or more T119M subunits into V30M homotetramers was shown to increase the kinetic barrier for tetramer dissociation, reducing its amyloidogenicity up to a 90%. This explains why patients carrying V30M and T119M TTR mutations on different alleles (compound heterozygotes) present a milder pathology. The T119M mutation is said to act as a *trans*-suppressor of amyloidosis[125].

Another intriguing observation concerns to the TTR variants that are mainly associated with LA (e.g., L12P, D18G, A25T and V30G). These variants exhibit a dramatically reduced monomer stability, often combined with a decreased tetramer stability[210]. For example, A25T tetramers were shown to dissociate extremely fast ($t_{1/2}$ = 2.1 minutes)[211], whereas D18G-TTR does not even assemble into tetramers[212]. Despite this extreme instability, these variants originate a selective, late onset, CNS pathology, instead of a severe systemic disease, as one would expect. The fact that patients with A25T and D18G ATTR present low or undetectable levels of these TTR variants in the serum, respectively, suggested that these proteins could be poorly secreted by the liver or rapidly degraded. In both cases, this would protect the patients from an early-onset systemic disease[211,212]. In this context, Sekijima et al. studied the secretion of WT-TTR and 32 variants, including those predominantly related to LA, in two cell lines, one from kidney and one from liver. Overall, the authors found that the secretion efficiency of TTR mutants depends both on their kinetic and thermodynamic stabilities, with those exhibiting a combined stability score lower than 0.8 being targeted for endoplasmic reticulum-assisted degradation. In agreement, A25T- and D18G-TTR, which had the lowest combined stability score from the variants analyzed, were secreted at significantly lower amounts than WT-TTR in both cell lines. Indeed, the secretion efficiency of D18G-TTR was almost null. Interestingly, choroid plexus cells were able to secrete A25T-TTR at similar levels than the WT protein and in greater amount than the other

two cell lines[210]. The high intracellular concentration of T_4 in the choroid plexus, together with the fact that TTR is the major T_4 binder in this tissue, led to the hypothesis that T_4 may act as a chaperone and help these proteins to escape degradation. Yet, once the protein is secreted into the CSF, the concentration of T_4 diminishes, facilitating amyloid formation. This could provide an explanation for the tissue-selective deposition of LA-associated TTR variants. Nevertheless, the first symptoms of LA appear late in life, which was proposed to be related to the low concentration of these TTR variants in the CSF[210-212].

Moreover, the role of TTR mutations in the pathogenesis of the disease could be also explained from a structural perspective. Accordingly, understanding the structural basis of TTR destabilization has been a pursued goal since the first TTR X-ray crystal structure was determined. Although numerous crystal structures of WT-TTR and pathogenic mutants have been determined, they have failed to reveal any significant structural changes that could account for their increased amyloidogenicity. In fact, almost all TTR variants crystallize in the same space group as the WT protein, $P2_12_12$, with a dimer in the asymmetric unit, emphasizing that there is little perturbation to the overall structure of the protein, at least under native like conditions[213]. The L55P variant is one of the few exceptions, as it was observed to crystallize in the space group C2, containing a tetramer and two dimers in the asymmetric unit. The analysis of this crystal structure revealed the disruption of hydrogen bonds between strands D and A, which led to the formation of different intermolecular contacts[214]. In an attempt to derive information relative to amyloidogenesis, some TTR variants have been crystallized at low pH, which is expected to disclose structural changes that are relevant for fibril formation[215,216]. For example, the structure I84S at pH 4.6 showed significant conformational changes in the EF helix/loop region that were not detected at pH 7.0[215]. Yet, not all TTR variants crystallized at lower pH showed differences, making it difficult to understand the impact of the mutations[216].

Importantly, a crystal structure provides a static snapshot of the protein, which disregards its flexibility, likely masking the conformational changes that occur in solution[213]. In this context, recent works on the effect of pathogenic mutations on TTR structure have used techniques that provide more information on protein dynamics, such as NMR or molecular dynamics simulations[217-219]. In one study, the structure of V30M- and L55P-TTR, and the suppressor variant T119M, was investigated by native-state NMR-based hydrogen exchange. The authors observed that the protection factors in L55P were much lower than the ones of V30M- and T119M-TTR, including the residues at the interface, which suggests that it is highly prone to undergo conformational fluctuations. On the other hand, V30M appeared to affect mostly the tertiary structure of TTR, as the protection factors at both interfaces resemble the ones of T119M-TTR. In particular, V30M, which is located in the β-strand B, seems to destabilize the strands B and E from the front sheet (CBEF) and, to a lower extent, the strands A and G of the back sheet and the β-turn between strands A and B. These residues presented remarkable stability in T119M-TTR. Of note, the residues on the β-strands C and D had the lowest protection factors for any of the variants studied[218]. The different structural perturbations caused by the V30M and L55P mutations were also shown by analysis of the NMR chemical shifts of these two variants. Whereas L55P causes significant structural changes in both β-sheets, V30M mainly perturbs the CBEF sheet[217]. In agreement with the X-ray crystal structure of L55P-TTR[214], the β-strand D is disrupted in solution. Additionally, the conformation of strand A varies significantly, further affecting the strands G and H. In this work, the authors have also investigated the impact of the

V122I mutation on TTR structure and verified that, contrarily to V30M and L55P, it mainly disturbs the mutation site, affecting both the strong and weak subunit interfaces. Moreover, in line with the idea that aggregation can be initiated by small unfolding events that occur under native conditions (e.g., thermal fluctuations), NMR relaxation dispersion experiments were performed. Interestingly, these assays showed that V30M-, L55P- and V122I-TTR transiently populate an excited state with an altered conformation in the subunit interfaces that resembles the one sampled by the WT protein. However, the population of the excited state and the rate at which it is formed was different for each protein. According to its lower overall stability, L55P-TTR had the highest population of excited state. On the other hand, V30M- and V122I-TTR presented lower excited state populations, which were identical to the one of WT-TTR. The fact that V30M tetramers are at least as stable as WT tetramers, might explain their similar excited state populations. For V122I-TTR, this was unexpected as this variant dissociates faster than the WT protein. This could justify that the rate of formation of the excited state was higher than for WT-TTR, despite both states are similarly populated[217].

In the future, the combination of X-ray crystallography with methods that incorporate protein flexibility will hopefully increase our knowledge on the molecular mechanisms by which TTR mutations enhance its amyloidogenicity and, ultimately, assist the rational design of aggregation inhibitors.

3.5 TTR aggregated species and tissue damage

TTR aggregation has been shown to exert its toxic effect through distinct pathways. On one hand, the build-up of amyloid fibrils in ATTR may induce tissue damage by direct compression, obstruction, or disturbance of local blood circulation. The incidence of CTS, vitreous opacities and glaucoma are clear examples of tissue damage caused by TTR fibrils[100]. Additionally, a recent electron microscope study demonstrated that fibril elongation leads to the distortion and subsequent atrophy of Schwan cells, the glial cells of the peripheral nervous system, supporting the idea that TTR fibrils themselves can be toxic[220]. On the other hand, it has been proposed that TTR cellular toxicity is mainly mediated by TTR monomers and, especially, low molecular weight oligomers[221-223]. The relevance of protein oligomers in the pathogenesis of amyloidosis is well-established and it has been reported for several amyloid diseases, including AD and PD[224,225]. Moreover, age-related oxidized forms of TTR were shown to be cytotoxic to a human cardiomyocyte cell line, suggesting that oxidative modifications of TTR may contribute to the onset of SSA[226].

Several mechanisms have been proposed to explain the cytotoxicity of TTR. For example, low molecular weight TTR oligomers (<100 nm diameter) were shown to induce an influx of extracellular Ca^{2+} in human neuroblastoma cells, disrupting the cytoplasmic Ca^{2+} homeostasis. The increase in intracellular Ca^{2+} was due to the activation of voltage-gated calcium channels and was more pronounced for L55P-TTR than V30M-TTR, which agrees with their different amyloidogenic potential[222]. The perturbation of Ca^{2+} homeostasis can trigger the endoplasmic reticulum-specific stress response. Accordingly, the incubation of a mouse neuronal cell line with TTR oligomers caused the activation of the ER stress response, in a process dependent on Ca^{2+} efflux from the endoplasmic reticulum to the cytosol. As a consequence, caspase-3 was found to be activated, suggesting that TTR oligomers can induce cell death[227]. In addition, Saraiva and

coworkers observed an increased expression of the receptor for advanced glycation end products (RAGE) beginning at the stage 0 of FAP, i.e., when amyloid deposition is not evident. The cellular receptor RAGE is a member of the immunoglobulin super family and a key player in the inflammatory response. Upon engagement, RAGE activates multiple intracellular signal molecules, such as the nuclear transcription factor kB, which, in turn, can induce the expression of proinflammatory cytokines as IL-1β and TNF-α. In agreement, patients at the stage 0 of FAP exhibited higher levels of IL-1β and TNF-α in a pattern overlapping with RAGE expression. Moreover, as cytokines can stimulate the expression of the inducible form of nitric oxide synthase (iNOS), which produces nitric oxide, the authors examined the levels of iNOS in FAP patients. As expected, enhanced expression of iNOS was observed, already from the stage 0, in a similar distribution that for RAGE and proinflammatory cytokines. Altogether, the sustained activation of RAGE could trigger apoptosis, a mechanism which involves the action of several caspases, including caspase-3. Accordingly, upregulated levels of caspase-3, which overlapped with the expression of the three molecules commented before, were observed in FAP patients, especially in the late stage of the disease. Finally, the authors addressed whether TTR fibrils were also able to induce these responses in cell culture models. The results of the *in vitro* studies revealed a RAGE-dependent increase in the levels of cytokines and iNOS upon incubation with TTR fibrils. The fact that the fibrillar preparations used in the study contained short fibrils and amorphous aggregates, together with the presence of neuronal stress at early stages of the disease (i.e, before amyloid deposition), supports the hypothesis that early aggregated species may underlie TTR cytotoxicity[228]. The role of RAGE in TTR pathogenesis has been described in another work from the same group. In this study, the authors observed a marked up-regulation of the extracellular signal-regulated kinases 1 and 2 (ERK 1/2) in FAP patients, which started at the stage 0 of FAP and was sustained during the course of the disease. The activation of ERK 1/2 was also seen in Schwann-like cells treated with TTR aggregates and was found to be mediated by RAGE. Additionally, it was shown that inhibiting ERK activation abolishes the TTR aggregates-mediated caspase-3 activation, suggesting that ERK cascades may be key players in the cytotoxicity of TTR aggregates[229]. Other mechanisms by which TTR aggregation can elicit damage have been proposed and include the disturbance of the actin cytoskeleton, the disruption of endothelial cells of blood vessels, among others[162].

4. The landscape of disease-modifying therapies for ATTR

Currently available therapeutic strategies for ATTR can be divided into two major groups: those that reduce the amount of circulating TTR, and those that modulate TTR aggregation. Liver transplantation (LT) to suppress the main source of TTR has been the gold standard treatment for ATTR. More recently, gene-silencing approaches have emerged as a new strategy to block TTR synthesis. On the other hand, therapies targeting the amyloidogenic cascade mostly rely in the use of pharmacologic compounds, such as TTR stabilizers, aggregation inhibitors and amyloid fibril disruptors[85,230].

4.1 Liver transplantation

The first LT in patients with FAP was done in 1990 and replaced almost all V30M-TTR in circulation by the donor WT-TTR[231]. The efficacy of LT has been demonstrated in follow-up

studies showing an arrest in disease progression, as well as an improvement in sensory and motor impairment[232]. The data accumulated from 20 years of experience with LT by the Familial Amyloidotic Polyneuropathy World Transplant Registry reveals that approximately 125 LTs were performed and reported annually worldwide. The 20-year survival after LT was 55.3%; improved survival was more pronounced in patients carrying the V30M mutation that non-V30M mutations. Apart from the presence of a V30M mutation, an early AO (< 50 years), a short disease duration before LT and a better nutritional status have been associated with a better outcome[233]. Additionally, there are reports of amyloid deposition even after LT, mainly in the cardiac tissue[234], but also in the peripheral nerves[235], vitreous humor[236] and leptomeninges[237]. The analysis of the amyloid fibrils from cardiac and peripheral nerve tissue of patients that undergone LT showed that they were mostly composed of WT protein[235,238]. The deposition of WT-TTR after LT was proposed to occur by a seeding mechanism caused by previously existing amyloid fibrils[235,239]. Of note, seeding of TTR aggregation has not been observed *in vitro*, which probably stems from the different conformation of TTR aggregates formed *in vitro* versus *in vivo*[240]. On the contrary, the accumulation of amyloid fibrils in the vitreous humor and in the leptomeninges is likely due to the local synthesis of variant TTR in the retinal pigment epithelium and in the choroid plexus, respectively, which cannot be halted by LT[236,237]. In either case, this can contribute to disease progression, decreasing the effectiveness of LT. Indeed, cardiovascular complications were responsible for 22% of deaths after LT in the World Transplant Registry[233]. In addition to these limitations, posttransplant complications, and the need of organ donors and life-long immunosuppression, has fueled the development of other disease-modifying therapies for ATTR[118,135].

4.2 Gene-silencing agents

Gene-silencing therapies using small interfering RNA (siRNA) and antisense oligonucleotides (ASOs) have recently emerged as a treatment for ATTR. Patisiran (ONPATTRO®, Alnylam Pharmaceuticals Inc.) and inotersen (Tegdsedi®, Ionis Pharmaceuticals Inc.) were the first gene-silencing drugs approved for ATTR[147]. Indeed, patisiran was the first siRNA agent approved in the United States and Europe[241].

Regarding patisiran, it is a double-stranded siRNA formulated as a lipid nanoparticle that is predominantly delivered to hepatocytes. After being released into the cytosol, the siRNA associates with a genetically conserved sequence in the 3'-untranslated region (3'-UTR) of TTR mRNA (both WT and mutated), triggering its degradation[241] (**Figure 10**). Patisiran was approved based on the phase 3, double-bind, placebo-controlled, 18-month-long APOLLO study, which demonstrated improvements in polyneuropathy and all secondary endpoints (quality of life, autonomic neuropathy, and cardiac function) in patients with FAP compared with placebo. The clinical benefits were evident regardless the degree of polyneuropathy, TTR variant and AO. Patisiran administration was generally considered to be safe, with mild-moderate infusion-related reactions reported[242]. The intravenous infusion of patisiran (0.3 mg/kg every 3 weeks) is now approved in more than 30 countries for the treatment of stage 1 and stage 2 FAP[243]. In addition, there is an ongoing phase 3 clinical trial to evaluate the safety and efficacy of patisiran in patients with ATTR-related cardiomyopathy (NCT03997383).

In what concerns inotersen, it is a 20-mer single stranded ASO that binds to the complementary 3'-UTR of TTR mRNA in the nucleus, inducing its degradation. In resemblance to patisiran, inotersen targets the destruction of both WT and mutated TTR mRNA, yet by a different mechanism than the first one (**Figure 10**). The safety and efficacy of inotersen in patients with FAP (stages 1 and 2) was assessed in the phase III, double-bind, placebo-controlled, 15-month, NEURO-TTR trial. This study demonstrated that the patients that received weekly subcutaneous injections of inotersen (300 mg) experienced an improvement in polyneuropathy impairment and quality of life in comparison to those taking placebo. These effects were observed independently of disease stage, TTR mutation and the degree of cardiomyopathy at baseline. The principal safety concerns that were raised in this trial were the occurrence of thrombocytopenia and glomerulonephritis in patients administered with inotersen. Nonetheless, with close monitoring of renal function and platelet count the drug can be given safely[244]. Therefore, inotersen was approved in the United States, Europe and Canada, in 2018, for treating stage 1 and stage 2 FAP[245]. Additionally, inotersen was shown to delay the progression ATTR-related cardiomyopathy in patients with moderate-to-severe disease[246] and there is a phase 2 clinical trial currently testing its tolerability and efficacy in this disorder (NCT03702829).
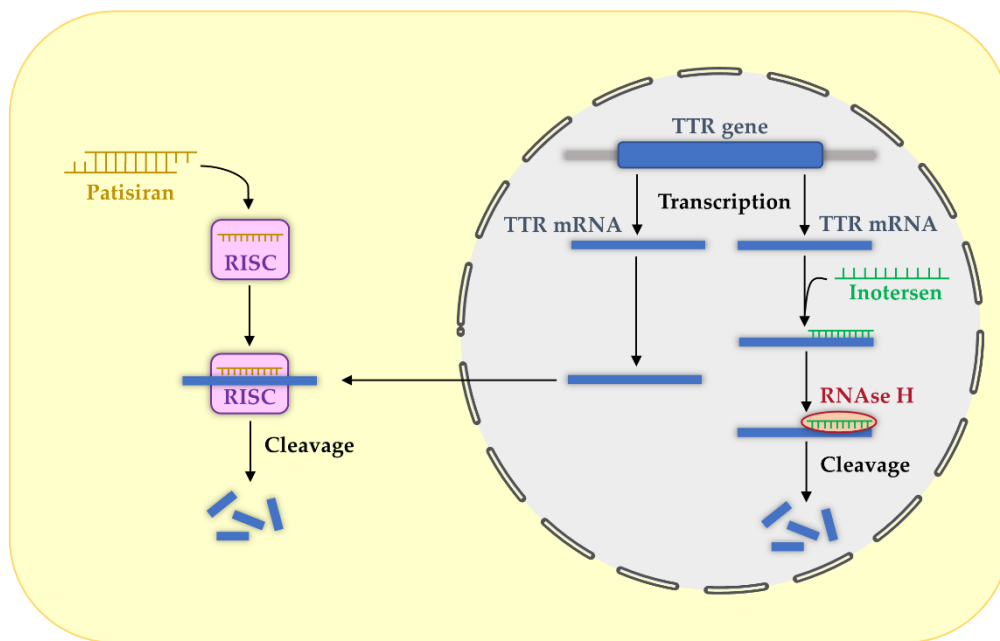
Figure 10. Schematic representation of the mechanism of action of patisiran and inotersen. Patisiran and inotersen bind to TTR mRNA (both WT and mutated), triggering its degradation either in the cytoplasm (patisiran) by the RNA-induced silencing complex (RISC) or in the nucleus (inotersen) by ribonuclease H (RNAseH). In the case of patisiran, the double stranded siRNA is cleaved by Dicer (not shown here) before binding to RISC.

Other gene-silencing drugs that are under investigation for the treatment of hATTR include vutrisiran and eplontersen. Vutrisiran (AMVUTTRA®, Alnylam Pharmaceuticals Inc.) is a siRNA that is conjugated with N-acetylgalactosamine, allowing its direct delivery to the liver. Due to its increased chemical stability, vutrisiran can be administered once every 3 months by subcutaneous injection[243]. Vutrisiran was approved in the United States and Europe for the treatment of FAP (stages 1 and 2) based on the positive results from the phase 3 HELIOS-A

study[243] and is currently undergoing clinical trials for ATTR-related cardiomyopathy (NCT04153149). Eplontersen is an ASO that has been ligand-conjugated to allow receptor-mediated uptake by hepatocytes. Enhanced delivery of the drug to the liver was shown to improve the safety and potency of the drug, in comparison to inotersen[247]. Phase 3 studies have been initiated to evaluate the efficacy and tolerability of eplontersen in patients with ATTR-related polyneuropathy (NCT04136184) and cardiomyopathy (NCT04136171).

4.3 TTR kinetic stabilizers

TTR kinetic stabilizers are small molecules that bind to the largely unoccupied T_4-binding sites, in both WT and mutant proteins, increasing the kinetic stability of the native structure, thereby preventing TTR tetramer dissociation and amyloidogenesis[85,248]. The kinetic stabilizer strategy has been inspired by the discovery of the *trans*-suppressor mutation T119M[125]. The X-ray crystal structure of T119M-TTR revealed that this mutation introduces new inter-subunit contacts, increasing both the monomer-monomer and the dimer-dimer contact area[249]. In the same manner, researchers hypothesized that small molecules that can bind with high affinity to one or both T_4-binding sites could bridge the AB and CD dimers, stabilizing the weak dimer-dimer interface[250]. The proof of concept came from the observation that T_4 itself inhibits the aggregation of TTR *in vitro*[251] and fueled numerous screening[252-254] and structure-based drug design[255-257] programs for finding stabilizers that bind with high affinity and selectivity to TTR. Most of the TTR kinetic stabilizers discovered thus far have two substituted aromatic rings (aryl rings) connected by a linker (**Figure 11A**). Typically, one aromatic ring bears polar substituents while the other is substituted with alkyl groups, halogen atoms, or a combination of both. Although some TTR ligands bind in the reverse mode, i.e., with the polar substituents pointing to the inner binding cavity (**Figure 11B**), the majority prefers the other way around, the so-called forward binding mode (**Figure 11C**). Another common characteristic of TTR ligands, including T_4, is their tendency to bind with negative cooperativity, meaning that when they bind to the first binding-site, there is a loss of affinity for the second binding-site[250,258]. The mechanism of negative cooperativity is thought to arise from conformational changes that occur when the molecule binds to the primary site, which are transmitted to the second site, affecting its ability to bind to the second molecule[259,260].

Despite more than one thousand small-molecule stabilizers have been discovered and synthesized, only four have undergone clinical trials in ATTR: diflunisal, tafamidis, tolcapone and AG10 (**Figure 11A**).
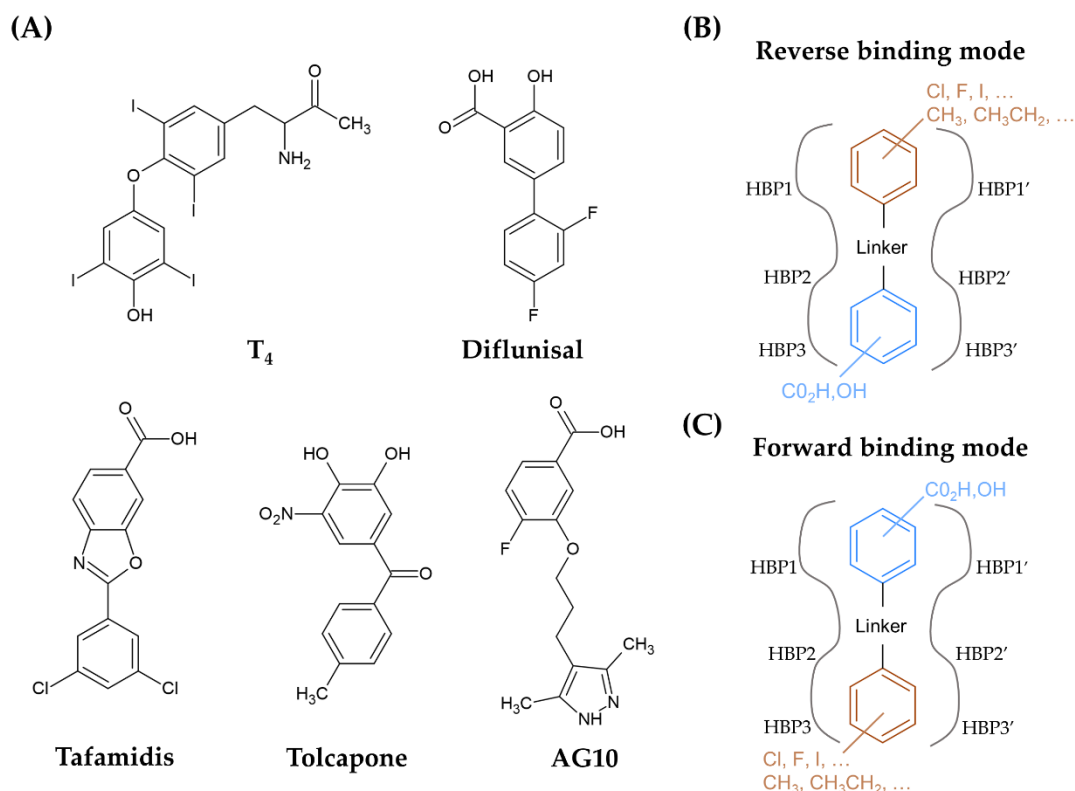
Figure 11. **Structure of TTR kinetic stabilizers.** (A) Chemical structures of T_4 and of the four TTR small molecule stabilizers that have reached clinical trials in ATTR. (B,C) Schematic illustration of the reverse (A) and forward (C) binding mode. Examples of polar substituents (in cyan) and alkyl groups/halogens (in brown) that can replace the hydrogen atoms on the aromatic rings are depicted.

4.3.1 Diflunisal

Diflunisal is a Food and Drug Administration (FDA)-approved non-steroid anti-inflammatory drug that binds to TTR with negative cooperativity (Kd1 = 75 nM; Kd2 = 1 100 nM). The X-ray crystal structure of diflunisal bound to TTR revealed that it binds in both the forward and reverse binding mode. In the forward binding mode, the difluorophenyl ring occupies the HBP2/2', whereas the carboxyl group is placed in the outer binding cavity, forming a salt bridge with K15 (**Figure 12A**). In the reverse mode of binding, the difluorophenyl ring is positioned in the HBP1/1', while the carboxyl group interacts electrostatically with A108 and T119[261].

Despite its modest binding affinity and selectivity, diflunisal was shown to effectively stabilize TTR in human plasma, both *in vitro* and after oral administration. The high plasma concentration of orally administered diflunisal was proposed to underlie its ability to prevent TTR tetramer dissociation[262,263]. To determine if diflunisal can slow the progression of the disease in patients with FAP, a placebo-controlled phase III clinical trial was conducted. The results of this study revealed that the intake of diflunisal (250 mg b.i.d.) for 2 years slowed the progression of neurological impairment and improved the quality of life, in comparison with placebo. Noteworthy, the effect of diflunisal was not dependent on the TTR mutation, nor on the severity of the disease at baseline[264]. The beneficial impact of diflunisal on clinical outcomes was observed to be sustained after 2 years of treatment[265]. Moreover, diflunisal was reported to improve cardiac function[265,266] and autonomic symptoms[267]. However, diflunisal can induce

some undesired effects related with its NSAID activity, such as renal dysfunction and gastro-intestinal problems[265,266]. Importantly, diflunisal is not approved for ATTR and can only be used off-label.
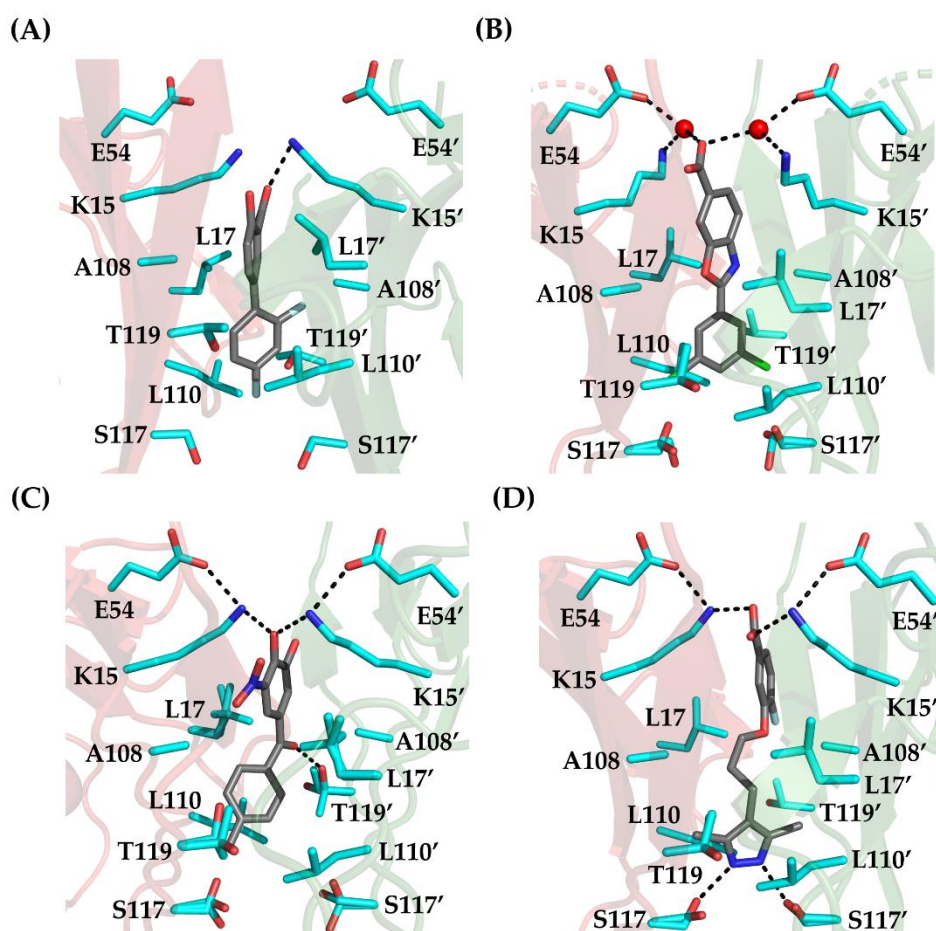
Figure 12. Interaction of the ligands with TTR. (A-D) Detailed view of the binding of WT-TTR to diflunisal (A), tafamidis (B) and tolcapone (C), and of V122I-TTR binding to AG10 (D). Although diflunisal can bind TTR in both the forward and reverse binding modes, only the forward mode is shown in this illustration. TTR residues that are known to be relevant for the binding of ligands are represented as sticks (in cyan). Black dashed lines indicate the most important interactions between the molecules and TTR. Figure prepared from PDB structures 3D2T (A), 3TCT (B), 4D7B (C) and 4HIQ (D).

4.3.2 Tafamidis

Using a structure-based drug design approach, Kelly's group discovered tafamidis (Vyndaqel®, Pfizer Inc.). Tafamidis is a benzoxazole that binds TTR with high affinity and negative cooperativity (Kd1 = 3 nM; Kd2 = 278 nM), protecting the tetramer from dissociation both under denaturing and physiological conditions. Moreover, tafamidis was shown to bind with high selectivity and kinetically stabilize TTR in human plasma from healthy individuals (WT-TTR) or patients carrying different amyloidogenic mutations, including V30M and V122I. The crystal structure of WT-TTR with tafamidis shows that it binds in the forward binding mode, with the 3,5-dichloro moiety pointing to the inner binding cavity and the carboxyl group to the outer binding cavity (**Figure 12B**). In this orientation, the chloride atoms establish hydrophobic

interactions with the residues in the HBPs 3/3' and the carboxyl group forms water mediated hydrogen bonds with K15/15' and E54/E54'[268]. The higher binding affinity of tafamidis, in relation to diflunisal, is hardly explained from the crystal structures and has been attributed to an enhanced halogen binding capability of the chloride atoms[248].

The efficacy and safety of tafamidis (20 mg q.d.) was evaluated on an 18-month double-blind placebo-controlled trial in patients with the V30M mutation and early-stage disease. Although it was not possible to achieve statistical significance in the coprimary endpoints, likely due to the high number of patients that discontinued the treatment to undergo LT, patients who received tafamidis had less neurological deterioration, better nutritional status and maintained their quality of life[269]. The long-term (up to 6 years) safety and efficacy of tafamidis was addressed in an open-label extension study[270], which included patients with V30M and non-V30M mutations that completed previous studies[269,271,272]. Regarding patients with V30M-ATTR, this study demonstrated that those who received tafamidis from day 1 experienced less polyneuropathy progression than those that started treatment after 18 months, supporting the value of early intervention. In patients with non-V30M-ATTR, the neurologic function seemed to get worse throughout the years, which could be related with their older age and the more advanced state of the disease[270]. Although other studies have reported clinical efficacy of tafamidis in patients with advanced disease and non-V30M mutations[273,274], it appears to be lower[270,273,274]. Remarkably, tafamidis did not raise safety concerns in any of these studies[269-274]. Altogether, these results led to the approval of tafamidis for the treatment of early-stage FAP in Europe, Japan, and several other countries (e.g., Mexico and Argentina). Of note, the use of tafamidis in patients with early-stage FAP was not approved by the FDA.

Recently, a phase III clinical trial was conducted to address the efficacy of tafamidis on cardiomyopathy. The primary analysis revealed that the administration of tafamidis to patients with cardiomyopathy (hATTR and SSA) was associated with lower mortality and cardiovascular-related hospitalizations, and with slower decline in functional capacity and quality of life. Tafamidis was approved for the treatment of ATTR-related cardiomyopathy in several countries, including the United States[275].

4.3.3 Tolcapone

Tolcapone is a catechol-*O*-methyltransferase inhibitor approved by the FDA for the treatment of PD, which has been repurposed for ATTR. *In vitro*, tolcapone was shown to inhibit the aggregation of WT- and V122I-TTR more effectively than tafamidis. Additionally, it was observed that tolcapone selectively binds to TTR in plasma, displaying a higher *ex vivo* stabilizing activity than tafamidis in samples from control individuals and V30M-TTR carriers. The interaction of tolcapone with WT-TTR was assessed by isothermal titration calorimetry and revealed that it has a similar binding affinity for the first binding site (Kd1 = 21 nM) than tafamidis (Kd1 = 5.7 nM), but a much higher affinity for the second one (Kd2 for tolcapone = 58 nM; Kd2 for tafamidis = 260 nM), which could explain its increased activity. For V122I-TTR, tolcapone was found to bind with high affinity and no-cooperativity to both binding sites (Kd = 56 nM); remarkably, the Kd2 for binding of tafamidis to this TTR variant was estimated to be 1.1 µM. In both cases, tolcapone binding to TTR was enthalpically driven, suggesting that it establishes specific contacts with the protein. The X-ray co-crystal structure of WT-TTR with tolcapone showed that it binds in the

forward binding mode, with the 4-methyl-phenyl group occupying the inner binding cavity and the 3,4-dihydroxy-5-nitrophenyl placed in the outer binding region (**Figure 12C**). In the inner binding cavity, the 4-methyl-phenyl ring establishes hydrophobic interactions with the residues in the HBPs 2/2' and 3/3' and the central carbonyl group of tolcapone forms a hydrogen bond with the side chain of T119. In the outer binding cavity, one of the hydroxyl groups of the 3,4-dihydroxy-phenyl ring forms electrostatic interactions with K15 from both subunits, which, in turn, stabilize the salt bridges between K15/15' and E54/54'. These electrostatic interactions by K15, together with hydrogen bonding to T119M, probably underlie the higher binding affinity and stabilizing activity of tolcapone, in respect to tafamidis. The crystal structure of V122I-TTR bound to tolcapone revealed similar interactions than the ones described for the WT protein, explaining why it binds with higher affinity to this variant and has a higher anti-aggregational effect than tafamidis[276]. All in all, these results highlighted the potential of tolcapone for the treatment of ATTR and, indeed, it already passed a phase IIa open-label clinical trial for FAP. In this study, tolcapone caused a clear stabilization of plasmatic TTR in all participants, with no major adverse effects[277].

Remarkably, tolcapone is able to cross the blood-brain barrier[278] and was shown to inhibit the aggregation of the LA-associated variant A25T[276], suggesting that it could become the first small-molecule treatment for LA.

4.3.4 AG10

AG10 is an effective and selective TTR stabilizer that was discovered by combining high-throughput screening with structure-based drug design[279,280]. AG10 presented a higher selectivity and tetramer stabilizing activity than tafamidis in plasma samples from healthy individuals and patients harboring the V122I mutation. More importantly, the stabilizing effect of AG10 was similar for WT- and V122I-TTR tetramers, whereas tafamidis had a significantly lower effect on V122I-TTR, especially in plasma from a homozygous patient (V122I homotetramers). The enhanced potency of AG10 in comparison to tafamidis could not be explained by their binding affinities, as they were essentially identical (Kd1 for AG10 = 4.8 nM; Kd2 for AG10 = 314 nM; Kd1 for tafamidis = 4.4 nM; Kd2 for tafamidis = 280 nM). Nonetheless, the nature of AG10 binding to TTR was completely different. While the binding of tafamidis was almost equally driven by enthalpy and entropy, AG10 binding was entirely enthalpically driven. The X-ray crystal structure of AG10 bound to V122I-TTR revealed that it binds in the forward binding mode, with the 3,5-dimethyl-1*H*-pyrazole ring sitting in the inner binding cavity, where it establishes two hydrogen bonds with S117/117'. Additionally, the methyl groups of the ring engage in hydrophobic interactions with the residues lining the HBP3/3' (**Figure 12D**). In the outer binding cavity, the carboxylate group of the *para*-fluoro-aryl ring interacts electrostatically with K15/K15', while the fluorine atom enters in contact with a hydrophobic region of HBP1. The additional interactions that AG10 forms within the binding site, especially at the base of the pocket, were proposed to underlie the larger enthalpic contribution for AG10 binding in comparison to tafamidis[280]. Importantly, binding enthalpy was found to be correlated with the potency and selectivity of TTR ligands in plasma[281,282], which might explain why AG10 has a higher tetramer stabilizing activity than tafamidis, despite their similar binding affinities[282]. Recent results from a phase II clinical trial demonstrated the safety and efficacy of AG10 for the

treatment of patients with ATTR-related cardiomyopathy, either carrying WT-TTR or pathogenic mutations[283]. A phase III clinical trial is currently ongoing (NCT03860935).

4.4 Other therapeutic approaches

Apart from the abovementioned therapies, other options for treating ATTR have been explored. For example, the combination of doxycycline, an antibiotic with potent TTR fibril disruption activity, and tauroursodeoxycholic acid, a biliary acid that decreases the amount of cytotoxic nonfibrillar TTR aggregates, was shown to have a synergistic effect in reducing TTR deposition in a mouse model carrying V30M-TTR[284]. Preliminary data from a small phase 2 clinical trial revealed that the combined administration of doxycycline and tauroursodeoxycholic acid for 1 year stabilizes the progression of polyneuropathy and cardiac disease in patients with hATTR, with no major adverse events[285]. Additionally, a humanized monoclonal antibody designed to target and clear misfolded TTR species has been developed (NNC6019). Of note, NNC6019 (formerly known as PRX-004) does not recognize the native protein, since it binds to residues 89-97, which are buried in the tetramer[286]. In preclinical studies, NNC6019 was shown to inhibit amyloid fibril formation and to promote the elimination of fibrils by antibody-mediated phagocytosis[287]. This antibody has completed a phase I study in patients with hATTR (NCT03336580) and has already entered in phase 2 clinical trials (NCT05442047). Despite the preliminary positive data on these two therapeutic approaches, further studies are required to evaluate their benefits.

RESEARCH GOALS AND OBJECTIVES

The main goal of this thesis is to develop small molecules that bind with high affinity and selectivity to TTR, efficiently stabilizing the protein and inhibiting its aggregation, and with optimal pharmacokinetic properties. For this purpose, we have mostly relied on the structure of TTR:kinetic stabilizer complexes as they provide important information regarding protein-ligand interactions that are likely to play a role in transthyretin stabilization. Importantly, we intend to evolve kinetic stabilizers that can target both non-hereditary and hereditary forms of ATTR, that are devoid of toxicity, and that are more economic than the current drugs in the market. Additionally, we aim at exploring, for the first time, the use of mass spectrometry-based hydrogen deuterium exchange (HDX) and fast photochemical oxidation of proteins (FPOP) for studying the impact of pathogenic mutations and kinetic stabilizers on the structural dynamics of TTR. In this context, we intend to investigate the application of these techniques as a screening methodology that allows to monitor stabilizing/destabilizing effects, while being faster and requiring lower amounts of protein than the current assays.

The principal objectives of the present thesis are:

Objective 1: To evaluate the effect of tolcapone on the aggregation and stability of TTR variants related to familial leptomeningeal amyloidosis (A25T-, V30G- and Y114C-TTR).

Objective 2: To apply molecular dynamics simulations to the rational design of tolcapone derivatives with optimized anti-amyloidogenic activity.

Objective 3: To design a derivative of the potent anti-amyloidogenic compound identified in objective 2 with enhanced pharmacokinetic parameters.

Objective 4: To explore the potential of HDX and FPOP techniques for structure-based drug design, using TTR as a model.

CHAPTER 1

Tolcapone, a potent aggregation inhibitor for the treatment of familial amyloid leptomeningeal amyloidosis

Tolcapone, a potent aggregation inhibitor for the treatment of familial leptomeningeal amyloidosis

Francisca Pinheiro[1] (iD), Nathalia Varejão[1] (iD), Sebastian Esperante[2] (iD), Jaime Santos[1] (iD), Adrián Velázquez-Campoy[3,4,5,6] (iD), David Reverter[1] (iD), Irantzu Pallarès[1] (iD) and Salvador Ventura[1] (iD)

1 Departament de Bioquímica i Biologia Molecular, Institut de Biotecnologia i Biomedicina, Universitat Autònoma de Barcelona, Spain
2 INFANT Foundation, CONICET, Buenos Aires, Argentina
3 Department of Biochemistry and Molecular & Cellular Biology, Institute for Biocomputation and Physics of Complex Systems (BIFI), Joint Units IQFR-CSIC-BIFI and GBsC-CSIC-BIFI, Universidad de Zaragoza, Spain
4 Aragon Institute for Health Research, Zaragoza, Spain
5 Biomedical Research Network Center in Hepatic and Digestive Diseases (CIBERehd), Madrid, Spain
6 ARAID Foundation, Gobierno de Aragón, Zaragoza, Spain

Hereditary transthyretin amyloidosis (ATTR) is a disease characterized by the extracellular deposition of transthyretin (TTR) amyloid fibrils. Highly destabilizing TTR mutations cause leptomeningeal amyloidosis, a rare, but fatal, disorder in which TTR aggregates in the brain. The disease remains intractable, since liver transplantation, the reference therapy for systemic ATTR, does not stop mutant TTR production in the brain. In addition, despite current pharmacological strategies have shown to be effective against *in vivo* TTR aggregation by stabilizing the tetramer native structure and precluding its dissociation, they display low brain permeability. Recently, we have repurposed tolcapone as a molecule to treat systemic ATTR. Crystal structures and biophysical analysis converge to demonstrate that tolcapone binds with high affinity and specificity to three unstable leptomeningeal TTR variants, stabilizing them and, consequently, inhibiting their aggregation. Because tolcapone is an FDA-approved drug that crosses the blood–brain barrier, our results suggest that it can translate into a first disease-modifying therapy for leptomeningeal amyloidosis.

Databases

PDB codes for A25T-TTR, V30G-TTR, and Y114C-TTR bound to tolcapone are 6TXV, 6TXW, and 6XTK, respectively.

Introduction

The misfolding and subsequent aggregation of proteins into amyloid deposits are associated with the onset of a variety of debilitating human disorders, affecting millions of people worldwide [1]. In transthyretin (TTR) amyloidosis, secreted soluble TTR undergoes a conformational change to generate toxic extracellular deposits that lead to disease. Plasma-circulating TTR is synthesized by the liver. The protein can also be found in the cerebrospinal fluid (CSF) and in the eye, produced by the brain's choroid plexus and the retinal pigment epithelial cells [2,3], respectively. In the blood, TTR is one of the proteins responsible for the transport and delivery of thyroxine (T_4) and retinol to cells, whereas, in the CSF, TTR is the primary T_4 transporter [2,4].

Abbreviations

BBB, blood–brain barrier; CSF, cerebrospinal fluid; FAC, familial amyloid cardiomyopathy; FAP, familial amyloid polyneuropathy; HBP, halogen-binding pocket; ITC, isothermal titration calorimetry; K_d, dissociation constant; n_H, Hill coefficient; SEC, size-exclusion chromatography; T_4, thyroxine; TTR, transthyretin.

Amyloidogenesis of wild-type TTR (WT-TTR) is associated with senile systemic amyloidosis, a cardiomyopathy affecting up to 25% of the population over age 80 [5,6]. Hereditary transthyretin amyloidosis comprises a life-threatening group of rare monogenic diseases inherited in an autosomal dominant fashion, with most affected individuals being heterozygous for one of the approximately 140 disease-associated TTR mutations [7]. Familial amyloid polyneuropathy (FAP) [8,9] and the familial amyloid cardiomyopathy (FAC) [10] are the most common forms of hereditary amyloidosis. A reduced number of TTR mutations lead to leptomeningeal amyloidosis, a less well-characterized and rare phenotype restricted to the central nervous system (CNS) and defined by preferential amyloid deposition in the leptomeningeal vessels, the brain parenchyma, and the eyes. The predominant CNS symptoms include stroke, recurrent subarachnoid hemorrhage, dementia, ataxia, seizures, depression, and periods of decreased consciousness, usually with a poor prognosis [11,12].

Human TTR is a 55 kDa homotetrameric protein consisting of four β-sheet-rich subunits of 127 amino acid residues each, usually labeled from A to D. The AB/CD dimer–dimer interface creates two identical funnel-shaped T_4-binding sites located in opposite sides of the molecule [13,14]. Scission along this interface is the most probable mechanism of TTR tetramer dissociation, as it is the weakest of the two interfaces in the tetramer [15] and constitutes the rate-limiting step in TTR aggregation. After tetramer dissociation, the dimers readily convert into monomers, which experiment tertiary structural changes to become aggregation-competent units [15,16]. Disease-associated mutations accelerate TTR amyloidosis by thermodynamic or kinetic destabilization of the protein [17,18].

By removing the main source of systemic mutant TTR, liver transplantation has become the reference therapy for hereditary TTR amyloidosis [19,20]. However, these patients continue to produce mutant TTR in the choroid plexus and in the eye. Accordingly, CNS TTR deposition has been reported in more than 500 FAP patients after liver transplantation [21,22].

The pursuit of noninvasive therapies for TTR amyloidosis has fueled the development of small molecules that prevent tetramer dissociation by binding to the two T_4 pockets, kinetically stabilizing the TTR native state, thus stalling protein aggregation [23,24]. Only one of these molecules reached the market for the treatment of TTR amyloidosis, the benzoxazole tafamidis [25].

Tafamidis has been shown to slow down the progression of polyneuropathy [26] and cardiomyopathy

[27]. Accordingly, it has been approved in Europe and Japan for the treatment of early-stage FAP [28] and very recently by the Food and Drug Administration (FDA) for the treatment of TTR cardiomyopathy [27]. In contrast, to date, there are no concluding studies on the molecule's ability to halt disease progression in CNS amyloidosis patients. One study suggests that it can attain moderate levels in CSF and the vitreous body [29], whereas others indicate that its blood–brain barrier (BBB) permeability is too low to reach therapeutic concentrations able to abrogate the aggregation of mutant TTR in the CNS [30,31].

Using a drug repurposing approach, our group identified tolcapone as a molecule that binds with high affinity and specificity to the two T_4-binding sites of TTR, promoting its stabilization and preventing the formation of amyloid fibrils and cytotoxic oligomeric species [32]. Tolcapone is an FDA-approved molecule for Parkinson's disease that has already passed Phase IIa clinical trials for FAP (ClinicalTrials.gov Identifier: NCT02191826) [33,34]. In this study, tolcapone induced a clear and robust stabilization of plasmatic TTR in all patients studied, the drug was well tolerated, and treatment raised no safety concerns. Of note, tolcapone penetrates the BBB [35] and preliminary data indicated that it might inhibit the aggregation of highly destabilized variants [32]. Together, these evidences suggested that tolcapone might find therapeutic application in the rare, but fatal, CNS amyloidosis, which, as described, cannot be treated efficiently by liver transplantation or current pharmacological approaches.

In this work, we have characterized in detail the activity of tolcapone on three TTR variants linked to familial leptomeningeal amyloidosis, A25T-TTR [36], V30G-TTR [37], and Y114C-TTR [38], which are among the most destabilized and fastest dissociating TTR tetramers. Our results indicate that tolcapone binds with high affinity to the T_4-binding sites of these variants, establishing specific contacts with the tetramer interface that stabilize the mutant proteins and, consequently, reduce their aggregation. Overall, these findings converge to demonstrate that tolcapone might become a first broad-spectrum drug to treat TTR-related amyloidosis.

Results and Discussion

Tolcapone inhibits the aggregation of TTR leptomeningeal amyloidosis-associated variants

As a first step to assess whether tolcapone can be considered a candidate for treating familial leptomeningeal

amyloidosis, we evaluated its ability to prevent the aggregation of the TTR CNS amyloidosis-associated variants A25T-TTR, V30G-TTR, and Y114C-TTR (Fig. 1). TTR solutions were incubated in the absence or presence of tolcapone, and aggregation was induced by acidification. The molecule final concentration ranged between 0 and 50 μM. Orthogonal light scattering at 340 nm was recorded to follow aggregation and normalized to the maximum scattering value in the absence of tolcapone for each individual variant. Interestingly, as shown in Fig. 1, tolcapone inhibits up to 71% the aggregation of A25T-TTR and 76% of V30G-TTR and reaches 100% for Y114C-TTR, the potency for this last mutant being very close to that exerted for WT-TTR. Remarkably, at 5 μM of tolcapone, which corresponds to less than twofold the protein concentration (3.5 μM), the inhibition was already evident for all the TTR variants. Ten molar equivalents of tolcapone (35 μM) reduced around 70% of A25T-TTR aggregation, being equivalent to the anti-aggregational activity of T_4 at the same concentration and solution conditions [12].

Tolcapone stabilizes TTR leptomeningeal amyloidosis-associated variants under denaturing conditions

After demonstrating that tolcapone can inhibit the aggregation of TTR variants linked to familial leptomeningeal amyloidosis, we addressed whether this effect depends on native tetramer stabilization, as previously reported for WT-TTR and the FAC-associated V122I-TTR variant [32].

It is well established that in urea, TTR monomer unfolding is preceded by tetramer destabilization [39], and once the tetramer is dissociated, tertiary structural changes can be monitored by tryptophan (Trp) intrinsic fluorescence. Accordingly, to evaluate the effect of tolcapone on the stability of our variants, the proteins were incubated with increasing concentrations of urea (0–9.5 M) for 96 h, allowing the solutions to reach the equilibrium [17,40], both in the absence and in the presence of tolcapone (20 and 50 μM). Trp fluorescence was monitored and used to calculate the fraction of unfolded protein at any given urea concentration (Fig. 2). For A25T-TTR, the obtained curves in both conditions are similar, indicating that, surprisingly, tolcapone does not seem to exert a significant stabilizing effect over this variant in the assayed conditions. In stark contrast, for V30G-TTR and Y114C-TTR a clear stabilizing effect is observed in the presence of tolcapone, being specially dramatic in the case of Y114C-TTR, where tolcapone permits > 50% of the protein to remain folded at 9.5 M urea, a stabilization that approaches the one exerted over WT-TTR.

The low stabilization observed for A25T-TTR might indicate that in this brain aggregating variant, at the assay protein concentration (1.8 μM), the tetramer dissociates at such low urea concentrations that the obtained curves report mostly on monomer unfolding. This is consistent with previous findings, indicating that in the 0.72–7.2 μM protein concentration range, the denaturation curves show a single transition that is concentration-independent [18]. This suggests that, at low protein concentrations, A25T-TTR tetramer dissociation and monomer unfolding are not significantly
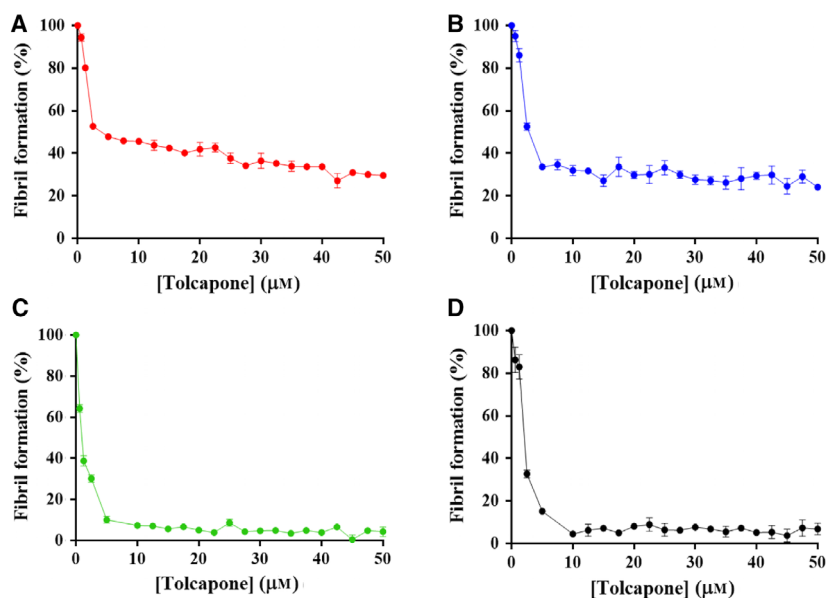
Fig. 1. Tolcapone effect over the aggregation of TTR leptomeningeal amyloidosis-associated variants. (A) A25T-TTR (in red), (B) V30G-TTR (in blue), (C) Y114C-TTR (in green), and WT-TTR (in black). Light scattering at 340 nm was measured and plotted as percentage of TTR aggregation. The values represent mean ± SEM (*n* = 3).
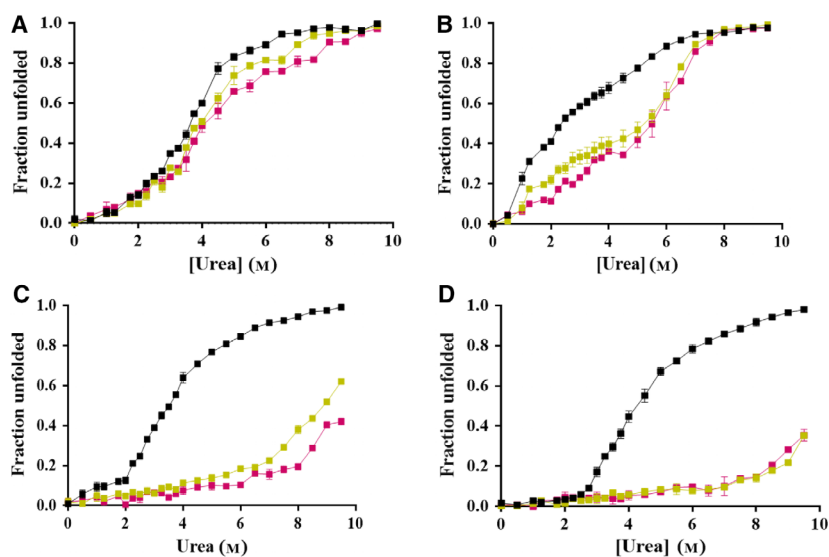
Fig. 2. Tolcapone effect on urea-induced denaturation of TTR leptomeningeal amyloidosis-associated variants. (A) A25T-TTR, (B) V30G-TTR, (C) Y114C-TTR, and (D) WT-TTR. Black squares represent the control without tolcapone, while gold and magenta squares correspond to the samples incubated with 20 and 50 μM of tolcapone, respectively. The values represent mean ± SEM (n = 3).

linked. The behavior of A25T-TTR is in stark contrast with that of WT-TTR, for which it is described that tetramer dissociation and monomer unfolding are thermodynamically linked at the protein concentration used in these experiments [18]. Further evidence for these different unfolding mechanisms is provided by the observation that, for A25T-TTR, the urea denaturation curve assessed by resveratrol binding differs significantly from the one monitored by Trp intrinsic fluorescence, whereas for WT-TTR, the two curves are nearly coincident (Fig. 3) [12,18]. Resveratrol has been described to display a substantial increase in its fluorescence quantum yield when bound to at least one of the two T$_4$-binding sites in the tetramer, being thus a reporter for the native-state TTR conformation [17,18].

V30G-TTR and Y114C-TTR are clearly more stable, and the data herein indicate that they would behave like WT-TTR. Indeed, for these two mutants, the denaturation curves in the presence of tolcapone resemble the ones described for molecules that impose kinetic stability on TTR, stabilizing the AB/CD dimer–dimer interface and delaying tetramer dissociation [41,42].

The analysis emphasizes the complexity of the denaturation mechanism of TTR leptomeningeal-type variants, for which, in contrast to what occurred for WT-TTR and V122I-TTR [32], a direct relationship between tolcapone stabilizing and anti-aggregational effects could not be established. A possible explanation for this lack of correlation would be that the CNS amyloidosis-associated variants are so destabilized
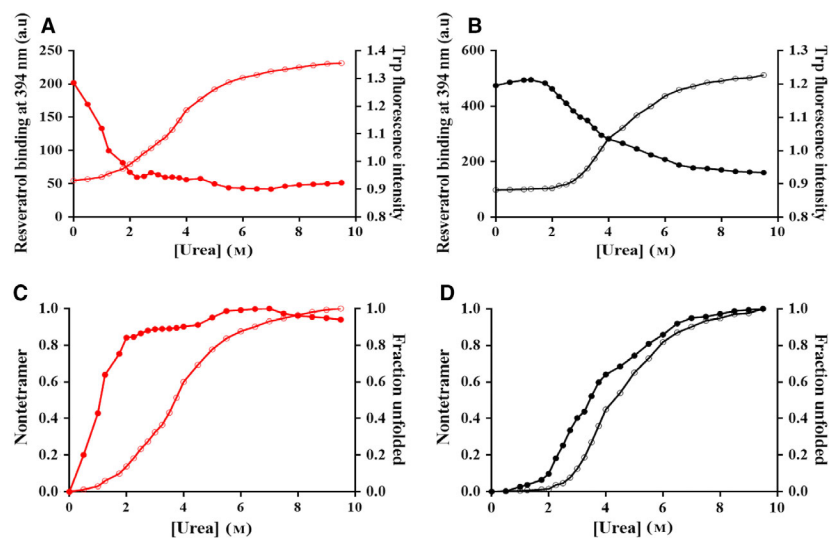
Fig. 3. Urea denaturation of the leptomeningeal-associated TTR variant A25T-TTR and WT-TTR. Stability of A25T-TTR (in red) and WT-TTR (in black) was assessed both by resveratrol binding (filled circles, left axis) and by Trp intrinsic fluorescence (open circles, right axis). Raw resveratrol binding and Trp intrinsic fluorescence data are shown in (A) and (B). These values were used to calculate the nontetrameric fraction and unfolded fraction, respectively, which are presented in (C) and (D).
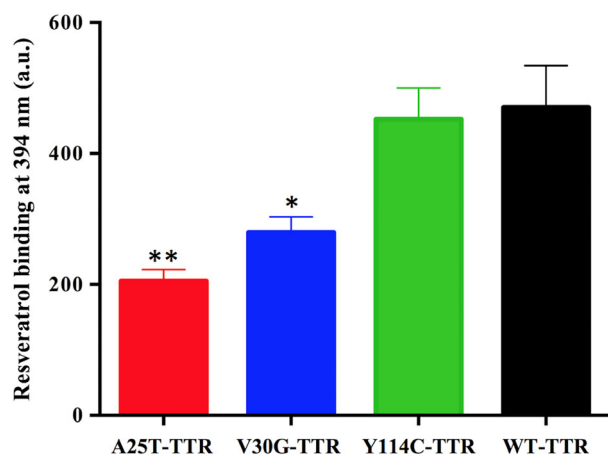
Fig. 4. Resveratrol binding of TTR leptomeningeal amyloidosis-associated variants. Resveratrol fluorescence at 394 nm when incubated with A25T-TTR (in red), V30G-TTR (in blue), Y114C-TTR (in green), and WT-TTR (in black). The values represent mean $\pm$ SEM ($n = 3$). One-way ANOVA with Dunnett's test revealed differences between A25T- and V30G-TTR binding to resveratrol, in comparison with WT-TTR; *$P < 0.05$ and **$P < 0.01$.

that, even in the absence of denaturant, only a fraction of the protein remains in a native tetrameric form in the assay conditions. We evaluated the initial tetramer population for each of the TTR mutants under native conditions using resveratrol binding assays (Fig. 4). The proportion of tetramer under native conditions differed among variants, as calculated from resveratrol binding experiments. A25T-TTR, V30G-TTR, and Y114C-TTR displayed $43.7 \pm 3.6\%$, $59.5 \pm 5.0\%$, and $96.2 \pm 10.2\%$ of tetramer relative to that in WT-TTR, respectively. The calculated tetramer populations fairly correlated with the aggregation inhibitory effect that tolcapone exerts in these mutants.

The influence of the mutations on the quaternary structural stability of the different TTR mutants under native conditions was also assessed by analytical size-exclusion chromatography (SEC) at 7 μM in PBS and monitored by absorbance at 280 nm (Fig. 5). This is the lowest TTR concentration at which our chromatography setup has enough detection sensitivity. V30G-TTR and Y114C-TTR appear as a unique species with an elution volume corresponding to that of the WT-TTR tetramer. In contrast, in agreement with a lower tetramer stability, A25T-TTR seems to adopt both higher and lower molecular weight species other than the tetramer, likely corresponding to soluble aggregates and a monomer, respectively. This suggests that A25T-TTR dissociates spontaneously at this concentration, generating unfolded monomers that

assemble into the majoritarian high-weight species. If this is the case, the equilibrium between the tetrameric and monomeric forms of the mutant protein should be concentration-dependent.

Effectively, when analytical SEC was performed at a higher protein concentration (20 μM), the elution profile was identical for all the variants, presenting a single peak with an elution volume compatible with the TTR tetramer. This suggests that the amount of initial tolcapone-targetable tetramer depends on both the stability of the protein and its concentration in the assay, since both factors impact the equilibrium between the tetrameric and monomeric forms of TTR. It is possible that for highly unstable variants, tolcapone not only would stabilize the available tetramer, but might also displace partially the equilibrium toward the population of the tetrameric form, as a result of Le Chatelier's principle.

Tolcapone binds with high affinity to TTR leptomeningeal amyloidosis-associated variants

The above-described data suggest that tolcapone can inhibit the aggregation of even highly destabilized mutants, as long as they remain in the tetrameric state and the molecule can bind to them. We used isothermal titration calorimetry (ITC) to confirm that tolcapone effectively interacts with the brain-associated variants and to determine the mechanisms of binding. The thermodynamic parameters (ΔG, ΔH, $-T\Delta S$) for the binding reactions as well as the cooperativity of the interaction were analyzed for the three mutants and WT-TTR according to two models: (a) two identical, but independent binding sites; (b) two identical and cooperative binding sites [43,44]. Our data indicated that tolcapone binds with high affinity to the first TTR T_4-binding site of all proteins, but they exhibit differences in the degree of cooperativity for the binding to the second T_4 pocket (Table 1 and Fig. 6).

Importantly, although we first reported that tolcapone binds to WT-TTR with a weak negative cooperativity [32], a reevaluation of the protein–ligand interaction in the present study revealed that under the present assay conditions, the interaction is best described as noncooperative, with $K_d = 29$ nM. Binding of tafamidis to WT-TTR under the same conditions was assessed as a control and, as expected, a strong negative cooperativity was found, displaying $K_{d_1} = 9.9$ nM and $K_{d_2} = 260$ nM values, consistent with those previously reported [25]. In agreement with three recent studies [32,45,46], these data confirm that the concentration of tolcapone required to occupy simultaneously the two WT-TTR T_4 cavities is
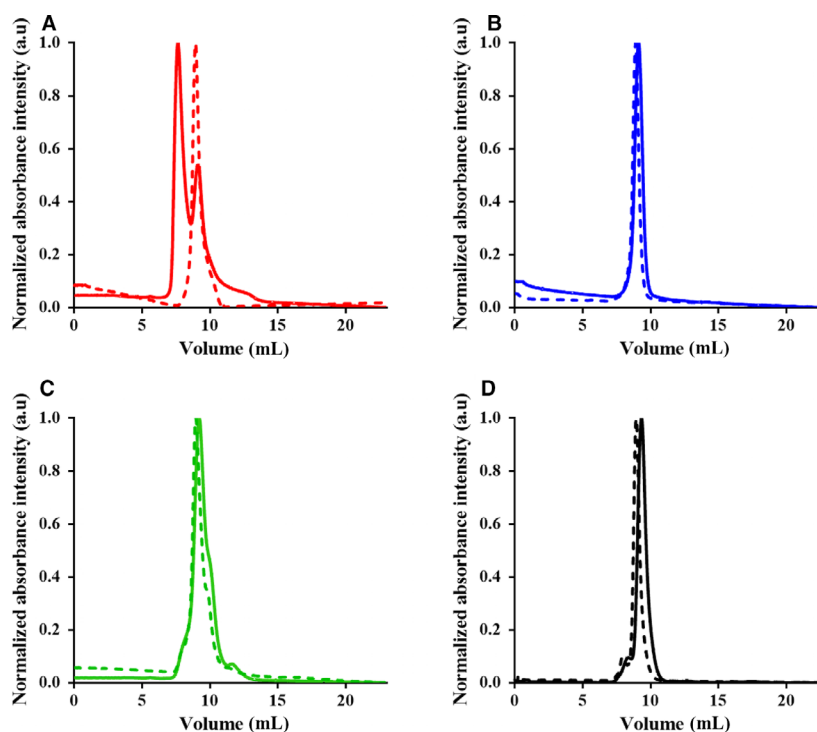
**Fig. 5.** Effect of protein concentration on the quaternary structure adopted by TTR leptomeningeal amyloidosis-associated variants. (A-D) Elution profiles of A25T-TTR (in red), V30G-TTR (in blue), Y114C-TTR (in green), and WT-TTR (in black) at 7 (solid line) or 20 μM (dashed line).

Table 1. Thermodynamic parameters obtained by ITC experiments for the binding of tolcapone to TTR leptomeningeal amyloidosis-associated variants[a].

	K_{d_1} (μM)	ΔG_1 (kcal·mol^{-1})	ΔH_1 (kcal·mol^{-1})	$-T\Delta S_1$ (kcal·mol^{-1})	K_{d_2} (μM)	ΔG_2 (kcal·mol^{-1})	ΔH_2 (kcal·mol^{-1})	$-T\Delta S_2$ (kcal·mol^{-1})	n_H
A25T	0.063	−9.8	−17.1	7.3	3.1	−7.5	−12.3	4.8	0.25
V30G	0.110	−9.5	−12.3	2.8	0.110	−9.5	−12.3	2.8	1
Y114C	0.045	−10.0	−14.4	4.4	0.045	−10.0	−14.4	4.4	1
WT	0.029	−10.3	−8.8	−1.5	0.029	−10.3	−8.8	−1.5	1

[a]1 and 2 correspond to the parameters associated with the first and second binding sites of TTR, respectively.

significantly lower than that of tafamidis in the same conditions, and therefore that tolcapone is a stronger stabilizer of this protein.

The binding of tolcapone to V30G-TTR and Y114C-TTR was also noncooperative, with Kds for the two binding sites of 110 and 45 nM, respectively, indicating that tolcapone binds more to the less destabilized Y114C-TTR mutant. Indeed, although the binding of tolcapone to Y114C-TTR is slightly weaker than that to WT-TTR, the ΔG of the interactions are fairly similar, justifying why, for these initially folded and tetrameric proteins, tolcapone exerts a very similar anti-aggregational effect, being able to abrogate completely TTR deposition at 1 : 1 T$_4$-binding sites : tolcapone ratio (Fig. 1). In sharp contrast to the other two leptomeningeal variants, the binding of tolcapone

to A25T-TTR displays a high negative cooperativity, reflected in a Hill coefficient (n_H) of 0.25. Accordingly, whereas the binding to the first site is strong, with K_{d_1} = 63 nM, the affinity for the second cavity is significantly decreased with a K_{d_2} in the low μM range (3.1 μM).

Irrespectively of the considered TTR mutant and T$_4$ pocket, the binding is always enthalpically driven. This is important because it has been suggested that the enthalpic component of binding plays a predominant role in stabilizing TTR [46] and enthalpic forces correlate with the selectivity of transthyretin-binding ligands in plasma [47], explaining why tolcapone binds selectively and stabilizes TTR in the blood of healthy volunteers and patients bearing the polyneuropathy-associated V30M mutation [32,34]. From our
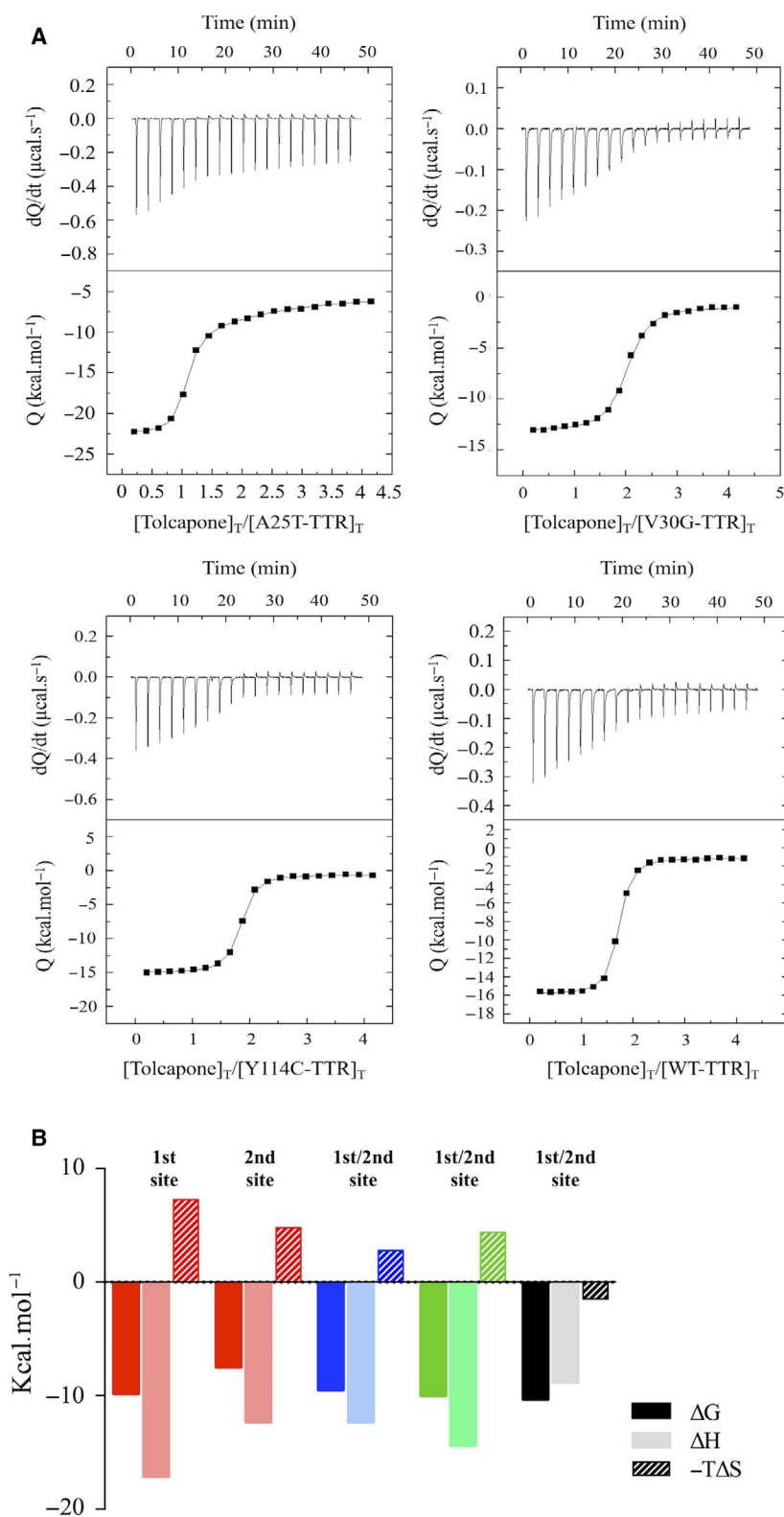
Fig. 6. Calorimetric titration of TTR leptomeningeal amyloidosis-associated variants with tolcapone. (A) The top panel (thermogram) shows how the thermal power changes with time. The bottom panel (binding isotherm) is obtained from the transformation of the thermogram and represents the normalized heat of reaction per injection as a function of the ratio between the molar concentration of tolcapone and protein. The solid line in the binding isotherm corresponds to the best fitting to each curve. (B) Graphical representation of ΔG (dark bars), ΔH (light bars), and $-T\Delta S$ (striped bars) for the binding of tolcapone to the first and second sites of A25T-TTR (in red), V30G-TTR (in blue), Y114C-TTR (in green), and WT-TTR (in black). In the case of V30G-, Y114C-, and WT-TTR, the binding parameters for both sites are the same.

thermodynamic data, the same should be true for the TTR CNS amyloidosis-associated variants in the brain, since the enthalpic component of the binding for these unstable mutants is very similar to the one exhibited for WT-TTR (Fig. 6).

Tolcapone binds TTR leptomeningeal amyloidosis-associated variants at the dimer–dimer interface

The fact that enthalpic contributions dominate the binding of tolcapone to the three mutant proteins suggests that, as previously shown for WT-TTR [32], there exist specific interactions between the protein and the ligand. To confirm that these destabilized brain variants could accommodate tolcapone in their tetrameric structure, we obtained crystals of A25T-TTR, V30G-TTR, and Y114C-TTR in the presence of tolcapone that diffracted beyond 1.60, 1.15, and 1.69 Å resolution, respectively (Fig. 7 and Table 2).

These high-resolution crystal structures clearly indicated the placement of tolcapone in the butterfly-shaped electron density map located in the 'weak' dimer–dimer interface of TTR tetramer. As expected, the three new structures were virtually identical to that

of WT-TTR in the presence of tolcapone (PDB: 4D7B), with overall root-mean-square deviation values for the Cα of 0.20 Å for A25T-TTR (PDB: 6TXV), 0.45 Å for V30G-TTR (PDB: 6TXW), and 0.43 Å for Y114C-TTR (PDB: 6XTK). A closer view into the mutation sites confirms that the mutations do not disturb the structure of TTR and, indeed, the local environment around the mutated residues remains unaltered (Fig. 8). This is consistent with the reported data for a vast majority of mutant TTR crystal structures [48]. To the best of our knowledge, the structure of V30G-TTR/tolcapone complex (PDB: 6TXW) represents the first one for this protein variant. Val30 maps to the monomer B-strand, our structure indicating that the removal of the side chains of the four buried Val30 residues leads only to minor perturbations of the native tetrameric structure, which are restricted to the vicinity of the mutated residues, for example, the loss of the intramolecular contacts made with Val71 side chain in the E-strands. However, the B-factor of Val71 in V30G-TTR remains similar to the one measured in the WT-TTR/tolcapone complex structure, indicating that the mutation does not even affect local flexibility. The structure of the Y114C-TTR/tolcapone complex is the first one to show that a kinetic
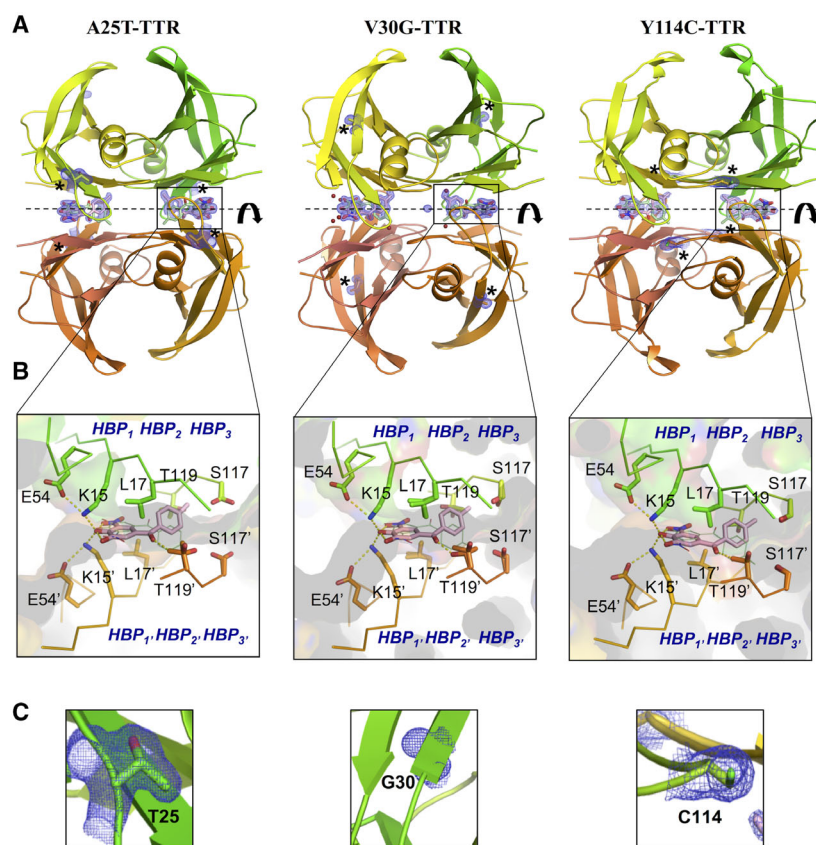
Fig. 7. Crystal structures of A25T-TTR, V30G-TTR, and Y114C-TTR in complex with tolcapone. (A) Global view of TTR variants bound to tolcapone (cartoon representation). The electron density maps of the two tolcapone-binding sites of tolcapone are depicted. The position of the mutated residues in the structure is specified with asterisks. Dashed lines represent the twofold symmetry axis of the dimer–dimer interface. (B) Detailed and close-up views of one of the TTR tolcapone-binding sites of the variants (PDB: 6TXV, 6TXW, 6XTK); tolcapone and some of the TTR tetramer residues in contact with it are represented by sticks. (C) Close-up views of the electron density map of the mutated residues. All structures were generated with PYMOL (DeLano Scientific, LLC).

Table 2. Data collection and refinement statistics of transthyretin variants in complex with tolcapone. Values in parenthesis are for the last resolution shell.

	A25T-TTR	V30G-TTR	Y114C-TTR
Data collection			
Space group	$P2_1 2 2_1$	$P2_1 2 2_1$	$P2_1 2 2_1$
Unit cell	43.83,	43.67,	42.92,
parameters (Å)	65.41,	65.63,	65.74,
	84.67	84.35	83.95
Wavelength (nm)	0.9794	0.9790	0.9795
Resolution range (Å)	42.34–1.55	65.63–1.15	65.74–1.69
R_{merge}	0.04 (0.47)	0.12 (0.96)	0.05 (0.90)
$CC_{1/2}$	0.99 (0.92)	0.98 (0.63)	0.99 (0.63)
I/σ_I	23.5 (3.8)	8.1 (1.5)	8.0 (0.9)
Completeness (%)	99.5 (98.2)	96.5 (95.3)	99.4 (97.0)
Multiplicity	5.4 (5.0)	6.3 (5.1)	3.4 (3.2)
Structure refinement			
Resolution range (Å)	42.33–1.60	65.63–1.15	38.22–1.70
No. of unique reflections	32836	82985	26585
R_{work}/R_{free} (%)	19.0/21.5	15.9/18.5	19.2/22.0
No. of atoms	2070	2165	1905
Protein	1854	1854	1764
Ligands	40	40	40
Water molecules	188	279	105
Average B factors (Å^2)	26.1	25.7	42.6
Protein	25.3	23.8	42.4
Ligands	25.1	21.7	44.5
Water	34.5	39.5	45.2
RMS deviations			
Bonds (Å)	0.003	0.007	0.009
Angles (°)	0.60	0.89	0.96
PDB code	6TXV	6TXW	6XTK

stabilizer can diffuse into the T_4-binding site of this particular mutant.

In all structures, tolcapone binds to the TTR tetramer in the forward mode, with the 4-methyl-phenyl ring occupying the inner binding cavity and the 3,4-dihydroxy-5-nitrophenyl ring of tolcapone oriented to the outer binding cavity. The presence of tolcapone inside of the T_4-binding pocket stabilizes the orientation of key residues that form the halogen-binding pockets (HBP) HBP1-1′ (Lys15 and Leu17), HBP2-2′ (Ala108 and Leu110), and HBP3-3′ (Ser117 and Thr119), as inferred from their very well-defined electron maps (Fig. 9). This results in virtually identical polar, hydrophobic contacts and electrostatic interactions inside the T_4 pocket to those stabilizing the tetramers in WT-TTR/tolcapone complex structure, including a specific hydrogen bond interaction between the carbonyl group of tolcapone and the hydroxyl side chain of Thr119. The distances between the carbonyl

group of tolcapone and the hydroxyl side chain of Thr119 in our structures are similar to the ones observed in the WT-TTR/tolcapone structure and suggest the formation of hydrogen bonds (Table 3). These bonds are buried in the low dielectric context of the T_4 pocket, in such a way that these interactions are predicted to be strong (Fig. 7 and Table 3). The establishment of hydrogen bonds between kinetic stabilizers and TTR residues in the inner binding cavity seems to be an important determinant of the binding affinity [32,46].

As in the case of WT-TTR, in the leptomeningeal amyloidosis mutants the ε-amino groups of Lys15/Lys15′ are sandwiched between the hydroxyl groups of the phenyl ring of tolcapone and the carboxylate group of Glu54 (Fig. 7 and Table 3). These specific electrostatic interactions by Lys15 close the cavity around tolcapone hampering the entrance of solvent into the pocket and stabilizing the protein–compound complex.

The new structures highlight how the tolcapone–protein interactions at the T_4-binding site in the 'weak' dimer–dimer interface are not significantly affected by the mutations, providing an explanation for the enthalpy driving binding of the TTR CNS amyloidosis-associated variants and suggesting that the observed anti-aggregational activity of the compound responds to a canonical kinetic stabilization of the tetramer once the molecule occupies the hormone-binding sites of the pathogenic proteins.

Conclusions

In the present study, we have described in detail the activity of tolcapone, a potent kinetic stabilizer originally intended to treat Parkinson's disease, on TTR variants associated with leptomeningeal amyloidosis, a rare, but fatal form of amyloidosis. We could confirm that A25T-, V30G-, and Y114C-TTR variants present lower structural stability compared with WT-TTR, especially A25T-TTR. Mutations impact the tetramer–monomer equilibrium, lowering the ability of these variants to remain in the functional native tetrameric structure and hence enhancing the protein susceptibility to aggregation. Our study demonstrates that tolcapone binds strongly and canonically at the T_4-binding sites of all the assayed TTR leptomeningeal amyloidosis-associated variants, restoring the structural stability of the tetramer and, consequently, inhibiting the pathogenic protein aggregation. This activity, together with the compound's ability to pass the BBB, suggests that tolcapone might become a first broad-spectrum pharmacologic treatment for all forms
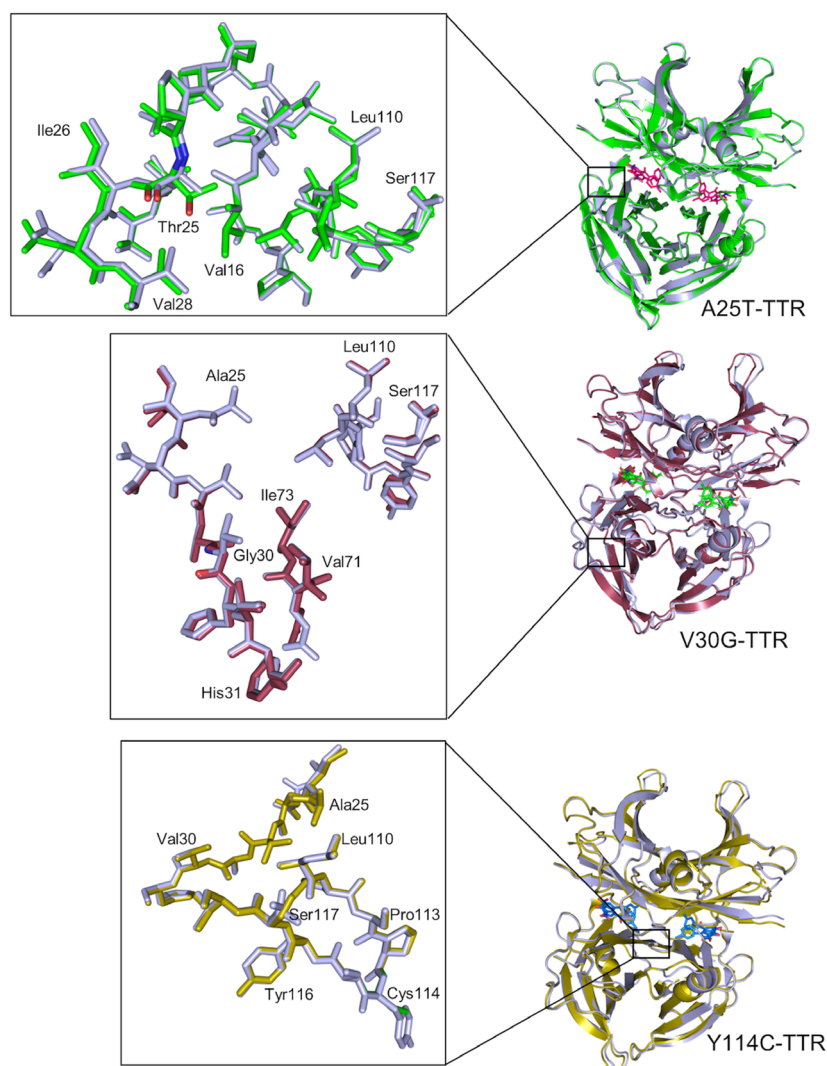
Fig. 8. Comparison between the crystal structures of WT-TTR with A25T-TTR, V30G-TTR, and Y114C-TTR in complex with tolcapone. Superposition of WT-TTR (light blue) and A25T (green), V30G (raspberry), and Y114C (olive) variant structures. (Right) Superposed tetramers are depicted in cartoon representation, and tolcapone molecules are showed in stick. (Left) Close-up view showing the local environment of the mutated residues in monomer A (stick representation); Thr25, Gly30, and Cys114 are colored by elements. The overall root-mean-square deviation for the superposed Cα atoms is 0.20, 0.45, and 0.43 Å, respectively. All structures were generated with PYMOL (DeLano Scientific, LLC).

of TTR-related amyloidosis, including the devastating CNS forms of the disease.

All in all, our study provides solid biophysical and structural rationale for a recent proof-of-principle clinical trial aimed to test the ability of tolcapone to stabilize TTR in symptomatic and asymptomatic leptomeningeal TTR patients (ClinicalTrials.gov Identifier: NCT03591757).

Materials and methods

TTR expression and purification

The vectors coding for TTR variants were prepared by PCR site-directed mutagenesis using the QuikChange Lightning kit (Agilent Technologies, Santa Clara, CA, USA). pET28a vector (Novagen, Addgene, Cambridge, MA, USA) encoding for the WT protein was used as a template.

For protein expression, *Escherichia coli* BL21 (DE3) cells, previously transformed with the corresponding plasmid, were grown in LB medium supplemented with 50 μg·mL^{-1} kanamycin at 37 °C to an optical density of 0.8 at 600 nm, and the culture was induced with 1 mM iso-propyl β-D-thiogalactopyranoside for 16 h. Cells were harvested by centrifugation and sonicated, and the soluble fraction was recovered by centrifugation. The TTR-containing fraction was obtained by two consecutive steps of ammonium sulfate precipitation (50% and 90%, respectively). The precipitate was solubilized in 25 mM Tris/HCl, pH 8, and dialyzed against the same buffer. The sample was loaded onto a HiTrap Q HP column (GE Healthcare, Chicago, IL, USA) and eluted with a linear gradient 0–0.5 M NaCl in 25 mM Tris/HCl, pH 8. The TTR-enriched fractions were precipitated in 90% ammonium sulfate, and the obtained precipitate was redissolved in a small volume of buffer (25 mM Tris, 100 mM NaCl, pH 8). TTR was finally purified by gel filtration chromatography on a

A   **A25T-TTR**

B   **V30G-TTR**
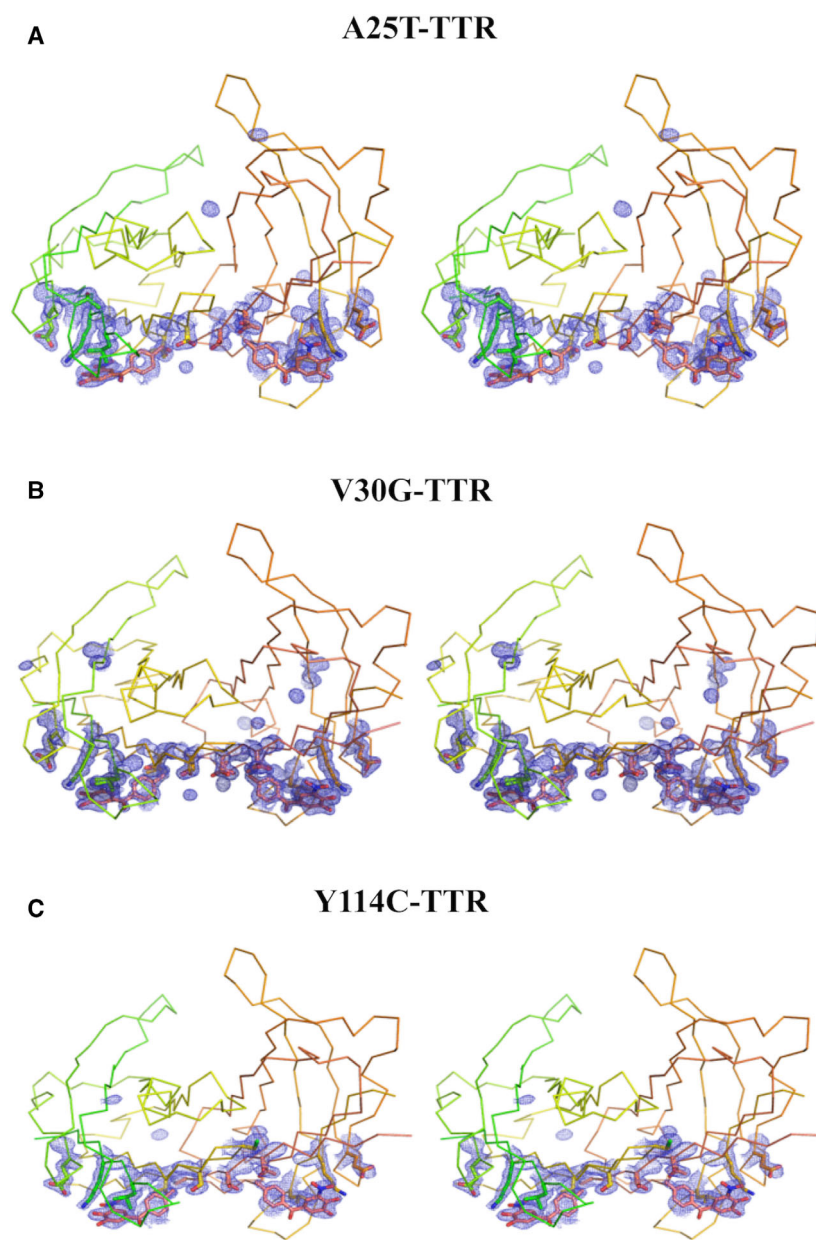
C   **Y114C-TTR**

Fig. 9. Stereo images of TTR leptomeningeal amyloidosis-associated variants and electron density maps of tolcapone and of residues involved in binding. Stereo views of (A) A25T-TTR, (B) V30G-TTR, and (C) Y114C-TTR in complex with tolcapone with a 2Fo-Fc map (blue mesh) contoured at 1.0 σ. All structures were generated with PYMOL (DeLano Scientific, LLC).

HiLoad 26/600 Superdex 75 prep-grade column (GE Healthcare) and eluted with 25 mM Tris, 100 mM NaCl. Purest fractions were combined and stored at −20 °C. Protein concentration was determined spectrophotometrically at 280 nm using an extinction coefficient of 77 600 $M^{-1} \cdot cm^{-1}$. All the TTR variants, including the WT, were expressed and purified following the same procedure.

TTR aggregation inhibition *in vitro*

TTR solutions (7 μM in 10 mM sodium phosphate, 100 mM KCl, 1 mM EDTA, 1 mM DTT, pH 7.0) were incubated with increasing concentrations of tolcapone for 30 min at 37 °C. Since the stock solutions of tolcapone were prepared in dimethyl sulfoxide (DMSO), the percentage of DMSO in all the samples was adjusted to 5% (v/v). After the incubation period, the pH was dropped to 5.0 via dilution 1 : 1 with acidification buffer (100 mM sodium acetate, 100 mM KCl, 1 mM EDTA, 1 mM DTT, pH 5.0) and the samples were incubated for more 22 h at 37 °C. For WT-TTR and Y114C-TTR, a pH of 4.2 and an incubation period of 72 h were used instead. The formation of aggregates was assessed by light scattering, with the excitation and emission wavelengths set at 340 nm, using a Varian Cary

Table 3. Comparison of the interatomic distances (in Å) between the two tolcapone molecules of the tetramer and residues of WT-TTR and TTR variants that form HBP1 and HBP1′ and HBP2 and HBP2′ binding sites. Values in parenthesis correspond to the second tolcapone molecule.

	WT-TTR	A25T-TTR	V30G-TTR	Y114C-TTR
Thr119 OG1 – tolcapone O13	2.6 (2.5)	2.6 (2.6)	2.5 (2.5)	3.0 (3.0)
Lys15 NZ – tolcapone O8	2.7 (2.9)	2.8 (2.8)	3.1 (2.7)	2.9 (2.6)
Lys15 NZ – Glu54 OE2	2.8 (2.9)	3.2 (3.3)	3.1 (3.4)	2.9 (3.9)

Eclipse Fluorescence Spectrophotometer (Agilent Technologies). TTR aggregation was considered maximum in the absence of tolcapone (100% aggregation).

Urea denaturation curves in the absence or presence of tolcapone

Denaturation curves were obtained as described previously [40]. TTR solutions at 1.8 μM in PBS were incubated for 30 min with tolcapone, and urea in 50 mM sodium phosphate, 100 mM KCl, pH 7.0, was added to obtain a range of final concentration from 0 to 9.5 M. A control sample was prepared with DMSO, instead of tolcapone. The concentration of urea in the solutions was verified by refractive index, using a Manual Hand-held Refractometer HR901 (A. Krüss Optronic, Hamburg, Germany). After 96-h incubation at RT, the fraction unfolded was determined by intrinsic fluorescence spectroscopy, using a FP-8200 Spectrofluorometer (Jasco, Easton, MD, USA). The samples were excited at 295 nm, allowing the selective excitation of the Trp residues on the protein, and fluorescence emission spectra were recorded from 310 to 400 nm. Upon denaturation, the Trp residues become more solvent-exposed and the maximum fluorescence changes from 335 to 355 nm, approximately. The 355/335 nm fluorescence emission intensity was normalized from minimum (folded) to maximum (unfolded), with the maximum being the sample without tolcapone, and plotted as a function of urea concentration.

Urea-mediated transthyretin dissociation measured by resveratrol binding

A25T- and WT-TTR solutions (1.8 μM in PBS) were incubated with different concentrations of urea buffered with 50 mM sodium phosphate, 100 mM KCl, 1 mM EDTA, and 1 mM DTT (pH 7.0) for 96 h at RT. After this time, 1.8 μL of resveratrol from a 1 mM stock solution in DMSO was added to a 100 μL sample just before the measurement, in order not to shift the equilibrium toward the tetramer [17]. The incubation time with resveratrol was the same for all samples. The samples were excited at 320 nm and the fluorescence was recorded from 350 to 550 nm, using a FP-8200 Spectrofluorometer (Jasco). The fluorescence emission intensity of resveratrol at 394 nm was used to calculate the amount of nontetrameric TTR and plotted as a function of urea concentration.

Resveratrol binding to TTR

In order to assess resveratrol binding to TTR, 1.8 μL of resveratrol from a 1 mM stock solution in DMSO was added to 100 μL TTR samples (1.8 μM in PBS) and the samples were excited at 320 nm, using a FP-8200 Spectrofluorometer (Jasco). The resveratrol fluorescence intensity at 394 nm was used as an indicator of the amount of tetrameric TTR present in the samples. The difference between TTR leptomeningeal amyloidosis-associated variants and WT-TTR was analyzed by one-way ANOVA with Dunnett's test using GRAPHPAD PRISM 6.0 software (GraphPad Software Inc., San Diego, CA, USA). $P < 0.05$ was considered statistically significant.

Analytical size-exclusion chromatography

TTR samples (500 μL at 7 μM or 100 μL at 20 μM, in PBS) were filtered and injected into a Superdex 75 10/300 GL column (GE Healthcare), previously equilibrated with PBS. Elution was done with the same buffer, at a flow rate of 0.4 mL·min^{-1}, and monitored by absorbance at 280 nm, which was normalized from 0 to 1.

Isothermal titration calorimetry

The thermodynamic parameters that describe the interaction between TTR and tolcapone were determined by ITC, using a MicroCal Auto-iTC200 Calorimeter (MicroCal, Malvern Panalytical, UK). A25T-, Y114C-, and WT-TTR at 5 μM located in the calorimetric cell were titrated against tolcapone at 100 μM in the injection syringe in 137 mM NaCl, 100 mM KCl, 10 mM Na$_2$HPO$_4$, 1.8 mM KH$_2$PO$_4$, 1 mM EDTA, 2.5% DMSO, pH 7.0, at 25 °C. A stirring speed of 750 r.p.m. and 2 μL injections were programmed, with consecutive injections separated by 150 s to allow the calorimetric signal (thermal power) to return to baseline. For V30G-TTR, the concentration of protein was increased to 20 μM, since the concentration of TTR able to bound tolcapone was low. For each protein, two replicates were performed, and the experimental data were analyzed with a general model for a protein with two ligand-binding sites [43,44] implemented in ORIGIN 7.0 (OriginLab, Northampton, MA, USA), which allows to establish whether the two binding sites are identical and independent. Appropriate control blank experiments were performed to test for unwanted heat artifacts or unspecific phenomena.

Crystal structures of TTR/tolcapone complexes

Cocrystals of A25T-TTR/tolcapone, V30G-TTR/tolcapone, and Y114C-TTR/tolcapone were obtained as described previously [32]. Briefly, purified proteins (140 μM) were incubated with 10-fold molar excess of ligand for 5 min at 22 °C. The complex was crystallized at 18 °C by hanging-drop vapor diffusion by mixing 1 μL of the complex with 1 μL of the reservoir solution containing 25% and 30% PEG 400, 200 mM CaCl$_2$, 100 mM HEPES, pH 7.0–7.5. Since PEG400 is a cryoprotectant itself, crystals were removed from the drop and directly flash-frozen in liquid nitrogen before diffraction analysis. Diffraction data were recorded from PEG400 cryo-cooled crystals (100 K) at the ALBA Synchrotron in Barcelona (BL13-XALOC beamline) [49]. Data were integrated and merged using XDS [50] and scaled, reduced, and further analyzed using CCP4 [51]. The structure of TTR/tolcapone complex was determined from the X-ray data by molecular replacement with PHENIX (1.17.1_3660) [52] using the crystal structure of TTR (PDB code 1F41) as a search model. The initial electron density maps showed the well-defined electron density map corresponding to tolcapone in the TTR dimer–dimer interface. Refinement was performed with PHENIX [52], and model building was performed with COOT [53]. Ramachandran analysis shows 98.0% of residues (230) are in preferred regions and only 2.0% of residues (4) are in allowed regions for the A25T-TTR/tolcapone structure. For the V30G-TTR/tolcapone structure, 98.0% of residues (235) are in preferred regions and only 2.0% of residues (4) are in allowed regions. For the Y114C-TTR/tolcapone structure, 96.0% of residues (227) are in preferred regions and only 4.0% of residues (10) are in allowed regions. Refinement and data statistics are provided in Table 2. Figures were prepared with PYMOL (The PyMOL Molecular Graphics System, Version 2.0, Schrödinger, LLC).

Acknowledgements

Conflict of interest

The authors declare no conflict of interest.

Author contributions

FP, SV, and IP designed the study. FP, SE, JS, NV, and AV-C conducted the experiments. FP, NV, DR, SV, and IP analyzed the results. FP, NV, AV-C, and IP prepared the figures. FP, SV, and IP wrote the main manuscript text. All authors reviewed the manuscript.

References

1 Chiti F & Dobson CM (2017) Protein misfolding, amyloid formation, and human disease: a summary of progress over the last decade. *Annu Rev Biochem* **86**, 27–68.

2 Haggen G & Elliott W (1973) Transport of thyroid hormones in serum and cerebrospinal fluid. *J Clin Endocrinol Metab* **37**, 415–422.

3 Schreiber G, Aldred A, Jaworowski A, Nilsson C, Achen M & Segal M (1990) Thyroxine transport from blood to brain via transthyretin synthesis in the choroid plexus. *Am J Physiol* **258**, R338–R345.

4 Kanai M, Raz A & Goodman D (1968) Retinol-binding protein: the transport protein for vitamin A in human plasma. *J Clin Invest* **47**, 2025–2044.

5 Westermark P, Sletten K, Johansson B & Cornwell GG (1990) Fibril in senile systemic amyloidosis is derived from normal transthyretin. *Proc Natl Acad Sci USA* **87**, 2843–2845.

6 Tanskanen M, Peuralinna T, Polvikoski T, Notkola IL, Sulkava R, Hardy J, Singleton A, Kiuru-Enari S, Paetau A, Tienari PJ *et al.* (2008) Senile systemic amyloidosis affects 25% of the very aged and associates with genetic variation in alpha2-macroglobulin and tau: a population-based autopsy study. *Ann Med* **40**, 232–239.

7 Rowczenio DM, Noor I, Gillmore JD, Lachmann HJ, Whelan C, Hawkins PN, Obici L, Westermark P, Grateau G & Wechalekar AD (2014) Online registry for mutations in hereditary amyloidosis including nomenclature recommendations. *Hum Mutat* **35**, E2403–E2412.

8 Andrade C (1952) A peculiar form of peripheral neuropathy. *Brain* **75**, 408–427.

9 Saraiva MJ, Birken M, Costa P & Goodman D (1984) Amyloid fibril protein in familial amyloidotic polyneuropathy, Portuguese type definition of molecular abnormality in transthyretin (prealbumin). *J Clin Invest* **74**, 104–119.

10 Jacobson D, Pastore R, Yaghoubian R, Kane I, Gallo G, Buck F & Buxbaum JN (1997) Variant-sequence transthyretin (isoleucin 122) in late-onset cardiac amyloidosis in black Americans. *N Engl J Med* **336**, 466–473.

11 Goren H & Steinberg MC (1980) Familial oculoleptomeningeal amyloidosis. *Brain* **103**, 473–495.

12 Sekijima Y, Hammarström P, Matsumura M, Shimizu Y, Iwata M, Tokuda T, Ikeda SI & Kelly JW (2003) Energetic characteristics of the new transthyretin variant A25T may explain its atypical central nervous system pathology. *Lab Invest* **83**, 409–417.

13 Blake CCF, Geisow MJ, Swan IDA, Rerat C & Rerat B (1974) Structure of human plasma prealbumin at 2.5 A resolution. A preliminary report on the polypeptide

chain conformation, quaternary structure and thyroxine binding. *J Mol Biol* **88**, 1–12.

14 Blake CCF, Geisow MJ, Oatley SJ, Rérat B & Rérat C (1978) Structure of prealbumin: secondary, tertiary and quaternary interactions determined by Fourier refinement at 1.8 A. *J Mol Biol* **121**, 339–356.

15 Foss TR, Wiseman RL & Kelly JW (2005) The pathway by which the tetrameric protein transthyretin dissociates. *Biochemistry* **44**, 15525–15533.

16 Zhihong L, Wilfredo C & Kelly JW (1996) The acid-mediated denaturation pathway of transthyretin yields a conformational intermediate that can self-assemble into amyloid. *Biochemistry* **35**, 6470–6482.

17 Hammarstrom P, Jiang X, Hurshman AR, Powers ET & Kelly JW (2002) Sequence-dependent denaturation energetics: a major determinant in amyloid disease diversity. *Proc Natl Acad Sci USA* **99** (Suppl 4), 16427–16432.

18 Hurshman Babbes AR, Powers ET & Kelly JW (2008) Quantification of the thermodynamically linked quaternary and tertiary structural stabilities of transthyretin and its disease-associated variants: the relationship between stability and amyloidosis. *Biochemistry* **47**, 6969–6984.

19 Holmgren G, Steen L, Ekstedt J, Groth CG, Ericzon BG, Eriksson S, Andersen O, Karlberg I, Nordén G, Nakazato M *et al.* (1991) Biochemical effect of liver transplantation in two Swedish patients with familial amyloidotic polyneuropathy (FAP-met[30]). *Clin Genet* **40**, 242–246.

20 Rapezzi C, Quarta CC, Riva L, Longhi S, Gallelli I, Lorenzini M, Ciliberti P, Biagini E, Salvi F & Branzi A (2010) Transthyretin-related amyloidoses and the heart: a clinical overview. *Nat Rev Cardiol* **7**, 398–408.

21 Maia LF, Magalhaes R, Freitas J, Taipa R, Pires MM, Osorio H, Dias D, Pessegueiro H, Correia M & Coelho T (2015) CNS involvement in V30M transthyretin amyloidosis: clinical, neuropathological and biochemical findings. *J Neurol Neurosurg Psychiatry* **86**, 159–167.

22 Sakashita N, Ando Y, Jinnouchi K, Yoshimatsu M, Terazaki H, Obayashi K & Takeya M (2001) Familial amyloidotic polyneuropathy (ATTR Val30Met) with widespread cerebral amyloid angiopathy and lethal cerebral hemorrhage. *Pathol Int* **51**, 475–480.

23 Johnson SM, Wiseman RL, Sekijima Y, Green NS, Adamski-Werner SL & Kelly JW (2005) Native state kinetic stabilization as a strategy to ameliorate protein misfolding diseases: a focus on the transthyretin amyloidoses. *Acc Chem Res* **38**, 911–921.

24 Hammarstrom P (2003) Prevention of transthyretin amyloid disease by changing protein misfolding energetics. *Science* **299**, 713–716.

25 Bulawa CE, Connelly S, Devit M, Wang L, Weigel C, Fleming JA, Packman J, Powers ET, Wiseman RL, Foss TR *et al.* (2012) Tafamidis, a potent and selective

transthyretin kinetic stabilizer that inhibits the amyloid cascade. *Proc Natl Acad Sci USA* **109**, 9629–9634.

26 Coelho T, Maia LF, da Silva AM, Cruz MW, Plante-Bordeneuve V, Suhr OB, Conceicao I, Schmidt HH, Trigo P, Kelly JW *et al.* (2013) Long-term effects of tafamidis for the treatment of transthyretin familial amyloid polyneuropathy. *J Neurol* **260**, 2802–2814.

27 Maurer MS, Schwartz JH, Gundapaneni B, Elliott PM, Merlini G, Waddington-Cruz M, Kristen AV, Grogan M, Witteles R, Damy T *et al.* (2018) Tafamidis treatment for patients with transthyretin amyloid cardiomyopathy. *N Engl J Med* **379**, 1007–1016.

28 Coelho T, Maia LF, da Silva AM, Cruz MW, Plante-Bordeneuve V, Lozeron P, Suhr OB, Campistol JM, Conceicao I, Schmidt H *et al.* (2012) Tafamidis for familial amyloid polyneuropathy. A randomized, controlled trial. *Neurology* **79**, 785–792.

29 Monteiro C, Martins da Silva A, Ferreira N, Mesgarzadeh J, Novais M, Coelho T & Kelly JW (2018) Cerebrospinal fluid and vitreous body exposure to orally administered tafamidis in hereditary ATTRV30M (p.TTRV50M) amyloidosis patients. *Amyloid* **25**, 120–128.

30 Casal I, Monteiro S & Beirao JM (2016) Tafamidis in hereditary ATTR amyloidosis – our experience on monitoring the ocular manifestations. *Amyloid* **23**, 262–263.

31 Salvi F, Volpe R, Pastorelli F, Bianchi A, Vella A, Rapezzi C & Mascalchi M (2018) Failure of tafamidis to halt progression of Ala36Pro TTR oculomeningovascular amyloidosis. *J Stroke Cerebrovasc Dis* **27**, e212–e214.

32 Sant'Anna R, Gallego P, Robinson LZ, Pereira-Henriques A, Ferreira N, Pinheiro F, Esperante S, Pallares I, Huertas O, Almeida MR *et al.* (2016) Repositioning tolcapone as a potent inhibitor of transthyretin amyloidogenesis and associated cellular toxicity. *Nat Commun* **7**, 10787.

33 Gomes J, Salvadó M, Reig N, Suñé P, Casanovas C, Rojas-Garcia R & Insa R (2019) Transthyretin stabilization activity of the catechol-*O*-methyltransferase inhibitor tolcapone (SOM0226) in hereditary ATTR amyloidosis patients and asymptomatic carriers: proof-of-concept study. *Amyloid* **26**, 74–84.

34 Reig N, Ventura S, Salvadó M, Gámez J & Insa R (2015) SOM0226, a repositioned compound for the treatment of TTR amyloidosis. *Orphanet J Rare Dis* **10**, P9.

35 Russ H, Müller T, Woitalla D, Rahbar A, Hahn J & Kuhn W (1999) Detection of tolcapone in the cerebrospinal fluid of parkinsonian subjects. *Naunyn-Schmiedeberg's Arch Pharmacol* **360**, 719–720.

36 Hagiwara K, Ochi H, Suzuki S, Shimizu Y, Tokuda T, Murai H, Shigeto H, Ohyagi Y, Iwata M, Iwaki T *et al.* (2009) Highly selective leptomeningeal

amyloidosis with transthyretin variant ala25thr. *Neurology* **72**, 1358–1359.

37 Petersen RB, Goren H, Cohen M, Richardson SL & Tresser N (1997) Transthyretin amyloidosis: a new mutation associated with dementia. *Ann Neurol* **41**, 307–313.

38 Ueno S, Uemichi T, Yorifuji S & Tarui S (1990) A novel variant of transthyretin (Tyr114 to Cys) deduced from nucleotide sequences of gene fragments from familial amyloidotic polyneuropathy in Japanese sibling cases. *Biochem Biophys Res Commun* **169**, 143–147.

39 Hammarstrom P, Jiang X, Deechongkit S & Kelly JW (2001) Anion shielding of electrostatic repulsions in transthyretin modulates stability and amyloidosis: insight into the chaotrope unfolding dichotomy. *Biochemistry* **40**, 11453–11459.

40 Sant'Anna R, Almeida MR, Varejao N, Gallego P, Esperante S, Ferreira P, Pereira-Henriques A, Palhano FL, de Carvalho M, Foguel D *et al.* (2017) Cavity filling mutations at the thyroxine-binding site dramatically increase transthyretin stability and prevent its aggregation. *Sci Rep* **7**, 44709.

41 McCammon MG, Scott DJ, Keetch CA, Greene LH, Purkey H, Petrassi HM, Kelly JW & Robinson CV (2002) Screening transthyretin amyloid fibril inhibitors: characterization of novel multiprotein, multiligand complexes by mass spectrometry. *Structure* **10**, 851–863.

42 Pullakhandam R, Srinivas PN, Nair MK & Reddy GB (2009) Binding and stabilization of transthyretin by curcumin. *Arch Biochem Biophys* **485**, 115–119.

43 Vega S, Abian O & Velazquez-Campoy A (2015) A unified framework based on the binding polynomial for characterizing biological systems by isothermal titration calorimetry. *Methods* **76**, 99–115.

44 Freire E, Schön A & Velazquez-Campoy A (2009) Chapter 5 Isothermal titration calorimetry. General formalism using binding polynomials. *Methods Enzymol* **455**, 127–155.

45 Verona G, Mangione PP, Raimondi S, Giorgetti S, Faravelli G, Porcari R, Corazza A, Gillmore JD, Hawkins PN, Pepys MB *et al.* (2017) Inhibition of the mechano-enzymatic amyloidogenesis of transthyretin:

role of ligand affinity, binding cooperativity and occupancy of the inner channel. *Sci Rep* **7**, 182.

46 Miller M, Pal A, Albusairi W, Joo H, Pappas B, Haque Tuhin MT, Liang D, Jampala R, Liu F, Khan J *et al.* (2018) Enthalpy-driven stabilization of transthyretin by AG10 mimics a naturally occurring genetic variant that protects from transthyretin amyloidosis. *J Med Chem* **61**, 7862–7876.

47 Iakovleva I, Brännström K, Nilsson L, Gharibyan A, Begum A, Anan I, Walfridsson M, Sauer-Eriksson AE & Olofsson A (2015) Enthalpic forces correlate with the selective of transthyretin-stabilizing ligands in human plasma. *J Med Chem* **58**, 6507–6515.

48 Palaninathan SK (2012) Nearly 200 X-ray crystal structures of transthyretin: what do they tell us about this protein and the design of drugs for TTR amyloidoses? *Curr Med Chem* **19**, 2324–2342.

49 Juanhuix J, Gil-Ortiz F, Cuni G, Colldelram C, Nicolas J, Lidon J, Boter E, Ruget C, Ferrer S & Benach J (2014) Developments in optics and performance at BL13-XALOC, the macromolecular crystallography beamline at the ALBA synchrotron. *J Synchrotron Radiat* **21**, 679–689.

50 Kabsch W (2010) Integration, scaling, space-group assignment and post-refinement. *Acta Crystallogr D* **66**, 133–144.

51 Winn MD, Ballard CC, Cowtan KD, Dodson EJ, Emsley P, Evans PR, Keegan RM, Krissinel EB, Leslie AG, McCoy A *et al.* (2011) Overview of the CCP4 suite and current developments. *Acta Crystallogr D* **67**, 235–242.

52 Adams PD, Afonine PV, Bunkoczi G, Chen VB, Davis IW, Echols N, Headd JJ, Hung LW, Kapral GJ, Grosse-Kunstleve RW *et al.* (2010) PHENIX: a comprehensive Python-based system for macromolecular structure solution. *Acta Crystallogr D* **66**, 213–221.

53 Emsley P, Lohkamp B, Scott WG & Cowtan K (2010) Features and development of Coot. *Acta Crystallogr D* **66**, 486–501.

CHAPTER 2

Development of a highly potent transthyretin amyloidogenesis inhibitor: design, synthesis and evaluation

Article

Development of a Highly Potent Transthyretin Amyloidogenesis Inhibitor: Design, Synthesis, and Evaluation

Francisca Pinheiro, Irantzu Pallarès, Francesca Peccati, Adrià Sánchez-Morales, Nathalia Varejão, Filipa Bezerra, David Ortega-Alarcon, Danilo Gonzalez, Marcelo Osorio, Susanna Navarro, Adrián Velázquez-Campoy, Maria Rosário Almeida, David Reverter, Félix Busqué, Ramon Alibés, Mariona Sodupe, and Salvador Ventura*

Read Online

ACCESS | Metrics & More | Article Recommendations | Supporting Information

ABSTRACT: Transthyretin amyloidosis (ATTR) is a group of fatal diseases described by the misfolding and amyloid deposition of transthyretin (TTR). Discovering small molecules that bind and stabilize the TTR tetramer, preventing its dissociation and subsequent aggregation, is a therapeutic strategy for these pathologies. Departing from the crystal structure of TTR in complex with tolcapone, a potent binder in clinical trials for ATTR, we combined rational design and molecular dynamics (MD) simulations to generate a series of novel halogenated kinetic stabilizers. Among them, **M-23** displays one of the highest affinities for TTR described so far. The TTR/**M-23** crystal structure confirmed the formation of unprecedented protein−ligand contacts, as predicted by MD simulations, leading to an enhanced tetramer stability both *in vitro* and in whole serum. We demonstrate that MD-assisted design of TTR ligands constitutes a new avenue for discovering molecules that, like **M-23**, hold the potential to become highly potent drugs to treat ATTR.
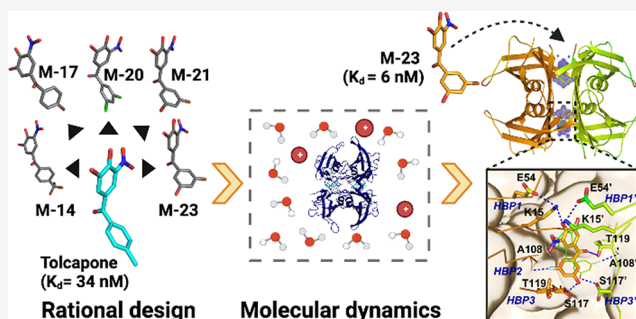
INTRODUCTION

Amyloid diseases constitute a diverse group of pathologies characterized by protein misfolding, aggregation, and the buildup of insoluble fibrils in tissues and organs throughout the body.[1] Transthyretin (TTR) is one of many proteins related with these disorders.[2]

The liver and the choroid plexus are the major sites of TTR synthesis. TTR transports the retinol-binding protein−retinol complex and functions as a backup carrier for thyroxine (T_4) in the blood and as a main transporter of T_4 in the cerebrospinal fluid.[3−5] The extracellular misfolding of TTR and subsequent accumulation of amyloid fibrils in a variety of tissues underlie the onset of a group of disorders known as transthyretin amyloidosis (ATTR).[6]

Native TTR is a homotetramer comprising four β-sheet rich subunits of 127 amino acid residues each, termed A, B, C, and D. The monomers associate via their edge β-strands, yielding two dimers (AB and CD) that further associate back-to-back to render the tetramer. The AB/CD dimer−dimer interface defines two identical funnel-shaped T_4-binding sites at opposite sides of the molecule.[7,8] TTR-tetramer dissociation at the T_4-binding interface creates dimers that promptly dissociate into aggregation-prone monomers, representing the rate-limiting step during TTR misfolding and amyloid formation.[9,10]

Pathogenic mutations accelerate TTR aggregation by thermodynamic or kinetic destabilization of the protein.[11,12] To date, more than 130 mutations in the TTR gene have been described, which result in autosomal dominant familial forms of the disease.[13] The majority of disease-associated variants are caused by missense mutations and display tissue specificity and pathology. Familial amyloid polyneuropathy (FAP) and familial amyloid cardiomyopathy (FAC) are the most prevalent presentations of ATTR, compromising the peripheral nervous system and the heart, respectively.[14−16] For some rare TTR mutations, central nervous system (CNS) involvement has been reported.[17,18]

Aging is another risk factor for ATTR, and deposition of wild-type (WT) TTR, preferentially in the myocardium, causes senile systemic amyloidosis (SSA), an underdiagnosed late-onset sporadic cardiomyopathy impacting up to 10−20% of the population over 65 years old.[19,20] Notably, SSA is the

leading cause of mortality in human subjects aged over 110 years.[21]

An alternative pathway for TTR amyloid formation *in vivo* proposes that TTR aggregation is triggered by proteolytic cleavage. It is supported by the fact that the amyloid deposits formed by most TTR variants *in vivo* contain the truncated 49-127 polypeptide.[22,23] This mechanism might be especially relevant in organs with substantial shear stress, such as the heart, where the physiological fluid flow, together with the hydrophobic forces acting on the protein, might increase its susceptibility to proteolytic cleavage.[24,25]

In the last years, new therapies have been developed for the treatment of ATTR that aim to replace liver transplantation, the standard therapy for hereditary ATTR.[26,27] Current therapeutic approaches mainly rely on reducing amyloid formation through TTR kinetic stabilization[28] or inhibition of TTR protein synthesis (e.g., inotersen[29] and patisiran[30]).

The kinetic stabilizer strategy gained momentum upon the identification of a TTR disease protective substitution, T119M.[31] The T119M mutation reduces the rate of TTR tetramer dissociation and, consequently, the amyloidogenic propensity of the native ensemble.[32]

Thyroglobulin and albumin are the main transporters of T_4 in the blood, with only 1% of TTR being bound to the hormone, and thus, T_4 pockets are largely empty. Ligand binding at the T_4 sites kinetically stabilizes TTR, increasing the energy barrier for tetramer dissociation. Thus, small molecules displaying selectivity and affinity for docking at T_4 cavities have emerged as therapeutic options for treating ATTR (Figure 1).
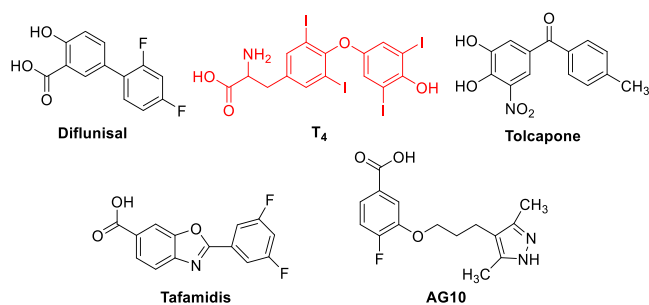

Figure 1. Chemical structures of T_4[7] (in red), the natural ligand of TTR, and examples of T_4-inspired kinetic stabilizers.[33,37–39]

So far, only the benzoxazole tafamidis[33] (Vyndaqel and Vyndamax) has reached the market. Treatment with tafamidis was well tolerated and has shown to delay the progression of neuropathy and cardiomyopathy in FAP[34] and FAC,[35] thus being approved for these indications. However, disease progression occurs in ~30% of patients with familial ATTR,[36] highlighting the need for developing alternative TTR kinetic stabilizers.

More recently, our group repurposed tolcapone for the treatment of ATTR. Tolcapone (Tasmar, 3,4-dihydroxy-4′-methyl-5-nitrobenzophenone) is a potent inhibitor of catechol-*O*-methyltransferase (COMT) approved in the United States and Europe as an adjunct to levodopa and carbidopa for the treatment of Parkinson's disease. Tolcapone binds with high affinity and specificity to TTR, stabilizing the tetramer and thus preventing amyloidogenesis and protecting from TTR cytotoxicity.[39] In a Phase IIa clinical study for FAP,[40,41] tolcapone completely stabilized plasmatic TTR in all patients studied, and no adverse events were registered. In addition,

tolcapone has been shown to inhibit TTR aggregation induced by proteolytic cleavage at physiological pH,[42] a process that might underlie TTR amyloidogenesis *in vivo*. Noteworthily, tolcapone penetrates the blood–brain barrier[43] and effectively inhibits the aggregation of the extremely destabilized and fast dissociating variants that cause the rare, but lethal, CNS amyloidosis.[44]

Thermodynamic analysis revealed that tolcapone binds and stabilizes TTR more effectively than tafamidis, exhibiting higher *ex vivo* anti-amyloidogenic activity. More enthalpically favorable binding to TTR, together with the lack of negative cooperativity, which in the case of tafamidis significantly reduces the affinity for the second T_4 site, seems to underlie the higher potency of tolcapone.

Tolcapone was the best performer of our repurposed compound library. However, this does not mean that the contacts it established with the TTR T_4-binding cavities were optimal. In a way, a new repurposed drug may be considered as a hit to be further optimized to increase its target potency and selectivity, especially if atomic structural information of the protein–drug complex is available. Here, we exploited this concept with the purpose of generating a TTR kinetic stabilizer with improved binding affinity and anti-amyloidogenic activity relative to tolcapone.

Up to now, more than 300 TTR crystal structures are available in the Protein Data Bank,[45,46] most of them complexed to small-molecule ligands. A detailed structural study of a set of 23 high-resolution TTR structures comprising WT, non-amyloidogenic, and amyloidogenic variants concluded that they are almost exactly superimposable. Moreover, differences in the positioning of certain loops or in the side chain rotamers of some residues, including those of the T_4-binding sites, were not significant.[47] Accordingly, the binding of kinetic stabilizers does not result in significant TTR structural rearrangements, and indeed, the structures of TTR with or without ligands are essentially identical except for a reduced number of side chain rotamers in the vicinity of the binders (Figure 2A). This indicates that crystallographic structures correspond to static pictures where it is difficult to discern the dynamic impact of both mutations and ligands on the native TTR stability, challenging the use of structure–activity relationships to evolve stronger TTR binders.

Molecular dynamics (MD) simulations allow studying the structural dynamics of biological systems at atomic resolution.[48] MD simulations are especially useful in modeling and assessing the binding capacity of small molecules to target proteins since they not only provide atomic information on the interaction but also allow estimation of the binding energetics.[49,50] MD simulations have been used to investigate the impact of mutations on TTR conformational flexibility[51,52] and to investigate the mechanism of TTR protection by existent kinetic stabilizers.[53–55] However, to the best of our knowledge, MD-based methods for estimating binding affinities have not been employed to assist in the design of novel molecules aimed to interact with T_4-binding sites.

Here we combined rational design and MD simulations to generate a series of tolcapone-inspired kinetic stabilizers. The candidates were chemically synthesized and experimentally validated. As a result, we describe **M-23**, a noncooperative kinetic stabilizer that binds TTR with an affinity >5-fold than tolcapone. Thermodynamic analysis indicates that this high affinity results from an optimized enthalpy of binding, whereas the TTR/**M-23** crystal structure demonstrates the effective
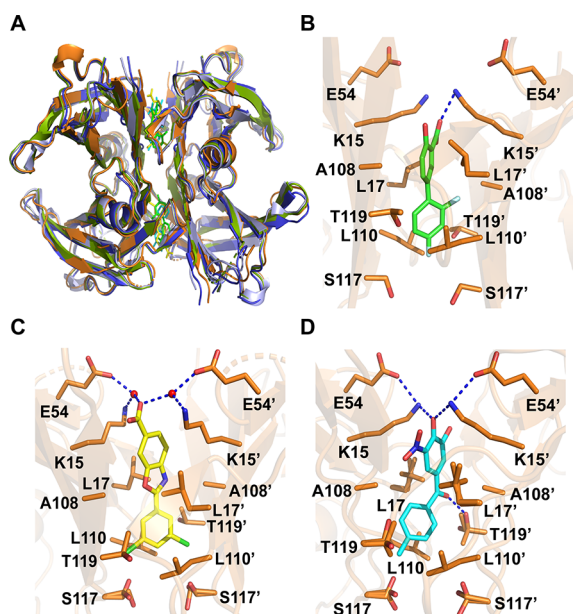
Figure 2. (A) Superposition of WT-TTR in Apo-form (light blue) and complexed to diflunisal (olive), tolcapone (blue), and tafamidis (orange). Overlaid tetramers are shown in cartoon, and diflunisal (green), tafamidis (yellow), and tolcapone (cyan) are represented as sticks. (B−D) Close-up view of the binding of diflunisal, tolcapone, and tafamidis to WT-TTR. Compounds are colored as in panel A. Residues interacting with TTR are shown as sticks (orange). Blue dashed lines signal the hydrogen bonds and the salt bridges. Structures prepared from PDB structures (B) 3D2T,[37] (C) 3TCT,[33] and (D) 4D7B.[39]

existence of new contacts between the two moieties, as predicted by MD simulations. These interactions result in a significantly higher stabilization of the TTR tetramer *in vitro* and *ex vivo* relative to tolcapone, turning **M-23** into a promising candidate for therapeutic intervention in ATTR.

■ RESULTS AND DISCUSSION

Rationale for the Design of Tolcapone Analogues. Each TTR T_4-binding site contains three pairs of symmetric depressions known as halogen-binding pockets (HBPs: HBP1 and HBP1′, HBP2 and HBP2′, and HBP3 and HBP3′), wherein the four iodine atoms of the hormone reside. The innermost pocket is HBP3 and is established by Ser117, Leu110, Thr119, and Ala108 side chains. HBP1 is placed at the entrance of the T_4-binding site and comprises Lys15, Leu17, Thr106, and Val121, whereas the central pocket HBP2 is formed by Leu17, Ala108, Ala109, and Leu110 along with the methylene carbons of Lys15.

Typically, TTR kinetic stabilizers have two aromatic rings, one ring substituted with halogens, placed at HBP2/HBP3, and the other displaying hydrophilic substituents, placed at HBP1. The nonsteroidal anti-inflammatory drug diflunisal (Figure 2B), already in clinical trials,[56] exemplifies these properties, with the difluorophenyl group pointing to the inner part of the channel and the two fluor atoms located in HBP2. In HBP1, the carboxy group of diflunisal establishes a salt bridge with the amino group of Lys15.

In tafamidis (Figure 2C), the 3,5-dichloro moiety is surrounded by the residues in the HBPs 3/3′, whereas the carboxy end forms a water-mediated hydrogen bond with the amino group of Lys15. The highest binding affinity of

tafamidis, in respect to diflunisal, is difficult to explain from the crystal structure in terms of specific protein−compound interactions and has been attributed to a stronger halogen bonding capability of the chloride moiety.

In tolcapone (Figure 2D), the 4-methyl-phenyl ring occupies HBP3, and a specific hydrogen bond is established between the linker carbonyl group of the compound and the hydroxyl side chain of Thr119. The 3,4-dihydroxy-5-nitrophenyl ring of tolcapone is positioned in HBP1, forming a hydrogen bond with Lys15, which in turn stabilizes the ionic interactions between Lys15 and Glu54. These direct interactions in the outer face of the cavity, together with hydrogen bonding to Thr119, likely contribute to the favorable enthalpic binding of this molecule, explaining why it stabilizes TTR more effectively than tafamidis.

In contrast to diflunisal and tafamidis, tolcapone does not possess halogen atoms, and although the methyl group is placed in a favorable environment in HBP3, it cannot establish the halogen bonds that characterize T_4, diflunisal, and tafamidis. Halogenation has been shown to be effective at increasing the affinity of certain TTR ligands, like in the case of iododiflunisal.[57] Therefore, we decided to use MD simulations to study if endorsing tolcapone with different halogen moieties, while trying to keep the optimal hydrogen bonding capability of the upper ring and the middle carbonyl group intact, might result in optimized kinetic stabilizers.

Molecular Dynamics Simulations of Halogenated Tolcapone Analogues. All the new ligands developed in the present work are benzophenone derivatives with two phenyl moieties, one common to all ligands, i.e., the 3,4-dihydroxy-5-nitrophenyl ring, more exposed to the solvent, and a second one including different halogen substituents pointing toward the inner binding pocket (Figure 3). Differences are thus expected to arise from the distinct contacts between this inner aryl moiety and TTR at the binding site.
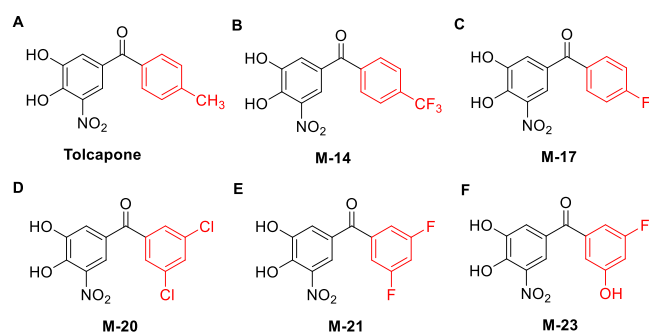
Figure 3. (A−F) Chemical structures of tolcapone derivatives synthesized and evaluated in this study . The second aryl ring is shown in red to highlight the differences between the compounds.

In the first two ligands, the 4-CH$_3$ group of tolcapone was substituted by either a −CF$_3$ group or −F, rendering compounds **M-14** and **M-17**, respectively (Figure 3A−C). The computed binding energies of tolcapone, **M-14**, and **M-17** to human WT-TTR and the main ligand−TTR hydrogen bond contacts (>10% frequency along the trajectory) are given in Table 1. Simulations are expected to provide the proper trends, although not absolute values. Note that for absolute affinities, the entropy term, particularly that owing to the decrease of translational and rotational freedom when the ligand binds to the protein, should be included. However, this entropic term

Table 1. Ligand-TTR Binding Energies (ΔG_{bind}), Gas Phase Binding Energies (ΔE_{gp}), Ligand Solvation Energies ($\Delta G_{L\text{-}solv}$), in kcal mol^{-1}, and Main Ligand−TTR H-Bond Contacts

compound	$\Delta G_{bind}{}^a$	$\Delta E_{gp}{}^b$	$\Delta G_{L\text{-}solv}$	ligand···TTR contacts
tolcapone	59.7	81.5	−10.9	C=O···T119
M-14	55.4	76.6	−10.6	
M-17	68.0	90.2	−11.1	C=O···T119, F···S117, F···T119

$^a\Delta G_{bind} = \Delta E_{gp} + 2 \times \Delta G_{L\text{-}solv}$. $^b\Delta E_{gp} = E_{TTR} + 2E_L - E_{TTR\text{-}2L}$.

should not vary significantly between our candidate molecules,[58] and as such, it is not expected to affect ligand comparisons.

As expected, all starting structures, derived from the crystal structure of the TTR−tolcapone complex (PDB: 4D7B), with the two ligands related by a C_2 symmetry axis, lose their initial symmetry along the simulation; i.e., the interactions between each ligand with AB or CD, albeit similar, are not identical. Furthermore, in all cases, the specific interactions in the outer binding pocket between the hydroxyl groups of the 3,4-dihydroxy-5-nitrophenyl moiety and Lys15 or between Glu54 and Lys15 identified in the crystal structure are only maintained in less than 5% of the trajectory due to temperature effects. Thus, from now on, we will focus on the interaction between the central C=O of the ligand and the hydroxyl group of Thr119 and on the additional ligand−TTR specific interactions resulting from the new substitutions on the phenyl moiety. The main structures, together with the H-bond evolution along the trajectories, are provided in Figure S1. Specific ligand−TTR contacts, with their frequency and shortest and average distances, are given in Table S1.

Regarding tolcapone, the C=O···Thr119 interaction appears with a frequency of 10%, with the minimum distance value being 2.63 Å, which resembles the one observed in the crystal structure (2.55 Å). For **M-14**, this interaction is lost,

appearing in less than 1% of the trajectory. This is due to the presence of the −CF$_3$ bulkier substituent, which introduces larger repulsive interactions that hinder the entrance into the cavity and leave the ligand more exposed to the solvent. Indeed, the shortest distance between the two ligands in t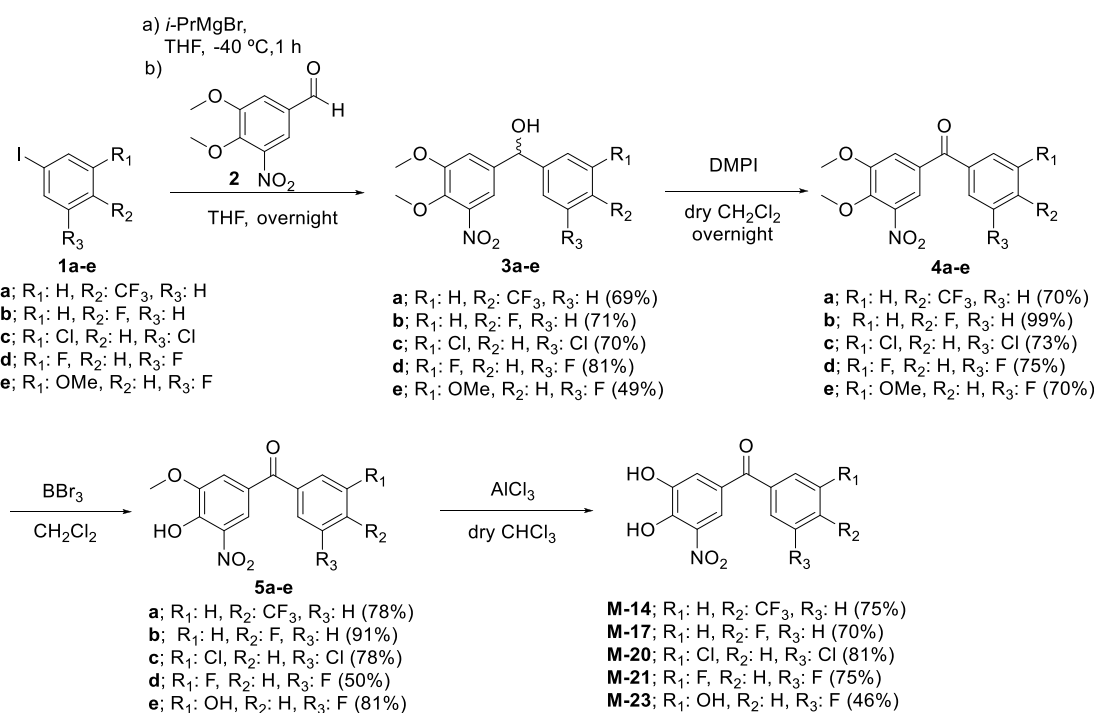hese two complexes, taken as the distance between the C atoms of the two ligands' C=O groups, is significantly larger in **M-14** (19.9 Å) than in tolcapone (15.8 Å). Consequently, **M-14** exhibits a smaller calculated binding energy (55.4 kcal mol^{-1}) than tolcapone (59.7 kcal mol^{-1}). In contrast, for **M-17**, with a −F in the para position instead of a −CF$_3$ group, the C=O···Thr119 interaction is maintained with an average frequency of ∼50%, with the shortest C=O···HO$_{T119}$ distance being 2.55 Å. In addition, new contacts between the −F substituents and both Thr119 and Ser117 appear, which further enhance the calculated ligand−TTR binding energy (68.0 kcal mol^{-1}) as compared to tolcapone (59.7 kcal mol^{-1}).

Binding of Halogenated Tolcapone Analogues to TTR. **M-14** and **M-17** were chemically synthesized as shown in Scheme 1. The synthesis procedure is explained in detail in the Experimental Section.

Isothermal titration calorimetry (ITC) was used to characterize their binding affinities for WT-TTR, and the thermodynamic parameters that describe the reaction were determined. Ligand binding to TTR can be cooperative (positive or negative cooperativity) or noncooperative.[59−61] Non- or positive cooperativity is desired; however, most reported ligands exhibit negative cooperativity,[33,62,63] which implies a loss of affinity for the second binding site after binding to the first one. Tolcapone, **M-14**, and **M-17** bound to TTR without any cooperativity (Figure 4A and Table 2), whereas tafamidis, included as a reference, exhibited the typical negative cooperative behavior (Kd$_1$ = 9.9 nM and Kd$_2$ = 260 nM).

Scheme 1. Synthesis of Tolcapone Analogues

1a-e
a; R$_1$: H, R$_2$: CF$_3$, R$_3$: H
b; R$_1$: H, R$_2$: F, R$_3$: H
c; R$_1$: Cl, R$_2$: H, R$_3$: Cl
d; R$_1$: F, R$_2$: H, R$_3$: F
e; R$_1$: OMe, R$_2$: H, R$_3$: F

3a-e
a; R$_1$: H, R$_2$: CF$_3$, R$_3$: H (69%)
b; R$_1$: H, R$_2$: F, R$_3$: H (71%)
c; R$_1$: Cl, R$_2$: H, R$_3$: Cl (70%)
d; R$_1$: F, R$_2$: H, R$_3$: F (81%)
e; R$_1$: OMe, R$_2$: H, R$_3$: F (49%)

4a-e
a; R$_1$: H, R$_2$: CF$_3$, R$_3$: H (70%)
b; R$_1$: H, R$_2$: F, R$_3$: H (99%)
c; R$_1$: Cl, R$_2$: H, R$_3$: Cl (73%)
d; R$_1$: F, R$_2$: H, R$_3$: F (75%)
e; R$_1$: OMe, R$_2$: H, R$_3$: F (70%)

5a-e
a; R$_1$: H, R$_2$: CF$_3$, R$_3$: H (78%)
b; R$_1$: H, R$_2$: F, R$_3$: H (91%)
c; R$_1$: Cl, R$_2$: H, R$_3$: Cl (78%)
d; R$_1$: F, R$_2$: H, R$_3$: F (50%)
e; R$_1$: OH, R$_2$: H, R$_3$: F (81%)

M-14; R$_1$: H, R$_2$: CF$_3$, R$_3$: H (75%)
M-17; R$_1$: H, R$_2$: F, R$_3$: H (70%)
M-20; R$_1$: Cl, R$_2$: H, R$_3$: Cl (81%)
M-21; R$_1$: F, R$_2$: H, R$_3$: F (75%)
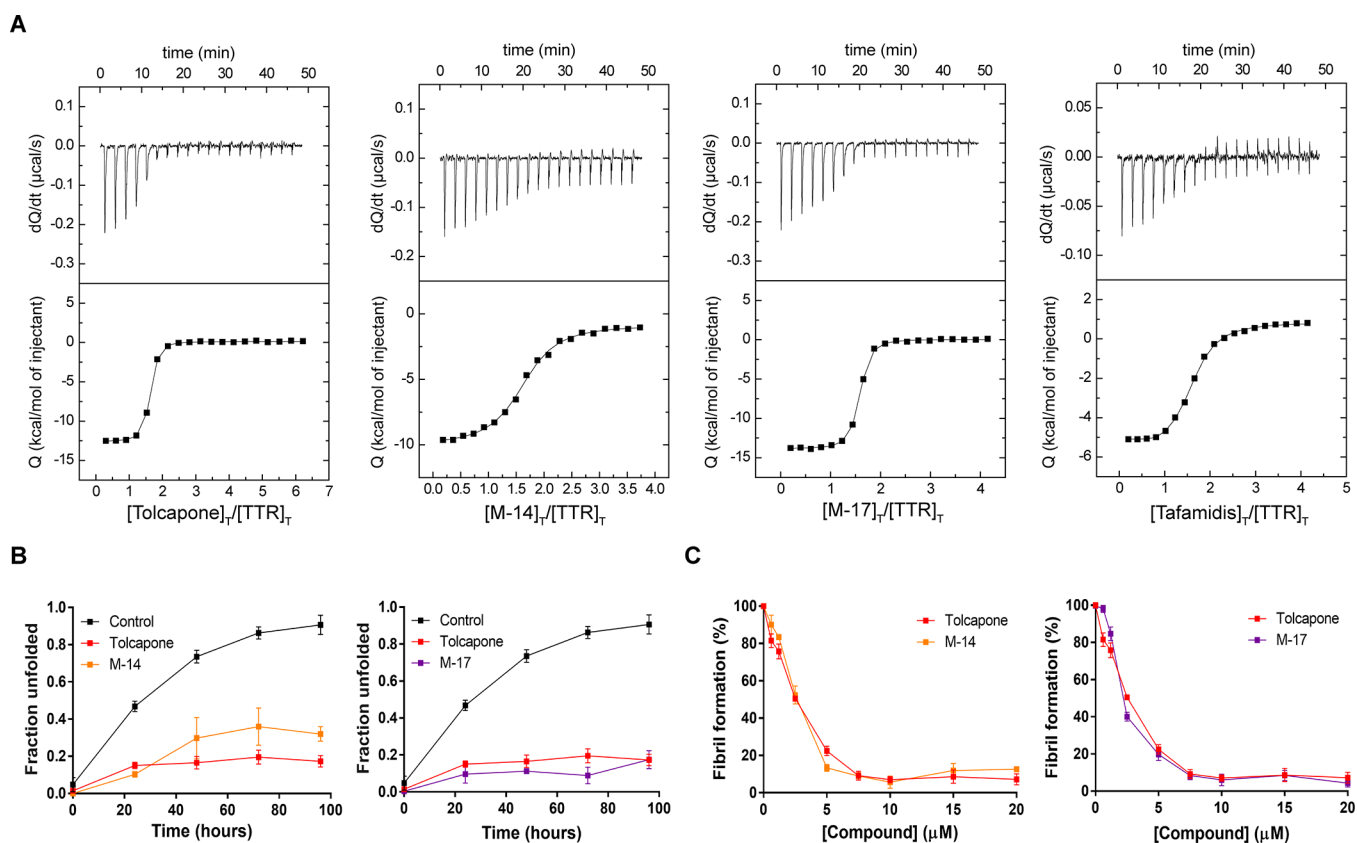**M-23**; R$_1$: OH, R$_2$: H, R$_3$: F (46%)

Figure 4. *In vitro* characterization of halogenated tolcapone analogues, **M-14**, and **M-17**. (A) Interaction of WT-TTR with tolcapone, **M-14**, and **M-17** as assessed by ITC. Tafamidis was tested as a reference. The top panels represent the raw data (thermogram), while the lower panels correspond to the integrated heat changes upon binding plotted against the ligand/TTR concentration ratio (binding isotherm). The solid line describes the best fit according to a two-site binding model (with or without cooperativity) for each test compound. (B) WT-TTR (1.8 μM) urea-induced tetramer dissociation (6 M urea) in the absence or presence of tolcapone, **M-14**, or **M-17** (at 3.6 μM), as measured by Trp fluorescence. The values correspond to mean $\pm$ SEM (n = 3). (C) Acid-mediated TTR (at a final assay concentration of 3.6 μM) aggregation as a function of inhibitor concentration determined by turbidity at 340 nm. The values refer to mean $\pm$ SEM (n = 3).

Table 2. Thermodynamic Parameters Determined by ITC for the Binding of M-14 and M-17 to WT-TTR

	K_d (nM)	ΔG (kcal mol^{-1})	ΔH (kcal mol^{-1})	$-T\Delta S$ (kcal mol^{-1})
tolcapone	34	−10.2	−12.8	2.6
tafamidis	9.9[a]	−10.9[a]	−6.0[a]	−4.9[a]
	260[b]	−9.0[b]	−6.5[b]	−2.5[b]
M-14	310	−8.9	−9.2	0.3
M-17	31	−10.3	−14.0	3.7

[a]Correspond to the values for the first binding site of TTR.
[b]Correspond to the values for the second binding site of TTR.

In agreement with the trend observed in the MD binding energy calculations, **M-14** exhibited a higher K_d (310 nM) and a lower enthalpic contribution to binding ($\Delta H = -9.2$ kcal mol^{-1}) than tolcapone (K_d = 34 nM and $\Delta H = -12.8$ kcal mol^{-1}), whereas the affinity and enthalpic binding term of **M-17** were higher (K_d = 31 nM and $\Delta H = -14.0$ kcal mol^{-1}). The strong binding of tolcapone and **M-17**, with dissociation constants in the low nanomolar range, was entirely enthalpically driven ($\Delta H < 0$; $-T\Delta S > 0$). As observed in MD simulations, this indicates the formation of specific non-covalent interactions between the protein and the ligand. Enthalpy−entropy compensation effects resulted in very similar ΔG values for **M-17** and tolcapone.

TTR Kinetic Stabilization by Halogenated Tolcapone Analogues. We addressed whether **M-14** and **M-17** kinetically stabilize TTR, inhibiting urea-induced tetramer dissociation. Using urea concentrations in the post-transition region for tertiary structural changes allows measuring tetramer dissociation, as the monomers unfold in a few milliseconds and remain unfolded.[11,64] Accordingly, TTR samples were incubated in the absence or presence of compounds, and TTR denaturation was triggered by adding 6 M urea. Tertiary structural changes were monitored along time by tryptophan (Trp) intrinsic fluorescence, which was used to determine the fraction of unfolded protein at any time (Figure 4B). Tolcapone was analyzed in parallel for comparative purposes.

The three molecules significantly decreased the amount of dissociated tetramer, as well as the rate of tetramer dissociation, when present at equimolar levels relative to T$_4$-binding sites. Tolcapone protected up to 82.7 $\pm$ 3.1% of TTR molecules from urea induced unfolding; **M-17** provided a similar degree of protection, whereas **M-14** was less effective.

TTR Anti-aggregation Activity of Halogenated Tolcapone Analogues. The anti-amyloidogenic activity of **M-14** and **M-17** was evaluated using a well-established fibril-formation assay[11,65] and compared with that of tolcapone. TTR (7.2 μM) was mixed with increasing concentrations of the compound (0−40 μM) for 30 min (pH 7.4, at 37 °C), and then, the pH was lowered to 4.2, which is the most favorable

pH for TTR fibrilization.[66] After an additional incubation of 72 h, the percentage of conversion of native TTR into amyloid fibrils was calculated by measuring turbidity at 340 nm and is reported relative to TTR incubated in the same conditions in the absence of an inhibitor (100%) in Figure 4C.

The three molecules displayed a strong anti-amyloidogenic activity, decreasing TTR aggregation in a concentration-dependent manner. In all cases, the protection was >60% at the equimolar total concentration (one molecule of the test compound bound per molecule of the TTR tetramer) and ≥87.4 when the compound concentration was greater than or equal to the one of T_4-binding sites. These results indicate that tolcapone is already a very potent inhibitor of TTR aggregation, reaching up to 92.8% inhibition at 20 μM; accordingly, despite M-17 being a slightly better binder and kinetic stabilizer than the original molecule, these properties do not translate into an optimization of its anti-aggregation properties, at least at acidic pH.

Molecular Dynamics Simulations of Demethylated 3,5-Disubstituted and Halogenated Tolcapone Analogues. In M-17, replacing tolcapone −CH_3 by −F resulted in increased affinity and a higher enthalpic contribution to the binding. This is in line with the suggestion that, in tafamidis, the −Cl atoms in the 3,5-dichloro moiety contribute significantly to binding in the innermost TTR HBP3 pocket. Therefore, we designed M-20, a chimeric molecule in which the 4-methyl-phenyl ring of tolcapone was replaced by the 3,5-dichloro-phenyl ring in tafamidis (Figure 3D). The idea was to combine the favorable noncovalent contacts of tolcapone in the outer and middle sections of the T_4 cavity with those established by tafamidis in the inner pocket. In addition, because −Cl and −F seemed to contribute differentially to binding in HPB3,[67] as deduced from the affinities for TTR of diflunisal and tafamidis, we designed M-21, in which the lower tolcapone ring was substituted by a 3,5-difluoro-phenyl ring (Figure 3E). Thus, in a way, M-21 is a chimera of tolcapone and diflunisal, although the −F substituents lay in different relative positions.

The computed binding energies of M-20 and M-21 to human WT-TTR and the main ligand−TTR hydrogen bond contacts (>10% frequency along the trajectory) are provided in Table 3. The main structures for all systems, together with the

M-21 (−F) since the distance between the C atoms of the two ligands' C═O groups is significantly larger in M-20 (19.4 Å) than in M-21 (15.3 Å) or tolcapone (15.8 Å). Because of this displacement toward the upper part of the T_4 cavity, one of the −Cl atoms contacts Thr119 in M-20. As in M-17, the −F atoms in M-21 establish additional interactions with Ser117 in the HBP3 pocket, whereas no such contacts were observed for M-20. The interplay of interactions results in the calculated binding energies for M-20 (57.0 kcal mol^{−1}) and M-21 (74.0 kcal mol^{−1}) being lower and higher than the one of tolcapone (59.7 kcal mol^{−1}), respectively.

The high binding energy of M-21 indicates that the contacts between the phenyl ring substituents and the inner Ser117 make important contributions to the molecule−TTR complex. With this idea in mind, we designed M-23 (Figure 3F), in which −F in R3 was substituted by an −OH to favor the formation of a specific hydrogen bond with the side chain of Ser117. The MD simulations indicate that this interaction is formed with a frequency that ranges from 15 to 90% (Table S2), with the shortest distance being 2.52 Å. In addition, the C═O···Thr119 contact is maintained in M-23, with a frequency of 37 and 49% for ligands 1 and 2, respectively, and a minimum distance of 2.59 Å. As a result, M-23 displays the highest binding energy among the modeled compounds (84.4 kcal mol^{−1}) and is expected to be a significantly better binder than tolcapone (Table 3, Figure S2C, and Table S2). Furthermore, and as found for M-21, a slightly larger internalization of the ligand is observed for M-23 compared to tolcapone, with the shortest distance between the C atoms of the two ligands' C═O groups being 15.3 Å for M-23 and 15.8 Å for tolcapone.

Of note, in addition to the molecule−protein interactions, potential new residue−residue contacts induced by the binding of the compound might contribute to the tetramer stability. In particular, the buried Ser117 residue in each TTR subunit can establish an intersubunit hydrogen bond with Ser117 in the other monomer in the dimer (A−B or C−D contacts). MD simulations indicate that these interactions are far more frequent when TTR is bound to the ligands than when the T_4-binding cavity is empty (Table S3). Noticeably, among the double substituted compounds, M-23 is the one rendering the smaller average distances between the Ser117 residues in the weaker AB/CD dimer−dimer interface (Table S4).

Binding of Demethylated 3,5-Disubstituted and Halogenated Tolcapone Analogues. Compounds M-20, M-21, and M-23 were obtained according to Scheme 1. The chemical synthesis is detailed in the Experimental Section. ITC experiments indicated that the three molecules bound strongly to TTR without apparent cooperativity (Figure 5A and Table 4). In excellent agreement with MD simulations, M-20 exhibited a higher K_d (85 nM) and lower enthalpic contribution to binding ($\Delta H = -11.7$ kcal mol^{−1}) than tolcapone ($K_d = 34$ nM and $\Delta H = -12.8$ kcal mol^{−1}). The affinity of M-21 was higher ($K_d = 26$ nM) than that of tolcapone, whereas the enthalpic binding term was lower ($\Delta H = -11.3$ kcal mol^{−1}). However, a lower entropic penalty for binding in M-21 results in a slightly higher ΔG (−10.4 kcal mol^{−1}) relative to tolcapone (−10.2 kcal mol^{−1}).

The K_d of M-23 is exceptionally low (6.2 nM), corresponding to a binding affinity >5-fold than that of tolcapone, with a very high enthalpy for binding ($\Delta H = -16.6$ kcal mol^{−1}). The binding of M-23 is completely enthalpically driven, with an entropy penalty (5.4 kcal mol^{−1}) higher than

Table 3. Ligand−TTR Binding Energies (ΔG_{bind}), Gas Phase Binding Energies (ΔE_{gp}), Ligand Solvation Energies (ΔG_{L-solv}), in kcal mol^{−1}, and Main Ligand−TTR H-Bond Contacts

compound	ΔG_{bind}[a]	ΔE_{gp}[b]	ΔG_{L-solv}	ligand···TTR contacts
M-20	57.0	79.0	−11.0	Cl···T119
M-21	74.0	95.2	−10.6	C═O···T119, F···S117
M-23	84.4	116.2	−15.9	C═O···T119, OH···S117, F···S117

[a]$\Delta G_{bind} = \Delta E_{gp} + 2 \times \Delta G_{L-solv}$. [b]$\Delta E_{gp} = E_{TTR} + 2E_L - E_{TTR-2L}$.

H-bond evolution along the trajectories, are shown in Figure S2A,B. Specific ligand−TTR contacts, with their frequency and shortest and average distances, are given in Table S2.

For M-21, the C═O···Thr119 interaction appears with a frequency of 20%, with the shortest C═O···HO_{T119} distance being 2.63 Å. In M-20, this interaction is lost, occurring only in less than 1% of the trajectory. As in M-14, this seems to respond to the bulkier substituents of M-20 (−Cl) relative to
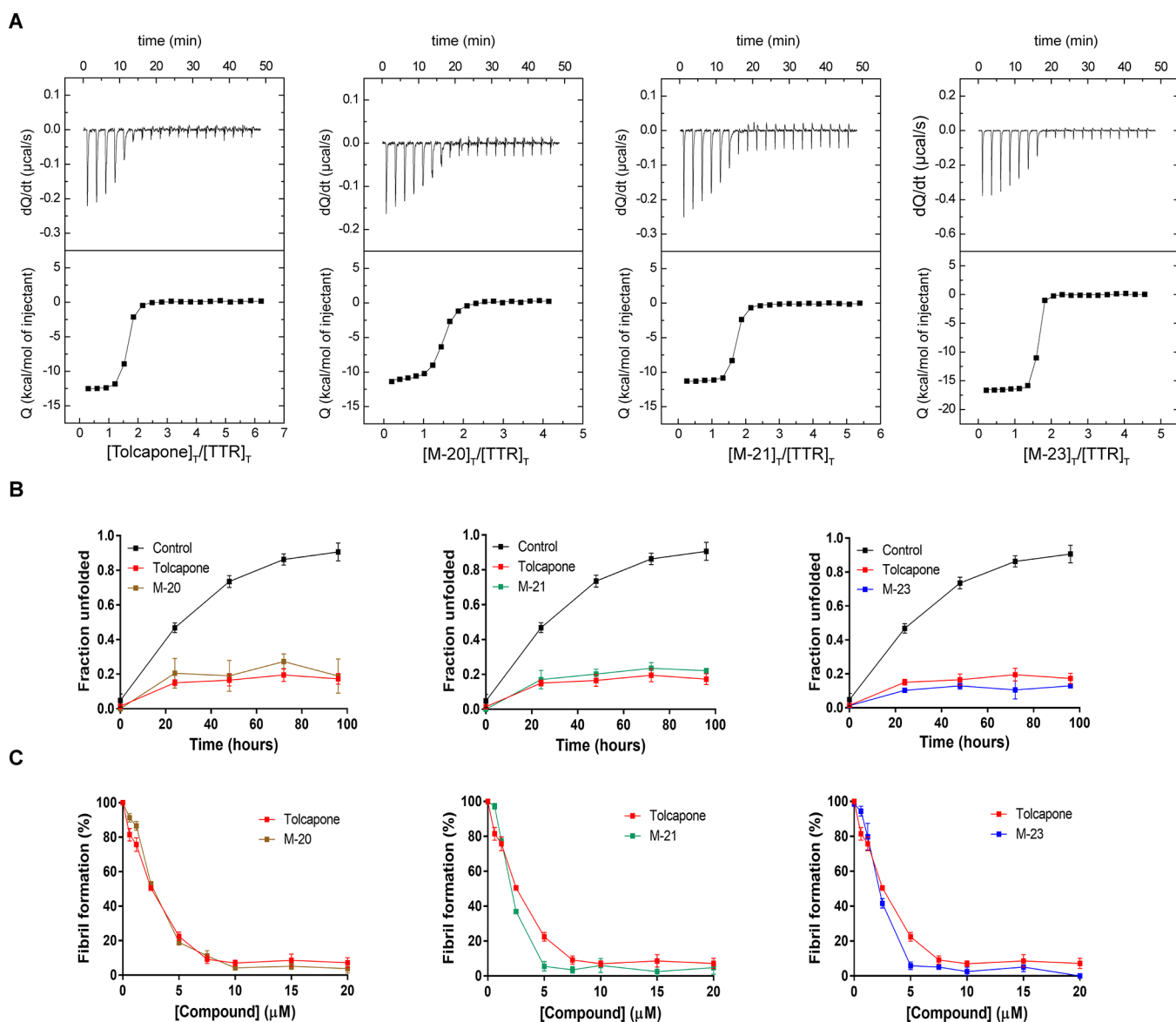
Figure 5. *In vitro* characterization of demethylated 3,5-disubstituted and halogenated tolcapone analogues, **M-20**, **M-21**, and **M-23**. (A) Interaction of WT-TTR with **M-20**, **M-21**, and **M-23** as assessed by ITC. The top and the lower panels correspond to the thermogram and the binding isotherm, respectively. The solid line describes the best fit according to a two-site binding model without cooperativity for each compound. (B) WT-TTR (1.8 μM) urea-induced tetramer dissociation (6 M urea) in the absence or presence of **M-20**, **M-21**, or **M-23** (at 3.6 μM), as measured by Trp fluorescence. The values correspond to mean $\pm$ SEM ($n = 3$). (C) Acid-mediated TTR (at a final assay concentration of 3.6 μM) aggregation as a function of inhibitor concentration determined by turbidity at 340 nm. The values represent mean $\pm$ SEM ($n = 3$).

Table 4. Thermodynamic Parameters Determined by ITC for the Binding of M-20, M-21, and M-23 to WT-TTR

	K_d (nM)	ΔG (kcal mol^{-1})	ΔH (kcal mol^{-1})	$-T\Delta S$ (kcal mol^{-1})
tolcapone	34	−10.2	−12.8	2.6
M-20	85	−9.7	−11.7	2.0
M-21	26	−10.4	−11.3	0.9
M-23	6.2	−11.2	−16.6	5.4

tolcapone (2.6 kcal mol^{-1}), likely due to its higher polarity, but a still higher ΔG (−11.2 kcal mol^{-1}). Compared with tafamidis, **M-23** displays a higher affinity for the first and especially for the second binding site where its binding is >40-fold stronger. In addition, the enthalpy contribution for binding to any of the two sites is at least 2.5-fold higher in **M-23** than in tafamidis. Overall, the thermodynamic analysis

perfectly agrees with MD simulations and demonstrates a significantly optimized TTR binding in **M-23**.

TTR Kinetic Stabilization by Demethylated 3,5-Disubstituted and Halogenated Tolcapone Analogues. Analysis of the kinetic stability induced by **M-20**, **M-21**, and **M-23** by monitoring TTR tertiary structural changes in the presence of 6 M urea indicated that all of them significantly decreased the amount of dissociated tetramer, as well as the rate of tetramer dissociation, when present at an equimolar ratio relative to T$_4$-binding sites (Figure 5B). **M-20** and **M-21** performed worse and equal to tolcapone, respectively. **M-23** appears as the strongest kinetic stabilizer in the assay conditions, protecting as much as 87.0 $\pm$ 0.1% of TTR molecules from urea-induced unfolding.

TTR Anti-aggregation Activity of Demethylated 3,5-Disubstituted and Halogenated Tolcapone Analogues.

M-20, **M-21**, and **M-23** effectively prevented TTR amyloid formation at acidic pH (Figure 5C). They decreased TTR aggregation in a concentration-dependent mode, with >60% reduction at 1:1 TTR/compound ratio and a decrease of >90% when the compound concentration was greater than or equal to that of T_4-binding sites. As mentioned above, tolcapone is a very potent TTR aggregation inhibitor. The weaker binder in this series (**M-20**) equals its potency, while **M-21** and **M-23** perform better, completely abolishing amyloid fibril formation when present at 20 μM.

M-23 Stabilizes TTR in Human Plasma. Altogether, the previous results suggested **M-23** as the most promising compound in our set and encouraged us to investigate its activity further. First, we assessed the performance of **M-23** in human plasma, a complex biological fluid where different issues, including unspecific binding to other plasma proteins, can compromise ligand efficacy.

The capacity of **M-23** to inhibit TTR tetramer dissociation in human plasma was evaluated by isoelectric focusing (IEF) electrophoresis under partially denaturing conditions (4 M urea). Tolcapone was used as a control. The assay allows one to quantify the proportion of monomer and tetramer in the sample and to calculate the extent of tetramer stabilization.

First, we wanted to assess if this assay can detect differences in tetramer stabilization by **M-23** and tolcapone when using purified recombinant proteins. TTR (6 μM) was incubated in the presence or absence of 30 and 60 μM compound overnight at 4 °C. As shown in Figure 6A, **M-23** exerted a higher stabilizing effect than tolcapone at both tested concentrations. Then, the same assay was performed in human plasma (Figure 6B). **M-23** was significantly more effective than tolcapone, with a stabilizing effect >5-fold the one exerted by the original molecule. This indicates selective and tight binding of **M-23** to circulating TTR in plasma, as confirmed using the T_4 binding competition assay. **M-23** decreased the binding of T_4 to TTR in human plasma by 84.6 ± 9.7%, outperforming tolcapone in the same conditions (Figure 6C,D). The aqueous solubility of the two molecules was determined to rule out that differences in solubility could underlie the observed differences in binding (Table 5). **M-23** and tolcapone showed similar solubility values (0.045 mg/mL for **M-23** and 0.056 mg/mL for tolcapone), suggesting that these parameters do not influence the results obtained. Importantly, in our assays, **M-23** has a stabilizing effect in human plasma >10-fold the one exerted by tafamidis (Figure S3), the only marketed molecule for ATTR.

The increased binding selectivity and stabilization potency of **M-23** in human plasma, relative to tolcapone, likely result from its higher enthalpy for binding, as deduced from ITC data. This is in accordance with recently reported data that suggest that the correlation between ΔH and the selectivity and efficacy of TTR stabilizers in human plasma is greater than with ΔG or K_d,[68] two parameters that in any case are also better in **M-23**.

M-23 Is Innocuous for Human Cells. Cytotoxicity analyses were performed for evaluating the potential **M-23** chemical toxicity to human cells. Two cell lines were chosen for this purpose: HeLa, a human epithelioid cervix carcinoma cell line, and HepG2, a human hepatocellular carcinoma cell line. These cell lines are well characterized and have been widely used for *in vitro* assessment of compound toxicity.[69−71] In particular, HepG2 is the most frequently used cell line in the testing and investigation of drug-induced liver damage,[72,73]
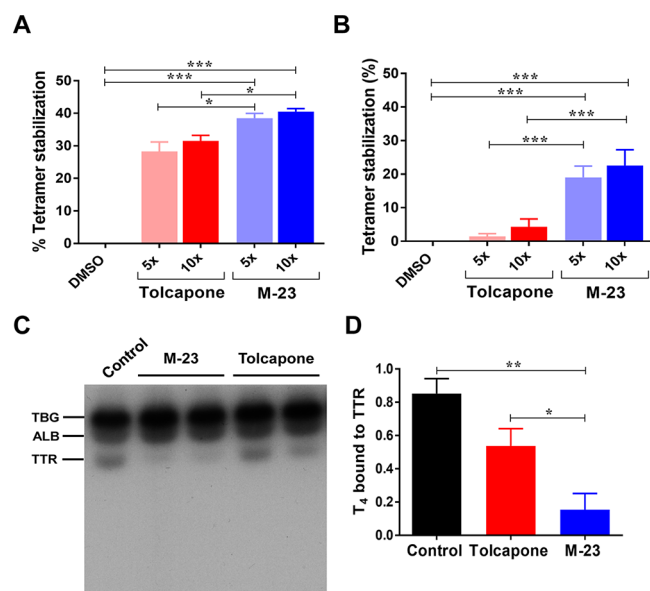

Figure 6. **M-23** tetramer stabilization effect assessed by IEF and its binding to TTR in human plasma. (A, B) Percentage of TTR tetramer stabilization upon incubation of **M-23** with recombinant (A) WT-TTR or (B) human plasma as evaluated by IEF under partially denaturing conditions. **M-23** was 5 or 10 times more concentrated than WT-TTR. Error bars represent SEM of mean values ($n = 3$ for recombinant protein; $n = 6$ for plasma samples); *$p < 0.05$; **$p < 0.01$; ***$p < 0.001$. (C) Representative native gel electrophoresis showing the distribution of [^{125}I]-T_4 after incubation with human plasma in the absence or presence of compounds. In the absence of compounds, three bands can be observed that correspond to the major plasma T_4 binding proteins: T_4-binding globulin (TBG), albumin (ALB), and TTR. Plasma incubated with DMSO was used as negative control. (D) Fraction of T_4 bound to TTR in the plasma of individuals incubated with or without compounds as determined by densitometry. The values were normalized to the control, which corresponds to the maximum. The values represent mean ± SEM ($n = 4$).

Table 5. Solubility Experiments Performed for M-23 and Tolcapone[a]

	weight (g)	weight (mg)	water (mL)	solubility (mg/mL)
M-23 assay 1	0.0154	15.4	350	0.044
M-23 assay 2	0.0147	14.7	326	0.045
M-23 assay 3	0.0150	15.0	333	0.045
M-23 average				0.045
tolcapone assay 1	0.0150	15.0	267	0.056
tolcapone assay 2	0.0144	14.4	261	0.055
tolcapone assay 3	0.0153	15.3	273	0.056
tolcapone average				0.056

[a]The experiments were performed in triplicate.

which is especially relevant in the context of this study, as tolcapone has been associated with cases of hepatotoxicity.[74,75]

In this study, HeLa and HepG2 cells were exposed to increasing concentrations of **M-23** or tolcapone for 72 h at 37 °C using the PrestoBlue cell viability reagent. For both cell lines, **M-23** showed significantly lower toxicity than tolcapone above 10 μM compound concentration (Figure 7). These results are biologically relevant, particularly for HepG2, as they recapitulate tolcapone's *in vivo* hepatotoxicity and suggest that **M-23** is not only a better TTR stabilizer but might also
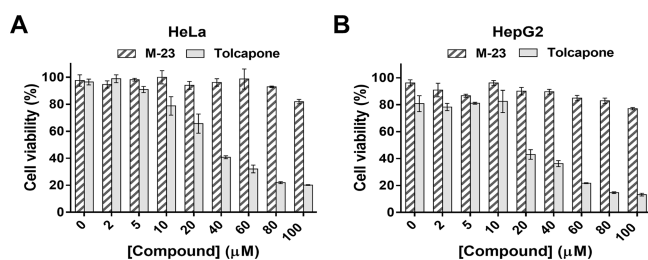
Figure 7. (A) HeLa and (B) HepG2 cell viability of cells exposed to increasing concentrations of **M-23** (striped bars) or tolcapone (empty bars) as measured by the PrestoBlue assay. The values correspond to mean ± SEM (n = 3).

overcome one of the major concerns related with tolcapone therapy.

M-23 Stabilizes the TTR Dimer−Dimer Interface. The MD simulations, together with the thermodynamic analysis, point to a higher number and/or strength of interactions established between **M-23** and the residues within the TTR T_4-binding sites as responsible for the enhanced affinity and the high enthalpic contribution to binding in this molecule with respect to tolcapone. To inspect this possibility, we determined the crystal structure of TTR with **M-23** at 1.2 Å resolution (Figure 8). The atomic coordinates have been deposited in the PDB (PDB code 7QC5). This high-resolution crystal allows one to unequivocally place **M-23** in the AB/CD dimer−dimer interface in the forward binding mode. As a result of the twofold symmetry of the binding sites, **M-23** adopts two equivalent binding modes related by a 180° rotation. As designed, **M-23** sits deeper in the innermost section of the hormone-binding cavity relative to tolcapone (Figure 8).

As in tolcapone, the 3,4-dihydroxy-5-nitrophenyl ring of **M-23** is oriented to the outer binding cavity, being surrounded by the hydrophobic residues from the HBPs 2/2′ and 1/1′ (Figure 8B). Remarkably, the ε-amino group of Lys15 is placed between the two hydroxyl groups of the phenyl ring of **M-23** and the carboxylate group of Glu54, establishing important electrostatic interactions. These interactions close the cavity
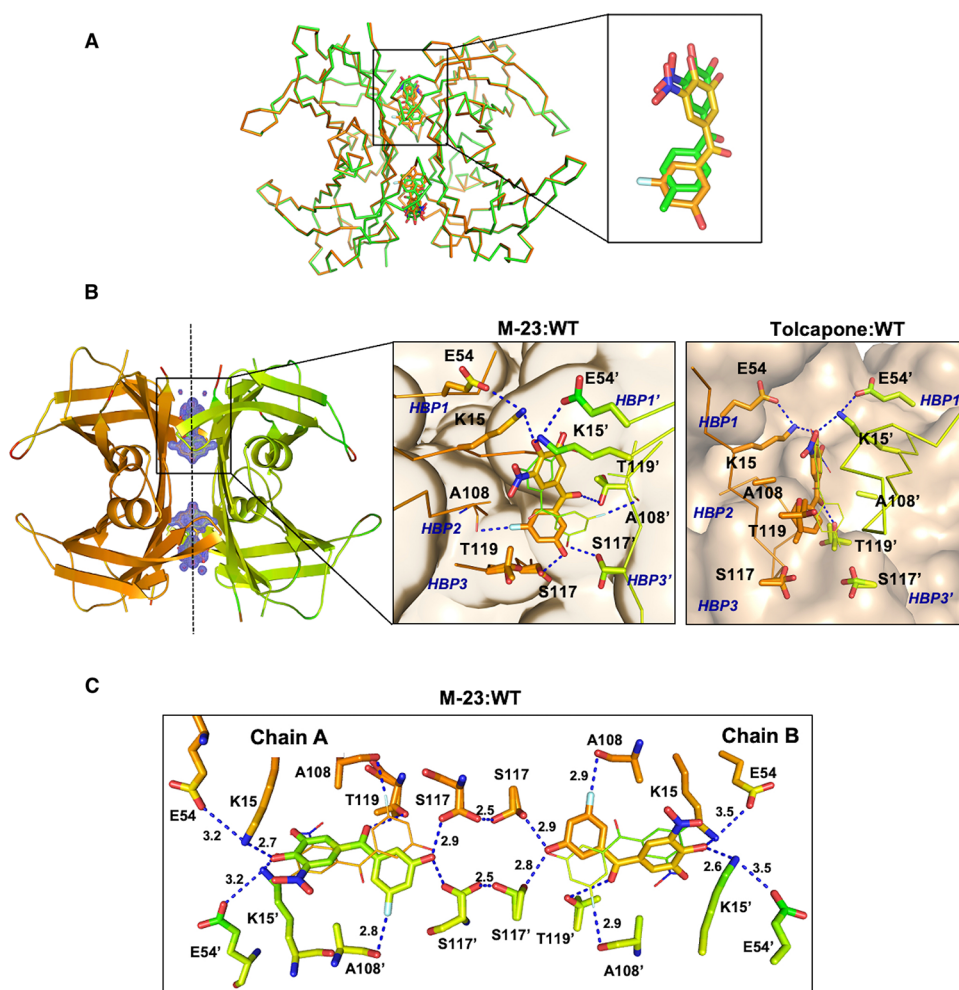
Figure 8. Crystal structure of WT-TTR complexed with **M-23**. (A) Superposition of WT-TTR complexed with **M-23** (orange) or tolcapone (green). Cα rmsd from 116 residues is 0.19 Å. A close-up view of one conformation of the superposed compounds is shown on the inset. (B) General view of WT-TTR bound to **M-23** at 1.2 Å, represented as cartoon. The electron density maps of the two binding sites of **M-23** are shown. Dashed line depicts the twofold symmetry axis of the dimer−dimer interface. The insets represent the close-up view of one of the WT-TTR T_4-binding sites for **M-23** and for tolcapone (PDB: 4D7B). Ligands and the most important interacting residues are illustrated as sticks. (C) **M-23** binding at the WT-TTR dimer−dimer interface. **M-23** and some of the TTR residues interacting with the ligand are represented by sticks. Dashed lines represent key interactions between **M-23** and WT-TTR and between the hydroxyl groups of S117/S117′.

around **M-23**, protecting the compound and the interactions it establishes with the protein, from the solvent. Although **M-23** is more buried into the cavity than tolcapone, the distances between Lys15 and the −OH are equal or shorter, resulting in Lys15 moving inward the cavity, whereas Glu54 keeps essentially the same position (Figure S4).

As in the TTR−tolcapone structure, the **M-23** central carbonyl group establishes a specific H-bond with the hydroxyl side chain of Thr119. As indicated by MD simulations, the 3-fluoro-5-hydroxyphenyl ring projects deep within the inner cavity where it participates in hydrophobic and van der Waals interactions with residues forming the two symmetrical T_4-HBPs, HBP2 and HBP3 (Ala108, Leu110, Ser117, and Thr119). In addition, the **M-23** 5-OH group forms a short hydrogen bond with Ser117 (2.7/2.8 Å), and the 3-F substituent is in contact with Ala108 (2.8/2.8 Å). Such a short F···Ala108 distance matches the shortest one observed in the MD simulation (2.76 Å). These two interactions are absent in the TTR−tolcapone and the TTR−tafamidis structures, confirming that, as designed, **M-23** establishes a higher number of noncovalent H-bond contacts with the protein. They are expected to be stronger because they are buried in the low dielectric hydrophobic interior of the T_4-binding cavity. These new contacts are likely the driving force for **M-23** higher affinity and exceptional enthalpy for binding.

Interestingly, the H-bond interactions of **M-23** with Ser117 in HBP3 and HBP3′ mimic the ones observed between these two residues in the kinetically stable T119M-TTR variant. These H-bond interactions in the two symmetric cavities help bring the dimer subunits closer and strengthen the molecular contacts between them, increasing the energy barrier for dissociation.[76,77] Indeed, the O−O distances between facing Ser117 residues in the two dimers are shorter in T119M-TTR (A−C = 4.7 Å, B−D = 4.8 Å) than in WT-TTR (A−C = 5.5 Å, B−D = 5.4 Å). In the same manner, these distances are shorter in the TTR/**M-23** structure (A−C = 5.0 Å, B−D = 4.8 Å) than in the TTR/tolcapone complex (A−C = 5.4 Å, B−D = 5.4 Å). Actually, Ser117-compound contacts seem to hold the key for the enthalpy-driven stabilization of TTR by AG10,[38,68] a novel TTR ligand that has already shown effectivity in the clinic for TTR cardiomyopathy.[78] In one of the Ser117 side-chain conformations, they can establish a short hydrogen intradimer H-bond (2.5 Å), which might further contribute to stabilize the quaternary structure (Figure 8C).

CONCLUSIONS

We have developed **M-23**, a disubstituted and halogenated tolcapone congener. This novel TTR kinetic stabilizer keeps the interactions established by the parental molecule in the outer and central sides of the binding cavity while being more internalized and establishing new and specific contacts with the innermost residues. Under the same conditions, tolcapone exhibits a superior stabilizing and anti-aggregational activity than tafamidis. The advantage of tolcapone is that, although it binds worse than tafamidis to the first TTR T_4-binding site, it binds significantly better to the second one due to its lack of negative cooperativity. Here, we show that due to the unique network of interactions it establishes with TTR, **M-23** displays a higher affinity than any of these two therapeutically relevant molecules for both binding sites, becoming one of the strongest TTR ligands described so far. Accordingly, **M-23** stabilizes and protects TTR from aggregation *in vitro* at very low compound concentrations. Furthermore, the binding of

M-23 is entirely enthalpy driven, displaying an enthalpic contribution to the binding significantly higher than those of tafamidis and tolcapone, a parameter associated with the molecule potency and selectivity. Consequently, **M-23** strongly binds to TTR in human plasma, exhibiting a higher TTR stabilizing activity than the two reference molecules, thus becoming a candidate for further preclinical and clinical investigation. Crucial to identify **M-23** has been the application of MD simulations on top of rationally designed tolcapone variants since modeling the flexibility of the T_4-binding cavity has allowed one to anticipate protein−compound interactions at atomic resolution and rank the molecules according to the energetics of binding. This integral approach constitutes a time- and cost-effective strategy to assist in the search of potent ATTR disease modifiers, allowing the evaluation of small molecules rapidly and accurately.

EXPERIMENTAL SECTION

Computational Simulations. Binding energies have been estimated from gas-phase interaction energies of a collection of frames generated from a classical molecular dynamics (MD) simulation and including solvent effects as the ligand solvation energy. This means that we assumed that the complex and the receptor have approximately the same solvation energy and that the solvation contribution to the binding energy only arises from ligands' desolvation. MD simulations were performed with the Amber suite[79] using the ff14SB force field.[80] Organic ligands were parametrized using the gaff2 force field.[81]

Production was run for 150 ns in the NPT ensemble at a constant temperature of 300 K, and binding energies were estimated from 140 structures evenly sampled from the last 140 ns. Ligand solvation energies were computed with the SMD continuum model[82] at the DFT (B3LYP/6-31+G(d,p)) level of theory with the Gaussian09 program.[83]

Models were built by replacing tolcapone molecules with their derivatives in the high-resolution X-ray diffraction tetrameric WT-TTR-tolcapone complex structure PDB: 4D7B.[39] Complex structures were neutralized with the appropriate number of Na^+ counterions, and water molecules were added up to a minimum distance of 8 Å from the protein. It should be noted that while in the tetrameric WT-TTR-tolcapone crystal structure the two ligands are symmetrically placed, simulations without any structural constraints led to an asymmetric organization with one ligand at the center of the TTR tetramer and the second in the binding channel, though further exposed to the solvent than in the crystallographic structure (Figure S5). This striking difference between our simulations and the X-ray structure may be due either to (i) a dynamic disorder of the two ligands in the complex in solution, which collapses to a symmetric organization upon crystallization, or (ii) the inadequacy of the molecular mechanics model to properly describe the system's structural features. Thus, we decided to enforce a small harmonic constraint on the protein backbone so that the structure does not drift significantly apart from the crystallographic one. After extensive testing, we found that when including a constraint of 2 kcal/mol^{-1} Å^{-2} on the backbone, the symmetry of the two binding sites is preserved while allowing a reorganization of the ligand binding residues. Thus, this is the protocol adopted all along this work.

Molecular Dynamics Protocol. The molecular dynamics protocol includes (i) a 200 ps equilibration run in the NVT ensemble, raising the temperature from 0 to 100 K; (ii) a 2 ns equilibration run in the NPT ensemble, raising the temperature from 100 to 300 K; and (iii) a 150 ns production run in the NPT ensemble with the temperature kept constant to 300 K. A Langevin thermostat and a Monte Carlo barostat were employed. Hydrogen bonds were calculated with cpptraj default values (distance cutoff of 3 Å) in all cases except for Cl···X contacts for which the threshold was set to 3.5 Å. Visualization and postprocessing were done with VMD and MDtraj packages.[84,85]

General Methods and Compound Characterization. Commercially available reagents were used as received. Solvents were dried by distillation over the appropriate drying agents. All reactions were monitored by analytical thin-layer chromatography (TLC) using silica gel 60 precoated aluminum plates (0.20 mm thickness). Flash column chromatography was performed using silica gel Geduran SI 60 (40−63 μm). ^{1}H NMR and ^{13}C NMR spectra were recorded at 250, 360, 400 MHz and 90, 100 MHz, respectively. ^{19}F NMR spectra were recorded at 250 MHz. Proton chemical shifts are reported in ppm (δ) (CDCl$_3$; δ 7.26, acetone-d_6; δ 2.05, dimethyl sulfoxide (DMSO)-d_6; δ 2.50, methanol-d_4; δ 3.31). Carbon chemical shifts are reported in ppm (δ) (CDCl$_3$; δ 77.16, acetone-d_6; δ 29.84, DMSO-d_6; δ 39.52 methanol-d_4; δ 49.00). NMR signals were assigned with the help of HSQC, HMBC, and DEPT135. ^{1}H NMR and ^{13}C NMR spectra of new compounds are shown in Figures S6-S27. Melting points were determined on a hot stage and are uncorrected. HRMS was recorded using electrospray ionization. All final compounds are >95% pure by HPLC analysis (Figures S28-S32).

General Synthesis Procedure to Prepare Compounds M-14 to M-23. Tolcapone derivatives **M-14** to **M-23** were chemically synthesized as described in Scheme 1. The synthesis started with the coupling reaction of different preformed aryl Grignard reagents, from the corresponding iodoarene derivatives **1a−e**, to the known methyl diprotected catechol **2** to furnish alcohols **3a−e** in 49−81% yield. The Grignard reagents were freshly prepared by an iodine−magnesium exchange reaction[86] with *i*-PrMgBr at −40 °C in THF of the iodoarene derivatives **1a−e** that were commercially available except for 3-fluoro-5-iodomethoxybenzene **1e**, obtained from 3-fluoro-5-methoxyaniline through the appropriated arenediazonium chloride and an ion exchange reaction with KI in 77% yield.[87] Catechol **2** was prepared in excellent yield by the methylation of commercially available 5-nitrovainillin using a phase-transfer catalytic process.[88,89] The following Dess−Martin periodinane oxidation on **3a−e** provided ketones **4a−e** in 70−99% yield.

Removal of both methyl protecting groups of the catechol moiety was first attempted under conventional conditions using boron tribromide in CH$_2$Cl$_2$.[90] However, under these standard conditions, a complex mixture of products was obtained. The presence of the relatively sensitive nitro-group prevents the use of other routine reagents. After some experimentation, it was found that by controlling the reaction time and the equivalents of BBr$_3$, a single ether cleavage was promoted delivering the expected monoprotected catechol. These optimized conditions were applied to the methyl deprotected compounds **4a−d** to furnish monoprotected catechols **5a−d** in 50−91% yield. For compound **4e**, the applied reaction conditions also led to the removal of the methyl protecting group of R$_1$, delivering compound **5e** in 81% yield.

It has been described that the demethylation of ortho-hydroxy nitroarylmethyl ethers can be accomplished in good yields by a milder procedure in the presence of aluminum chloride (AlCl$_3$).[91,92] Accordingly, treatment of **5a−e** with AlCl$_3$ and pyridine in refluxing chloroform smoothly provided the target tolcapone analogues **M-14**, **M-17**, **M-20**, **M-21**, and **M-23** in reasonably good yields (46−81%).

Synthesis Procedure. Tolcapone was purchased from Fisher. All tolcapone derivatives used in this study were prepared as described below.

3,4-Dimethoxy-5-nitrobenzaldehyde, 2. To a solution of 5-nitrovanillin (500 mg, 2.50 mmol), NaOH 3 M (1.7 mL, 5.00 mmol), and TBAB (82 mg, 0.25 mmol) in a mixture of CH$_2$Cl$_2$/H$_2$O (1:1, 10 mL), dimethyl sulfate (1.3 mL, 13.40 mmol) was added slowly under a nitrogen atmosphere. The final mixture was stirred vigorously for 24 h (TLC, hexane/EtOAc 3:2). The aqueous layer was extracted with CH$_2$Cl$_2$ (3 × 10 mL). Then, the organic layer was concentrated under a vacuum and washed with water (20 mL), a 2 M ammonia solution (20 mL), and a 2 M NaOH solution (20 mL) to remove unreacted phenol and dimethyl sulfate. The organic layer was dried over anhydrous Na$_2$SO$_4$ and concentrated under a vacuum. Purification by flash column chromatography using a mixture of hexane/EtOAc (3:2) furnished **2** as a pale brown solid (498 mg, 2.36 mmol, 93% yield). ^{1}H NMR (250 MHz, CDCl$_3$) δ 9.91 (s, 1H,

−COH), 7.83 (d, $J_{6,2}$ = 1.8 Hz, 1H, H-6), 7.62 (d, $J_{2,6}$ = 1.8 Hz, 1H, H-2), 4.08 (s, 3H, CH$_3$O-4), 4.00 (s, 3H, CH$_3$O-3). The spectroscopic data were consistent with the literature.[88]

1-Fluoro-3-iodo-5-methoxybenzene, 1e. To a solution of 3-fluoro-5-methoxyaniline (1.02 g, 7.08 mmol) in H$_2$O (3.3 mL) was added concentrated HCl (3.3 mL) at 0 °C. After stirring for 30 min, a 1.8 M solution of NaNO$_2$ in H$_2$O (4.5 mL, 8.14 mmol) was added dropwise. The resulting mixture was stirred for 15 min at 0 °C, and then an ice-cold 3 M solution of KI (5 mL) was added slowly. The ice bath was removed, and the reaction mixture was heated at the reflux temperature for 1 h. The reaction mixture was allowed to cool to room temperature (rt) and extracted with EtOAc (3 × 33 mL). The organic layer was washed with brine (2 × 50 mL), dried over anhydrous Na$_2$SO$_4$, and concentrated under a vacuum. The residue was purified by flash column chromatography (hexanes 100%) to afford **1e** as a colorless oil (1.37 g, 5.41 mmol, 77% yield). ^{1}H NMR (400 MHz, CDCl$_3$) δ 7.05−7.02 (m, 2H, H-2, H-4), 6.58 (dt, $J_{6,F}$ = 10.6 Hz, $J_{6,4}$ = 2.3 Hz, 1H, H-6), 3.78 (s, 3H, CH$_3$O-5); ^{19}F NMR (250 MHz, CDCl$_3$) δ −110.76 (s, F-3''); ^{13}C NMR (100.5 MHz, CDCl$_3$) δ 163.2 (d, $J_{1,F}$ = 250.0 Hz, C$_1$), 161.4 (d, $J_{5,F}$ = 11.1 Hz, C$_5$), 119.5 (d, $J_{4,F}$ = 3.2 Hz, C$_4$), 117.4 (d, $J_{2,F}$ = 24.0 Hz, C$_2$), 102.0 (d, $J_{6,F}$ = 25.2 Hz, C$_6$), 93.3 (d, $J_{3,F}$ = 11.0 Hz, C$_3$), 55.9 (CH$_3$O-5). IR (ATR) ν 2941, 1738, 1601, 1578, 1423, 1277, 1143 cm^{-1}.

(3,4-Dimethoxy-5-nitrophenyl)[4-(trifluoromethyl)phenyl]-methanol, 3a. To a solution of 4-iodobenzotrifluoride, **1a** (100 μL, 0.68 mmol), in dry THF (1 mL) at −40 °C, *i*-PrMgBr (1 M in THF, 680 μL, 0.68 mmol) was added dropwise in 5 min under a nitrogen atmosphere, and the reaction mixture was stirred at the same temperature for 1 h. Then, a solution of 3,4-dimethoxy-5-nitro-benzaldehyde, **2** (151 mg, 0.72 mmol), in dry THF (1.2 mL) was added. The final mixture was warmed to rt and stirred overnight (ON). The reaction was quenched by slow addition of brine (4 mL), and the aqueous layer was extracted with EtOAc (3 × 10 mL). All organic layers were collected, dried over anhydrous Na$_2$SO$_4$, and concentrated under a vacuum, obtaining a yellow oil that was purified by flash column chromatography (hexanes/EtOAc, 2:1) to furnish **3a** (167 mg, 0.47 mmol, 69% yield) as an orange oil. ^{1}H NMR (400 MHz, CDCl$_3$) δ 7.61 (d, $J_{3'',2''}$ = 8.1 Hz, 2H, H-3''), 7.48 (d, $J_{2'',3''}$ = 8.1 Hz, 2H, H-2''), 7.29 (dd, $J_{6',2}$ = 2.0 Hz, $J_{6',1}$ = 0.7 Hz, 1H, H-6'), 7.09 (d, $J_{2',6}$ = 2.0 Hz, 1H, H-2'), 5.83 (s, 1H, H-1), 3.93 (s, 3H, CH$_3$O-4'), 3.88 (s, 3H, CH$_3$O-3'), 2.77 (br s, 1H, −OH); ^{19}F NMR (250 MHz, CDCl$_3$) δ −63.04 (s, −CF$_3$); ^{13}C NMR (100.6 MHz, CDCl$_3$) δ 154.4 (C$_{3'}$), 146.5 (C$_{1''}$), 144.6 (C$_{5'}$), 142.2 (C$_{4'}$), 139.5 (C$_{1'}$), 130.4 (q, $J_{4'',F}$ = 32.2 Hz, C$_{4''}$), 126.8 (C$_{2''}$, C$_{6''}$, C$_{5''}$), 125.9 (q, $J_{3'',F}$ = 3.8 Hz, C$_{3''}$), 124.1 (q, $J_{CF3,F}$ = 272.0 Hz, −CF$_3$), 114.0 (C$_{2'}$), 113.8 (C$_{6'}$), 74.7 (C$_1$), 62.1 (CH$_3$O-4'), 56.5 (CH$_3$O-3'). IR (ATR) ν 3422, 1534, 1325, 1165, 1124 cm^{-1}. HRMS (ESI+) calcd for [C$_{16}$H$_{14}$F$_3$NO$_5$ + H]$^+$ ([M + H]$^+$) 358.2932, found 358.0900.

(3,4-Dimethoxy-5-nitrophenyl)(4-fluorophenyl)methanol, 3b. Compound **3b** was prepared as described for **3a** by using a solution of 4-fluoroiodobenzene, **1b** (200 μL, 0.90 mmol), in dry THF (2 mL), *i*-PrMgBr (1 M in THF, 900 μL, 0.90 mmol), and a solution of **2** (210 mg, 0.99 mmol) in dry THF (2.2 mL). Purification by flash column chromatography (hexanes/EtOAc, 4:1) afforded **3b** (213 mg, 0.69 mmol, 77% yield) as a colorless oil. ^{1}H NMR (400 MHz, acetone-d_6) δ 7.50 (br ddd, $J_{2'',3}$ = $J_{6'',5}$ = 9.0 Hz, $J_{2'',F}$ = $J_{6'',F}$ = 5.5 Hz, $J_{2'',1}$ = $J_{6'',1}$ = 0.6 Hz, 2H, H-2'', H-6''), 7.41 (d, $J_{2',6}$ = 2.0 Hz, 1H, H-2'), 7.38 (dd, $J_{6',2}$ = 2.0 Hz, 1H, H-6'), 7.09 (br t, $J_{2'',F}$ = $J_{2',6}$ = $J_{3'',2}$ = $J_{5'',6}$ = 9.0 Hz, 1H, H-3'', H-5''), 5.91 (d, $J_{1,OH}$ = 3.3 Hz, 1H, H-1), 5.26 (d, $J_{1,OH}$ = 3.3 Hz, 1H, −OH), 3.93 (s, 3H, CH$_3$O-4'), 3.90 (s, 3H, CH$_3$O-3'); ^{19}F NMR (250 MHz, CDCl$_3$) δ −117.36 (m, F-4''); ^{13}C NMR (100.6 MHz, acetone-d_6) δ 162.9 (d, $J_{4'',F}$ = 243.6 Hz, C$_{4''}$), 154.8 (C$_{3'}$), 145.8 (C$_{5'}$), 142.9 (C$_{1'}$), 141.7 (C$_{3'}$), 141.5 (C$_{1''}$), 129.3 (d, $J_{2'',F}$ = $J_{6'',F}$ = 7.8 Hz, C$_{2''}$, C$_{6''}$), 115.8 (d, $J_{4'',F}$ = 21.6 Hz, C$_{3''}$, C$_{5''}$), 115.0 (C$_{2'}$), 113.6 (C$_{6'}$), 74.4 (C$_1$), 62.0 (CH$_3$O-4'), 56.9 (CH$_3$O-3'). IR (ATR) ν 3416, 1531, 1359, 1280, 1223 cm^{-1}. HRMS (ESI+) calcd for [C$_{15}$H$_{14}$FNO$_5$ + H]$^+$ ([M + H]$^+$) 308.0934, found 308.0931.

(3,5-Dichlorophenyl)(3,4-dimethoxy-5-nitrophenyl)methanol, 3c. Compound **3c** was prepared as described for **3a** by using a solution of 3,5-dichloroiodobenzene, **1c** (558 mg, 2.04 mmol), in dry

THF (5 mL), *i*-PrMgBr (1 M in THF, 2.0 mL, 2.00 mmol), and a solution of **2** (360 mg, 1.70 mmol) in dry THF (5 mL). Purification by flash column chromatography (hexanes/EtOAc, 1:1) furnished **3c** (427 mg, 1.19 mmol, 70% yield) as an orange solid. Mp 100−103 °C (from acetone). ^{1}H NMR (400 MHz, acetone-d_6) δ 7.50 (dd, $J_{2'',4}$ = $J_{6'',4}$ = 1.9 Hz, $J_{2'',1}$ = $J_{6'',1}$ = 0.6 Hz, 2H, H-2″, H-6″), 7.48 (d, $J_{2',6}$ = 2.0 Hz, 1H, H-2′), 7.44 (dd, $J_{6',2}$ = 2.0 Hz, $J_{6',1}$ = 0.6 Hz, 1H, H-6′), 7.35 (t, $J_{4'',2}$ = $J_{4'',6}$ = 1.9 Hz, 1H, H-4″), 5.95 (d, $J_{1,OH}$ = 3.8 Hz, 1H, H-1), 5.50 (d, $J_{OH,1}$ = 3.9 Hz, 1H, −OH), 3.95 (s, 3H, CH_3O-3′), 3.90 (s, 3H, CH_3O-4′); ^{13}C NMR (90.5 MHz, acetone-d_6) δ 155.0 (C$_{3'}$), 149.5 (C$_{1'}$), 145.9 (C$_{5'}$), 142.0 (C$_{4'}$), 141.7 (C$_{1''}$), 135.5 (C$_{3''}$, C$_{5''}$), 127.9 (C$_{4''}$), 125.9 (C$_{2''}$, C$_{6''}$), 115.0 (C$_{2'}$), 113.7 (C$_{6'}$), 73.9 (C$_1$), 62.0 (CH$_3$O-4′), 57.0 (CH$_3$O-3′). IR (ATR) ν 3470, 2948, 1530, 1431, 1370 cm^{-1}. HRMS (ESI−) calcd for [C$_{15}$H$_{13}$Cl$_2$NO$_5$-H$_2$O]$^-$ ([M-H$_2$O]$^-$) 340.0143, found 340.0145.

(3,5-Difluorophenyl)(3,4-dimethoxy-5-nitrophenyl)methanol, 3d. Compound **3d** was prepared as described for **3a** by using a solution of 3,5-difluoroiodobenzene, **1d** (555 mg, 2.31 mmol), in dry THF (5 mL), *i*-PrMgBr (1 M in THF, 2.5 mL, 2.5 mmol), and a solution of **2** (582 mg, 2.78 mmol) in dry THF (5 mL). Purification by flash column chromatography (hexanes/EtOAc, 3:1) afforded **3d** (612 mg, 1.88 mmol, 81% yield) as an orange oil. ^{1}H NMR (400 MHz, CDCl$_3$) δ 7.25 (d, $J_{6',2}$ = 2.0 Hz, 1H, H-6′), 7.07 (d, $J_{2',6}$ = 2.0 Hz, 1H, H-2′), 6.87 (m, $J_{2'',F}$ = $J_{6'',F}$ = 6.0 Hz, 2H, H-2″, H-6″), 6.70 (tt, $J_{4'',2}$ = $J_{4'',6''}$ = 2.4 Hz, $J_{4'',F}$ = 8.9 Hz, 1H, H-4″), 5.71 (br s, 1H, H-1), 3.92 (s, 3H, CH_3O-4′), 3.88 (s, 3H, CH_3O-3′), 3.10 (br s, 1H, −OH); ^{19}F NMR (250 MHz, CDCl$_3$) δ −108.97 (m, F-3″, F-5″); ^{13}C NMR (100.6 MHz, CDCl$_3$) δ 163.2 (dd, $J_{3'',F}$ = $J_{5'',F}$ = 12.5 Hz, $J_{3'',F}$ = $J_{5'',F}$ = 249.7 Hz, C$_{3''}$,C$_{5''}$), 154.3 (C$_{3'}$), 146.6 (t, $J_{1'',F}$ = 8.6 Hz, C$_{1''}$), 144.4 (C$_{5'}$), 142.2 (C$_{4'}$), 139.3 (C$_{1'}$), 114.0 (C$_{2'}$), 113.8 (C$_{6'}$), 109.4 (m, $J_{2'',F}$ = $J_{6'',F}$ = 18.7 Hz, C$_{2''}$, C$_{6''}$), 103.4 (t, $J_{4'',F}$ = 25.3 Hz, C$_{4''}$), 74.2 (C$_1$), 62.1 (CH$_3$O-4′), 56.5 (CH$_3$O-3′). IR (ATR) ν 3415, 1598, 1534, 1281 cm^{-1}. HRMS (ESI+) calcd for [C$_{15}$H$_{13}$F$_2$NO$_5$ + Na]$^+$ ([M + Na]$^+$) 348.0659, found 348.0663.

(3,4-Dimethoxy-5-nitrophenyl)(3-fluoro-5-methoxyphenyl)-methanol, 3e. Compound **3e** was prepared as described for **3a** by using a solution of 1-fluoro-3-iodo-5-methoxybenzene, **1e** (308 mg, 1.22 mmol), in dry THF (3 mL), *i*-PrMgBr (1 M in THF, 1.9 mL, 1.90 mmol), and a solution of **2** (310 mg, 1.20 mmol) in dry THF (4 mL). Purification by flash column chromatography (hexanes/EtOAc, 5:1) afforded **3e** (191 mg, 0.57 mmol, 49% yield) as a white solid. Mp 100−101 °C (from CHCl$_3$). ^{1}H NMR (400 MHz, CDCl$_3$) δ 7.28 (dd, $J_{6',2}$ = 2.0 Hz, $J_{6',1}$ = 0.6 Hz, 1H, H-6′), 7.11 (d, $J_{2',6}$ = 2.0 Hz, 1H, H-2′), 6.69 (m, H-6″), 6.65 (br dm, $J_{2'',F}$ = 9.1 Hz, $J_{2'',4}$ = $J_{2'',6}$ = 2.0 Hz, 1H, H-2″), 6.53 (dt, $J_{4'',F}$ = 10.5 Hz, $J_{4'',2}$ = $J_{4'',2}$ = 2.3 Hz, 1H, H-4″), 5.70 (s, 1H, H-1), 3.94 (s, 3H, CH_3O-4′), 3.88 (s, 3H, CH_3O-3′), 3.78 (s, 3H, CH_3O-5″), 2.72 (br s, 1H, −OH); ^{19}F NMR (250 MHz, CDCl$_3$) δ −110.76 (s, F-3″); ^{13}C NMR (100.6 MHz, CDCl$_3$) δ 163.9 (d, $J_{3'',F}$ = 246.3 Hz, C$_{3''}$), 161.3 (d, $^3J_{5'',F}$ = 11.2 Hz, C$_{5''}$), 154.3 (C$_{3'}$), 145.8 (d, $J_{1'',F}$ = 8.8 Hz, C$_{1''}$), 144.6 (s, C$_{5'}$), 142.2 (s, C$_{4'}$), 139.5 (C$_{1'}$), 114.0 (C$_{2'}$), 113.8 (C$_{6'}$), 108.4 (d, $J_{6'',F}$ = 3.8 Hz, C$_{6''}$), 105.7 (d, $J_{2'',F}$ = 22.7 Hz, C$_{2''}$), 101.1 (d, $J_{4'',F}$ = 25.4 Hz, C$_{4''}$), 74.8 (d, $J_{1,F}$ = 2.3 Hz, C$_1$), 62.1 (CH$_3$O-4′), 56.6 (CH$_3$O-3′), 55.7 (CH$_3$O-5″). IR (ATR) ν 3230, 2837, 1594, 1530, 1453, 1344, 1133 cm^{-1}. HRMS (ESI−) calcd for [C$_{16}$H$_{16}$FNO$_6$-H$_2$O]$^-$ ([M-H$_2$O]$^-$) 320.0934, found 320.0936.

(3,4-Dimethoxy-5-nitrophenyl)[4-(trifluoromethyl)phenyl]-methanone, 4a. To a solution of alcohol **3a** (167 mg, 0.52 mmol) in dry CH$_2$Cl$_2$ (2 mL) under a nitrogen atmosphere, a solution of DMPI (338 mg, 1.07 mmol) in CH$_2$Cl$_2$ (3 mL) was added dropwise, and the mixture was stirred ON at RT. The reaction was quenched with the addition of 4 mL of a prepared solution of Na$_2$S$_2$O$_3$ (1.13 g) in a saturated aqueous solution of NaHCO$_3$ (6 mL), and the mixture was stirred for 15 min. The aqueous phase was extracted with CH$_2$Cl$_2$ (3 × 15 mL), and the combined organic extracts were dried over anhydrous Na$_2$SO$_4$ and concentrated under a vacuum. Purification by flash column chromatography (hexanes/EtOAc, 3:1) of the resulting residue provided ketone **4a** (131 mg, 0.37 mmol, 70% yield) as a white solid. Mp 118−119 °C (from CH$_2$Cl$_2$). ^{1}H NMR (400 MHz, CDCl$_3$) δ 7.87 (d, $J_{2'',3}$ = 8.2 Hz, 2H, H-2″), 7.79 (d, $J_{3'',2}$ = 8.2 Hz,

2H, H-3″), 7.67 (d, $J_{2',6}$ = 2.0 Hz, 1H, H-2′), 7.65 (d, $J_{6',2}$ = 2.0 Hz, 1H, H-6′), 4.08 (s, 3H, CH_3O-4′), 4.00 (s, 3H, CH_3O-3′); ^{19}F NMR (250 MHz, CDCl$_3$) δ −63.58 (s, −CF$_3$); ^{13}C NMR (100.6 MHz, CDCl$_3$) δ 192.7 (C$_1$), 154.6 (C$_{3'}$), 147.0 (C$_{4'}$), 144.2 (C$_{5'}$), 139.8 (C$_{1''}$), 134.4 (q, $J_{4'',F}$ = 33.2 Hz, C$_{4''}$), 131.7 (C$_{1'}$), 130.1 (C$_{2''}$), 125.9 (q, $J_{3'',F}$ = 3.9 Hz, C$_{3''}$), 123.6 (q, $J_{CF3,F}$ = 272.6 Hz, −CF$_3$), 118.9 (C$_{6'}$), 116.2 (C$_{2'}$), 62.4 (CH$_3$O-4′), 56.9 (CH$_3$O-3′). IR (ATR) ν 3086, 2950, 2840, 1655, 1531, 1364, 1323, 1292, 1243, 1163 cm^{-1}. HRMS (ESI+) calcd for [C$_{16}$H$_{12}$F$_3$NO$_5$ + H]$^+$ ([M + H]$^+$) 356.0746, found 356.0740.

(3,4-Dimethoxy-5-nitrophenyl)(4-fluorophenyl)methanone, 4b. Compound **4b** was prepared as described for **4a** by using alcohol **3b** (230 mg, 0.75 mmol) in CH$_2$Cl$_2$ (3 mL) and a solution of DMPI (475 mg, 1.12 mmol) in CH$_2$Cl$_2$ (5 mL). Purification by flash column chromatography (hexanes/EtOAc, 3:1) afforded **4b** (226 mg, 0.74 mmol, 99% yield) as a brown solid. Mp 73−75 °C (from CHCl$_3$). ^{1}H NMR (400 MHz, DMSO-d_6) δ 7.89 (br dd, $J_{2'',3}$ = $J_{6'',5}$ = 8.9 Hz, $J_{2'',F}$ = $J_{6'',F}$ = 5.5 Hz, 2H, H-2″, H-6″), 7.70 (d, $J_{6',2}$ = 2.0 Hz, 1H, H-6′), 7.66 (d, $J_{2',6}$ = 2.0 Hz, 1H, H-2′), 7.41 (br t, $J_{3'',2}$ = $J_{5'',F}$ = $J_{3'',2}$ = $J_{5'',6}$ = 8.9 Hz, 2H, H-3″, H-5″), 3.97 (s, 3H, CH_3O-4′), 3.96 (s, 3H, CH_3O-3′); ^{19}F NMR (250 MHz, DMSO-d_6) δ −106.21 (F-4″); ^{13}C NMR (100.6 MHz, DMSO-d_6) δ 191.8 (C$_1$), 165.0 (d, $J_{4'',F}$ = 252.0 Hz, C$_{4''}$), 153.4 (C$_{3'}$), 144.7 (C$_{4'}$), 143.8 (C$_{5'}$), 132.8 (d, $J_{2'',F}$ = $J_{6'',F}$ = 9.3 Hz, C$_{2''}$, C$_{6''}$), 132.7 (C$_{1''}$), 132.4 (C$_{1'}$), 117.2 (C$_{6'}$), 116.9 (C$_{2'}$), 115.9 (d, $J_{3'',F}$ = $J_{5'',F}$ = 22.1 Hz, C$_{3''}$, C$_{5''}$), 61.8 (CH$_3$O-4′), 56.8 (CH$_3$O-3′). IR (ATR) ν 2954, 1650, 1598, 1531, 1229 cm^{-1}. HRMS (ESI+) calcd for [C$_{15}$H$_{12}$FNO$_5$ + Na]$^+$ ([M + Na]$^+$) 328.0597, found 328.0595.

(3,5-Dichlorophenyl)(3,4-dimethoxy-5-nitrophenyl)methanone, 4c. Compound **4c** was prepared as described for **4a** by using alcohol **3c** (374 mg, 1.00 mmol) in CH$_2$Cl$_2$ (4.7 mL) and a solution of DMPI (505 mg, 1.60 mmol) in CH$_2$Cl$_2$ (4.5 mL). Purification by flash column chromatography (hexanes/EtOAc, 3:1) afforded **4c** (268 mg, 0.75 mol, 73% yield) as a white solid. Mp 112−114 °C (from acetone). ^{1}H NMR (400 MHz, DMSO-d_6) δ 7.96 (m, 1H, H-4″), 7.75 (m, 2H, H-2″, H-6″), 7.75 (m, 1H, H-6′), 7.69 (d, $J_{2',6}$ = 2.0 Hz, H-2′), 3.98 (s, 3H, CH_3O-4′), 3.96 (s, 3H, CH_3O-3′); ^{13}C NMR (100.6 MHz, DMSO-d_6) δ 190.8 (C$_1$), 153.5 (C$_{3'}$), 145.3 (C$_{4'}$), 143.9 (C$_{5'}$), 139.6 (C$_{1''}$), 134.6 (C$_{3''}$, C$_{5''}$), 132.1 (C$_{4''}$), 131.3 (C$_{1'}$), 128.0 (C$_{2''}$, C$_{6''}$), 117.9 (C$_{6'}$), 116.9 (C$_{2'}$), 61.9 (CH$_3$O-4′), 56.9 (CH$_3$O-3′). IR (ATR) ν 3077, 1659, 1535, 1365, 1290 cm^{-1}. HRMS (ESI+) calcd for [C$_{15}$H$_{11}$Cl$_2$NO$_5$ + H]$^+$ ([M + H]$^+$) 356.0093, found 356.0087.

(3,5-Difluorophenyl)(3,4-dimethoxy-5-nitrophenyl)methanone, 4d. Compound **4d** was prepared as described for **4a** by using alcohol **3d** (233 mg, 716 μmol) in CH$_2$Cl$_2$ (4 mL) and a solution of DMPI (456 mg, 1.07 mmol) in CH$_2$Cl$_2$ (5 mL). Purification by flash column chromatography (hexanes/EtOAc, 3:1) afforded **4d** (259 mg, 0.80 mmol, 75% yield) as a white solid. Mp 151−152 °C (from CH$_2$Cl$_2$). ^{1}H NMR (360 MHz, CDCl$_3$) δ 7.67 (d, $J_{6',2}$ = 2.0 Hz, 1H, H-6′), 7.63 (d, $J_{2',6}$ = 2.0 Hz, 1H, H-2′), 7.28 (m, $J_{2'',F}$ = $J_{6'',F}$ = 5.2 Hz, 2H, H-2″, H-6″), 7.09 (tt, $J_{4'',2}$ = $J_{4'',6}$ = 2.2 Hz, $J_{4'',F}$ = 8.5 Hz, 1H, H-4″), 4.09 (s, 3H, CH_3O-4′), 4.00 (s, 3H, CH_3O-3′); ^{19}F NMR (250 MHz, CDCl$_3$) δ −107.50 (t, J = 6.9 Hz, F-3″, F-5″); ^{13}C NMR (90.5 MHz, CDCl$_3$) δ 191.2 (br t, $J_{CO,F}$ = 2.3 Hz, C$_1$), 163.0 (dd, $J_{3'',F}$ = $J_{5'',F}$ = 12.0 Hz, $J_{3'',F}$ = $J_{5'',F}$ = 252.5 Hz, C$_{3''}$, C$_{5''}$), 154.6 (C$_{3'}$), 147.0 (C$_{4'}$), 144.2 (C$_{5'}$), 139.6 (t, $J_{1'',F}$ = 7.8 Hz, C$_{1''}$), 131.4 (C$_{1'}$), 118.7 (C$_{6'}$), 116.2 (C$_{2'}$), 112.9 (m, $J_{2'',F}$ = $J_{6'',F}$ = 18.6 Hz, C$_{2''}$, C$_{6''}$), 108.5 (t, $J_{4'',F}$ = 25.5 Hz, C$_{4''}$), 62.4 (CH$_3$O-4′), 56.9 (CH$_3$O-3′). IR (ATR) ν 3084, 1665, 1589, 1437, 1320 cm^{-1}. HRMS (ESI+) calcd for [C$_{15}$H$_{11}$F$_2$NO$_5$ + Na]$^+$ ([M + Na]$^+$) 346.0503, found 346.0501.

(3,4-Dimethoxy-5-nitrophenyl)(3-fluoro-5-methoxyphenyl)-methanone, 4e. Compound **4e** was prepared as described for **4a** by using alcohol **3e** (287 mg, 0.85 mmol) in CH$_2$Cl$_2$ (4 mL) and a solution of DMPI (546 mg, 1.28 mmol) in CH$_2$Cl$_2$ (6 mL). Purification by flash column chromatography (hexanes/EtOAc, 5:2) afforded **4e** (199 mg, 0.59 mmol, 70% yield) as a white solid. Mp 95 °C (from CHCl$_3$). ^{1}H NMR (400 MHz, CDCl$_3$) δ 7.69 (d, $J_{6',2}$ = 2.0 Hz, 1H, H-6′), 7.63 (d, $J_{2',6}$ = 2.0 Hz, 1H, H-2′), 7.08 (m, H-6″), 7.02 (ddd, $J_{2'',F}$ = 8.4 Hz, $J_{2'',4}$ = 2.3 Hz, $J_{2'',6}$ = 1.4 Hz, 1H, H-2″), 6.86 (dt,

$J_{4'',F}$ = 10.2 Hz, $J_{4'',2}$ = $J_{4'',6}$ = 2.3 Hz, 1H, H-4''), 4.07 (s, 3H, CH_3O-4'), 3.99 (s, 3H, CH_3O-3'), 3.85 (s, 3H, CH_3O-5''); ^{19}F NMR (250 MHz, CDCl₃) δ −110.1 (s, F-3''); ^{13}C NMR (90.5 MHz, CDCl₃) δ 192.4 (d, $J_{1,F}$ = 2.8 Hz C₁), 163.3 (d, $J_{3'',F}$ = 248.3 Hz, C₃''), 161.1 (d, $J_{5'',F}$ = 10.8 Hz, C₅''), 154.4 (C₃'), 146.7 (C₄'), 144.2 (C₅'), 139.0 (d, $J_{1'',F}$ = 8.4 Hz, C₁''), 132.0 (C₁'), 118.7 (C₆'), 116.3 (C₂'), 111.2 (d, $J_{6'',F}$ = 2.8 Hz, C₆''), 109.1 (d, $J_{2'',F}$ = 23.1 Hz, C₂''), 106.4 (d, $J_{4'',F}$ = 25.0 Hz, C₄''), 62.4 (CH_3O-4'), 56.8 (CH_3O-3'), 56.1 (CH_3O-5''). IR (ATR) ν 2921, 1597, 1530, 1429, 1318, 1146 cm⁻¹. HRMS (ESI+) calcd for $[C_{16}H_{14}FNO_6 + Na]^+$ ($[M + Na]^+$) 358.0703, found 358.0705.

(4-Hydroxy-3-methoxy-5-nitrophenyl)[4-(trifluoromethyl)-phenyl]methanone, 5a. To a solution of **4a** (359 mg, 1.01 mmol) in CH₂Cl₂ (5.5 mL) was added dropwise BBr₃ (1 M in CH₂Cl₂, 8.0 mL, 8.0 mmol) at −10 °C. The reaction was allowed to proceed at RT for 2 h. The reaction mixture was quenched carefully with water (5 mL), and the resulting aqueous layer was extracted with EtOAc (2 × 20 mL). The organic extracts were dried with Na₂SO₄, and the solvent was removed under a vacuum to give the crude product. Purification by flash column chromatography (CH₂Cl₂/MeOH, 30:1) afforded **5a** (270 mg, 0.79 mmol, 78% yield) as a yellow solid. Mp 178−181 C (from MeOH). ^{1}H NMR (400 MHz, DMSO-d_6) δ 7.95−7.93 (m, 4H, H-2'', H-3'', H-5'', H-6''), 7.78 (d, $J_{6',2}$ = 1.9 Hz, 1H, H-6'), 7.64 (d, $J_{2',6}$ = 1.9 Hz, 1H, H-2'), 3.96 (s, 3H, CH₃O-3'); ^{19}F NMR (250 MHz, CDCl₃) δ −63.51 (−CF₃); ^{13}C NMR (100.6 MHz, DMSO-d_6) δ 192.2 (C₁), 149.7 (C₃'), 146.9 (C₄'), 140.5 (C₁''), 136.5 (C₅'), 132.0 (q, $J_{4'',F}$ = 32.1 Hz, C₄''), 130.1 (C₂'', C₆''), 125.9 (C₁'), 125.6 (q, $J_{3'',F}$ = $J_{5'',F}$ = 4.2 Hz, C₃'',C₅''), 123.8 (q, $J_{CF3,F}$ = 272.4, −CF₃), 120.0 (C₂'), 115.0 (C₆'), 56.8 (CH₃O-3'). IR (ATR) ν 3198, 2926, 1652, 1614, 1551, 1287 cm⁻¹. HRMS (ESI−) calcd for $[C_{15}H_{10}F_3NO_5-H]^-$ ($[M − H]^-$) 340.0439, found 340.0439.

(4-Fluorophenyl)(4-hydroxy-3-methoxy-5-nitrophenyl)-methanone, 5b. Compound **5b** was prepared as described for **5a** by using ketone **4b** (259 mg, 0.85 mmol) in CH₂Cl₂ (4 mL) and BBr₃ (1 M in CH₂Cl₂, 6.8 mL, 6.8 mmol). Purification by flash column chromatography (CH₂Cl₂/MeOH, 30:1) delivered **5b** (225 mg, 0.77 mmol, 91% yield) as a green solid. Mp 120−122 °C (from CH₂Cl₂). ^{1}H NMR (400 MHz, methanol-d_4) δ 7.92 (d, $J_{6',2}$ = 1.9 Hz, 1H, H-6'), 7.85 (br dd, $J_{2'',3}$ = $J_{6'',5}$ = 8.8 Hz, $J_{2'',F}$ = $J_{6'',F}$ = 5.4 Hz, 2H, H-2'', H-6''), 7.63 (d, $J_{2',6}$ = 1.8 Hz, 1H, H-2'), 7.28 (br t, $J_{3'',F}$ = $J_{5'',F}$ = $J_{3'',2}$ = $J_{5'',6}$ = 8.8 Hz, 2H, H-3'', H-5''), 3.98 (s, 3H, CH_3O-3'); ^{19}F NMR (250 MHz, methanol-d_4) δ −108.63 (F-4''); ^{13}C NMR (100.6 MHz, methanol-d_4) δ 194.0 (C₁), 166.8 (d, $J_{4'',F}$ = 252.9 Hz, C₄''), 151.8 (C₃'), 150.2 (C₄'), 136.4 (C₅'), 134.9 (d, $J_{1'',F}$ = 3.0 Hz, C₁'), 133.5 (d, $J_{2'',F}$ = $J_{6'',F}$ = 9.2 Hz, C₂'', C₆''), 128.2 (C₁'), 121.2 (C₆'), 116.6 (d, $J_{3'',F}$ = $J_{5'',F}$ = 22.3 Hz, C₃'', C₅''), 116.5 (C₂'), 57.3 (CH₃O-3'). IR (ATR) ν 3170, 2924, 1599, 1547, 1229 cm⁻¹. HRMS (ESI−) calcd for $[C_{14}H_{10}FNO_5-H]^-$ ($[M − H]^-$) 290.0475, found 290.0465.

(3,5-Dichlorophenyl)(4-hydroxy-3-methoxy-5-nitrophenyl)-methanone, 5c. Compound **5c** was prepared as described for **5a** by using ketone **4c** (130 mg, 0.37 mmol) in CH₂Cl₂ (2 mL) and BBr₃ (1 M solution in CH₂Cl₂, 2.9 mL, 2.9 mmol). Purification by recrystallization from acetone furnished **5c** (98 mg, 0.28 mmol, 78% yield) as a yellow solid. Mp 204−205 °C (from acetone). ^{1}H NMR (400 MHz, DMSO-d_6) δ 7.94 (t, $J_{4'',2}$ = $J_{4'',6}$ = 2.0 Hz, 1H, H-4''), 7.78 (d, $J_{6',2}$ = 2.0 Hz, 1H, H-6'), 7.73 (d, $J_{2'',4}$ = $J_{6'',4}$ = 2.0 Hz, 2H, H-2'', H-6''), 7.59 (d, $J_{2',6}$ = 2.0 Hz, 1H, H-2'), 3.95 (s, 3H, CH_3O-3'); ^{13}C NMR (100.6 MHz, DMSO-d_6) δ 190.5 (C₁), 149.8 (C₃'), 147.3 (C₄'), 140.3 (C₅'), 136.6 (C₁'), 134.4 (C₃'', C₅''), 131.6 (C₄''), 127.7 (C₂'', C₆''), 125.4 (C₁''), 120.2 (C₆'), 114.8 (C₂'), 56.8 (CH₃O-3'). IR (ATR) ν 3190, 3079, 1543, 1405, 1285 cm⁻¹. HRMS (ESI−) calcd for $[C_{14}H_9Cl_2NO_5-H]^-$ ($[M − H]^-$) 339.9780, found 339.9786.

(3,5-Difluorophenyl)(4-hydroxy-3-methoxy-5-nitrophenyl)-methanone, 5d. Compound **5d** was prepared as described for **5a** by using ketone **4d** (216 mg, 0.67 mmol) in CH₂Cl₂ (4 mL) and BBr₃ (1 M in CH₂Cl₂, 5.4 mL, 5.4 mmol). Purification by recrystallization from acetone afforded **5d** (103 mg, 0.33 mmol, 50% yield) as a yellow solid. Mp 190−192 °C (from acetone). ^{1}H NMR (400 MHz, CDCl₃) δ 11.18 (s, 1H, −OH), 8.08 (br d, $J_{6',2}$ = 1.6 Hz, 1H, H-6'), 7.70 (br

d, 1H, H-2'), 7.28 (m, 2H, H-2'', H-6''), 7.10 (tt, $J_{4'',2}$ = $J_{4'',6}$ = 2.2 Hz, $J_{4'',F}$ = 8.5 Hz, 1H, H-4''), 4.04 (s, 3H, CH_3O-3'); ^{19}F NMR (250 MHz, CDCl₃) δ −110.05 (t, J = 7.6 Hz, F-3'', F-5''); ^{13}C NMR (100.6 MHz, CDCl₃) δ 191.1 (C₁), 163.0 (dd, $J_{3'',F}$ = $J_{5'',F}$ = 12.0 Hz, $J_{3'',F}$ = $J_{5'',F}$ = 252.5 Hz, C₃'',C₅''), 150.9 (C₃'), 150.4 (C₄'), 139.7 (t, $J_{1'',F}$ = 7.8 Hz, C₁''), 132.9 (C₅'), 127.3 (C₁'), 119.7 (C₆'), 117.0 (C₂'), 112.8 (m, $J_{2'',F}$ = $J_{6'',F}$ = 18.8 Hz, C₂'', C₆''), 108.4 (t, $J_{4'',F}$ = 25.4 Hz, C₄'), 57.2 (CH_3O-3'). IR (ATR) ν 3098, 1590, 1326, 1242 cm⁻¹. HRMS (ESI−) calcd for $[C_{14}H_9F_2NO_5-H]^-$ ($[M − H]^-$) 308.0371, found 308.0378.

3-Fluoro-5-hydroxyphenyl)(4-hydroxy-3-methoxy-5-nitrophenyl)methanone, 5e. Compound **5e** was prepared as described for **5a** by using ketone **4e** (199 mg, 0.56 mmol) in CH₂Cl₂ (3 mL) and BBr₃ (1 M in CH₂Cl₂, 4.5 mL, 4.5 mmol). Purification by flash column chromatography (CH₂Cl₂/MeOH, 20:1) delivered **5e** (139 mg, 0.45 mmol, 81% yield) as a yellow solid. Mp 155−156 °C (from CHCl₃). ^{1}H NMR (250 MHz, CDCl₃) δ 8.11 (d, $J_{6',2}$ = 1.9 Hz, 1H, H-6'), 7.69 (d, $J_{2',6}$ = 1.9 Hz, 1H, H-2'), 7.04 (m, H-6''), 6.99 (ddd, $J_{2'',F}$ = 8.4 Hz, $J_{2'',4}$ = 2.3 Hz, $J_{2'',6}$ = 1.4 Hz, 1H, H-2''), 6.85 (dt, $J_{4'',F}$ = 9.4 Hz, $J_{4'',2}$ = $J_{4'',6}$ = 2.3 Hz, 1H, H-4''), 4.02 (s, 3H, CH_3O-3'); ^{19}F NMR (250 MHz, CDCl₃) δ −110.01 (F-3''); ^{13}C NMR (90.5 MHz, CDCl₃) δ 192.3 (C₁), 163.4 (d, $J_{3'',F}$ = 248.5 Hz, C₃''), 157.5 (d, $J_{5'',F}$ = 11.8 Hz, C₅''), 150.7 (C₃'), 150.2 (C₄'), 139.4 (d, $J_{1'',F}$ = 8.1 Hz, C₁''), 132.9 (C₅'), 127.8 (C₁'), 119.7 (C₆'), 117.2 (C₂'), 112.6 (d, $J_{6'',F}$ = 2.7 Hz, C₆''), 109.3 (d, $J_{2'',F}$ = 23.1 Hz, C₂''), 107.8 (d, $J_{4'',F}$ = 25.0 Hz, C₄'), 57.2 (CH₃O-3'). IR (ATR) ν 3213, 2922, 1738, 1600, 1546, 1330, 1242, 1134 cm⁻¹. HRMS (ESI−) calcd for $[C_{14}H_{10}FNO_6-H]^-$ ($[M − H]^-$) 306.0414, found 306.0424.

(3,4-Dihydroxy-5-nitrophenyl)-[4-(trifluoromethyl)phenyl]-methanone, M-14. To a mixture of monoprotected catechol **5a** (20 mg, 62 μmol) and AlCl₃ (15 mg, 0.11 mmol) in dry CHCl₃ (1 mL) in an argon atmosphere, pyridine (13 μL, 0.17 mmol) was added dropwise at 0 °C. The reaction mixture was heated to the reflux temperature and stirred until the starting material was consumed. The orange suspension was concentrated under a vacuum, and HCl (5 M, 2 mL) was added, keeping the temperature <25 °C. The aqueous layer was extracted with EtOAc (3 × 10 mL), and the combined organic yellow extracts were dried over anhydrous Na₂SO₄ and concentrated under a vacuum to give the crude product. Purification by recrystallization from acetone and water provided **M-14** (15 mg, 45 μmol, 75% yield) as a pale brown solid. Mp 68−71 °C (from CH₂Cl₂). ^{1}H NMR (360 MHz, acetone-d_6) δ 8.02−8.00 (m, $J_{2'',3}$ = $J_{6'',5}$ = 8.1 Hz, 3H, H-2'', H-6'', H-6'), 7.94 (br d, $J_{3'',2}$ = $J_{6'',5}$ = 8.1 Hz, 2H, H-3'', H-5''), 7.68 (d, $J_{2',6}$ = 1.9 Hz, 1H, H-2'); ^{19}F NMR (250 MHz, acetone-d_6) δ −68.53 (−CF₃); ^{13}C NMR (90.5 MHz, acetone-d_6) δ 193.0 (C₁), 148.9 (C₃'), 148.2 (C₄'), 141.6 (C₁''), 135.3 (C₅'), 133.8 (q, $J_{4'',F}$ = 32.4 Hz, C₄''), 130.9 (C₂'', C₆''), 128.5 (C₁'), 126.4 (q, $J_{3'',F}$ = $J_{5'',F}$ = 3.8 Hz, C₃'',C₅''), 125.0 (q, $J_{CF3,F}$ = 286.7, −CF₃), 121.7 (C₂'), 119.3 (C₆'). IR (ATR) ν 3247, 1655, 1545, 1408, 1247 cm⁻¹. HRMS (ESI−) calcd for $[C_{14}H_8F_3NO_5-H]^-$ ($[M − H]^-$) 326.0276, found 326.0284.

(3,4-Dihydroxy-5-nitrophenyl)-(4-fluorophenyl)methanone, M-17. Compound **M-17** was prepared as described for **M-14** by using **5b** (60 mg, 0.21 mmol), AlCl₃ (57 mg, 0.41 mmol), and pyridine (50 μL, 0.62 mmol) in dry CHCl₃ (3 mL). Purification by digestion in hexane afforded **M-17** (42 mg, 0.15 mmol, 70% yield) as a pale brown solid. Mp 162−165 °C (from CH₂Cl₂). ^{1}H NMR (360 MHz, acetone-d_6) δ 7.98 (d, $J_{6',2}$ = 2.0 Hz, 1H, H-6'), 7.91 (br dd, $J_{2'',3}$ = $J_{6'',5}$ = 8.7 Hz, $J_{2'',F}$ = $J_{6'',F}$ = 5.5 Hz, 2H, H-2'', H-6''), 7.65 (d, $J_{2',6}$ = 2.0 Hz, 1H, H-2'), 7.35 (br t, $J_{3'',2}$ = $J_{6'',5}$ = 8.7 Hz, $J_{3'',F}$ = $J_{5'',F}$ = 8.7 Hz, 2H, H-3'', H-5''); ^{19}F NMR (250 MHz, acetone-d_6) δ −105.17 (F-4''); ^{13}C NMR (90.5 MHz, acetone-d_6) δ 192.5 (C₁), 166.2 (d, $J_{3'',F}$ = 252.0 Hz, C₄''), 148.6 (C₃'), 147.7 (C₄'), 135.1 (C₅'), 134.5 (d, $J_{1'',F}$ = 2.8 Hz, C₁''), 133.4 (d, $J_{2'',F}$ = $J_{6'',F}$ = 9.1 Hz, C₂'', C₆''), 129.2 (C₁'), 121.9 (C₂'), 118.9 (C₆'), 116.4 (d, $J_{3'',F}$ = $J_{5'',F}$ = 22.0 Hz, C₃'',C₅''). IR (ATR) ν 3194, 2923, 1651, 1585, 1296 cm⁻¹. HRMS (ESI−): calcd for $[C_{13}H_8FNO_5-H]^-$ 276.0308 ($[M − H]^-$); found 276.0315.

(3,5-Dichlorophenyl)-(3,4-dihydroxy-5-nitrophenyl)methanone, M-20. Compound **M-20** was prepared as described for **M-14** by using **5c** (45 mg, 0.13 mmol), AlCl₃ (35 mg, 0.26 mmol), and pyridine (50

μL, 0.39 mmol) in dry $CHCl_3$ (4 mL). Purification by recrystallization from acetone and water provided **M-20** (35 mg, 0.10 mmol, 81% yield) as a green light solid. Mp 182−184 °C (from acetone). ^{1}H NMR (250 MHz, acetone-d_6) δ 10.70 (br s, 1H, −OH), 8.02 (d, $J_{6',2'}$ = 2.0 Hz, 1H, H-2'), 7.79 (t, $J_{4'',2''}$ = $J_{4'',6''}$ = 1.9 Hz, 1H, H-4''), 7.74 (d, $J_{2'',4''}$ = $J_{2'',4''}$ = 1.9 Hz, 2H, H-2'', H-6''), 7.66 (d, $J_{2',6'}$ = 2.0 Hz, H-2'); ^{13}C NMR (100.6 MHz, acetone-d_6) δ 191.3 (C_1), 148.9 ($C_{3'}$), 148.4 ($C_{4'}$), 141.2 ($C_{5'}$), 135.9 ($C_{3''}$, $C_{5''}$), 135.3 ($C_{1''}$), 132.6 ($C_{4''}$), 128.7 ($C_{2''}$, $C_{6''}$), 128.2 ($C_{1''}$), 121.7 ($C_{2'}$), 119.3 ($C_{6'}$). IR (ATR) ν 3331, 1617, 1544, 1308 cm^{-1}. HRMS (ESI−) calcd for $[C_{13}H_7Cl_2NO_5$-H]$^-$ ([M − H]$^-$) 325.9623, found 325.9630.

(3,5-Difluorophenyl)-(3,4-dihydroxy-5-nitrophenyl)methanone, M-21. Compound **M-21** was prepared as described for **M-14** by using **5d** (100 mg, 0.32 mmol), $AlCl_3$ (86 mg, 0.65 mmol), and pyridine (105 μL, 1.29 mmol) in dry $CHCl_3$ (10 mL). Purification by recrystallization from acetone and water furnished **M-21** (71 mg, 0.24 mmol, 75% yield) as a yellow light solid. Mp 135−137 °C (from acetone). ^{1}H NMR (360 MHz, DMSO-d_6) δ 10.96 (br s, 2H, 2 × −OH), 7.70 (d, $J_{6',2'}$ = 2.0 Hz, 1H, H-6'), 7.60 (br tt, $J_{4'',2''}$ = $J_{4'',6''}$ = 2.2 Hz, $J_{4'',F}$ = 9.3 Hz, 1H, H-4''), 7.48 (d, $J_{2',6'}$ = 2.0 Hz, 1H, H-2'), 7.43 (m, $J_{2'',F}$ = $J_{2'',F}$ = 5.8 Hz, 2H, H-2'', H-6''); ^{19}F NMR (250 MHz, DMSO-d_6) δ −110.07 (s, F-3'', F-5''); ^{13}C NMR (90.5 MHz, DMSO-d_6) δ 190.7 (C_1), 162.0 (dd, $J_{3'',F}$ = $J_{5'',F}$ = 12.6 Hz, $J_{3'',F}$ = $J_{5'',F}$ = 249.9 Hz, $C_{3''}$,$C_{5''}$), 147.9 ($C_{3'}$), 146.6 ($C_{4'}$), 140.4 (t, $J_{1'',F}$ = 8.0 Hz, $C_{1''}$), 136.9 ($C_{5'}$), 125.4 ($C_{1'}$), 118.5 ($C_{6'}$), 118.5 ($C_{2'}$), 112.5 (m, $J_{2'',F}$ = $J_{6'',F}$ = 18.5 Hz, $C_{2''}$, $C_{6''}$), 107.7 (t, $J_{4'',F}$ = 25.8 Hz, $C_{4''}$). IR (ATR) ν 3363, 1617, 1587, 1436, 1323 cm^{-1}. HRMS (ESI−) calcd for $[C_{13}H_7F_2NO_5$-H]$^-$ ([M − H]$^-$) 294.0214, found 294.0221.

(3,4-Dihydroxy-5-nitrophenyl)-(3-fluoro-5-hydroxyphenyl)-methanone, M-23. Compound **M-23** was prepared as described for **M-14** by using **5e** (158 mg, 0.52 mmol), $AlCl_3$ (511 mg, 3.80 mmol), and pyridine (360 μL, 4.45 mmol) in dry $CHCl_3$ (10 mL). Purification by flash column chromatography (CH_2Cl_2/MeOH, 19:1) afforded catechol **M-23** (69 mg, 0.24 mmol, 46% yield) as a yellow solid. Mp 215−217 °C (from acetone). ^{1}H NMR (360 MHz, acetone-d_6) δ 10.61 (br s, 1H, −OH), 9.28 (br s, 2H, 2 × −OH), 8.02 (d, $J_{6',2'}$ = 2.0 Hz, 1H, H-6'), 7.65 (d, $J_{2',6'}$ = 2.0 Hz, 1H, H-2'), 7.08 (s, C-6''), 7.00 (br dt, $J_{2'',F}$ = 8.8 Hz, 1H, H-2''), 6.90 (br dt, $J_{4'',2''}$ = 2.2 Hz, $J_{4'',F}$ = 10.3 Hz, 1H, H-4''); ^{19}F NMR (250 MHz, acetone-d_6) δ −112.87 (t, J = 9.5 Hz, F-3''); ^{13}C NMR (90.5 MHz, acetone-d_6) δ 192.4 (d, $J_{CO,F}$ = 2.7 Hz, C_1), 164.1 (d, $J_{3'',F}$ = 254.0 Hz, $C_{3''}$), 159.9 (d, $J_{5'',F}$ = 11.7 Hz, $C_{5''}$), 148.8 ($C_{3'}$), 148.1 ($C_{4'}$), 140.6 (d, $J_{1'',F}$ = 8.4 Hz, $C_{1''}$), 135.2 ($C_{5'}$), 128.7 ($C_{1'}$), 121.8 ($C_{2'}$), 119.1 ($C_{6'}$), 113.5 (d, $J_{6'',F}$ = 2.2 Hz, $C_{6''}$), 108.1 (d, $J_{2'',F}$ = 23.3 Hz, $C_{2''}$), 107.4 (d, $J_{4'',F}$ = 24.2 Hz, $C_{4''}$). IR (ATR) ν 3229, 1599, 1442, 1252 cm^{-1}. HRMS (ESI−) calcd for $[C_{13}H_8FNO_6$-H]$^-$ ([M − H]$^-$) 292.0257, found 292.0265.

Isothermal Titration Calorimetry. The thermodynamic parameters that characterize the binding of TTR ligands to WT-TTR were determined using a MicroCal Auto-iTC200 Calorimeter (MicroCal, Malvern-Panalytical), as detailed before.[44] A 100 μM solution of the compound (in a PBS buffer pH 7.0 containing 100 mM KCl, 1 mM EDTA and 2.5% DMSO) was titrated into an ITC cell containing a 5 μM solution of WT-TTR in the same buffer at 25 °C. A stirring speed of 750 rpm and 2 μL injections were programmed, with a 150 s equilibration period between each injection to allow the calorimetric signal (thermal power) to return to baseline and a 10 μcal/s reference power. Two independent titrations were done for each TTR ligand. The experimental data were analyzed with a general model for a protein with two ligand-binding sites[93,94] implemented in Origin 7.0 (OriginLab) accounting for cooperative and noncooperative binding. The best fit of the binding isotherm was attained with a model considering two identical binding sites (i.e., no cooperativity) for tolcapone and its derivatives.

Urea-Induced TTR Tetramer Dissociation Kinetics. TTR solutions (1.8 μM in PBS) were incubated with the different TTR ligands (3.6 μM) for 30 min at RT, and 6 M urea was added. A control sample containing the same amount of DMSO rather than the compound was prepared. The process of unfolding was tracked by intrinsic fluorescence spectroscopy using an FP-8200 Spectrofluor-

ometer (Jasco). Trp residues were excited at 295 nm, and emission spectra was collected from 310 to 400 nm. Trp exposure upon denaturation red shifts the wavelength of maximum fluorescence from 335 to 355 nm, approximately. The 355/335 fluorescence emission intensity was normalized from minimum (100% folded) to maximum (0% folded) and plotted as a function of time. The TTR fluorescence of the control sample after incubation at RT for 96 h in 6 M urea was considered the maximum.

TTR *In Vitro* Aggregation Assay. The anti-aggregational activity of TTR ligands was evaluated using the established acid-mediated aggregation assay.[44] In short, WT-TTR solutions (7 μM in 10 mM sodium phosphate, 100 mM KCl, 1 mM EDTA, 1 mM DTT, pH 7.0) were mixed with increasing concentrations of test compounds (prepared in 100% DMSO). The percentage of DMSO was adjusted to 5% (v/v) in the final reaction assay mixture. After incubating for 30 min at 37 °C, the pH of the samples was dropped to 4.2 by the addition of acetate buffer (100 mM sodium acetate, 100 mM KCl, 1 mM EDTA, 1 mM DTT, pH 4.2), and the solutions were further incubated for 72 h at 37 °C. The extent of TTR aggregation was assessed by measuring turbidity at 340 nm using a Varian Cary Eclipse Fluorescence Spectrophotometer (Agilent Technologies). As some of the compounds present dose-dependent absorbance at 340 nm, each measurement was corrected with a buffer containing the same concentration of the test compound but lacking TTR. For each inhibitor concentration, the percentage of TTR aggregation was given by the ratio of the turbidity of the sample of interest to that of a control sample incubated without compound multiplied by 100%.

TTR Stabilization Studies by Isoelectric Focusing. Isoelectric focusing (IEF) under semidenaturing conditions was performed as described previously[95] to evaluate the stabilizing effect of both tolcapone and **M-23** on recombinant TTR and in plasma TTR. Recombinant WT-TTR was produced using an *Escherichia coli* bacterial expression system, as detailed elsewhere.[96] For the plasma assays, human plasma from control individuals (n = 6), carrying WT-TTR ($\approx$3.9 μM), was incubated ON at 4 °C with tafamidis, tolcapone, or **M-23** at two different concentrations (19.5 and 39 μM). Similarly, recombinant WT-TTR (6 μM) was also treated ON at 4 °C with the same compounds at concentrations of 30 and 60 μM. DMSO (5%) was used as vehicle. Control samples were incubated in similar conditions without the compounds. After incubation, the samples were loaded into a native PAGE, and the gel band containing TTR was excised and applied to an IEF gel. The IEF gel contained 4 M urea (semidenaturing conditions) and 5% (v/v) ampholytes, pH 4−6.5 (Sigma-Merck), and was run at 1200 V for 5 h. Proteins were fixed and stained with Coomassie blue. The gels were scanned using a GS-900 calibrated densitometer (Bio-Rad) and analyzed by densitometry using the QuantityOne software version 4.6.6 (Bio-Rad). The ratio of the TTR tetramer over total TTR (TTR tetramer + monomer) was calculated for each plasma sample, and the percentage of tetramer stabilization was calculated as ((ratio treated sample − ratio control sample)/ratio control sample) × 100. Treated and control plasma samples come from the same donor.

T$_4$ Binding Competition Assay. Binding competition assays with radioactive T$_4$ were performed by incubation of 5 μL of human plasma samples of WT-TTR carriers (n = 4) with 1 μL of $[^{125}$I]-T$_4$ (specific radioactivity 1250 μCi/μg; concentration 320 μCi/mL; Perkin Elmer) in the presence of 39 μM compounds. The negative control was performed by adding the same percentage of DMSO in the samples. After 1 h incubation at rt, plasma proteins were fractionated by native PAGE,[97] and the gels were dried and exposed to an autoradiography film. The films were scanned, and the intensity of the bands was determined by densitometry using Image Lab software version 5.2.1 (Bio-Rad). The ratio of T$_4$ bound to TTR over total T$_4$ (TBG + ALB + TTR) was calculated for each sample and normalized to the maximum value, which corresponds to the negative control sample.

Solubility Measurements. The solubility tests were carried out by weighing **M-23** and tolcapone (solid samples). Then, distilled or deionized water was added under gentle agitation until total dissolution. All the experiments were performed in triplicate.

Cytotoxicity Assay. Cytotoxicity analyses were performed for evaluating the potential **M-23** chemical toxicity to human cells. Tolcapone was used for comparison. Two cell lines, HeLa and HepG2 cells, were cultured in MEM ALPHA (Gibco) and 10% FBS at 37 °C in 5% CO_2 humidified atmosphere. HeLa cells were seeded at 3500 cells/well and HepG2 cells at 4500 cells/well in 96-well plates and incubated with increasing concentrations of compound at a range of concentrations from 2 to 100 μM during 72 h at 37 °C. Controls were performed with the equivalent amount of DMSO relative to each concentration of compound diluted in MilliQ water. Then, cell viability was determined by adding 10 μL of the PrestoBlue reagent (Thermo Fisher Scientific), and after an incubation period of 15 min at 37 °C, the fluorescence intensity was collected using a 590/20 filter with an excitation wavelength of 535 in a Victor3 Multilabel Reader (PerkinElmer). Experiments were carried out in triplicate, and the percentage of cell viability for each well was calculated as (intensity sample − mean intensity blank)/(mean intensity control − mean intensity blank) × 100, where "mean intensity blank" corresponds to the mean intensity of wells with PrestoBlue alone and "mean intensity control" is the mean intensity of wells that contain the corresponding percentage of DMSO.

Crystallization and Structure Determination of the WT-TTR/M-23 Complex. Co-crystals of WT-TTR/M-23 were obtained as described previously.[44] In short, WT-TTR (85 μM) was mixed with 10-fold molar excess of **M-23** and co-crystallized at 18 °C by the hanging-drop vapor diffusion method (1:1, complex and reservoir solution). Crystals were grown from a solution containing 30% PEG 400, 200 mM $CaCl_2$, and 100 mM HEPES (pH 8.0) and directly flash-frozen in liquid nitrogen before analysis. Diffraction data were recorded from PEG400 cryo-cooled crystals (100 K) at the ALBA Synchrotron in Barcelona (BL13-XALOC beamline).[98] Data were integrated and merged using XDS[99] and scaled, reduced, and further analyzed using Ccp4.[100] The structure of TTR/M-23 complex was determined by molecular replacement with Phenix (version 1.19.2-4158)[101] using the crystal structure of TTR (PDB code 1F41) as a search model. Refinement was performed with Phenix, and model building was performed with Coot.[102] Refinement and data statistics are provided in Table S5. Figures were prepared with Pymol (The PyMOL Molecular Graphics System, Version 2.0, Schrödinger, LLC).

Statistical Analysis. All the graphs were generated with GraphPad Prism software version 6.0 (GraphPad Software, La Jolla, California, USA). Data are shown as means ± standard error of mean (SEM). The results obtained from TTR stabilization studies in human plasma were analyzed by one-way ANOVA Tukey's test using GraphPad Prism 6.0. $p < 0.05$ was considered statistically significant (* statistically significant at $p < 0.05$; ** statistically significant at $p < 0.01$; *** statistically significant at $p < 0.001$).

■ ASSOCIATED CONTENT

Ⓢ Supporting Information

The Supporting Information is available free of charge at https://pubs.acs.org/doi/10.1021/acs.jmedchem.2c01195.

Main structures together with H-bond evolution along the MD trajectories for all the systems; TTR tetramer stabilization effect of tafamidis, tolcapone, and **M-23** in human plasma as assessed by IEF; overlay of the WT-TTR binding pocket when bound to **M-23** and tolcapone; tolcapone−TTR binding poses from MD simulations in the absence of backbone constrains; ^{1}H and ^{13}C NMR spectra of all synthesized compounds; and the HPLC traces for the final compounds (PDF)

PDB coordinates for tolcapone (PDB)

PDB coordinates for **M-14** (PDB)

PDB coordinates for **M-17** (PDB)

PDB coordinates for **M-20** (PDB)

PDB coordinates for **M-21** (PDB)

PDB coordinates for **M-23** (PDB)

Molecular formula strings for the new compounds described in the study (CSV)

Accession Codes

The atomic coordinates have been deposited into the Protein Data Bank with accession code 7QC5. The authors will release the atomic coordinates and experimental data upon article publication.

■ AUTHOR INFORMATION

Corresponding Author

Salvador Ventura − *Institut de Biotecnologia i Biomedicina and Departament de Bioquímica i Biologia Molecular, Universitat Autònoma de Barcelona, Barcelona 08193, Spain; ICREA, E-08010 Barcelona, Spain;* ● orcid.org/0000-0002-9652-6351; Email: salvador.ventura@uab.es

Authors

Francisca Pinheiro − *Institut de Biotecnologia i Biomedicina and Departament de Bioquímica i Biologia Molecular, Universitat Autònoma de Barcelona, Barcelona 08193, Spain*

Irantzu Pallarès − *Institut de Biotecnologia i Biomedicina and Departament de Bioquímica i Biologia Molecular, Universitat Autònoma de Barcelona, Barcelona 08193, Spain;* ● orcid.org/0000-0002-8205-2060

Francesca Peccati − *Departament de Química, Universitat Autònoma de Barcelona, Barcelona 08193, Spain;* Present Address: Center for Cooperative Research in Biosciences (CIC bioGUNE), Basque Research and Technology Alliance (BRTA), 48160 Derio, Spain; ● orcid.org/0000-0002-7813-8216

Adrià Sánchez-Morales − *Departament de Química, Universitat Autònoma de Barcelona, Barcelona 08193, Spain*

Nathalia Varejão − *Institut de Biotecnologia i Biomedicina and Departament de Bioquímica i Biologia Molecular, Universitat Autònoma de Barcelona, Barcelona 08193, Spain*

Filipa Bezerra − *Molecular Neurobiology Group, i3S−Instituto de Investigação e Inovação em Saúde, IBMC−Instituto de Biologia Molecular e Celular, Universidade do Porto, 4200-135 Porto, Portugal; Departamento de Biologia Molecular, ICBAS−Instituto de Ciências Biomédicas Abel Salazar, Universidade do Porto, 4050-313 Porto, Portugal*

David Ortega-Alarcon − *Department of Biochemistry and Molecular & Cellular Biology, and Institute for Biocomputation eand Physics of Complex Systems (BIFI), Joint Unit GBsC-CSIC-BIFI, Universidad de Zaragoza, 50018 Zaragoza, Spain; Aragon Institute for Health Research, 50009 Zaragoza, Spain; Biomedical Research Network Center in Hepatic and Digestive Diseases (CIBERehd), 28029 Madrid, Spain*

Danilo Gonzalez − *Departament de Química, Universitat Autònoma de Barcelona, Barcelona 08193, Spain*

Marcelo Osorio − *Departament de Química, Universitat Autònoma de Barcelona, Barcelona 08193, Spain*

Susanna Navarro − *Institut de Biotecnologia i Biomedicina and Departament de Bioquímica i Biologia Molecular, Universitat Autònoma de Barcelona, Barcelona 08193, Spain;* ● orcid.org/0000-0001-8160-9536

Adrián Velázquez-Campoy − *Department of Biochemistry and Molecular & Cellular Biology, and Institute for Biocomputation eand Physics of Complex Systems (BIFI), Joint Unit GBsC-CSIC-BIFI, Universidad de Zaragoza, 50018 Zaragoza, Spain; Aragon Institute for Health*

Research, 50009 Zaragoza, Spain; Biomedical Research Network Center in Hepatic and Digestive Diseases (CIBERehd), 28029 Madrid, Spain; ● orcid.org/0000-0001-5702-4538

Maria Rosário Almeida − *Molecular Neurobiology Group, i3S—Instituto de Investigação e Inovação em Saúde, IBMC—Instituto de Biologia Molecular e Celular, Universidade do Porto, 4200-135 Porto, Portugal; Departamento de Biologia Molecular, ICBAS—Instituto de Ciências Biomédicas Abel Salazar, Universidade do Porto, 4050-313 Porto, Portugal*

David Reverter − *Institut de Biotecnologia i Biomedicina and Departament de Bioquímica i Biologia Molecular, Universitat Autònoma de Barcelona, Barcelona 08193, Spain*

Félix Busqué − *Departament de Química, Universitat Autònoma de Barcelona, Barcelona 08193, Spain*

Ramon Alibés − *Departament de Química, Universitat Autònoma de Barcelona, Barcelona 08193, Spain;* ● orcid.org/0000-0002-7997-2691

Mariona Sodupe − *Departament de Química, Universitat Autònoma de Barcelona, Barcelona 08193, Spain;* ● orcid.org/0000-0003-0276-0524

Complete contact information is available at:
https://pubs.acs.org/10.1021/acs.jmedchem.2c01195

Author Contributions

The manuscript was written through contributions of all authors. All authors have given approval to the final version of the manuscript.

Notes

The authors declare no competing financial interest.

■ ABBREVIATIONS

ATTR, transthyretin amyloidosis; TTR, transthyretin; T_4, thyroxine; FAP, familial amyloid polyneuropathy; FAC, familial amyloid cardiomyopathy; SSA, senile systemic amyloidosis; HBP, halogen binding pocket; ITC, isothermal titration calorimetry; IEF, isoelectric focusing

■ REFERENCES

(1) Eisenberg, D.; Jucker, M. The amyloid state of proteins in human diseases. *Cell* **2012**, *148*, 1188−1203.

(2) Sipe, J. D.; Benson, M. D.; Buxbaum, J. N.; Ikeda, S.-i.; Merlini, G.; Saraiva, M. J. M.; Westermark, P. Amyloid fibril proteins and amyloidosis: chemical identification and clinical classification Interna-tional Society of Amyloidosis 2016 Nomenclature Guidelines. *Amyloid* **2016**, *23*, 209−213.

(3) Kanai, M.; Raz, A.; Goodman, D. S. Retinol binding-protein: the transport protein for vitamin A in human plasma. *J. Clin. Invest.* **1968**, *47*, 2025−2044.

(4) Schreiber, G.; Richardson, S. J. The Evolution of Gene Expression, Structure and Function of Transthyretin. *Comp. Biochem. Physiol. Part B Biochem. Mol. Biol.* **1997**, *116*, 137−160.

(5) Hagen, G. A.; Elliott, W. J. Transport of thyroid hormones in serum and cerebrospinal fluid. *J. Clin. Endocrinol. Metab.* **1973**, *37*, 415−422.

(6) Benson, M. D. Transthyretin amyloidosis: a little history of hereditary amyloidosis. *Amyloid* **2017**, *24*, 76−77.

(7) Blake, C. C. F.; Geisow, M. J.; Swan, I. D. A.; Rerat, C.; Rerat, B. Structure of human plasma prealbumin at 2-5 A resolution. A preliminary report on the polypeptide chain conformation, quaternary structure and thyroxine binding. *J. Mol. Biol.* **1974**, *88*, 1−12.

(8) Blake, C. C. F.; Geisow, M. J.; Oatley, S. J.; Rérat, B.; Rérat, C. Structure of prealbumin: secondary, tertiary and quaternary interactions determined by Fourier refinement at 1.8 A. *J. Mol. Biol.* **1978**, *121*, 339−356.

(9) Foss, T. R.; Wiseman, R. L.; Kelly, J. W. The pathway by which the tetrameric protein transthyretin dissociates. *Biochemistry* **2005**, *44*, 15525−15533.

(10) Lai, Z.; Colón, W.; Kelly, J. W. The acid-mediated denaturation pathway of transthyretin yields a conformational intermediate that can self-assemble into amyloid. *Biochemistry* **1996**, *35*, 6470−6482.

(11) Hammarström, P.; Jiang, X.; Hurshman, A. R.; Powers, E. T.; Kelly, J. W. Sequence-dependent denaturation energetics: A major determinant in amyloid disease diversity. *Proc. Natl. Acad. Sci. U. S. A.* **2002**, *99*, 16427−16432.

(12) Hurshman Babbes, A. R.; Powers, E. T.; Kelly, J. W. Quantification of the thermodynamically linked quaternary and tertiary structural stabilities of transthyretin and its disease-associated variants: the relationship between stability and amyloidosis. *Biochemistry* **2008**, *47*, 6969−6984.

(13) Finsterer, J.; Iglseder, S.; Wanschitz, J.; Topakian, R.; Löscher, W. N.; Grisold, W. Hereditary transthyretin-related amyloidosis. *Acta Neurol. Scand.* **2019**, *139*, 92−105.

(14) Jacobson, D. R.; Pastore, R. D.; Yaghoubian, R.; Kane, I.; Gallo, G.; Buck, F. S.; Buxbaum, J. N. Variant-sequence transthyretin (isoleucine 122) in late-onset cardiac amyloidosis in black Americans. *N. Engl. J. Med.* **1997**, *336*, 466−473.

(15) Andrade, C. A peculiar form of peripheral neuropathy; familiar atypical generalized amyloidosis with special involvement of the peripheral nerves. *Brain* **1952**, *75*, 408−427.

(16) Saraiva, M. J.; Birken, S.; Costa, P. P.; Goodman, D. S. Amyloid fibril protein in familial amyloidotic polyneuropathy, Portuguese type. Definition of molecular abnormality in transthyretin (prealbumin). *J. Clin. Invest.* **1984**, *74*, 104−119.

(17) Goren, H.; Steinberg, M. C.; Farboody, G. H. Familial oculoleptomeningeal amyloidosis. *Brain* **1980**, *103*, 473−495.

(18) Sekijima, Y.; Hammarström, P.; Matsumura, M.; Shimizu, Y.; Iwata, M.; Tokuda, T.; Ikeda, S.; Kelly, J. W. Energetic characteristics of the new transthyretin variant A25T may explain its atypical central nervous system pathology. *Lab. Invest.* **2003**, *83*, 409−417.

(19) Christmanson, L.; Betsholtz, C.; Gustavsson, A.; Johansson, B.; Sletten, K.; Westermark, P. The transthyretin cDNA sequence is normal in transthyretin-derived senile systemic amyloidosis. *FEBS Lett.* **1991**, *281*, 177−180.

(20) Buxbaum, J. N.; Reixach, N. Transthyretin: the servant of many masters. *Cell. Mol. Life Sci.* **2009**, *66*, 3095−3101.

(21) Coles, L. S.; Young, R. D. Supercentenarians and transthyretin amyloidosis: The next frontier of human life extension. *Prev. Med.* **2012**, *54*, S9−S11.

(22) Mangione, P. P.; Porcari, R.; Gillmore, J. D.; Pucci, P.; Monti, M.; Porcari, M.; Giorgetti, S.; Marchese, L.; Raimondi, S.; Serpell, L. C.; Chen, W.; Relini, A.; Marcoux, J.; Clatworthy, I. R.; Taylor, G. W.; Tennent, G. A.; Robinson, C. V.; Hawkins, P. N.; Stoppini, M.;

Wood, S. P.; Pepys, M. B.; Bellotti, V. Proteolytic cleavage of Ser52Pro variant transthyretin triggers its amyloid fibrillogenesis. *Proc. Natl. Acad. Sci. U. S. A.* **2014**, *111*, 1539−1544.

(23) Ihse, E.; Rapezzi, C.; Merlini, G.; Benson, M. D.; Ando, Y.; Suhr, O. B.; Ikeda, S.; Lavatelli, F.; Obici, L.; Quarta, C. C.; Leone, O.; Jono, H.; Ueda, M.; Lorenzini, M.; Liepnieks, J.; Ohshima, T.; Tasaki, M.; Yamashita, T.; Westermark, P. Amyloid fibrils containing fragmented ATTR may be the standard fibril composition in ATTR amyloidosis. *Amyloid* **2013**, *20*, 142−150.

(24) Marcoux, J.; Mangione, P. P.; Porcari, R.; Degiacomi, M. T.; Verona, G.; Taylor, G. W.; Giorgetti, S.; Raimondi, S.; Sanglier-Cianférani, S.; Benesch, J. L.; Cecconi, C.; Naqvi, M. M.; Gillmore, J. D.; Hawkins, P. N.; Stoppini, M.; Robinson, C. V.; Pepys, M. B.; Bellotti, V. A novel mechano-enzymatic cleavage mechanism underlies transthyretin amyloidogenesis. *EMBO Mol. Med.* **2015**, *7*, 1337−1349.

(25) Slamova, I.; Adib, R.; Ellmerich, S.; Golos, M. R.; Gilbertson, J. A.; Botcher, N.; Canetti, D.; Taylor, G. W.; Rendell, N.; Tennent, G. A.; Verona, G.; Porcari, R.; Mangione, P. P.; Gillmore, J. D.; Pepys, M. B.; Bellotti, V.; Hawkins, P. N.; Al-Shawi, R.; Simons, J. P. Plasmin activity promotes amyloid deposition in a transgenic model of human transthyretin amyloidosis. *Nat. Commun.* **2021**, *12*, 7112.

(26) Okumura, K.; Yamashita, T.; Masuda, T.; Misumi, Y.; Ueda, A.; Ueda, M.; Obayashi, K.; Jono, H.; Yamashita, S.; Inomata, Y.; Ando, Y. Long-term outcome of patients with hereditary transthyretin V30M amyloidosis with polyneuropathy after liver transplantation. *Amyloid* **2016**, *23*, 39−45.

(27) Banerjee, D.; Roeker, L. E.; Grogan, M.; Swiecicki, P.; Poterucha, J.; Heimbach, J.; Zeldenrust, S.; Gertz, M.; Edwards, B.; Daly, R.; Klarich, K. W.; Dispenzieri, A. Outcomes of Patients With Familial Transthyretin Amyloidosis After Liver Transplantation. *Prog. Transplant.* **2017**, *27*, 246−250.

(28) Johnson, S. M.; Connelly, S.; Fearns, C.; Powers, E. T.; Kelly, J. W. The Transthyretin Amyloidoses: From Delineating the Molecular Mechanism of Aggregation Linked to Pathology to a Regulatory-Agency-Approved Drug. *J. Mol. Biol.* **2012**, *421*, 185−203.

(29) Ackermann, E. J.; Guo, S.; Benson, M. D.; Booten, S.; Freier, S.; Hughes, S. G.; Kim, T. W.; Jesse Kwoh, T.; Matson, J.; Norris, D.; Yu, R.; Watt, A.; Monia, B. P. Suppressing transthyretin production in mice, monkeys and humans using 2nd-Generation antisense oligonucleotides. *Amyloid* **2016**, *23*, 148−157.

(30) Kristen, A. V.; Ajroud-Driss, S.; Conceição, I.; Gorevic, P.; Kyriakides, T.; Obici, L. Patisiran, an RNAi therapeutic for the treatment of hereditary transthyretin-mediated amyloidosis. *Neurodegener. Dis. Manag.* **2019**, *9*, 5−23.

(31) Hammarstrom, P.; Schneider, F.; Kelly, J. W. Trans-suppression of misfolding in an amyloid disease. *Science* **2001**, *293*, 2459−2462.

(32) Coelho, T.; Chorão, R.; Sousa, A.; Alves, I.; Torres, M. F.; Saraiva, M. J. M. Compound heterozygotes of transthyretin Met30 and transthyretin Met119 are protected from the devastating effects of familial amyloid polyneuropathy. *Neuromuscl. Disord.* **1996**, *6*, S20.

(33) Bulawa, C. E.; Connelly, S.; Devit, M.; Wang, L.; Weigel, C.; Fleming, J. A.; Packman, J.; Powers, E. T.; Wiseman, R. L.; Foss, T. R.; Wilson, I. A.; Kelly, J. W.; Labaudiniere, R. Tafamidis, a potent and selective transthyretin kinetic stabilizer that inhibits the amyloid cascade. *Proc. Natl. Acad. Sci. U. S. A.* **2012**, *109*, 9629−9634.

(34) Coelho, T.; Maia, L. F.; da Silva, A. M.; Cruz, M. W.; Planté-Bordeneuve, V.; Suhr, O. B.; Conceiçao, I.; Schmidt, H. H. J.; Trigo, P.; Kelly, J. W.; Labaudinière, R.; Chan, J.; Packman, J.; Grogan, D. R. Long-term effects of tafamidis for the treatment of transthyretin familial amyloid polyneuropathy. *J. Neurol.* **2013**, *260*, 2802−2814.

(35) Maurer, M. S.; Schwartz, J. H.; Gundapaneni, B.; Elliott, P. M.; Merlini, G.; Waddington-Cruz, M.; Kristen, A. V.; Grogan, M.; Witteles, R.; Damy, T.; Drachman, B. M.; Shah, S. J.; Hanna, M.; Judge, D. P.; Barsdorf, A. I.; Huber, P.; Patterson, T. A.; Riley, S.; Schumacher, J.; Stewart, M.; Sultan, M. B.; Rapezzi, C. Tafamidis Treatment for Patients with Transthyretin Amyloid Cardiomyopathy. *N. Engl. J. Med.* **2018**, *379*, 1007−1016.

(36) Monteiro, C.; Mesgazardeh, J. S.; Anselmo, J.; Fernandes, J.; Novais, M.; Rodrigues, C.; Brighty, G. J.; Powers, D. L.; Powers, E. T.;

Coelho, T.; Kelly, J. W. Predictive model of response to tafamidis in hereditary ATTR polyneuropathy. *JCI Insight* **2019**, *4*, DOI: 10.1172/jci.insight.126526.

(37) Adamski-Werner, S. L.; Palaninathan, S. K.; Sacchettini, J. C.; Kelly, J. W. Diflunisal analogues stabilize the native state of transthyretin. Potent inhibition of amyloidogenesis. *J. Med. Chem.* **2004**, *47*, 355−374.

(38) Penchala, S. C.; Connelly, S.; Wang, Y.; Park, M. S.; Zhao, L.; Baranczak, A.; Rappley, I.; Vogel, H.; Liedtke, M.; Witteles, R. M.; Powers, E. T.; Reixach, N.; Chan, W. K.; Wilson, I. A.; Kelly, J. W.; Graef, I. A.; Alhamadsheh, M. M. AG10 inhibits amyloidogenesis and cellular toxicity of the familial amyloid cardiomyopathy-associated V122I transthyretin. *Proc. Natl. Acad. Sci. U. S. A.* **2013**, *110*, 9992−9997.

(39) Sant'Anna, R.; Gallego, P.; Robinson, L. Z.; Pereira-Henriques, A.; Ferreira, N.; Pinheiro, F.; Esperante, S.; Pallares, I.; Huertas, O.; Almeida, M. R.; Reixach, N.; Insa, R.; Velazquez-Campoy, A.; Reverter, D.; Reig, N.; Ventura, S. Repositioning tolcapone as a potent inhibitor of transthyretin amyloidogenesis and associated cellular toxicity. *Nat. Commun.* **2016**, *7*, 10787.

(40) Games, J.; Salvadó, M.; Reig, N.; Suñé, P.; Casanovas, C.; Rojas-Garcia, R.; Insa, R. Transthyretin stabilization activity of the catechol-*O*-methyltransferase inhibitor tolcapone (SOM0226) in hereditary ATTR amyloidosis patients and asymptomatic carriers: proof-of-concept study. *Amyloid* **2019**, *26*, 74−84.

(41) Reig, N.; Ventura, S.; Salvadó, M.; Gámez, J.; Insa, R. SOM0226, a repositioned compound for the treatment of TTR amyloidosis. *Orphanet J. Rare Dis.* **2015**, *10*, P9.

(42) Verona, G.; Mangione, P. P.; Raimondi, S.; Giorgetti, S.; Faravelli, G.; Porcari, R.; Corazza, A.; Gillmore, J. D.; Hawkins, P. N.; Pepys, M. B.; Taylor, G. W.; Bellotti, V. Inhibition of the mechano-enzymatic amyloidogenesis of transthyretin: role of ligand affinity, binding cooperativity and occupancy of the inner channel. *Sci. Rep.* **2017**, *7*, 182.

(43) Russ, H.; Müller, T.; Woitalla, D.; Rahbar, A.; Hahn, J.; Kuhn, W. Detection of tolcapone in the cerebrospinal fluid of parkinsonian subjects. *Naunyn-Schmiedeberg's Arch. Pharmacol.* **1999**, *360*, 719−720.

(44) Pinheiro, F.; Varejão, N.; Esperante, S.; Santos, J.; Velázquez-Campoy, A.; Reverter, D.; Pallarès, I.; Ventura, S. Tolcapone, a potent aggregation inhibitor for the treatment of familial leptomeningeal amyloidosis. *FEBS J.* **2021**, *288*, 310−324.

(45) Goodsell, D. S.; Zardecki, C.; Di Costanzo, L.; Duarte, J. M.; Hudson, B. P.; Persikova, I.; Segura, J.; Shao, C.; Voigt, M.; Westbrook, J. D.; Young, J. Y.; Burley, S. K. RCSB Protein Data Bank: Enabling biomedical research and drug discovery. *Protein Sci.* **2020**, *29*, 52−65.

(46) Palaninathan, S. K. Nearly 200 X-ray crystal structures of transthyretin: what do they tell us about this protein and the design of drugs for TTR amyloidoses? *Curr. Med. Chem.* **2012**, *19*, 2324−2342.

(47) Hörnberg, A.; Eneqvist, T.; Olofsson, A.; Lundgren, E.; Sauer-Eriksson, A. E. A comparative analysis of 23 structures of the amyloidogenic protein transthyretin. *J. Mol. Biol.* **2000**, *302*, 649−669.

(48) Shaw, D. E.; Maragakis, P.; Lindorff-Larsen, K.; Piana, S.; Dror, R. O.; Eastwood, M. P.; Bank, J. A.; Jumper, J. M.; Salmon, J. K.; Shan, Y.; Wriggers, W. Atomic-level characterization of the structural dynamics of proteins. *Science* **2010**, *330*, 341−346.

(49) Liu, X.; Shi, D.; Zhou, S.; Liu, H.; Liu, H.; Yao, X. Molecular dynamics simulations and novel drug discovery. *Expert Opin. Drug Discov.* **2018**, *13*, 23−37.

(50) Ferreira, L. G.; Dos Santos, R. N.; Oliva, G.; Andricopulo, A. D. Molecular docking and structure-based drug design strategies. *Molecules* **2015**, *20*, 13384−13421.

(51) Yang, M.; Lei, M.; Huo, S. Why is Leu55–>Pro55 transthyretin variant the most amyloidogenic: insights from molecular dynamics simulations of transthyretin monomers. *Protein Sci.* **2003**, *12*, 1222−1231.

(52) Das, J. K.; Mall, S. S.; Bej, A.; Mukherjee, S. Conformational flexibility tunes the propensity of transthyretin to form fibrils through

non-native intermediate states. *Angew. Chem. Int. Ed. Engl.* **2014**, *53*, 12781−12784.

(53) Morris, K. F.; Geoghegan, R. M.; Palmer, E. E.; George, M., Jr.; Fang, Y. Molecular dynamics simulation study of AG10 and tafamidis binding to the Val122Ile transthyretin variant. *Biochem. Biophys. Rep.* **2020**, *21*, 100721.

(54) Yee, A. W.; Aldeghi, M.; Blakeley, M. P.; Ostermann, A.; Mas, P. J.; Moulin, M.; de Sanctis, D.; Bowler, M. W.; Mueller-Dieckmann, C.; Mitchell, E. P.; Haertlein, M.; de Groot, B. L.; Boeri Erba, E.; Forsyth, V. T. A molecular mechanism for transthyretin amyloido-genesis. *Nat. Commun.* **2019**, *10*, 925.

(55) Zhou, S.; Ge, S.; Zhang, W.; Zhang, Q.; Yuan, S.; Lo, G. V.; Dou, Y. Conventional Molecular Dynamics and Metadynamics Simulation Studies of the Binding and Unbinding Mechanism of TTR Stabilizers AG10 and Tafamidis. *ACS Chem. Neurosci.* **2020**, *11*, 3025−3035.

(56) Berk, J. L.; Suhr, O. B.; Obici, L.; Sekijima, Y.; Zeldenrust, S. R.; Yamashita, T.; Heneghan, M. A.; Gorevic, P. D.; Litchy, W. J.; Wiesman, J. F.; Nordh, E.; Corato, M.; Lozza, A.; Cortese, A.; Robinson-Papp, J.; Colton, T.; Rybin, D. V.; Bisbee, A. B.; Ando, Y.; Ikeda, S.; Seldin, D. C.; Merlini, G.; Skinner, M.; Kelly, J. W.; Dyck, P. J.; Diflunisal Trial Consortium. Repurposing diflunisal for familial amyloid polyneuropathy: a randomized clinical trial. *JAMA* **2013**, *310*, 2658−2667.

(57) Cotrina, E. Y.; Pinto, M.; Bosch, L.; Vilà, M.; Blasi, D.; Quintana, J.; Centeno, N. B.; Arsequell, G.; Planas, A.; Valencia, G. Modulation of the fibrillogenesis inhibition properties of two transthyretin ligands by halogenation. *J. Med. Chem.* **2013**, *56*, 9110−9121.

(58) Genheden, S.; Ryde, U. The MM/PBSA and MM/GBSA methods to estimate ligand-binding affinities. *Expert Opin. Drug Discov.* **2015**, *10*, 449−461.

(59) Hammarstrom, P.; Wiseman, R. L.; Powers, E. T.; Kelly, J. W. Prevention of transthyretin amyloid disease by changing protein misfolding energetics. *Science* **2003**, *299*, 713−716.

(60) Purkey, H. E.; Palaninathan, S. K.; Kent, K. C.; Smith, C.; Safe, S. H.; Sacchettini, J. C.; Kelly, J. W. Hydroxylated polychlorinated biphenyls selectively bind transthyretin in blood and inhibit amyloidogenesis: rationalizing rodent PCB toxicity. *Chem. Biol.* **2004**, *11*, 1719−1728.

(61) McCammon, M. G.; Scott, D. J.; Keetch, C. A.; Greene, L. H.; Purkey, H. E.; Petrassi, H. M.; Kelly, J. W.; Robinson, C. V. Screening transthyretin amyloid fibril inhibitors: characterization of novel multiprotein, multiligand complexes by mass spectrometry. *Structure* **2002**, *10*, 851−863.

(62) Green, N. S.; Palaninathan, S. K.; Sacchettini, J. C.; Kelly, J. W. Synthesis and characterization of potent bivalent amyloidosis inhibitors that bind prior to transthyretin tetramerization. *J. Am. Chem. Soc.* **2003**, *125*, 13404−13414.

(63) Ferguson, R. N.; Edelhoch, H.; Saroff, H. A.; Robbins, J.; Cahnmann, H. J. Negative cooperativity in the binding of thyroxine to human serum prealbumin. Preparation of tritium-labeled 8-anilino-1-naphthalenesulfonic acid. *Biochemistry* **1975**, *14*, 282−289.

(64) Jiang, X.; Buxbaum, J. N.; Kelly, J. W. The V122I cardiomyopathy variant of transthyretin increases the velocity of rate-limiting tetramer dissociation, resulting in accelerated amyloi-dosis. *Proc. Natl. Acad. Sci. U. S. A.* **2001**, *98*, 14943−14948.

(65) Hurshman, A. R.; White, J. T.; Powers, E. T.; Kelly, J. W. Transthyretin aggregation under partially denaturing conditions is a downhill polymerization. *Biochemistry* **2004**, *43*, 7365−7381.

(66) Dolado, I.; Nieto, J.; Saraiva, M. J.; Arsequell, G.; Valencia, G.; Planas, A. Kinetic assay for high-throughput screening of in vitro transthyretin amyloid fibrillogenesis inhibitors. *J. Comb. Chem.* **2005**, *7*, 246−252.

(67) Yokoyama, T.; Mizuguchi, M. Transthyretin Amyloidogenesis Inhibitors: From Discovery to Current Developments. *J. Med. Chem.* **2020**, *63*, 14228−14242.

(68) Miller, M.; Pal, A.; Albusairi, W.; Joo, H.; Pappas, B.; Haque Tuhin, M. T.; Liang, D.; Jampala, R.; Liu, F.; Khan, J.; Faaij, M.; Park, M.; Chan, W.; Graef, I.; Zamboni, R.; Kumar, N.; Fox, J.; Sinha, U.; Alhamadsheh, M. Enthalpy-Driven Stabilization of Transthyretin by AG10 Mimics a Naturally Occurring Genetic Variant That Protects from Transthyretin Amyloidosis. *J. Med. Chem.* **2018**, *61*, 7862−7876.

(69) Ekwall, B. Toxicity to HeLa cell of 205 drugs as determined by the metabolic inhibition test supplemented by microscopy. *Toxicology* **1980**, *17*, 273−295.

(70) Thabrew, M. I.; Hughes, R. D.; McFarlane, I. G. Screening of hepatoprotective plant components using a HepG2 cell cytotoxicity assay. *J. Pharm. Pharmacol.* **1997**, *49*, 1132−1135.

(71) Schoonen, W. G. E. J.; Westerink, W. M. A.; de Roos, J. A. D. M.; Debiton, E. Cytotoxic effects of 100 reference compounds on Hep G2 and HeLa cells and of 60 compounds on ECC-1 and CHO cells. I mechanistic assays on ROS, glutathione depletion and calcein uptake. *Toxicol. In Vitro* **2005**, *19*, 505−516.

(72) O'Brien, P. J.; Irwin, W.; Diaz, D.; Howard-Cofield, E.; Krejsa, C. M.; Slaughter, M. R.; Gao, B.; Kaludercic, N.; Angeline, A.; Bernardi, P.; Brain, P.; Hougham, C. High concordance of drug-induced human hepatotoxicity with in vitro cytotoxicity measured in a novel cell-based model using high content screening. *Arch. Toxicol.* **2006**, *80*, 580−604.

(73) Gonzalez, L. T.; Minsky, N. W.; Espinosa, L. E.; Aranda, R. S.; Meseguer, J. P.; Perez, P. C. In vitro assessment of hepatoprotective agents against damage induced by acetaminophen and CCl4. *BMC Complement. Altern. Med.* **2017**, *17*, 39.

(74) Olanow, C. W. Tolcapoene and hepatotoxic effects. Tasmar Advisory Panel. *Arch. Neurol.* **2000**, *57*, 263−267.

(75) Smith, K. S.; Smith, P. L.; Heady, T. N.; Trugman, J. M.; Harman, W. D.; Macdonald, T. L. In vitro metabolism of tolcapone to reactive intermediates: relevance to tolcapone liver toxicity. *Chem. Res. Toxicol.* **2003**, *16*, 123−128.

(76) Kim, J. H.; Oroz, J.; Zweckstetter, M. Structure of Monomeric Transthyretin Carrying the Clinically Important T119M Mutation. *Angew. Chem. Int. Ed. Engl.* **2016**, *55*, 16168−16171.

(77) Sebastião, M. P.; Lamzin, V.; Saraiva, M. J.; Damas, A. M. Transthyretin stability as a key factor in amyloidogenesis: X-ray analysis at atomic resolution. *J. Mol. Biol.* **2001**, *306*, 733−744.

(78) Judge, D. P.; Heitner, S. B.; Falk, R. H.; Maurer, M. S.; Shah, S. J.; Witteles, R. M.; Grogan, M.; Selby, V. N.; Jacoby, D.; Hanna, M.; Nativi-Nicolau, J.; Patel, J.; Rao, S.; Sinha, U.; Turtle, C. W.; Fox, J. C. Transthyretin Stabilization by AG10 in Symptomatic Transthyretin Amyloid Cardiomyopathy. *J. Am. Coll. Cardiol.* **2019**, *74*, 285−295.

(79) Case, D. A.; Betz, R. M.; Cerutti, D. S.; Cheatham, T. E. I.; Darden, T. A.; Duke, R. E.; Giese, T. J.; Gohlke, H.; Goetz, A. W.; Homeyer, N. *AMBER 2016*. University of California: San Francisco, 2016.

(80) Maier, J. A.; Martinez, C.; Kasavajhala, K.; Wickstrom, L.; Hauser, K. E.; Simmerling, C. ff14SB: Improving the Accuracy of Protein Side Chain and Backbone Parameters from ff99SB. *J. Chem. Theory Comput.* **2015**, *11*, 3696−3713.

(81) Wang, J.; Wolf, R. M.; Caldwell, J. W.; Kollman, P. A.; Case, D. A. Development and testing of a general amber force field. *J. Comput. Chem.* **2004**, *25*, 1157−1174.

(82) Marenich, A. V.; Cramer, C. J.; Truhlar, D. G. Universal solvation model based on solute electron density and on a continuum model of the solvent defined by the bulk dielectric constant and atomic surface tensions. *J. Phys. Chem. B* **2009**, *113*, 6378−6396.

(83) Frisch, M. J.; Trucks, G. W.; Petersson, G. A.; Nakatsuji, H. *Gaussian 09*, Revision D.01, Gaussian, Inc.: Wallingford CT, 2016.

(84) Humphrey, W.; Dalke, A.; Schulten, K. VMD: visual molecular dynamics. *J. Mol. Graph.* **1996**, *14*, 33−38.

(85) McGibbon, R. T.; Beauchamp, K. A.; Harrigan, M. P.; Klein, C.; Swails, J. M.; Hernandez, C. X.; Schwantes, C. R.; Wang, L. P.; Lane, T. J.; Pande, V. S. MDTraj: A Modern Open Library for the Analysis of Molecular Dynamics Trajectories. *Biophys. J.* **2015**, *109*, 1528−1532.

(86) Boymond, L.; Rottlander, M.; Cahiez, G.; Knochel, P. Preparation of Highly Functionalized Grignard Reagents by an

Iodine-Magnesium Exchange Reaction and its Application in Solid-Phase Synthesis. *Angew. Chem. Int. Ed. Engl.* **1998**, *37*, 1701−1703.

(87) Jorgensen, W. L.; Bollini, M.; Thakur, V. V.; Domaoal, R. A.; Spasov, K. A.; Anderson, K. S. Efficient discovery of potent anti-HIV agents targeting the Tyr181Cys variant of HIV reverse transcriptase. *J. Am. Chem. Soc.* **2011**, *133*, 15686−15696.

(88) Andrew, R. G.; Raphael, R. A. A new and total synthesis of aaptamine. *Tetrahedron* **1987**, *43*, 4803−4816.

(89) Bailey, K.; Tan, E. W. Synthesis and evaluation of bifunctional nitrocatechol inhibitors of pig liver catechol-O-methyltransferase. *Bioorg. Med. Chem.* **2005**, *13*, 5740−5749.

(90) Saiz-Poseu, J.; Alcón, I.; Alibés, R.; Busqué, F.; Faraudo, J.; Ruiz-Molina, D. Self-assembly of alkylcatechols on HOPG investigated by scanning tunneling microscopy and molecular dynamics simulations. *CrystEngComm* **2012**, *14*, 264−271.

(91) Learmonth, D. A.; Alves, P. C. Improved method for demethylation of nitro-catechol methyl ethers. *Synth. Commun.* **2002**, *32*, 641−649.

(92) Learmonth, D. A.; Vieira-Coelho, M. A.; Benes, J.; Alves, P. C.; Borges, N.; Freitas, A. P.; da Silva, P. S. Synthesis of 1-(3,4-dihydroxy-5-nitrophenyl)-2-phenyl-ethanone and derivatives as potent and long-acting peripheral inhibitors of catechol-O-methyltransferase. *J. Med. Chem.* **2002**, *45*, 685−695.

(93) Vega, S.; Abian, O.; Velazquez-Campoy, A. A unified framework based on the binding polynomial for characterizing biological systems by isothermal titration calorimetry. *Methods* **2015**, *76*, 99−115.

(94) Freire, E.; Schön, A.; Velazquez-Campoy, A. Isothermal titration calorimetry: general formalism using binding polynomials. *Methods Enzymol.* **2009**, *455*, 127−155.

(95) Ferreira, N.; Cardoso, I.; Domingues, M. R.; Vitorino, R.; Bastos, M.; Bai, G.; Saraiva, M. J.; Almeida, M. R. Binding of epigallocatechin-3-gallate to transthyretin modulates its amyloidogenicity. *FEBS Lett.* **2009**, *583*, 3569−3576.

(96) Almeida, M. R.; Macedo, B.; Cardoso, I.; Alves, I.; Valencia, G.; Arsequell, G.; Planas, A.; Saraiva, M. J. Selective binding to transthyretin and tetramer stabilization in serum from patients with familial amyloidotic polyneuropathy by an iodinated diflunisal derivative. *Biochem. J.* **2004**, *381*, 351−356.

(97) Saraiva, M. J.; Costa, P. P.; Goodman, D. S. Transthyretin (prealbumin) in familial amyloidotic polyneuropathy: genetic and functional aspects. *Adv. Neurol.* **1988**, *48*, 189−200.

(98) Juanhuix, J.; Gil-Ortiz, F.; Cuni, G.; Colldelram, C.; Nicolas, J.; Lidon, J.; Boter, E.; Ruget, C.; Ferrer, S.; Benach, J. Developments in optics and performance at BL13-XALOC, the macromolecular crystallography beamline at the ALBA synchrotron. *J. Synchrotron Radiat.* **2014**, *21*, 679−689.

(99) Kabsch, W. Integration, scaling, space-group assignment and post-refinement. *Acta Crystallogr. D Biol. Crystallogr.* **2010**, *66*, 133−144.

(100) Winn, M. D.; Ballard, C. C.; Cowtan, K. D.; Dodson, E. J.; Emsley, P.; Evans, P. R.; Keegan, R. M.; Krissinel, E. B.; Leslie, A. G.; McCoy, A.; McNicholas, S. J.; Murshudov, G. N.; Pannu, N. S.; Potterton, E. A.; Powell, H. R.; Read, R. J.; Vagin, A.; Wilson, K. S. Overview of the CCP4 suite and current developments. *Acta Crystallogr. D Biol. Crystallogr.* **2011**, *67*, 235−242.

(101) Adams, P. D.; Afonine, P. V.; Bunkoczi, G.; Chen, V. B.; Davis, I. W.; Echols, N.; Headd, J. J.; Hung, L. W.; Kapral, G. J.; Grosse-Kunstleve, R. W.; McCoy, A. J.; Moriarty, N. W.; Oeffner, R.; Read, R. J.; Richardson, D. C.; Richardson, J. S.; Terwilliger, T. C.; Zwart, P. H. PHENIX: a comprehensive Python-based system for macromolecular structure solution. *Acta Crystallogr. D Biol. Crystallogr.* **2010**, *66*, 213−221.

(102) Emsley, P.; Lohkamp, B.; Scott, W. G.; Cowtan, K. Features and development of Coot. *Acta Crystallogr. D Biol. Crystallogr.* **2010**, *66*, 486−501.

CHAPTER 3

PITB: a high affinity transthyretin aggregation inhibitor with optimal pharmacokinetic properties

PITB: a high affinity transthyretin aggregation inhibitor with optimal pharmacokinetic properties.

Francisca Pinheiro, Ramón Alibés, Maria Rosário Almeida, Filipa Bezerra, Félix Busqué, Susanna Navarro, Irantzu Pallarès, David Reverter, Adrià Sánchez-Morales, Nathalia Varejão, Adrián Velázquez-Campoy, and Salvador Ventura.

(except for the first author, the rest of authors are listed by alphabetical ordering of author surnames)

Abstract: The aggregation of wild-type transthyretin (TTR) and over 130 genetic TTR variants underlies a group of lethal disorders named TTR amyloidosis. TTR kinetic stabilizers are molecules that bind to TTR, precluding tetramer dissociation and subsequent aggregation. Recently, we developed M-23, a potent and selective kinetic stabilizer that presents one of the highest affinities reported for TTR thus far. Yet, the sub-optimal pharmacokinetic (PK) properties of M-23 might compromise its clinical use. In this context, we generated **PITB**, a M-23 derivative designed to improve its PK properties while maintaining its biological activity. **PITB** binds with high affinity to TTR, effectively inhibiting tetramer dissociation and aggregation of both the wild-type protein and the two most common disease-associated TTR variants. Importantly, **PITB** selectively binds and stabilizes TTR in plasma from patients, outperforming tolcapone, a drug that is in clinical trials for ATTR. Pharmacokinetic studies conducted on mice confirmed that, as intended, **PTIB** exhibits encouraging PK properties, including an excellent oral bioavailability, that combined with its lack of toxicity, position PTIB as a strong candidate for treating ATTR.

Introduction

Amyloid diseases constitute a group of disorders characterized by the accumulation of amyloid fibrils, highly organized structures that arise from the misfolding and subsequent aggregation of proteins[1]. Transthyretin amyloidosis (ATTR) is a group of life-threatening systemic disorders caused by the extracellular deposition of TTR amyloid fibrils[2] .

The most common forms of ATTR are related with the aggregation of TTR variants and inherited in an autosomal dominant manner[3]. To date, ATTR has been associated with more than 130 mutations[4], most of them causing peripheral neuropathy[5] (known as familial amyloid polyneuropathy - FAP) or cardiomyopathy[6] (known as familial amyloid cardiomyopathy - FAC). In some rare cases, TTR mutations can induce leptomeningeal amyloidosis, which is often accompanied by ocular involvement[7].

ATTR can also be caused by the wild-type (WT) protein. The deposition of WT-TTR, especially in the heart, underlies the development of senile systemic amyloidosis, a non-hereditary disease that mainly affects elderly man[8]. Senile systemic amyloidosis is increasingly recognized as an important cause of heart failure, affecting up to 25% of individuals over 80 years of age[9,10].

Native TTR is a 55 kDa homotetrameric protein, which is mainly synthesized in the liver, choroid plexus and retinal pigment epithelium[11,12]. Besides its well-known role as a transporter of thyroxine (T_4) and retinol binding protein-vitamin A complex, TTR is increasingly recognized as having a neuroprotective activity in the central nervous system[13].

Pathogenic mutations in TTR decrease its thermodynamic stability and/or lower the kinetic barrier for tetramer dissociation[14,15]. The latter is especially relevant as tetramer

dissociation is the rate-limiting step in TTR aggregation[16,17]. Dissociation of TTR tetramers is thought to occur through scission along the weaker dimer-dimer interface, where the T_4-binding sites are located[18]. Occupancy of the T_4-binding sites with rationally designed small molecules is known to stabilize TTR, inhibiting its dissociation and, thus, preventing ATTR onset[19,20]. The so-called kinetic stabilization strategy afforded the drug tafamidis[21], the only pharmacological treatment in the market for TTR-related polyneuropathy and cardiomyopathy[22,23]. However, the lack of complete effectiveness of tafamidis[24], together with its excessive cost[25], has prompted the development of alternative molecules to treat ATTR.

Using a drug repurposing approach, our group identified tolcapone, an FDA-approved drug for Parkinson's disease, as a potent and selective TTR stabilizer, presenting a higher *ex vivo* tetramer stabilizing activity than tafamidis[26]. The results of a Phase IIa clinical trial demonstrated that tolcapone strongly stabilizes TTR in patients with FAP, supporting its further development as a drug to treat ATTR[27,28]. Noteworthy, tolcapone can cross the blood-brain barrier, unlike tafamidis, and it was shown to bind and inhibit the aggregation of TTR variants associated with leptomeningeal amyloidosis[29].

The higher stabilizing activity of tolcapone compared to tafamidis was proposed to be related with its similar high affinity for both T_4-binding sites ($K_d = 34$ nM), which contrasts with the strong negative cooperativity displayed by tafamidis ($K_{d1} = 9.9$ nM; $K_{d2} = 260$ nM)[30]. Despite tolcapone binds better than tafamidis to the second binding cavity, tafamidis affinity for the first cavity is > 3-fold higher than the one of tolcapone. The high-resolution structure of TTR in complex with tolcapone revealed that its 4-methyl-phenyl ring does not establish any enthalpic interaction with the binding pocket,

suggesting that there was room for improvement[26]. In this context, we have designed M-23, a tolcapone derivative in which the 4-methyl-phenyl ring is replaced by a 3-fluoro-5-hydroxyphenyl ring (**Figure 1**). The TTR/M-23 crystal structure showed that, as intended, M-23 forms two additional contacts with the protein. As a result, M-23 presents an exceptional affinity for TTR ($K_d = 6.2$ nM), which is higher than the one of tolcapone and tafamidis for both binding sites. Accordingly, M-23 exhibited a higher TTR tetramer stabilizing activity *ex vivo* than any of these molecules, encouraging the development of M-23 as a therapeutic agent for ATTR[30].
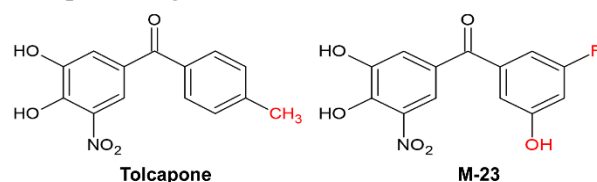

Figure 1. Chemical structures of tolcapone and M-23. The different substituents are highlighted in red.

Pharmacokinetic (PK) studies aimed at defining the ADME (absorption, distribution, metabolism, and excretion) properties of a molecule are a fundamental part of the preclinical development of any drug candidate. A poor PK profile can limit the clinical effectiveness of a drug and, indeed, it is one of the main causes of failure in drug development[31,32]. In this context, the low oral bioavailability (5.5%) and short plasma half-life (0.9 h) of M-23 can hinder its therapeutic use.

In this study, we aimed at improving the PK properties of M-23 while maintaining the specific attributes that drive its activity. Since the new contacts between the lower phenyl ring of M-23 and TTR were proposed to underlie its increased binding affinity and stabilizing activity[30], we kept this ring intact and focused on the 3,4-dihydroxy-5-nitrophenyl moiety. For tolcapone, the *in vivo* methylation of the 3-hydroxy substituent has been described to generate a long-lived metabolite with TTR

kinetic stabilizing activity[33,34]. Owing to the chemical similarity between the two compounds, we hypothesized that the methylation of M-23 could also improve its PK profile, while maintaining the specific contacts it establishes with TTR (**Figure 2**). In support of this idea, the 3-*O*-methylated form of M-23, was detected after M-23 administration in mice. Although this metabolite exhibits a higher stability than M-23, M-23 methylation is expected to be a minor metabolic route[33], thus being unlikely to contribute to the pharmacological action of M-23. On the other hand, this M-23 derivative, which we named **PITB** (Pharmacokinetically Improved TTR Binder), could become a lead compound for ATTR, provided it maintains its biological activity. In this context, we show that **PITB** binds tightly to both WT-TTR and TTR variants V30M (FAP) and V122I (FAC), stabilizing the proteins, and thus reducing their aggregation. The TTR/**PITB** crystal structures demonstrated the formation of new protein-ligand contacts at the dimer-dimer interface, identical to those of M-23, leading to a higher binding selectivity and stabilizing activity in serum from patients with FAP than tolcapone. Remarkably, PK studies in mice confirmed that **PITB** has an excellent PK profile, as intended, which together its apparent lack of toxicity, suggests that it holds the potential to become a highly potent drug to treat ATTR.
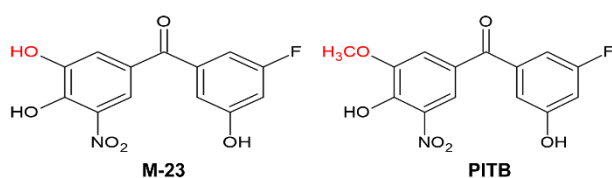

Figure 2. Chemical structures of M-23 and **PITB**. The 3-hydroxy group of M-23 and its methylated form, in **PITB**, are colored in red.

Results and discussion

PITB is formed *in vivo* from the *O*-methylation of M-23. As a first step in the preclinical development of M-23, its PK profile was evaluated using CD-1 mice. The results from this study revealed that M-23 has sub-optimal PK properties (**Figure S1** and **Table S1**), compromising its further development. Nonetheless, taking advantage of the plasma samples obtained in this study, we assessed whether the 3-*O*-methylation of M-23 occurs *in vivo* and, if that is the case, whether this metabolite presents a longer half-life ($t_{1/2}$). For that purpose, the 3-*O*-methylated form of M-23, named **PITB**, was chemically synthesized and is presence in plasma after administration of M-23 was evaluated.

The plasma concentration time curves of **PITB** after intravenous (IV) or oral (PO) administration of M-23 are shown in **Figure 3**, and the main PK parameters are summarized in **Table 1**. As expected, **PITB** was detected following the IV and PO administration of M-23. Remarkably, the peak plasma concentration (C_{max}) of **PITB** was achieved shortly after dosing, suggesting that M-23 is quickly metabolized. Moreover, the concentration of **PITB** in plasma declined at a slower rate than the one of M-23 ($t_{1/2}$ for IV = 1.5 h; $t_{1/2}$ for PO = 0.9 h), with a $t_{1/2}$ of 2.7 h (IV) and 2.8 h (PO), and it was still detected after 24 h. Overall, these results suggested Overall, these results supported our hypothesis that **PITB** might have a better PK profile *in vivo* than M-23, encouraging us to analyze its activity as a TTR kinetic stabilizer.
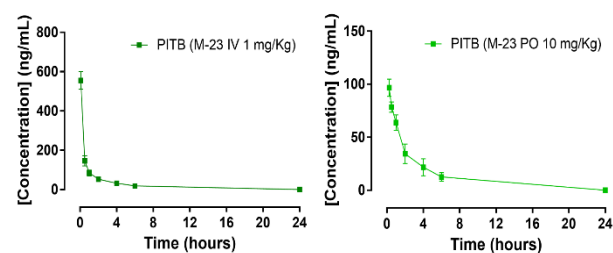

Figure 3. *In vivo* PK profiles of **PITB**, after IV (1 mg/Kg) and PO (10 mg/Kg) administration of M-23

in CD1 mice. **PITB** was detected after 24 h, in both cases. Data represents mean ± SEM (n = 3).

Table 1. PK parameters of PITB following IV (1 mg/Kg) and PO (10 mg/Kg) administration of M-23 in mice.

	PITB (M-23 IV)	PITB (M-23 PO)
T_{max} (h)	-	< 0.25
C_{max} (ng/mL)	555.3	96.7
AUC_{0-24h} (h·ng/mL)	462.1	209.1
$t_{1/2}$ (h)	2.7	2.8

PITB kinetically stabilizes TTR *in vitro*. The chemical structure of **PITB** maintains all the substituents that were proposed to be relevant for M-23 binding to TTR and its tetramer stabilizing activity[30]. Therefore, we envisioned that **PITB** could also bind to TTR and stabilize the native tetramer. To address that, we tested whether **PITB** could protect TTR from urea-induced tetramer dissociation. In urea, TTR cannot unfold before the tetramer dissociates[35]. Since monomer unfolding is much faster than tetramer dissociation, it is possible to evaluate the rate of tetramer dissociation by irreversibly linking these two processes. This can be achieved by using urea concentrations in the post-transition zone for tertiary structural changes, which assures that monomers unfold extremely fast and cannot refold[14,36]. Accordingly, WT-, V30M- and V122I-TTR (1.8 µM) were incubated in the absence or presence of **PITB** (3.6 µM) and TTR denaturation was initiated by adding urea to a final concentration of 6 M. Tryptophan (Trp) intrinsic fluorescence was measured each 24 h and used to calculate the fraction of unfolded protein (**Figure 4A**). The effect of **PITB** was compared to the one of tolcapone.

In the presence of equimolar levels of **PITB** relative to T4-binding sites, only 5 to 21% of TTR tetramers dissociate after a 96-h incubation period. Moreover, the incubation with **PITB** significantly decreased the rate of WT-, V30M- and V122I-TTR tetramer dissociation. Importantly, **PITB** stabilizing activity was similar to the one of tolcapone for each of the analyzed proteins.
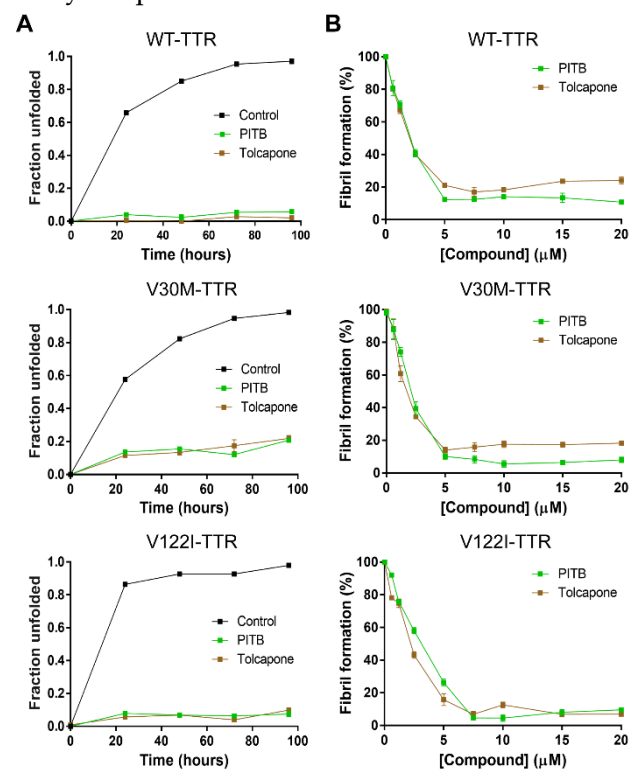

Figure 4. PITB effect over the kinetic stability and aggregation of WT-, V30M- and V122I-TTR. (A) Unfolding time course at 6 M urea in the absence or presence of two molar equivalents of **PITB** and tolcapone, as monitored by Trp fluorescence. The values correspond to mean ± SEM (n = 3). (B) Percentage of TTR aggregation as a function of **PITB** and tolcapone concentration as measured by turbidity at 340 nm. The values were normalized to 100%, which was assigned to the turbidity of samples aggregated in the absence of any compound. Data represents mean ± SEM (n = 3).

PITB protects TTR from aggregation *in vitro*. After confirming that **PITB** can prevent tetramer dissociation, we assessed whether this inhibits TTR aggregation. For that purpose, TTR samples were mixed with increasing concentrations of **PITB** and aggregation was induced by acidification[36,37]. After an incubation of 72 h at 37 °C, aggregation was quantified by

recording turbidity at 340 nm and normalized to the maximum turbidity value, which was assigned to the TTR samples incubated in the absence of compound (**Figure 4B**).

According to the obtained results, **PITB** is highly effective at inhibiting the aggregation of WT-TTR and, most importantly, of V30M- and V122I-TTR, the two most clinically relevant TTR variants. In all cases, there was a decrease in TTR aggregation >60% at a 1:1 TTR/**PITB** ratio and ≥87.5% when **PITB** concentration is higher than or equal to the one of T_4-binding sites. Remarkably, **PITB** performed better than tolcapone, inhibiting up to 89.2% and 92% the aggregation of WT-TTR and V30M-TTR, respectively. In the case of V122I-TTR, **PITB** equaled the potency of tolcapone, reaching up to 90% inhibition at 20 μM.

PITB binds with high affinity to TTR. The high stabilization and anti-aggregation effect of **PITB** on WT-, V30M- and V122I-TTR suggests that it binds with high affinity to these proteins. To determine the binding parameters of **PITB** to TTR, we used isothermal titration calorimetry (ITC) (**Figure 5**). The K_d values and thermodynamic parameters shown in **Table 2** were obtained by fitting the ITC data to an independent binding sites model.

Our data indicated that **PITB** binds with high affinity to both WT and TTR variants V30M and V112I. Noteworthy, **PITB** exhibited a higher affinity than tolcapone for WT- and V30M-TTR. In resemblance to tolcapone, the binding of **PITB** to TTR was entirely enthalpically driven ($\Delta H < 0$; $-T\Delta S > 0$), suggesting the establishment of noncovalent interactions (e.g., hydrogen bonds or ionic interactions) at the binding interface.

PITB stabilizes the weaker TTR dimer-dimer interface. To elucidate the interactions that drive the binding of **PITB** to WT-TTR and TTR variants V30M and V122I, we determined the X-ray crystal structures of TTR:**PITB** complexes at 1.85 (WT-TTR:**PITB**), 1.20 (V30M-TTR:**PITB**) and 1.42 (V122I-TTR:**PITB**) Å resolution (**Figure 6**). Additionally, we obtained, for the first time, the cocrystal structure of tolcapone with V30M-TTR, at a resolution of 1.57 Å.

As expected, **PITB** binds to TTR T_4-binding sites at the weaker AB/CD dimer-dimer interface. Because of the two-fold symmetry axis that runs through the binding pockets, two symmetry-related binding conformations appear for **PITB**. In all structures, **PITB** was found in the forward binding mode, with the 3-methoxy-4-hydroxy-5-nitrophenyl pointing to the outer binding cavity, where it makes hydrophobic interactions with the residues from halogen binding pockets (HBPs) 2/2' and 1/1' (**Figure 6**). In this orientation, the 4-hydroxy group of **PITB** forms hydrogen bonds with the K15/K15' residues of TTR, which in turn stabilize their electrostatic interactions with E54/E54'. These interactions by K15 are also observed in TTR:tolcapone complexes and were proposed to close the binding cavity, protecting the protein-ligand complex from the solvent[26].

In the WT-TTR:**PITB** structure, the hydroxyl side chain of T119 is not at a hydrogen bonding distance from the central carbonyl group, contrarily to what is observed for tolcapone (**Figure 6A**). This fact can be explained by the different conformation adopted by the side chain of T119 in the first structure (**Figure S2A**).

Table 2. Thermodynamic parameters for the interaction of PITB with WT-, V30M- and V122I-TTR determined by ITC.

	PITB				Tolcapone			
	Kd (nM)	ΔG (kcal/mol)	ΔH (kcal/mol)	-TΔS (kcal/mol)	Kd (nM)	ΔG (kcal/mol)	ΔH (kcal/mol)	-TΔS (kcal/mol)
WT-TTR	26.4	-10.3	-11.6	1.3	33.7	-10.2	-11.2	1.0
V30M-TTR	45.3	-10.0	-11.1	1.1	63.6	-9.8	-11.5	1.6
V122I-TTR	61.2	-9.8	-13.2	3.3	38.8	-10.1	-14.9	4.8
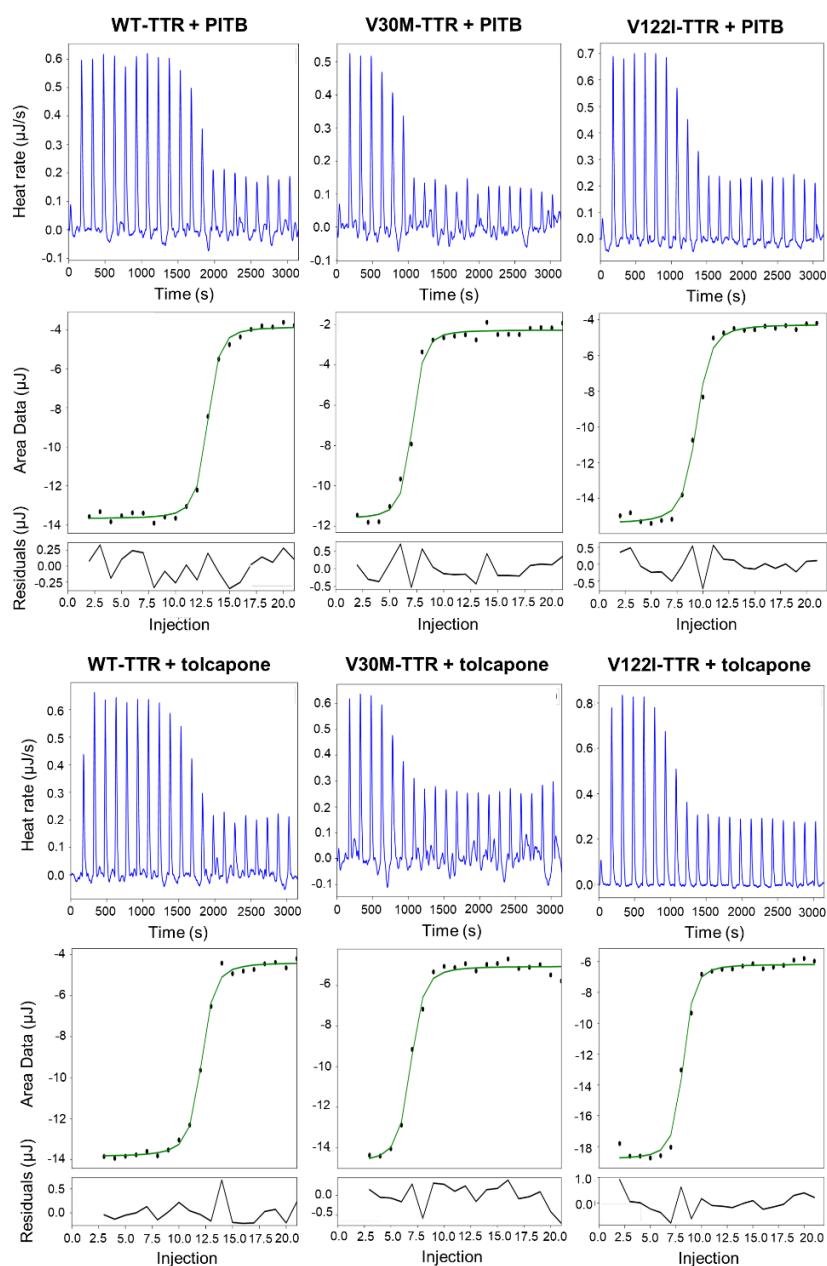
Figure 5. Interaction of **PITB** with WT-, V30M- and V122I-TTR. The top panels represent the raw data, with positive peaks assigned to exothermic reactions. The lower panels represent the integrated heat changes as a function of the number of injections, wherein the solid line corresponds to the fitting done to a model assuming

independent binding site. Residuals were calculated by subtracting the experimental value to the value obtained in the fitting.

Interestingly, for the same reason, no hydrogen bond is seen between the carbonyl group of both **PITB** and tolcapone, and the side chain of T119, when bound to V30M- and V122I-TTR (**Figure 6B,C and Figure S2B).** On the other hand, **PITB** establishes important interactions in the inner binding cavity, which are not present in the TTR:tolcapone structures. In particular, the fluorine atom of the 3-fluoro-5-hydroxyphenyl ring interacts with A108, while the hydroxy group forms hydrogen bonds with the S117 residues from adjacent subunits. These additional contacts by **PITB** might justify its increased affinity for WT- and V30M-TTR in comparison to tolcapone.

Remarkably, the hydrogen bonds between **PITB** and S117 help to bridge the dimers at the weaker dimer-dimer interface, increasing the kinetic barrier for tetramer dissociation[38,39]. Additionally, in one of the S117 side-chain conformations, a short hydrogen bond can be formed between the S117 residues from adjacent monomers in the same dimer (**Figure S3**). This inter-subunit interaction was also observed in the structure of the kinetically stabilized TTR variant T119M[40] and could further contribute to the overall stabilizing effect of **PITB**.

PITB selectively binds and stabilizes V30M-TTR in human plasma. To stabilize the native tetrameric TTR and thus prevent its aggregation in patients with ATTR, **PITB** must selectively bind to TTR in plasma over all other plasma proteins. To test this, we examined the capacity of **PITB** to compete with T_4 for TTR binding in human plasma from patients carrying V30M-TTR. Tolcapone was included as a control. In this assay, plasma samples were incubated with [^{125}I]-T_4, in the absence or presence of compounds, and subjected to native gel electrophoresis[41]. T_4-binding proteins were detected by autoradiography, as shown in **Figure 7A**. In the absence of any compound, three main plasma proteins bound to T_4: the main binding protein was T_4-binding globulin (TBG), followed by albumin (ALB) and TTR. The samples incubated with tolcapone and, especially, **PITB**, presented weaker T_4-TTR bands, suggesting that these molecules can preclude the binding of T_4 to TTR in human plasma. Densitometry analysis of the bands revealed that **PITB** is a more potent competitor than tolcapone, presenting an inhibition of T_4 binding to plasmatic TTR of $94.5 \pm 2.8\%$ (**Figure 7B**).

Once we confirmed that **PITB** selectively binds TTR in human plasma, we studied its effect on the stability of TTR in the plasma of FAP V30M patients. The ability of **PITB** to prevent tetramer dissociation was monitored *ex vivo* by isoelectric focusing (IEF) under partially dissociating conditions (4 M urea)[42]. Tolcapone was also used as a control. Briefly, plasma samples were incubated with or without compound overnight at 4 °C and, after IEF, the bands were compared. Under the conditions used, it is possible to distinguish two main sets of bands, one corresponding to monomers (normal and oxidized forms), and one including several bands of lower pI that represent different forms of tetramers. The tetramer/monomer ratios were used to calculate the degree of tetramer stabilization in each sample. The results showed that **PITB** has a higher stabilizing activity than tolcapone, with an increase in tetramer stability of $17.4 \pm 5.1\%$ (versus $4.9 \pm 2.3\%$ for tolcapone). The increased binding selectivity and stabilization effect of **PITB** in human plasma, in comparison with tolcapone, is likely due to the higher number of interactions it establishes with the protein, as observed in the crystal structure.
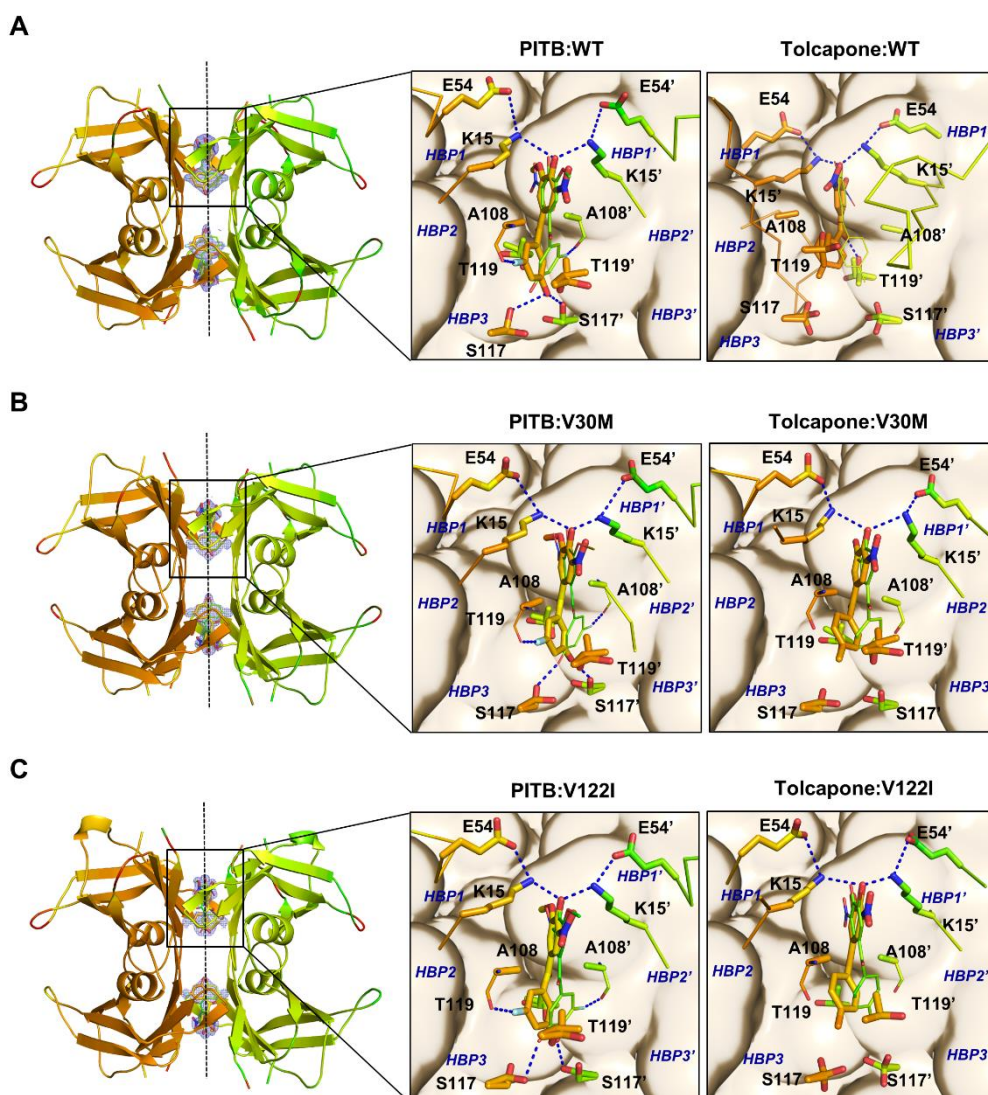
Figure 6. Crystal structures of WT-TTR (A), V30M-TTR (B) and V122I-TTR (C) in complex with **PITB**. On the left, the global view of TTR bound to **PITB** (cartoon representation). The dashed line corresponds to the twofold symmetry axis of the dimer-dimer interface. The insets show the detailed view of one the TTR binding sites for **PITB** and for tolcapone. **PITB**, tolcapone and some of the TTR interacting residues are shown as sticks. The dashed blue lines show key interactions between each ligand and TTR. The structural data for Tolcapone:WT and Tolcapone:V122I was obtained from PDB files 4D7B and 5A6I, respectively.

PITB displays no toxicity for human cells.
Compound toxicity is an important concern in the development of new drugs. Therefore, our next step was to examine the potential chemical toxicity of **PITB** for human cervical carcinoma (HeLa) and human hepatoblastoma (HepG2) cells. These cell lines have been extensively studied and used in *in vitro* cytotoxicity studies[43-45]. The HepG2 cell line, in particular, is the most commonly used for detecting drug-induced hepatotoxicity[46,47]. Liver injury is one of

the major causes of drug withdrawal[48] and, indeed, many medications require to monitor liver function during treatment, as it is the case of tolcapone[49].

In this work, HeLa and HepG2 cells were incubated with increasing concentrations of **PITB** or tolcapone and cell viability was assessed after 72 h using PrestoBlue®. For both cell lines, no significant toxicity was observed upon exposure to PITB, even at the high 100 µM concentration (**Figure 8**). Importantly, **PITB** was

substantially less toxic than tolcapone at concentrations higher than 10 µM, suggesting that **PITB** could be safer than tolcapone.
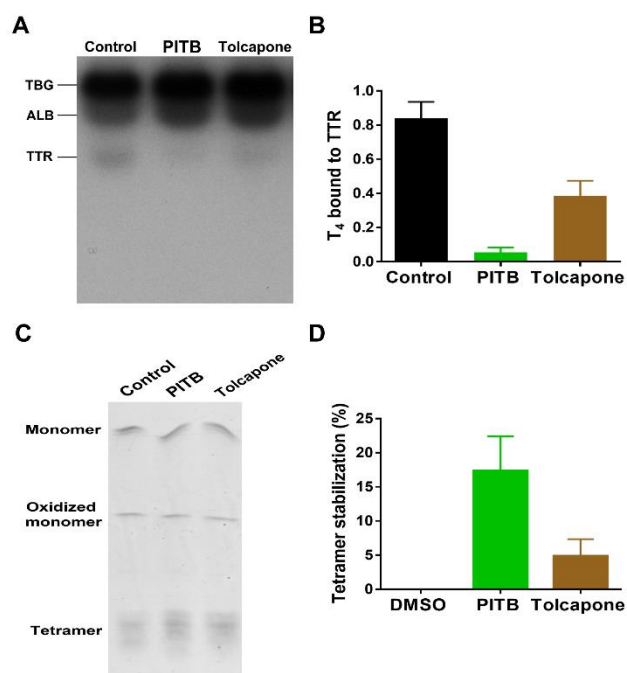

Figure 7. PITB binding and stabilizing activity in human plasma from patients with FAP. (A) Representative native gel electrophoresis of plasma samples of V30M-TTR carriers incubated with [^{125}I]-T$_4$, in the absence or presence of compounds. A plasma sample incubated with the same amount of DMSO was used as a negative control. The main T$_4$-binding proteins are indicated. (B) Fraction of [^{125}I]-T$_4$ bound to TTR determined by densitometry analysis of the native gel electrophoresis. The values were normalized to the control and correspond to mean ± SEM (n = 3). (C) IEF analysis under partially denaturing conditions of plasma samples from V30M carriers treated with **PITB**, tolcapone, or DMSO (as control). The distinct molecular species observed in the IEF gel are depicted. This gel is representative of others run in parallel. (D) Percentage of TTR tetramer stabilization calculated from the densitometry analysis of the IEF gels. Error bars represent SEM of mean values (n = 3).
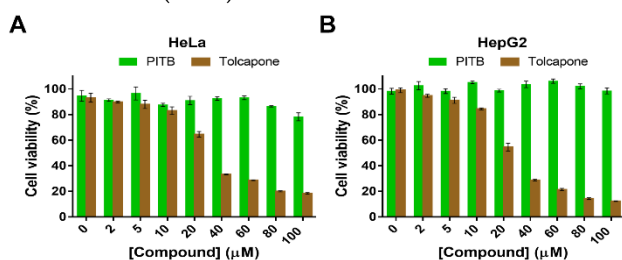

Figure 8. Toxicity of **PITB** to two human cell lines. Cell viability of HeLa (A) and HepG2 (B) cells after 72 h exposure to M-22 or tolcapone as assessed by the PrestoBlue assay. Data represents mean ± SEM (n = 3).

PK studies in mice confirm the bioavailability and stability of PITB. Altogether, the previous results support the potential of **PITB** to become a drug for the treatment of both hereditary and non-hereditary forms of ATTR. To further investigate this option, the PK parameters of **PITB** were determined from studies conducted in CD-1 mice. The PK profiles for **PITB** following IV (1 mg/Kg) or PO (10 mg/Kg) administration of the compound are shown in **Figure 9A**, and the calculated parameters are depicted in **Table 3**. Following the IV injection of **PITB**, a C$_{max}$ value of 4043.3 ng/mL and a t$_{1/2}$ of 3.5 h were determined. Additionally, our results demonstrated that **PITB** is rapidly absorbed after PO administration, reaching a C$_{max}$ of 4176.7 ng/mL, at 0.5 h (T$_{max}$). While the concentration achieved by the oral route was very similar to that observed for the IV infusion, the elimination of **PITB** was considerably slower in this case, with a t$_{1/2}$ of 10.1 h. In both cases, the concentration of **PITB** in plasma was still quantifiable 24 h post-dosing. The area under the plasma concentration-time curve (AUC) values were 3162.3 h·ng/mL and 26895.9 h·ng/ml for the IV (1 mg/Kg) and PO (10 mg/Kg) administration of **PITB**, respectively. This yields an excellent oral bioavailability (%F) for **PITB** of around 85.1%. Remarkably, the bioavailability of **PITB** is significantly higher than the one reported for AG10 (26.84%)[39], a TTR kinetic stabilizer that is under clinical trials for ATTR-related cardiomyopathy.
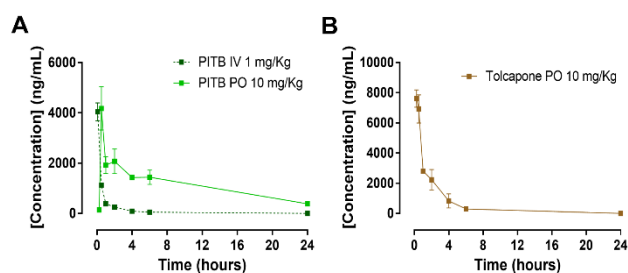
Figure 9. Plasma concentration-time profiles for **PITB** and tolcapone after administration in CD-1 mice. (A) PK profiles for **PITB** following IV (1 mg/Kg) and PO (10 mg/Kg) administration. Data represents mean ± SEM (n = 3). (B) Mean plasmatic levels of tolcapone (± SEM) over 24 h after PO administration (10 mg/Kg) (n = 3). Noteworthy, no tolcapone was detected after 24 h.

Table 3. PK parameters of PITB and tolcapone following administration in CD-1 mice.

	PITB		Tolcapone
	IV	PO	PO
	(1 mg/Kg)	(10 mg/Kg)	(10 mg/Kg)
T_{max} (h)	-	0.5	< 0.25
C_{max} (ng/mL)	4043.3	4176.7	7616.7
AUC_{0-24h} (h·ng/mL)	3162.3	26895.9	11927.5
$t_{1/2}$ (h)	3.5	10.1	1.4
k_e (h^{-1})	0.201	0.069	0.500
Vd (L/Kg)	1.572	4.482	1.600
Cl (L/h·Kg)	0.315	0.308	0.800
F (%)	-	85.1	-

For comparative purposes, the PK properties of tolcapone after PO administration (10 mg/Kg) in CD-1 mice were also determined (**Figure 9B and Table 3**). Tolcapone was chosen as a reference because it is an FDA-approved drug and, moreover, it has already demonstrated effectiveness in a phase IIa clinical trial for ATTR[27,28]. Following administration of equimolar doses of **PITB** and tolcapone, the last was more readily absorbed, achieving a C_{max} of 7616.7 ng/mL in less than 15 min (T_{max}). On the other hand, the elimination of **PITB** was significantly slower than the one of tolcapone ($t_{1/2}$ for **PITB** = 10.1 h; $t_{1/2}$ for tolcapone = 1.4 h), which is due to its higher volume of distribution

(Vd) and decreased clearance (Cl). In agreement, no tolcapone was detected in plasma after 24 h, contrarily to **PITB**. As a result, the exposure to **PITB** was substantially greater than the one of tolcapone (AUC_{0-24} for **PITB** = 26895.9 h·ng/mL; AUC_{0-24} for tolcapone = 11927.5 h·ng/mL).

Overall, **PITB** seems to have better PK properties than tolcapone, which might be translated into an improved pharmacologic activity *in vivo*. Moreover, preliminary data suggests that **PITB** can cross the BBB, as tolcapone, although further analysis are needed to confirm this observation.

Conclusions

In the present study we have developed **PITB**, a M-23 derivative with optimal PK properties. **PITB** was designed based on the known existence of 3-*O*-methyl tolcapone, a minor metabolite of tolcapone with an increased stability in plasma, and that acts as a TTR stabilizer[33,34]. Since methylation is a common pathway in the metabolism of catechol-containing compounds[50], we hypothesized that M-23 could have a similar fate. Accordingly, we detected the 3-*O*-methylated form of M-23 (**PITB**) in plasma from mice following administration of M-23. Most importantly, **PITB** exhibited a longer half-life in plasma than M-23, encouraging us to evaluate its potential as TTR kinetic stabilizer. Here, we show that **PITB** strongly binds to the T_4-binding sites of WT-TTR and the two most clinically relevant TTR variants V30M and V122I. As a result, **PITB** greatly increases the stability of TTR tetramers *in vitro*, inhibiting their aggregation. Remarkably, **PITB** presents a higher binding selectivity and stabilization potency in plasma samples obtained from patients with FAP than tolcapone. The high-resolution crystal structures of TTR:**PITB** complexes confirmed that, as intended, **PITB** keeps the interactions established by M-23, which might underlie its increased efficacy in plasma relative to

92

tolcapone. Additionally, cytotoxicity assays suggest a low risk associated with **PITB** administration. Most importantly, the PK evaluation of **PITB** showed that it has a remarkable PK profile in mice, with a 10.1 h half-life and 85.1% oral bioavailability. Surprisingly, **PITB** presents better PK parameters than tolcapone, a drug that is approved by the FDA. All in all, the work presented here highlights the enormous potential of **PITB** as a therapeutic agent for ATTR, strongly supporting its further preclinical and clinical development.

Experimental section

Synthesis procedure. Tolcapone was purchased from Fisher. **PITB** (**63e**) was chemically synthesized as shown in the following scheme. The detailed synthesis procedure is described below.
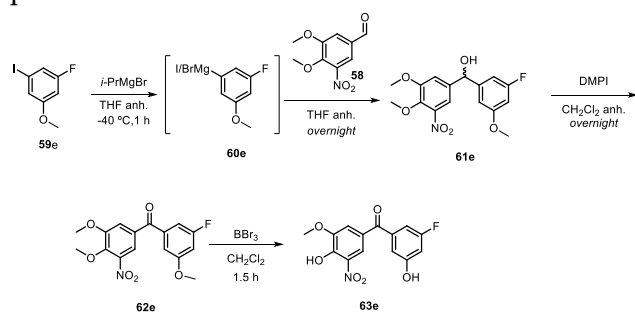
3,4-dimethoxy-5-nitrobenzaldehyde, 58. To a solution of commercially available 5-nitrovanillin, **57** (500 mg, 2.50 mmol), NaOH 3 M (1.7 ml, 5.00 mmol) and TBAB (82 mg, 0.25 mmol) in a mixture of CH_2Cl_2/H_2O (1:1, 10 mL), dimethyl sulphate (1.3 mL, 13.40 mmol) was added slowly under a N_2 atmosphere. The final mixture was stirred vigorously for 24 h (TLC, hexane/EtOAc, 3:2). The aqueous layer was extracted with CH_2Cl_2 (3 x 10 mL). Then, the organic layer was concentrated under vacuum and washed with 20 mL of water, 20 mL of ammonia 2 M solution and 20 mL of 2 M NaOH solution to remove unreacted phenol and dimethyl sulphate. The organic layer was dried with anhydrous Na_2SO_4 and concentrated under

vacuum. Purification by flash column chromatography (hexanes/EtOAc, 3:2) afforded aldehyde **58** (498 mg, 2.36 mmol, 93% yield) as a pale brown solid. ^{1}H NMR (250 MHz, CDCl$_3$): δ 9.91 (s, 1H, -COH), 7.83 (d, $J_{6,2}$ = 1.8 Hz, 1H, H-6), 7.62 (d, $J_{2,6}$ = 1.8 Hz, 1H, H-2), 4.08 (s, 3H, CH_3O-4), 4.00 (s, 3H, CH_3O-3).

1-fluoro-3-iodo-5-methoxybenzene. To a solution of commercially available 3-fluoro-5-methoxyaniline **66** (2.38 g, 16.86 mmol) in H_2O (7.7 mL) was added concentrated HCl (7.7 mL) at 0 °C. After stirring for 30 min, a solution of 1.8 M NaNO$_2$ in H_2O (11.00 mL, 20.30 mmol) was added dropwise. Then, the resulting mixture was stirred for 15 min at 0 °C and then an ice cold 3 M solution of KI (11.00 mL, 33.72 mmol) was added slowly. The ice bath was removed, and the reaction mixture was heated at reflux temperature for 1 h. The reaction mixture was allowed to cool to rt and extracted with EtOAc (3 x 50 mL). The organic layer was washed with brine (2 x 100 mL), dried over anhydrous Na_2SO_4 and concentrated under vacuum. The residue was purified by flash column chromatography (hexanes, 100%) to obtain **59e** (3.38 g, 13.40 mmol, 79% yield) as a colourless oil. ^{1}H NMR (400 MHz, CDCl$_3$): δ 7.05 - 7.02 (m, 2H, H-2, H-4), 6.58 (dt, $J_{6,F}$ = 10.6 Hz, $J_{6,4}$ = 2.3 Hz, 1H, H-6), 3.78 (s, 3H, CH$_3$O-5). ^{19}F NMR (250 MHz, CDCl$_3$): δ -110.76 (s, F-3). ^{13}C NMR (100.6 MHz, CDCl$_3$): δ 163.2 (d, $J_{1,F}$ = 250.0 Hz, C$_1$), 161.4 (d, $J_{5,F}$ = 11.1 Hz, C$_5$), 119.5 (d, $J_{4,F}$ = 3.2 Hz, C$_4$), 117.4 (d, $J_{2,F}$ = 24.0 Hz, C$_2$), 102.0 (d, $J_{6,F}$ = 25.2 Hz, C$_6$), 93.3 (d, $J_{3,F}$ = 11.0 Hz, C$_3$), 55.9 (CH$_3$O-5). IR (ATR): ν 1738, 1601, 1578, 1423, 1277, 1143, cm^{-1}.

(3,4-dimethoxy-5-nitrophenyl)(3-fluoro-5-methoxyphenyl)methanol, 61e. To a solution of **59e** (2.50 g, 9.93 mmol) in dry THF (25 mL) at -40 °C, *i*PrMgBr (1 M in THF, 15.9 mL, 11.92 mmol) was added dropwise in 5 min under a N_2 atmosphere and the reaction mixture was stirred at the same

temperature for 1 h. Then, a solution of 3,4-dimethoxy-5-nitrobenzaldehyde, **58**, (2.53 g, 12.00 mmol) in dry THF (20 mL) was added. The final mixture was warmed to rt and stirred overnight. The reaction was quenched by slow addition of brine (20 mL) and the aqueous layer was extracted with EtOAc (3 x 35 mL). All organic layers were collected, dried over anhydrous Na_2SO_4 and concentrated under vacuum obtaining a yellow oil that was purified by flash column chromatography (hexanes/EtOAc, 5:1) to furnish **61e** (1.68 mg, 4.98 mmol, 50% yield) as a white solid. Mp = 100 - 101 °C (from $CHCl_3$). ^1H NMR (400 MHz, $CDCl_3$): δ 7.28 (dd, $J_{6I,2I}$ = 2.0 Hz, $J_{6I,1}$ = 0.6 Hz, 1H, H-6^I), 7.11 (d, $J_{2I,6I}$ = 2.0 Hz, 1H, H-2^I), 6.69 (m, H-6^{II}), 6.65 (br dm, $J_{2II,F}$ = 9.1 Hz, $J_{2II,4II}$ = $J_{2II,6II}$ = 2.0 Hz, 1H, H-2^{II}), 6.53 (dt, $J_{4II,F}$ = 10.5 Hz, $J_{4II,2II}$ = $J_{4II,2II}$ = 2.3 Hz, 1H, H-4^{II}), 5.70 (s, 1H, H-1), 3.94 (s, 3H, CH$_3$O-4^I), 3.88 (s, 3H, CH$_3$O-3^I), 3.78 (s, 3H, CH$_3$O-5^{II}), 2.72 (br s, 1H, -OH). ^{19}F NMR (250 MHz, $CDCl_3$): δ -110.76 (s, F-3^{II}). ^{13}C NMR (100.6 MHz, $CDCl_3$): δ 163.9 (d, $J_{3II,F}$ = 246.3 Hz, C$_3$II), 161.3 (d, $J_{5II,F}$ = 11.2 Hz, C$_5$II), 154.3 (C$_3$I), 145.8 (d, $J_{1II,F}$ = 8.8 Hz, C$_1$II), 144.6 (C$_5$I), 142.2 (C$_4$I), 139.5 (C$_1$I), 114.0 (C$_2$I), 113.8 (C$_6$I), 108.4 (d, $J_{6II,F}$ = 3.8 Hz, C$_6$II), 105.7 (d, $J_{2II,F}$ = 22.7 Hz, C$_2$II), 101.1 (d, $J_{4II,F}$ = 25.4 Hz, C$_4$II), 74.8 (d, $J_{1,F}$ =2.3 Hz, C$_1$), 62.1 (CH$_3$O-4^I), 56.6 (CH$_3$O-3^I), 55.7 (CH$_3$O-5^{II}). IR (ATR): ν 3444, 2955, 2837, 1594, 1530, 1453, 1344, 1133 cm^{-1}. HRMS (ESI-): calcd. for [C$_{16}$H$_{16}$FNO$_6$-H$_2$O]$^-$: 320.0934; found [M-H$_2$O]$^-$: 320.0936. DEPT135 and $^1H/^{13}C$ correlation were recorded.

*(3,4-dimethoxy-5-nitrophenyl)(3-fluoro-5-methoxyphenyl)methanone, **62**.* To a solution of alcohol **61e** (784 mg, 2.32 mmol) in dry CH$_2$Cl$_2$ (50 mL) under a nitrogen atmosphere, a solution of DMPI (1.72 g, 3.49 mmol) in dry CH$_2$Cl$_2$ was added dropwise and the mixture was stirred overnight at rt. The reaction was quenched with

the addition of 1.1 mL of a prepared solution of Na$_2$S$_2$O$_3$ (1.70 g) in a saturated aqueous solution of NaHCO$_3$ (9 mL) and the mixture was stirred for 15 min. The aqueous phase was extracted with CH$_2$Cl$_2$ (3 x 20 mL) and the combined organic extracts were dried over anhydrous Na$_2$SO$_4$ and concentrated under vacuum. Purification by flash column chromatography (hexanes/EtOAc, 5:2) of the resulting residue provided the ketone **62e** as a white solid (746 mg, 2.23 mmol, 96% yield). Mp = 95 °C (from CHCl$_3$). ^1H NMR (400 MHz, CDCl$_3$): δ 7.69 (d, $J_{6I,2I}$ = 2.0 Hz, 1H, H-6^I), 7.63 (d, $J_{2I,6I}$ = 2.0 Hz, 1H, H-2^I), 7.08 (m, H-6^{II}), 7.02 (ddd, $J_{2II,F}$ = 8.4 Hz, $J_{2II,4II}$ = 2.3 Hz, $J_{2II,6II}$ = 1.4 Hz, 1H, H-2^{II}), 6.86 (dt, $J_{4II,F}$ = 10.2 Hz, $J_{4II,2II}$ = $J_{4II,2II}$ = 2.3 Hz, 1H, H-4^{II}), 4.07 (s, 3H, CH$_3$O-4^I), 3.99 (s, 3H, CH$_3$O-3^I), 3.85 (s, 3H, CH$_3$O-5^{II}). ^{19}F NMR (250 MHz, CDCl$_3$): δ -110.1 (s, F-3^{II}). ^{13}C NMR (90.5 MHz, CDCl$_3$): δ 192.4 (d, $J_{1,F}$ =2.8 Hz, C$_1$), 163.3 (d, $J_{3II,F}$ = 248.3 Hz, C$_3$II), 161.1 (d, $J_{5II,F}$ = 10.8 Hz, C$_5$II), 154.4 (C$_3$I), 146.7 (C$_4$I), 144.2 (C$_5$I), 139.0 (d, $J_{1II,F}$ = 8.4 Hz, C$_1$II), 132.0 (C$_1$I), 118.7 (C$_6$I), 116.3 (C$_2$I), 111.2 (d, $J_{6II,F}$ = 2.8 Hz, C$_6$II), 109.1 (d, $J_{2II,F}$ = 23.1 Hz, C$_2$II), 106.4 (d, $J_{4II,F}$ = 25.0 Hz, C$_4$II), 62.4 (CH$_3$O-4^I), 56.8 (CH$_3$O-3^I), 56.1 (CH$_3$O-5^{II}). IR (ATR): ν 2921, 2843, 1651, 1597, 1530, 1429, 1318, 1146 cm^{-1}. HRMS (ESI+): calcd. for [C$_{16}$H$_{14}$FNO$_6$+Na]$^+$: 358.0703; found [M+Na]$^+$: 358.0705. DEPT135 and $^1H/^{13}C$ correlations were recorded.

*(3-fluoro-5-hydroxyphenyl)(4-hydroxy-3-methoxy-5-nitrophenyl)methanone, **63e**.* To a solution of **62e** (199 mg, 0.56 mmol) in CH$_2$Cl$_2$ (3.0 mL) was added dropwise BBr$_3$ (1 M in CH$_2$Cl$_2$, 4.50 mL, 4.50 mmol) at -10 °C. The reaction was allowed to proceed at rt for 1.5 h (TLC, CH$_2$Cl$_2$/MeOH, 10:1). The reaction was quenched carefully with water (4 mL) and the resulting aqueous layer was extracted with EtOAc (2 x 20 mL). The organic extracts were dried with Na$_2$SO$_4$ and the solvent removed

under vacuum to give the crude product. Purification by flash column chromatography (CH$_2$Cl$_2$/MeOH, 20:1) afforded **63e** (**PITB**) as a yellow solid (139 mg, 0.45 mmol, 81% yield). Mp = 155 - 156 °C (from CHCl$_3$). ^{1}H NMR (250 MHz, CDCl$_3$): δ 8.11 (d, $J_{6I,2I}$ = 1.9 Hz, 1H, H-6'), 7.69 (d, $J_{2I,6I}$ = 1.9 Hz, 1H, H-2^I), 7.04 (m, H-6^{II}), 6.99 (ddd, $J_{2II,F}$ = 8.4 Hz, $J_{2II,4II}$ = 2.3 Hz , $J_{2II,6II}$ = 1.4 Hz, 1H, H-2^{II}), 6.85 (dt, $J_{4II,F}$ = 9.4 Hz, $J_{4II,2II}$ = $J_{4II,2II}$ = 2.3 Hz, 1H, H-4^{II}), 4.02 (s, 3H, CH$_3$O-3^I). ^{19}F NMR (250 MHz, CDCl$_3$): δ -110.01 (F-3^{II}). ^{13}C NMR (90.5 MHz, CDCl$_3$): δ 192.3 (C$_1$), 163.4 (d, $J_{3II,F}$ = 248.5 Hz, C$_3$II), 157.5 (d, $J_{5II,F}$ = 11.8 Hz, C$_5$II), 150.7 (C$_3$I), 150.2 (C$_4$I), 139.4 (d, $J_{1II,F}$ = 8.1 Hz, C$_1$II), 132.9 (C$_5$I), 127.8 (C$_1$I), 119.7 (C$_6$I), 117.2 (C$_2$I), 112.6 (d, $J_{6II,F}$ = 2.7 Hz, C$_6$II), 109.3 (d, $J_{2II,F}$ = 23.1 Hz, C$_2$II), 107.8 (d, $J_{4II,F}$ = 25.0 Hz, C$_4$II), 57.2 (CH$_3$O-3^I). IR (ATR): ν 3095, 2922, 2852, 1738, 1650, 1546, 1440, 1330, 1242, 1134 cm^{-1}. HRMS (ESI-): calcd. for [C$_{14}$H$_{10}$FNO$_6$-H]$^-$: 306.0414; found [M-H]$^-$: 306.0424.

Recombinant TTR expression and purification. The cDNA encoding for WT-TTR was cloned into a pET28a vector (Novagen). The vectors encoding for V30M- and V122I-TTR were prepared by classical site-directed mutagenesis protocols using the WT-TTR vector as a template. WT-, V30M- and V122I-TTR were expressed in *Escherichia coli* BL21 (DE3) and purified as previously described[29]. The purest fractions eluting from the gel filtration chromatography were combined and kept at -20 °C until use. The concentration of protein was determined spectrophotometrically at 280 nm, using a molar extinction coefficient of 77 600 M^{-1} cm^{-1}.

Urea-induced TTR tetramer dissociation measured by Trp fluorescence. Samples containing TTR (1.8 μM in PBS) were incubated with 3.6 μM **PITB** or tolcapone for 30 min at RT, and 6 M urea was added to trigger denaturation.

Since the stock solutions of both compounds were prepared in DMSO, a control sample containing the same percentage of DMSO instead of compound was prepared. Trp fluorescence spectra were recorded over time (λ$_{ex}$ = 295 nm; λ$_{em}$ = 310-410 nm) using an FP-8200 Spectrofluorometer (Jasco). Upon denaturation, the Trp residues become more exposed to the polar solvent, which is accompanied by a change in the emission maximum from ~ 335 to ~ 355 nm. The fluorescence intensity ratio 355/335 nm was calculated for each time point and the values normalized from minimum (folded state) to maximum (unfolded state), with the maximum being the one of the control sample after 96 h incubation.

TTR *in vitro* aggregation inhibition. To assess the effect of **PITB** and tolcapone in the aggregation of WT-, V30M- and V122I-TTR, a well-established TTR aggregation assay was employed[36,51]. Briefly, TTR solutions (7 μM in 10 mM sodium phosphate, 100 mM KCl, 1 mM EDTA, 1 mM DTT, pH 7.0) were incubated with varying concentrations of test compound for 30 min at 37 °C. The percentage of DMSO was the same in all samples (5%). Following incubation, the pH of the solutions was dropped to 4.2 via addition of an equal volume of acidification buffer (100 mM sodium acetate, 100 mM KCl, 1 mM EDTA, 1 mM DTT, pH 4.2) and the samples were kept at 37 °C for more 72 h. The aggregation was assessed by measuring turbidity at 340 nm using a Varian Cary Eclipse Fluorescence Spectrophotometer (Agilent Technologies). Since **PITB** and tolcapone display dose-dependent absorbance at 340 nm, the turbidity of a sample containing the same concentration of compound, but lacking TTR, was subtracted to every measurement. The percentage of TTR aggregation for each inhibitor concentration was calculated by dividing the turbidity of the test sample by that

of a sample aggregated in the absence of compound, and multiply by 100.

Isothermal titration calorimetry. All ITC measurements were carried out with protein and compounds dissolved in the same buffer (in a PBS buffer pH 7.0 containing 100 mM KCl, 1 mM EDTA and 2.5% DMSO), and degassed. The ITC measurements were performed at 25 °C using a Nano ITC calorimeter (TA Instruments). The NanoAnalyze software (TA Instruments) was used to study the binding isotherms. Titrations were performed as a set of 20 injections of 100 μM compound into protein (5 μM), programmed as a 2.02 μl injection with 150 s of equilibration period. Fittings were performed using the independent binding sites model provided with the system.

Crystallization and structure determination. Cocrystals of WT-TTR/**PITB**, V30M-TTR/**PITB**, V122I-TTR/**PITB** and V30M-TTR/tolcapone were obtained as explained previously[29]. Briefly, purified proteins (140 μM) were mixed with 1.4 mM of **PITB**/tolcapone and cocrystallized at 18 °C by hanging-drop vapor diffusion methods. The reservoir solution contained 20-30% PEG 400, 200 mM CaCl$_2$, 100 mM HEPES, pH 7.0-8.0. The crystals were flash-frozen in liquid nitrogen (100 K) and diffraction data were collected at the BL13-XALOC beamline from the ALBA Synchrotron in Barcelona[52]. Data were integrated and merged using XDS[53] and scaled, reduced, and further analyzed using CCP4[54]. The structures of TTR/**PITB** and V30M-TTR/tolcapone complexes were determined from the X-ray data by molecular replacement with Phenix (version 1.19.2-4158)[55] using a previous TTR structure (PDB 1F41) as a model. Model refinement and building were done with Phenix[55] and Coot[56], respectively. Refinement and data statistics are shown in **Table S2**. The structural representations were prepared using Pymol (The PyMOL Molecular Graphics System, Version 2.0, Schrödinger, LLC).

T$_4$ binding competition assays. The ability of **PITB** and tolcapone to displace T$_4$ from plasmatic TTR was evaluated by incubation of whole plasma (5 μl) with 1 μl of [^{125}I]-T$_4$ (specific radioactivity 1250 μCi/μg; concentration 320 μCi/mL; Perkin Elmer) in the presence of the test compounds (5 molar excess relative to TTR tetramer). A negative control containing the same percentage of DMSO than the samples was also prepared. Following 1 h incubation at room temperature, plasma proteins were separated by native PAGE[41], the gels were dried, and subjected to phosphor imaging using a Typhoon 8600 variable mode imager (Molecular Diagnostics, Amersham Biosciences). Then, the autoradiography films were scanned, and the bands quantified using Image Lab software version 5.2.1 (Bio-Rad). The amount of T$_4$ bound to TTR in comparison to total T$_4$ (T$_4$-TBG + T$_4$-ALB + T$_4$-TTR) was determined for each sample and normalized to the maximum value, which corresponds to the negative control. Plasma from three V30M-TTR carriers was analyzed.

TTR stabilization in human plasma assessed by isoelectric focusing. To assess the effect of **PITB** and tolcapone on the stability of TTR in plasma, isoelectric focusing (IEF) under semi-denaturing conditions was performed[42]. To carry out this assay, 30 μl of human plasma from V30M-TTR carriers (n = 3) were incubated overnight at 4 °C in the presence of 19.1 μM compounds. Additionally, control samples containing the same amount of DMSO rather than compound were prepared. After incubation, the samples were subjected to native PAGE, and the TTR gel band was excised and applied to an IEF gel. IEF was performed in the presence of 4 M urea (semi-denaturing conditions) and 5% (v/v) ampholytes (pH 4-6.5; Sigma-Merck), at 1200 V for 5 h. Proteins were then fixed with 20% trichloroacetic acid and stained with Coomassie blue. The gels were scanned using a GS-900 calibrated densitometer (Bio-Rad) and the bands analyzed by densitometry with the Image Lab software

version 5.2.1 (Bio-Rad). The ratio of the TTR tetramer over total TTR (TTR tetramer + monomer) was determined for each sample, and the percentage of tetramer stabilization was calculated as ((ratio treated sample − ratio control sample)/ratio control sample) × 100.

Cytotoxicity studies. The potential chemical toxicity of **PITB** was evaluated *in vitro* in HeLa and HepG2 human cell lines. Tolcapone was tested in parallel for comparison. HeLa and HepG2 cells were cultured in MEM ALPHA medium (Gibco) supplemented with 10% fetal bovine serum at 37 °C in a 5% CO_2 humidified atmosphere. HeLa cells were seeded at 3500 cells/well and HepG2 cells at 4500 cells/well in 96-well plates and incubated with increasing concentrations of compound (2-100 µM) for 72 h at 37°C. Controls were prepared with the equivalent amount of DMSO relative to each concentration of compound. Then, 10 µl of PrestoBlue® reagent (Thermo Fisher Scientific) were added to each well, and after incubating for 15 min at 37°C, the fluorescence emission was recorded using a 590/20 filter with an excitation wavelength of 535 in a Victor3 Multilabel Reader (PerkinElmer). The assays were performed in triplicate and the percentage of cell viability for each well was calculated as (intensity sample − mean intensity blank)/(mean intensity control − mean intensity blank) × 100, where "mean intensity blank" corresponds to the mean intensity of wells with PrestoBlue® alone and "mean intensity control" is the mean intensity of wells that contain the corresponding percentage of DMSO.

In vivo **pharmacokinetic studies in mice**. The PK studies of M-23 (IV and PO), **PITB** (IV and PO) and tolcapone (PO) in CD-1 mice were conducted by Draconis Pharma S.L. For each study, 24 male CD-1 mice were weighted and identified by a distinct number at the base of the tail. For the IV studies, M-23 was dissolved in PBS and **PITB** in 5% Cremophor/5% Mannitol/5% DMSO. Both compounds were administered at 1 mg/Kg, with an administration volume of 5 mL/Kg. At different timepoints after administration (0.0833, 0.5, 1, 2, 4, 6 and 24 h), three animals were anesthetized with isoflurane, and their blood collected by cava vein puncture in tubes containing K2-EDTA 5%. Three animals were not administered and referred as t = 0 h (predose). Blood samples were centrifuged at 10 000 rpm for 5 min to obtain the plasmas, which were stored at -80 °C until analysis. For the PO studies, M-23, **PITB** and tolcapone were formulated in 0.5% CMC/0.1% tween 80 and administered at 10 mg/Kg. The administered volume was 10 mL/Kg. Plasma samples were obtained as described above at 0.25, 0.5, 1, 2, 4, 6 and 24 h post-dosing (three animals for time point). Three animals were used as blank with no administration (predose). All plasma samples were analyzed using the API 3200 LC-MS/MS system (Sciex) coupled to an UPLC-Acquity (Waters). A calibration curve was done for each compound in plasma. The lower limit of quantification (LLOQ) for M-23, **PITB** and tolcapone were 2.93 ng/mL, 7.68 ng/mL and 2.73 ng/mL, respectively. For **PITB** quantification in plasma samples from the PK studies of M-23 (IV and PO), the same UPLC-MS/MS detection system was used. The calibration curve done for **PITB** PK studies was applied in this case. PK parameters were determined with a non-compartmental model using Phoenix 64 8.3 (WinNolin) software.

References

1   Chiti, F. & Dobson, C. M. Protein misfolding, functional amyloid, and human disease. *Annual review of biochemistry* **75**, 333-366, doi:10.1146/annurev.biochem.75.101304.123901 (2006).

2   Koike, H. & Katsuno, M. Transthyretin Amyloidosis: Update on the Clinical Spectrum,

Pathogenesis, and Disease-Modifying Therapies. *Neurology and therapy* **9**, 317-333, doi:10.1007/s40120-020-00210-7 (2020).

3   Carroll, A. *et al.* Novel approaches to diagnosis and management of hereditary transthyretin amyloidosis. *Journal of neurology, neurosurgery, and psychiatry* **93**, 668-678, doi:10.1136/jnnp-2021-327909 (2022).

4   Rowczenio, D. M. *et al.* Online registry for mutations in hereditary amyloidosis including nomenclature recommendations. *Human mutation* **35**, E2403-2412, doi:10.1002/humu.22619 (2014).

5   Andrade, C. A peculiar form of peripheral neuropathy; familiar atypical generalized amyloidosis with special involvement of the peripheral nerves. *Brain : a journal of neurology* **75**, 408-427, doi:10.1093/brain/75.3.408 (1952).

6   Ruberg, F. L., Grogan, M., Hanna, M., Kelly, J. W. & Maurer, M. S. Transthyretin Amyloid Cardiomyopathy: JACC State-of-the-Art Review. *Journal of the American College of Cardiology* **73**, 2872-2891, doi:10.1016/j.jacc.2019.04.003 (2019).

7   Goren, H., Steinberg, M. C. & Farboody, G. H. Familial oculoleptomeningeal amyloidosis. *Brain : a journal of neurology* **103**, 473-495, doi:10.1093/brain/103.3.473 (1980).

8   Westermark, P., Sletten, K., Johansson, B. & Cornwell, G. G., 3rd. Fibril in senile systemic amyloidosis is derived from normal transthyretin. *Proceedings of the National Academy of Sciences of the United States of America* **87**, 2843-2845, doi:10.1073/pnas.87.7.2843 (1990).

9   Tanskanen, M. *et al.* Senile systemic amyloidosis affects 25% of the very aged and associates with genetic variation in alpha2-macroglobulin and tau: a population-based autopsy study. *Annals of medicine* **40**, 232-239, doi:10.1080/07853890701842988 (2008).

10   Cornwell, G. G., 3rd, Murdoch, W. L., Kyle, R. A., Westermark, P. & Pitkanen, P. Frequency and distribution of senile cardiovascular amyloid. A clinicopathologic correlation. *The American journal of medicine* **75**, 618-623, doi:10.1016/0002-9343(83)90443-6 (1983).

11   Hagen, G. A. & Elliott, W. J. Transport of thyroid hormones in serum and cerebrospinal fluid. *The Journal of clinical endocrinology and metabolism* **37**, 415-422, doi:10.1210/jcem-37-3-415 (1973).

12   Schreiber, G. *et al.* Thyroxine transport from blood to brain via transthyretin synthesis in choroid plexus. *The American journal of physiology* **258**, R338-345, doi:10.1152/ajpregu.1990.258.2.R338 (1990).

13   Magalhaes, J., Eira, J. & Liz, M. A. The role of transthyretin in cell biology: impact on human pathophysiology. *Cellular and molecular life sciences : CMLS* **78**, 6105-6117, doi:10.1007/s00018-021-03899-3 (2021).

14   Hammarstrom, P., Jiang, X., Hurshman, A. R., Powers, E. T. & Kelly, J. W. Sequence-dependent denaturation energetics: A major determinant in amyloid disease diversity. *Proceedings of the National Academy of Sciences of the United States of America* **99 Suppl 4**, 16427-16432, doi:10.1073/pnas.202495199 (2002).

15   Hurshman Babbes, A. R., Powers, E. T. & Kelly, J. W. Quantification of the thermodynamically linked quaternary and tertiary structural stabilities of transthyretin and its disease-associated variants: the relationship between stability and amyloidosis. *Biochemistry* **47**, 6969-6984, doi:10.1021/bi800636q (2008).

16   Colon, W. & Kelly, J. W. Partial denaturation of transthyretin is sufficient for amyloid fibril formation in vitro. *Biochemistry* **31**, 8654-8660, doi:10.1021/bi00151a036 (1992).

17   Hurshman, A. R., White, J. T., Powers, E. T. & Kelly, J. W. Transthyretin aggregation under partially denaturing conditions is a downhill polymerization. *Biochemistry* **43**, 7365-7381, doi:10.1021/bi049621l (2004).

18   Foss, T. R., Wiseman, R. L. & Kelly, J. W. The pathway by which the tetrameric protein

transhyretin dissociates. *Biochemistry* **44**, 15525-15533, doi:10.1021/bi051608t (2005).

19 Hammarstrom, P., Wiseman, R. L., Powers, E. T. & Kelly, J. W. Prevention of transthyretin amyloid disease by changing protein misfolding energetics. *Science* **299**, 713-716, doi:10.1126/science.1079589 (2003).

20 Johnson, S. M. *et al.* Native state kinetic stabilization as a strategy to ameliorate protein misfolding diseases: a focus on the transthyretin amyloidoses. *Accounts of chemical research* **38**, 911-921, doi:10.1021/ar020073i (2005).

21 Bulawa, C. E. *et al.* Tafamidis, a potent and selective transthyretin kinetic stabilizer that inhibits the amyloid cascade. *Proceedings of the National Academy of Sciences of the United States of America* **109**, 9629-9634, doi:10.1073/pnas.1121005109 (2012).

22 Barroso, F. A. *et al.* Long-term safety and efficacy of tafamidis for the treatment of hereditary transthyretin amyloid polyneuropathy: results up to 6 years. *Amyloid : the international journal of experimental and clinical investigation : the official journal of the International Society of Amyloidosis* **24**, 194-204, doi:10.1080/13506129.2017.1357545 (2017).

23 Maurer, M. S. *et al.* Tafamidis Treatment for Patients with Transthyretin Amyloid Cardiomyopathy. *The New England journal of medicine* **379**, 1007-1016, doi:10.1056/NEJMoa1805689 (2018).

24 Monteiro, C. *et al.* Predictive model of response to tafamidis in hereditary ATTR polyneuropathy. *JCI insight* **4**, doi:10.1172/jci.insight.126526 (2019).

25 Kazi, D. S. *et al.* Cost-Effectiveness of Tafamidis Therapy for Transthyretin Amyloid Cardiomyopathy. *Circulation* **141**, 1214-1224, doi:10.1161/CIRCULATIONAHA.119.045093 (2020).

26 Sant'Anna, R. *et al.* Repositioning tolcapone as a potent inhibitor of transthyretin amyloidogenesis and associated cellular

toxicity. *Nature communications* **7**, 10787, doi:10.1038/ncomms10787 (2016).

27 Reig, N., Ventura, S., Salvadó, M., Gámez, J. & Insa, R. SOM0226, a repositioned compound for the treatment of TTR amyloidosis. *Orphanet Journal of Rare Diseases* **10**, P9, doi:10.1186/1750-1172-10-s1-p9 (2015).

28 Gamez, J. *et al.* Transthyretin stabilization activity of the catechol-O-methyltransferase inhibitor tolcapone (SOM0226) in hereditary ATTR amyloidosis patients and asymptomatic carriers: proof-of-concept study(). *Amyloid : the international journal of experimental and clinical investigation : the official journal of the International Society of Amyloidosis* **26**, 74-84, doi:10.1080/13506129.2019.1597702 (2019).

29 Pinheiro, F. *et al.* Tolcapone, a potent aggregation inhibitor for the treatment of familial leptomeningeal amyloidosis. *The FEBS journal* **288**, 310-324, doi:10.1111/febs.15339 (2021).

30 Pinheiro, F. *et al.* Development of a Highly Potent Transthyretin Amyloidogenesis Inhibitor: Design, Synthesis, and Evaluation. *Journal of medicinal chemistry* **65**, 14673-14691, doi:10.1021/acs.jmedchem.2c01195 (2022).

31 Andrade, E. L. *et al.* Non-clinical studies required for new drug development - Part I: early in silico and in vitro studies, new target discovery and validation, proof of principles and robustness of animal studies. *Brazilian journal of medical and biological research = Revista brasileira de pesquisas medicas e biologicas* **49**, e5644, doi:10.1590/1414-431X20165644 (2016).

32 Walker, D. K. The use of pharmacokinetic and pharmacodynamic data in the assessment of drug safety in early drug development. *British journal of clinical pharmacology* **58**, 601-608, doi:10.1111/j.1365-2125.2004.02194.x (2004).

33 Jorga, K., Fotteler, B., Heizmann, P. & Gasser, R. Metabolism and excretion of tolcapone, a novel inhibitor of catechol-O-

methyltransferase. *British journal of clinical pharmacology* **48**, 513-520, doi:10.1046/j.1365-2125.1999.00036.x (1999).

34   Loconte, V. *et al.* Interactions of tolcapone analogues as stabilizers of the amyloidogenic protein transthyretin. *Bioorganic chemistry* **103**, 104144, doi:10.1016/j.bioorg.2020.104144 (2020).

35   Hammarstrom, P., Jiang, X., Deechongkit, S. & Kelly, J. W. Anion shielding of electrostatic repulsions in transthyretin modulates stability and amyloidosis: insight into the chaotrope unfolding dichotomy. *Biochemistry* **40**, 11453-11459, doi:10.1021/bi010673+ (2001).

36   Jiang, X., Buxbaum, J. N. & Kelly, J. W. The V122I cardiomyopathy variant of transthyretin increases the velocity of rate-limiting tetramer dissociation, resulting in accelerated amyloidosis. *Proceedings of the National Academy of Sciences of the United States of America* **98**, 14943-14948, doi:10.1073/pnas.261419998 (2001).

37   Saelices, L. *et al.* Uncovering the Mechanism of Aggregation of Human Transthyretin. *The Journal of biological chemistry* **290**, 28932-28943, doi:10.1074/jbc.M115.659912 (2015).

38   Morais-de-Sa, E., Pereira, P. J., Saraiva, M. J. & Damas, A. M. The crystal structure of transthyretin in complex with diethylstilbestrol: a promising template for the design of amyloid inhibitors. *The Journal of biological chemistry* **279**, 53483-53490, doi:10.1074/jbc.M408053200 (2004).

39   Penchala, S. C. *et al.* AG10 inhibits amyloidogenesis and cellular toxicity of the familial amyloid cardiomyopathy-associated V122I transthyretin. *Proceedings of the National Academy of Sciences of the United States of America* **110**, 9992-9997, doi:10.1073/pnas.1300761110 (2013).

40   Sebastiao, M. P., Lamzin, V., Saraiva, M. J. & Damas, A. M. Transthyretin stability as a key factor in amyloidogenesis: X-ray analysis at atomic resolution. *Journal of molecular biology* **306**, 733-744, doi:10.1006/jmbi.2000.4415 (2001).

41   Almeida, M. R. *et al.* Selective binding to transthyretin and tetramer stabilization in serum from patients with familial amyloidotic polyneuropathy by an iodinated diflunisal derivative. *The Biochemical journal* **381**, 351-356, doi:10.1042/BJ20040011 (2004).

42   Ferreira, N. *et al.* Binding of epigallocatechin-3-gallate to transthyretin modulates its amyloidogenicity. *FEBS letters* **583**, 3569-3576, doi:10.1016/j.febslet.2009.10.062 (2009).

43   Schoonen, W. G., Westerink, W. M., de Roos, J. A. & Debiton, E. Cytotoxic effects of 100 reference compounds on Hep G2 and HeLa cells and of 60 compounds on ECC-1 and CHO cells. I mechanistic assays on ROS, glutathione depletion and calcein uptake. *Toxicology in vitro : an international journal published in association with BIBRA* **19**, 505-516, doi:10.1016/j.tiv.2005.01.003 (2005).

44   Thabrew, M. I., Hughes, R. D. & McFarlane, I. G. Screening of hepatoprotective plant components using a HepG2 cell cytotoxicity assay. *The Journal of pharmacy and pharmacology* **49**, 1132-1135, doi:10.1111/j.2042-7158.1997.tb06055.x (1997).

45   Ekwall, B. Toxicity to HeLa cell of 205 drugs as determined by the metabolic inhibition test supplemented by microscopy. *Toxicology* **17**, 273-295, doi:10.1016/0300-483x(80)90010-4 (1980).

46   Mostafavi-Pour, Z., Khademi, F., Zal, F., Sardarian, A. R. & Amini, F. In Vitro Analysis of CsA-Induced Hepatotoxicity in HepG2 Cell Line: Oxidative Stress and alpha2 and beta1 Integrin Subunits Expression. *Hepatitis monthly* **13**, e11447, doi:10.5812/hepatmon.11447 (2013).

47   Krithika, R., Verma, R. J. & Shrivastav, P. S. Antioxidative and cytoprotective effects of andrographolide against CCl4-induced hepatotoxicity in HepG2 cells. *Human &*

experimental toxicology **32**, 530-543, doi:10.1177/0960327112459530 (2013).

48   Lee, W. M. Drug-induced hepatotoxicity. *The New England journal of medicine* **349**, 474-485, doi:10.1056/NEJMra021844 (2003).

49   Olanow, C. W. Tolcapone and hepatotoxic effects. Tasmar Advisory Panel. *Archives of neurology* **57**, 263-267, doi:10.1001/archneur.57.2.263 (2000).

50   Weinshilboum, R. M., Otterness, D. M. & Szumlanski, C. L. Methylation pharmacogenetics: catechol O-methyltransferase, thiopurine methyltransferase, and histamine N-methyltransferase. *Annual review of pharmacology and toxicology* **39**, 19-52, doi:10.1146/annurev.pharmtox.39.1.19 (1999).

51   Jiang, X. *et al.* An engineered transthyretin monomer that is nonamyloidogenic, unless it is partially denatured. *Biochemistry* **40**, 11442-11452, doi:10.1021/bi011194d (2001).

52   Juanhuix, J. *et al.* Developments in optics and performance at BL13-XALOC, the macromolecular crystallography beamline at the ALBA synchrotron. *Journal of synchrotron radiation* **21**, 679-689, doi:10.1107/S160057751400825X (2014).

53   Kabsch, W. Integration, scaling, space-group assignment and post-refinement. *Acta crystallographica. Section D, Biological crystallography* **66**, 133-144, doi:10.1107/S0907444909047374 (2010).

54   Winn, M. D. *et al.* Overview of the CCP4 suite and current developments. *Acta crystallographica. Section D, Biological crystallography* **67**, 235-242, doi:10.1107/S0907444910045749 (2011).

55   Adams, P. D. *et al.* PHENIX: a comprehensive Python-based system for macromolecular structure solution. *Acta crystallographica. Section D, Biological crystallography* **66**, 213-221, doi:10.1107/S0907444909052925 (2010).

56   Emsley, P., Lohkamp, B., Scott, W. G. & Cowtan, K. Features and development of Coot. *Acta crystallographica. Section D, Biological crystallography* **66**, 486-501, doi:10.1107/S0907444910007493 (2010).

CHAPTER 4

Hydrogen deuterium exchange and fast photochemical oxidation of proteins coupled with mass spectrometry in transthyretin therapeutics

Hydrogen deuterium exchange and fast photochemical oxidation of proteins coupled with mass spectrometry in transthyretin therapeutics

Introduction

It is widely accepted that pathogenic mutations in transthyretin (TTR) gene lower the stability of the tetramer and/or monomer, enhancing TTR amyloidogenicity[1,2]. Understanding the structural basis of TTR destabilization has been a pursued goal since the first TTR X-ray crystal structure was determined. Although numerous crystal structures of wild-type TTR (WT-TTR) and pathogenic mutants have been determined, they have failed to reveal any significant structural changes that could account for their increased amyloidogenicity. Indeed, most TTR structures crystallize in the same space group as the WT protein, $P2_12_12$, reflecting their overall similar structure[3,4]. On the other hand, occupancy of the TTR thyroxine (T_4)-binding sites with rationally designed small molecules is known to stabilize TTR tetramers, inhibiting their dissociation and, thus, preventing the onset of transthyretin amyloidosis (ATTR)[5,6]. As for apo-TTR crystal structures, the structures of TTR:inhibitor complexes are almost exactly superimposable making it difficult to identify which features are important for tetramer stabilization[3]. Overall, this suggests that the impact of mutations and ligands on TTR tetramer stability goes beyond the structural details captured by X-ray crystallography and highlights the need to use methods that incorporate protein flexibility for studying TTR structural changes.

In recent years, mass spectrometry (MS)-based footprinting methods have become a powerful tool for assessing protein structure and dynamics[7]. Two major methods of protein footprinting are hydrogen-deuterium exchange (HDX) and fast photochemical oxidation of proteins (FPOP). Briefly, HDX relies on the exchange of backbone amide hydrogens with deuterium to assess changes in solvent accessibility and hydrogen bonding[8,9]. In FPOP, a pulsed laser is used to trigger the hydrolysis of hydrogen peroxide in solution, generating hydroxyl radicals that label solvent exposed amino acid side chains. This type of labeling is faster (microsecond time scale), irreversible, and provides residue specific information[10,11]. When coupled to MS, these methods can provide valuable insights into the conformational changes induced by ligand binding, mutations, and protein aggregation under close-to-native conditions in solution[12-14]. In comparison to other structural tools, such as NMR spectroscopy, MS-based methods present numerous strengths: (1) they require substantially less protein; (2) the proteins do not have to be isotopically labeled; (3) they can accommodate large proteins; (4) they can be used to study proteins that are difficult to purify or that can only be handled at low concentrations (e.g., membrane proteins or proteins with extensive intrinsically disordered regions)[7,15,16].

Here, we employed HDX to identify the structural variations that may underlie the increased amyloidogenicity of the FAP- and FAC-associated TTR variants V30M and V122I, and to investigate the binding of M-23[17] and tolcapone[18], two potent TTR kinetic stabilizers. For obtaining further insights into the conformational changes induced by these ligands, FPOP was used to evaluate alterations on TTR structure at the residue level. To our knowledge, this is the first time that MS-based techniques have been used for studying the effect of mutations and ligands on TTR stability. The results obtained in this work demonstrate that these techniques can be used to accurately monitor stabilizing/destabilizing effects on TTR structural dynamics, constituting an attractive approach for

the structure-based design and development of TTR kinetic stabilizers with optimized affinity and stabilization activity under near-physiological conditions.

Results and discussion

Analysis of the conformational dynamics of WT-, V30M- and V122I-TTR using HDX-MS.
The V30M and V122I mutations are located on strand B and H of TTR, respectively (**Figure 1A**). The crystal structures of V30M- and V122I-TTR are virtually identical to the one of the WT protein (**Figure 2B**)[19,20], suggesting that X-ray crystal structures are blind to the conformational changes induced by these pathogenic mutations.
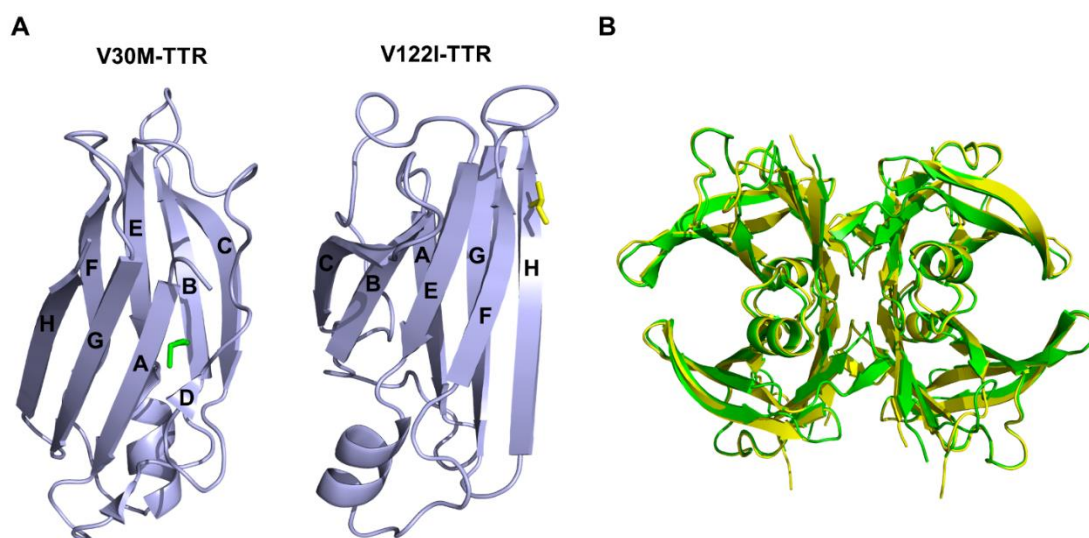
Figure 1. Structure of V30M- and V122I-TTR. (A) Cartoon representation of the structure of TTR monomer with the side chains of M30 (in green) and I122 (in yellow) shown as sticks. (B) Superposition between the X-ray crystal structures of V30M-TTR (in green) and V122I-TTR (in yellow). Figure prepared from PDB structures 4TL4 (V30M-TTR) and 1TTR (V122I-TTR).

To understand the impact of TTR mutations V30M and V122I on the structural dynamics of the protein, we performed HDX-MS on these two proteins and compared the results with those obtained for the WT protein under the same conditions.

For HDX experiments, the proteins were dissolved in a buffer containing D_2O and HDX was allowed to proceed for 4 h at 37 °C, pH 7.4. The reactions were quenched at different time points and the proteins subjected to double enzymatic digestion (fungal protease type XIII and pepsin) to assure high sequence coverage. For each TTR variant, cumulative HDX differences were calculated by subtracting the deuterium uptake of the protein from WT-TTR (**Figure 2**). Regarding V30M-TTR, the results showed significant differences in uptake across the whole structure (**Figure 2A**). Specifically, a significant increase in HDX was observed at amino acid residues ranging from V14 to N27 and V94 to A109, whereas peptides covering regions I73 to A91 and A109 to V121 showed a decrease in HDX. The location of these residues on TTR structure is indicated in **Figure 2C**. Contrarily to V30M-TTR, the HDX of V122I-TTR is statistically similar to the one of the WT protein, except for a short region between amino acid residues V94 and A109, where an increase in HDX is observed (**Figure 2B,D**).

Overall, these results indicate that the substitution of valine for methionine at position 30 perturbs the TTR structure to a greater extent than the substitution of valine for isoleucine at position

122. This in agreement with recent results from an NMR study[21] and might explain the different effect of these mutations on TTR stability. Whereas V30M has a similar kinetic stability than WT-TTR, but lower thermodynamic stability, V122I is thermodynamically stable, but is kinetically destabilized relative to the WT protein[2,22]. In other words, V122I mainly impacts the stability of the tetramer, increasing the rate of tetramer dissociation, while V30M mostly affects monomer stability, facilitating monomer misfolding once the tetramer is dissociated. The fact that the HDX data recapitulates the observed kinetic and thermodynamic stability differences between V30M- and V122I-TTR opens the possibility to apply this technique to the rational design of variant-specific TTR kinetic stabilizers.
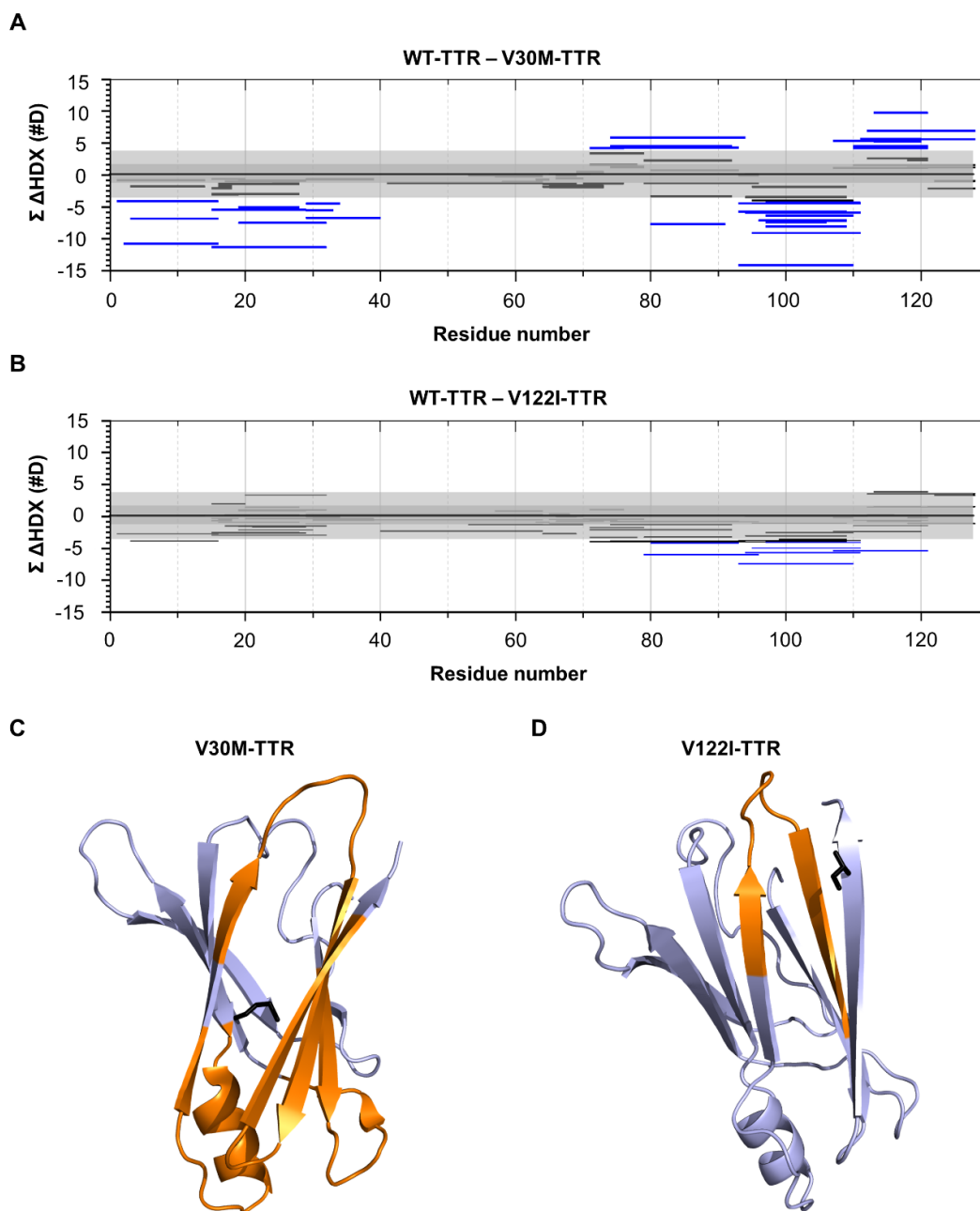
Figure 2. Differences in backbone dynamics between WT-TTR and TTR variants V30M and V122I as assessed by HDX-MS. (A,B) Wood's plot showing cumulative HDX differences on the Y-axis (horizontal bars) between WT-TTR and V30M-TTR (A) or V122I-TTR (B). Increases in deuterium uptake relative to the WT protein are shown as negative values and decreases are shown as positive values. The gray region indicates the global

significance limit (p < 0.01) which is compared with cumulative differences of the peptides to assign statistically significant differences. Peptides not reporting a significant difference are depicted in dark grey. (C, D) Statistically significant changes in HDX between WT-TTR and V30M-TTR (C) or V122I-TTR (D) mapped onto the X-ray crystal structure of the proteins (in orange). The mutated residues are shown as black sticks. Structures prepared from PDB files 4TL4 (C) and 1TTR (D).

Mapping the interaction of WT-TTR with M-23 and tolcapone by HDX and FPOP.

As a first step to validate the potential of MS-based methods for the design of TTR stabilizers, we assessed whether these techniques are able to discern the stabilizing effect of M-23 and tolcapone on WT-TTR. M-23 is a tolcapone derivative that binds WT-TTR with an affinity > 5-fold the one of the parental molecule, as determined by isothermal titration calorimetry (ITC), resulting in a higher tetramer stabilizing effect both *in vitro* and in human plasma. The increased affinity and potency of M-23 in relation to tolcapone was attributed to its higher enthalpy for binding, which in turn was associated to the formation of new contacts between M-23 and TTR in the binding cavity, as revealed by the X-ray crystal structure[17]. Nonetheless, as for most TTR:ligand structures, the structures of WT-TTR in complex with M-23 and tolcapone are almost completely superimposable (**Figure 3A**), precluding a thorough understanding of their effect on TTR structure. In this context, we performed HDX as described above, with the exception that for the bound state, WT-TTR was incubated with the compounds for 2 h before dilution in D₂O buffer. The HDX cumulative differences between bound and unbound states for M-23 and tolcapone are shown in **Figure 3B**. In both cases, the peptides covering residues from V14 to V28, K70 to Y78, and A109 to V121 show decreases in HDX, suggesting a higher stability after binding to the compounds. These regions include residues that are known to interact with M-23[17] and tolcapone[18] (e.g., K15 and T119), but also residues far from the binding pocket (**Figure 3C**). In particular, the loop between β-strands A and B (19-28) and part of the EF-helix (70-78) become protected on WT-TTR upon binding to M-23 and tolcapone. The AB loop participates in the contacts that stabilize the weaker AB/CD dimer-dimer interface[23], whereas the EF-helix enables the interaction between subunits A(C) and B(D) in one dimer[24]. Additionally, the EF-helix establishes contacts with the AB loop and, thus, changes in the EF-helix are expected to impact both the strong and weak interfaces of the tetramer[24,25]. Therefore, the remote conformational changes observed in the AB loop and the EF-helix of TTR could play a key role on the tetramer stabilizing effect of M-23 and tolcapone. Of note, the HDX differences are greater with M-23 than with tolcapone, especially in the EF-helix (**Figure 4D**). These larger differences in HDX indicate that M-23 has a more pronounced effect and stabilizes WT-TTR to a greater extent than tolcapone, which is in agreement with our previously published results[17].
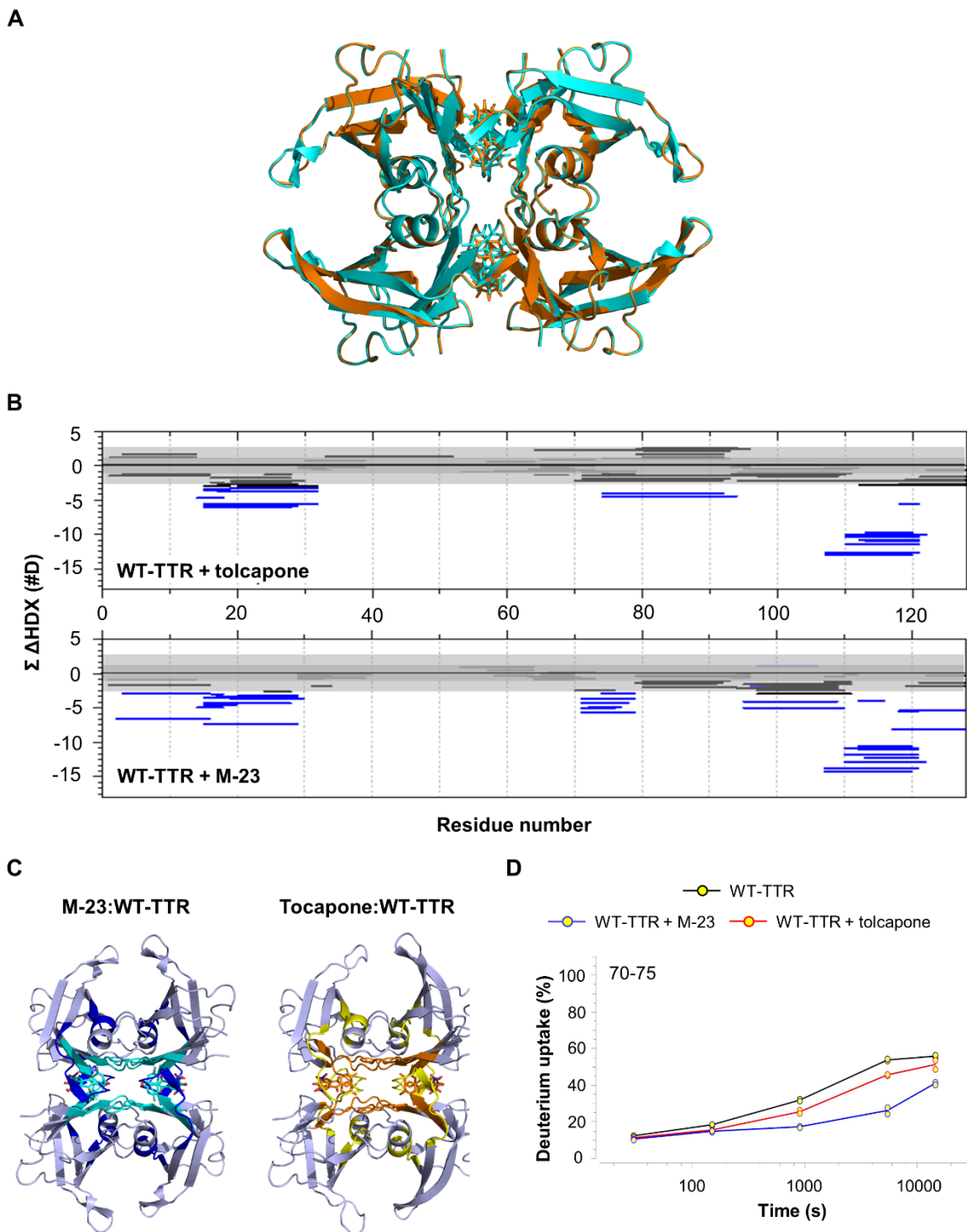
Figure 3. Effect of M-23 and tolcapone on WT-TTR structure as examined by HDX-MS. (A) Overlay of the crystal structure of WT-TTR bound to M-23 (in cyan; PDB: 7QC5) or tolcapone (in orange; PDB: 4D7B). (B) Wood's plots showing cumulative HDX differences on the Y-axis (horizontal bars) between the bound and unbound state for tolcapone (upper panel) and M-23 (lower panel). A negative change in the cumulative difference indicates protection upon binding to the compounds. The gray region depicts the global significance limit (p < 0.01) which is compared with cumulative differences of the peptides to assign statistically significant differences. Peptides not reporting a significant difference are shown in dark grey. (C) Statistically significant changes in HDX are mapped onto the structure of the WT-TTR/M-23 complex (PDB: 7QC5) and the WT-TTR/tolcapone complex (PDB: 4D7B). The regions 19-28 (AB loop) and 70-78 (part of the EF-helix) are colored

in either dark blue or yellow in the M-23:WT-TTR and Tolcapone:WT-TTR structures, respectively. Meanwhile, the regions closer to binding pocket are shown in cyan in the M-23:WT-TTR structure and orange in the Tolcapone:WT-TTR structure. (D) HDX kinetics of WT-TTR unbound (black) and bound to M-23 (blue) or tolcapone (red) for a peptide in the region of the EF-helix (residues 70-75).

Once we identified the regions on WT-TTR that present an altered dynamic behavior after binding to M-23 and tolcapone, we sought to evaluate the impact of these compounds directly at the residue level by using FPOP. Briefly, WT-TTR tetramers were incubated in the absence or presence of compounds and subjected to FPOP, using glutamine as scavenger. The samples were then subjected to trypsin digestion and the resulting peptides analyzed by LC-MS/MS. Residue level analysis of peptides with differential FPOP between the bound and unbound state showed that 16 residues were significantly protected from oxidation upon binding to M-23 and tolcapone (**Figure 4A**). In resemblance to the HDX data, some of these residues are near the binding pocket, while others are far from the interaction site. Additionally, M-23 appears to exert a stronger effect than tolcapone, especially on residues P11, I84 and D99/S100. Except for I84, which is close to the weaker dimer-dimer interface, these residues are at a great distance from the binding site (**Figure 4B**). P11 is located on the N-terminal end of the β-strand A. N-terminal stabilization of TTR has been proposed to underlie the increased stability of the non-pathogenic TTR variant R104H[26]. Residue I84 is situated on the EF loop. Mutations in the EF loop, including those in this specific residue, destabilize the EF-helix, increasing TTR aggregation propensity[25]. Residues D99/S100 are located in the FG loop. The higher flexibility of the FG loop has been related to the increased amyloidogenicity of A97S-TTR[27]. The lower solvent accessibility of these residues in presence of M-23 may be due to a change of side-chain orientation or dynamics that in any case could be related to its higher stabilizing effect compared to tolcapone[17].
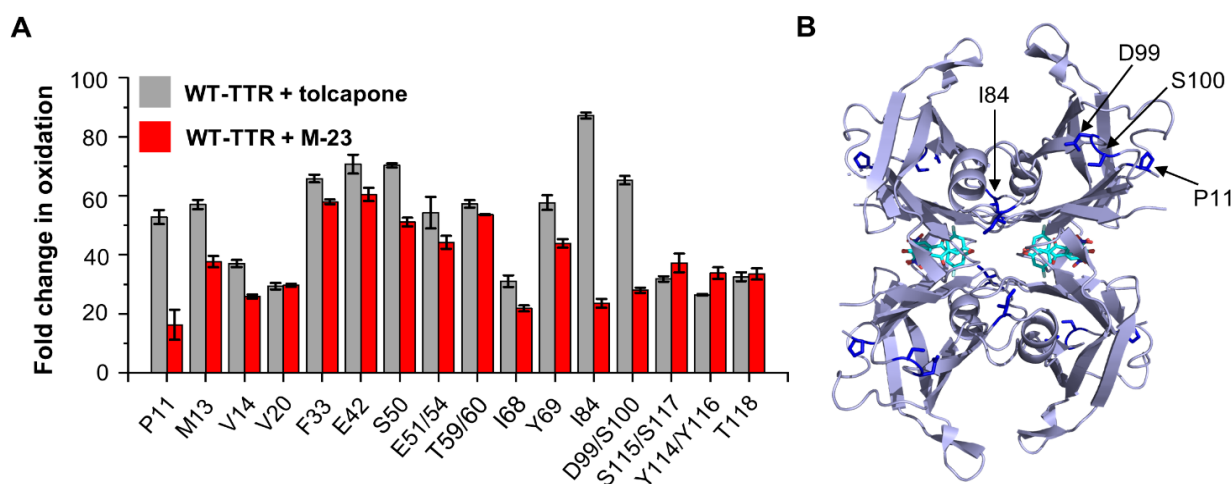

Figure 4. FPOP analysis of the binding of M-23 and tolcapone to WT-TTR. (A) Residues that undergo significantly lower oxidation in the presence of M-23 (red bars) or tolcapone (grey bars) relative to the unbound state, expressed as fold change in oxidation. (B) Cartoon representation of the WT-TTR:M-23 crystal structure (PDB: 7QC5) with the side chain of residues P11, I84 and D99/S100 shown as blue sticks. These residues are labelled in one of TTR subunits to highlight their position.

All in all, the results obtained by HDX and FPOP revealed that the binding of M-23 and tolcapone to WT-TTR causes short range conformational changes, but also remote allosteric effects, which are both likely to contribute to stabilize the protein. Importantly, the HDX and FPOP data suggest that M-23 binds stronger to the WT protein and exerts greater structural effects than tolcapone, in agreement with its higher binding affinity and potency[17]. Remarkably, these differences are especially pronounced in regions far from the binding pocket, such as the EF-helix, and have not been detected by X-ray crystallography.

Characterization of the binding and activity of M-23 and tolcapone on V30M-TTR and V122I-TTR. After confirming that HDX and FPOP are able to recapitulate our previous results regarding the binding and activity of M-23 and tolcapone on the WT protein, we aimed at extending this analysis to the TTR variants V30M and V122I. For that purpose, we have first characterized in detail the activity of M-23 and tolcapone on these proteins using biophysical and structural techniques that constitute the current pipeline for the development of TTR kinetic stabilizers.

As a starting point, we evaluated the anti-aggregation activity of M-23 and tolcapone using a standard acid-mediated aggregation assay[22,28]. Briefly, TTR solutions were incubated in the absence or presence of compound for 30 min (pH 7.4, 37 °C), and aggregation was triggered by decreasing the pH to 4.2. After 72 h, TTR aggregation was quantified by measuring turbidity at 340 nm and normalized to the maximum turbidity value, which corresponds to the samples incubated without compound. The incubation of V30M- and V122I-TTR with M-23 and tolcapone strongly decreased the aggregation of these TTR variants at acidic pH (**Figure 5A,B**). In particular, M-23 inhibited up to 78% and 81% the aggregation of V30M- and V122I-TTR, while tolcapone reached an inhibition of 72% and 82% for these two proteins. Remarkably, the occupancy of one binding site of V30M- and V122I-TTR by these two compounds decreased their aggregation by more than 60% and 70%, respectively.
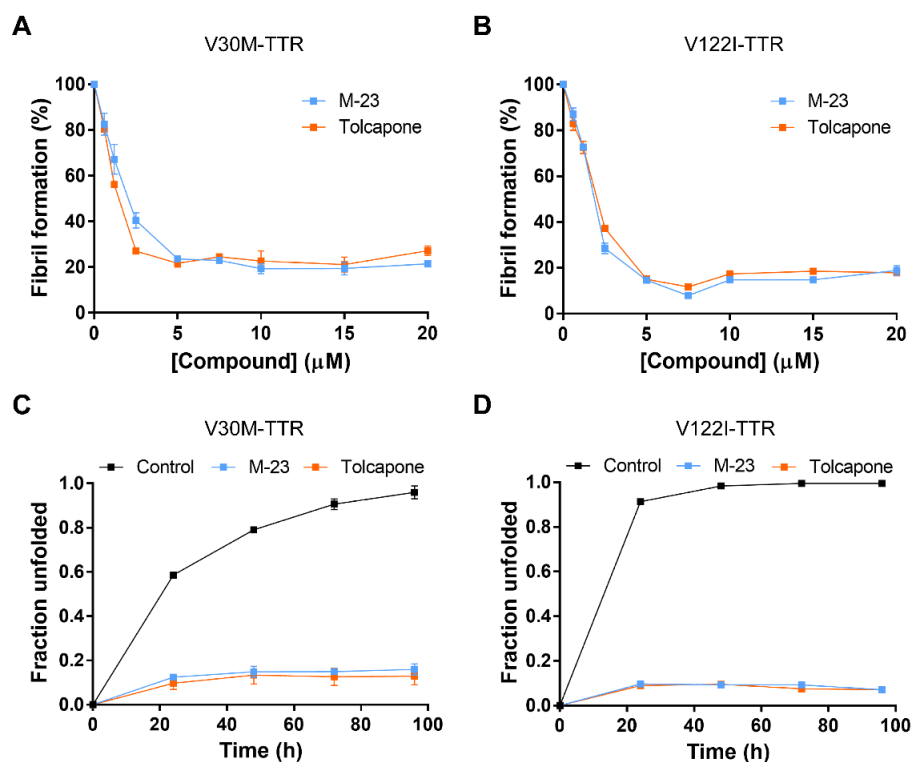
Figure 5. Anti-aggregation and stabilizing activity of M-23 and tolcapone over V30M- and V122I-TTR. (A,B) Percentage of V30M-TTR (A) and V122I-TTR (B) aggregation as a function of M-23 and tolcapone concentration as calculated by turbidity at 340 min. The values were normalized to the maximum value which was obtained in the absence of compound for each individual variant. The values correspond to mean ± SEM (n = 3). (C,D) V30M-TTR (C) and V122I-TTR (D) urea-induced tetramer dissociation (6 M urea) in the absence or presence of two molar equivalents of M-23 and tolcapone, as determined by Trp fluorescence. Data represents mean ± SEM (n = 3).

After examining the effect of M-23 and tolcapone over the aggregation of V30M- and V122I-TTR, we compared their ability to prevent tetramer dissociation in urea. Urea denaturation of TTR encompasses at least two equilibria: tetramer dissociation into folded monomers, and monomer unfolding[1]. By using urea concentrations exceeding those required for monomer unfolding, it is possible to assess the rate of tetramer dissociation, as the monomers unfold rapidly and irreversibly[2,22]. Therefore, TTR samples were incubated in the absence or presence of compounds (1:2 TTR tetramer:compound molar ratio) for 30 min and TTR denaturation was triggered by adding urea (6 M). Tryptophan (Trp) intrinsic fluorescence was measured along time and used to assess the fraction of unfolded protein at any time. The results showed that M-23 and tolcapone effectively stabilize V30M- and V122I-TTR, protecting >84% and >92% of TTR tetramers from dissociating in urea, respectively (**Figure 5C,D**). Additionally, M-23 and tolcapone substantially slowed the rate of V30M- and V122I-TTR tetramer dissociation.

To further characterize the interaction between these two TTR variants and M-23/tolcapone, we used ITC, which is the gold-standard technique for determining the binding constants for a ligand-macromolecule interaction. The thermodynamic parameters for the binding of M-23 and tolcapone to V30M- and V122I-TTR were obtained by fitting the ITC thermograms to a model that considers two independent binding sites (**Table 1** and **Figure 6**). M-23 presented a higher K_d (130 nM) and higher enthalpic contribution (ΔH = -12.3 kcal/mol) than tolcapone (K_d = 63.6 nM and ΔH = -11.5 kcal/mol) for binding to V30M-TTR. Despite the higher binding enthalpy for binding in M-23, the larger entropic penalty results in a slightly lower ΔG (-9.4 kcal/mol) in comparison with tolcapone (-9.8 kcal/mol). The affinity of M-23 for V122I-TTR was higher (K_d = 17.8 nM) than that of tolcapone (K_d = 38.8 nM), while the binding enthalpy was lower (ΔH for M-23 = -13.0 kcal/mol and ΔH for tolcapone = -14.9 kcal/mol). On the other hand, M-23 exhibits a lower entropic penalty for binding to V122I-TTR, which leads to a slightly higher ΔG (-10.6 kcal/mol) relative to tolcapone (-10.1 kcal/mol). In any case, the binding of M-23 and tolcapone is driven by enthalpic force, pointing to the formation of specific interactions between these ligands and TTR variants V30M and V122I.

Table 1. Thermodynamic parameters for the interaction of V30M- and V122I-TTR with M-23 and tolcapone analyzed by ITC.

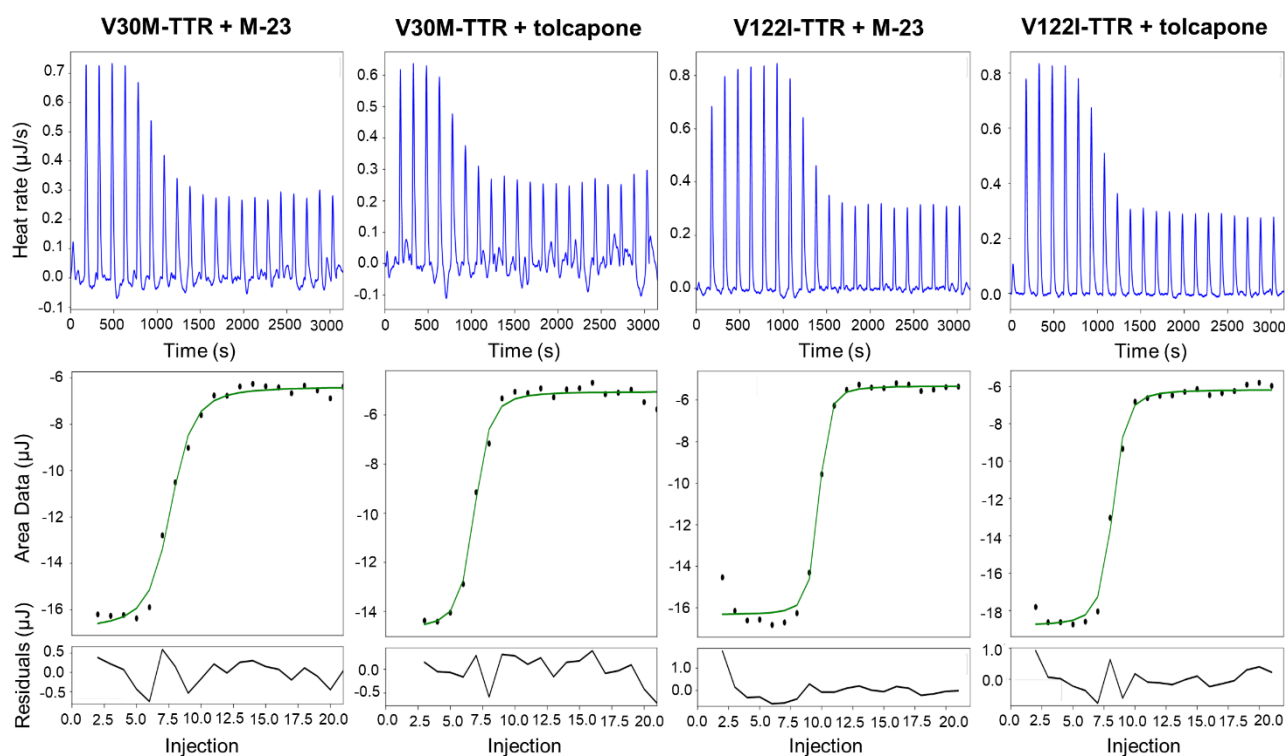|	M-23				Tolcapone			
	Kd (nM)	ΔG (kcal/mol)	ΔH (kcal/mol)	-TΔS (kcal/mol)	Kd (nM)	ΔG (kcal/mol)	ΔH (kcal/mol)	-TΔS (kcal/mol)
V30M-TTR	131	-9.4	-12.3	3.0	63.6	-9.8	-11.5	1.6
V122I-TTR	17.8	-10.6	-13.0	2.4	38.8	-10.1	-14.9	4.8

Figure 6. Interaction of M-23 and tolcapone with TTR variants V30M and V122I as assessed by ITC. The top panels represent the raw data, with positive peaks representing exothermic reactions. The lower panels show the integrated heat changes as a function of the number of injections, wherein the solid line corresponds to the fitting done to a model assuming independent binding site. Residuals were obtained by subtracting the experimental value to the value obtained in the fitting.

To gain insight into the interactions responsible for the binding of M-23 and tolcapone to V30M- and V122I-TTR, we analyzed their cocrystal structures in complex with these TTR variants. The crystal structure of V30M-TTR bound to M-23 and tolcapone was determined at 1.67 Å and 1.57 Å resolution, respectively, and the one of V122I-TTR bound to M-23 at 1.70 Å resolution (**Figure 7** and **Table 1**). The cocrystal structure of tolcapone in complex with V122I-TTR was previously reported[18] and used here for comparison. As for the WT protein[17,18], M-23 and tolcapone bind to V30M- and V122I-TTR in the so-called forward mode, with the 3,4-dihydroxy-5-nitrophenyl ring occupying the hydrophobic environment of the two symmetrical halogen-binding pockets (HBPs), 2/2' and 1/1', which are located in the outer binding cavity (**Figure 7**). In this orientation, the 4-hydroxy substituent can engage in hydrogen bonds with the ε-amino groups of K15/K15' residues of TTR, which in turn form salt bridges with the carboxylate group of E54/E54' (**Figure 7A**). These interactions were proposed to play a key role in stabilizing the protein-ligand interactions by restricting the entrance of solvent into the pocket[18]. Importantly, in the V122I-TTR:M-23 structure, the side chains of K15/K15' residues adopt a different conformation and cannot optimally bind to the 4-hydroxy group of M-23. Instead, the 3-hydroxy substituent forms a water-mediated hydrogen bond with K15, which is expected to be a weaker interaction and leave M-23 more exposed to the solvent (**Figure 7B**). In resemblance to the cocrystal structure of M-23 in complex with WT-TTR[17], the central carbonyl group of M-23 establishes a hydrogen bond with the hydroxyl side chain of T119 (**Figure 7**). Moreover, the 3-F and 5-OH substituents of the 3-fluoro-5-hydroxyphenyl ring establish hydrogen

bonds with A108 and S117/S117', respectively. These interactions in the inner binding cavity are not present in the crystal structures of V30M- and V122I-TTR bound to tolcapone and are expected to increase the enthalpic contribution for the binding of M-23 to these TTR variants. While it is true that M-23 presents a higher enthalpy for binding V30M-TTR relative to tolcapone, it has a lower binding enthalpy for V122I-TTR (**Figure 7C**). The fact that M-23 establishes weaker contacts in the outer binding cavity of V122I-TTR in comparison with tolcapone might explain its decreased enthalpy for binding to this protein. Surprisingly, despite its lower binding enthalpy, M-23 has a higher affinity for V122I-TTR than tolcapone. In the same manner, M-23 has a lower affinity for V30M-TTR relative to tolcapone, but a higher binding enthalpy. These discrepancies might be underlain by the lack of information on protein dynamics in X-ray crystal structures as the binding energy (ΔG) depends both on binding enthalpy and binding entropy. In agreement, even though M-23 establishes more interactions with V30M-TTR than tolcapone, its more unfavorable binding entropy leads to a lower ΔG and binding affinity. On the other hand, M-23 forms less contacts with V122I-TTR than tolcapone, but the binding entropy is more favorable, resulting in a higher ΔG and affinity (**Figure 7C**). These results highlight not only the need to incorporate techniques that allow to study protein-ligand interactions in solution to the rational design of TTR kinetic stabilizers, but also the importance of designing these molecules on top of the specific TTR variant that one wants to target.
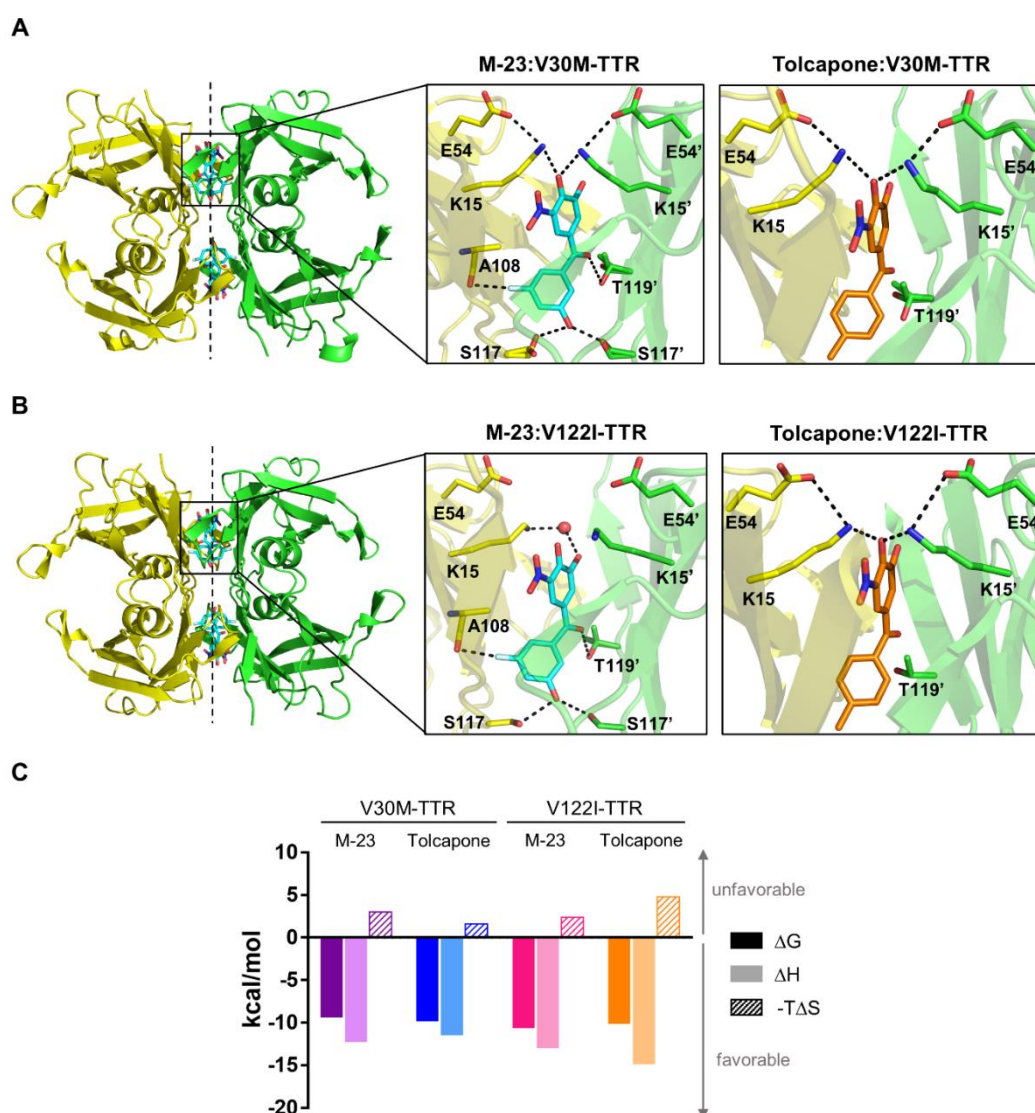
Figure 7. Binding of M-23 and tolcapone to TTR variants V30M and V122I. (A,B) Cartoon representation of V30M-TTR (A) and V122I-TTR (B) bound to M-23. The dashed lines depict the twofold symmetry axis of the AB/CD dimer-dimer interface. The insets show close-up views of one of the TTR binding sites for M-23 and tolcapone. Ligands and some of the TTR interacting residues are represented as sticks. The dashed lines illustrate key interactions between the ligand and TTR. The structural data for the interaction between tolcapone and V122I-TTR (B, right panel) was obtained from the PDB file 5A6I. (C) Graphical representation of ΔG (dark bars), ΔH (light bars) and $-T\Delta S$ (stripped bards) for the binding of M-23 and tolcapone to V30M- and V122I-TTR, as determined by ITC.

Table 1. Data collection and refinement statistics. Values in parenthesis are for the last resolution shell.

	M-23:V30M-TTR	M-23:V122I-TTR	Tolcapone:V30M-TTR
Data collection			
Beamline	ALBA-XALOC	ALBA-XALOC	ALBA-XALOC
Space group	$P2_122_1$	$P2_122_1$	$P2_122_1$
Wavelength (nm)	0.9793	0.9793	0.9794
Resolution range (Å)	42.94 – 1.67	43.71 – 1.70	42.80 – 1.57
a, b, c (Å)	42.94, 63.06, 85.34	43.71, 65.50, 83.73	42.80, 64.13, 85.00
α, β, γ (°)	α = β = γ = 90	α = β = γ = 90	α = β = γ = 90
Unique reflections	27,640	27,038	33,424
Data redundancy	6.2(5.7)	6.0(3.7)	5.9(3.4)
R_{merge}	0.067(1.085)	0.034(0.050)	0.05(1.06)
$CC_{1/2}$	0.99(0.64)	0.99(0.75)	0.99(0.50)
$(I/\sigma(I))$	10.8(1.3)	21.4(2.2)	11.8(0.9)
Completeness (%)	100(100)	99.5(95.5)	99.9(99.0)
Structure refinement			
Resolution range (Å)	42.67-1.67	41.86-1.70	65.41-1.60
Non-anomalous reflections	27,585	26,988	31,214
R_{work}/R_{free} (%)	20.9/23.5	19.8/22.6	16.0/20.4
Number of all atoms	2,031	2,036	2,011
RMSD bond (Å)/Angle (°)	0.007/1.05	0.006/1.14	0.02/1.77
Ramachandran plot			
Favored (%)	96.49	98.32	4
Allowed (%)	3.51	1.68	98
Disallowed (%)	0	0	0
Overall B factors (Å²)	28.66	27.46	26.49

HDX and FPOP analysis of the binding of V30M- and V122I-TTR to M-23 and tolcapone.
To further investigate whether MS-based footprinting techniques could open a new avenue for the development of TTR kinetic stabilizers, overcoming the drawbacks related to crystal structures, we examined their ability to provide accurate results for the interaction of M-23 and tolcapone with TTR variants V30M and V122I. For assessing which regions in V30M- and V122I-TTR become protected upon binding to M-23 and tolcapone, we performed HDX (**Figure 8A,B**). The results showed that regions 13-28, 70-78 and 111-120 on V30M- and V122I-TTR undergo less deuterium exchange after binding to M-23 and tolcapone, which implies the occurrence of both short- and long-range conformational changes on the proteins (**Figure 8C**). For V30M-TTR, the HDX protection in the C-terminal is greater with tolcapone than M-23 (**Figure 8D**). This region encompasses residues from the binding site, suggesting that V30M-TTR binds to a greater extent to tolcapone than M-23. This is in agreement with the ITC results that showed that M-23 has a lower affinity for V30M-TTR than tolcapone. For V122I-TTR, the overall effect of M-23 and tolcapone was similar (**Figure 8B**). Although the binding affinity of M-23 for V122I-TTR is higher than the one of tolcapone, it is possible that this difference is not substantially high as to detect a distinct conformational effect on the protein. The FPOP analysis of peptides with differential modification between the bound and unbound states revealed that 15 residues on V30M- and V122I-TTR were significantly less oxidized after binding to M-23 and tolcapone (**Figure 9**), including both residues that are close and far from the binding site. This confirms that the effect of M-23 and tolcapone on these proteins is not restricted to the immediate vicinity of the binding site, accordingly to the HDX data. Additionally, the results from FPOP revealed that tolcapone has a higher effect on residues from the C-terminal region of V30M-TTR than M-23 (**Figure 9A**), whereas their impact on V122I-TTR is largely similar (**Figure 9B**). Overall, the results obtained by HDX and FPOP strongly correlate with the binding affinities determined by ITC, supporting the use of these techniques to develop molecules that bind with high affinity to specific TTR variants. Moreover, these methods can identify not only short-, but also long-distance alterations on TTR structural dynamics, which cannot be detected by X-ray crystallography. In this manner, these methods provide key insights on the ligand-induced stabilization mechanism, allowing to evolve molecules with higher stabilizing potency.
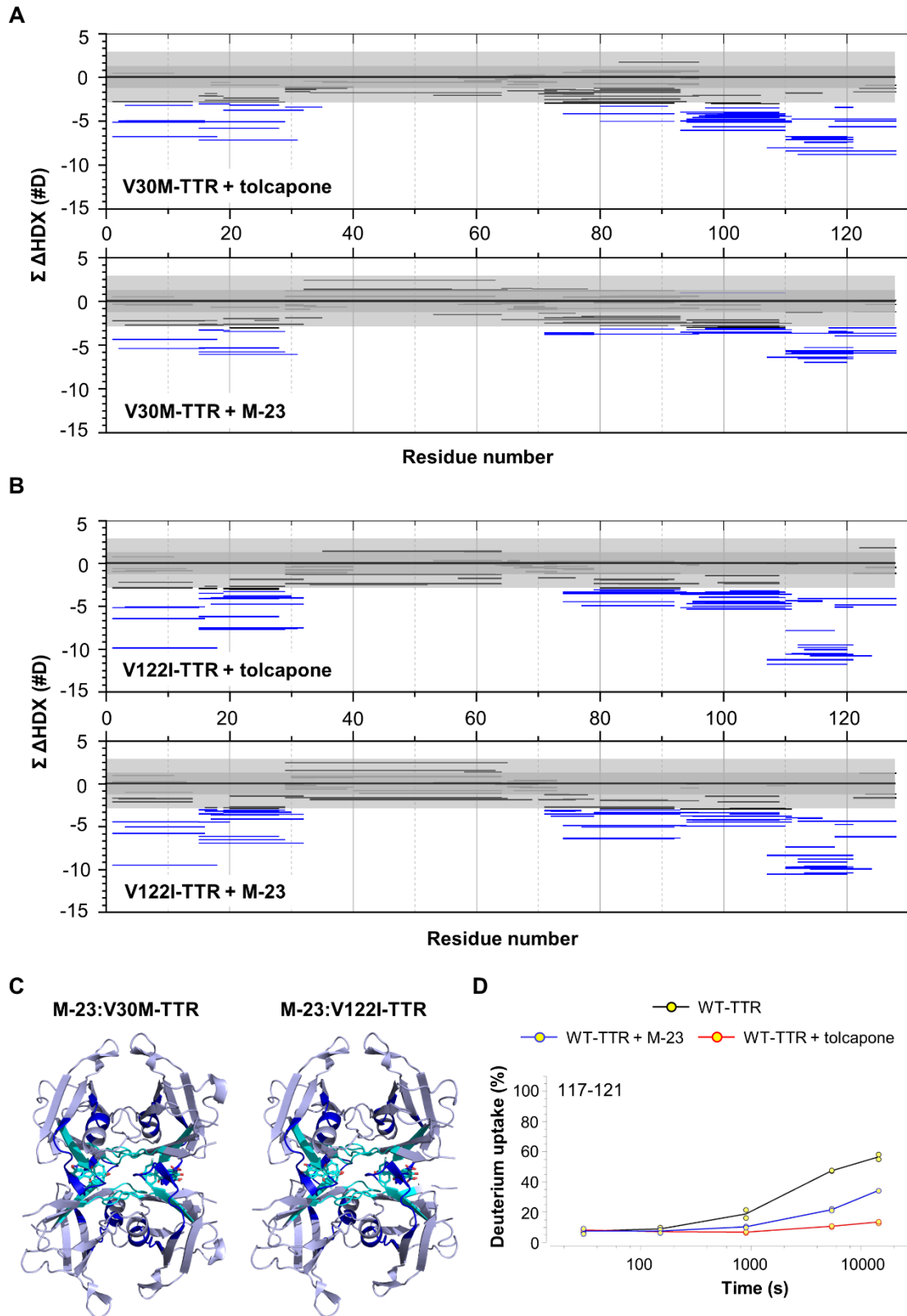
Figure 8. Effect of M-23 and tolcapone on V30M- and V122I-TTR structure as examined by HDX-MS. (A,B) Wood's plots showing cumulative HDX differences on the Y-axis (horizontal bars) between the bound and unbound state for V30M-TTR (A) and V122I-TTR (B). A negative change in the cumulative difference indicates protection upon binding to the compounds. The gray region depicts the global significance limit (p < 0.01) which is compared with cumulative differences of the peptides to assign statistically significant differences.

Peptides not reporting a significant difference are shown in dark grey. (C) Statistically significant changes in HDX are mapped onto the crystal structure of the V30M-TTR/M-23 and V122I-TTR/M-23 complex. The regions closer to the binding pocket are colored in cyan, whereas those that are further (i.e., 19-28 and 70-78) are shown in dark blue. TTR-tolcapone structures are not shown as the regions with decreased HDX are the same as for M-23. (D) HDX kinetics of V30M-TTR unbound (black) and bound to M-23 (blue) or tolcapone (red) for a peptide in the C-terminal region (117-121).
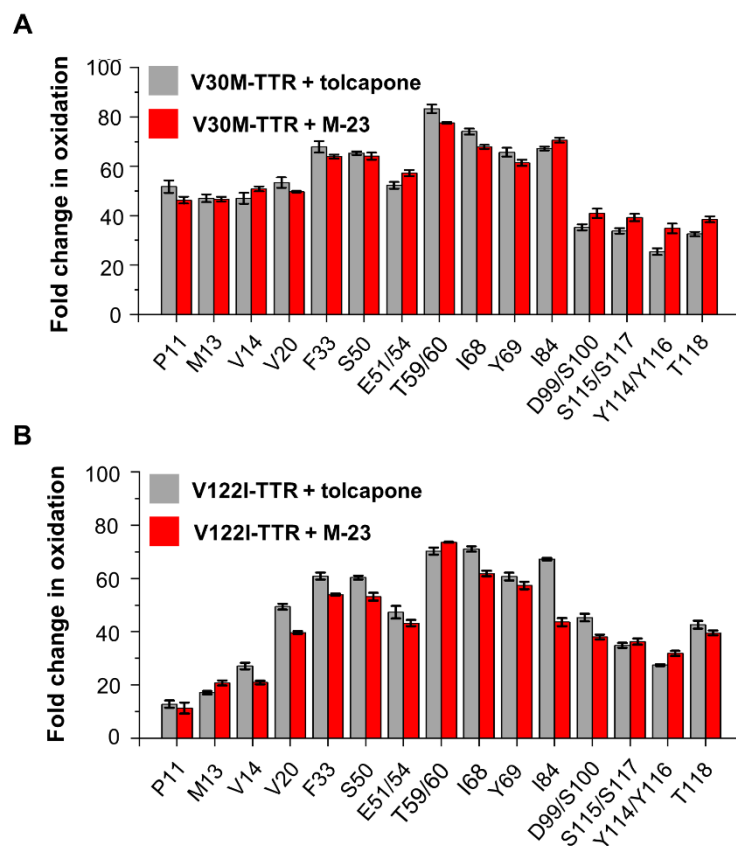
Figure 9. FPOP analysis of the binding M-23 and tolcapone to V30M- and V122I-TTR. (A,B) Residues showing substantially lower FPOP labeling after binding M-23 (red bars) and tolcapone (grey bars) relative to free V30M-TTR (A) and V122I-TTR (B).

Conclusions

In this work, we investigated, for the first time, the use of HDX and FPOP to evaluate the impact of mutations and kinetic stabilizers on TTR structure in a close-to-native environment, as well as their potential application for the design and development of potent stabilizers. According to their known impact on TTR stability[2,22], the HDX analysis of V30M- and V122I-TTR revealed that the conformational changes induced by the V30M mutation are transmitted across the entire TTR structure, whereas the ones caused by V122I are restricted to the vicinity of the mutation. Importantly, these structural differences are not captured by the X-ray crystal structures of TTR variants[19,20]. In the same manner, HDX and FPOP studies of TTR binding to M-23 and tolcapone showed that long-distance structural alterations not seen in the X-ray crystal structures could play an important role in stabilizing the protein. Moreover, we observed that both short- and long-range structural effects on WT-TTR are more pronounced with M-23 than with tolcapone, which is in

excellent agreement with its higher binding affinity and stabilizing activity[17]. On the other hand, M-23 binding to TTR variants V30M and V122I was largely similar to that of tolcapone or even slightly worse, as in the case of V122I-TTR. While these results strongly correlate with the binding affinities determined by ITC, they seem to contradict the structural insights obtained by X-ray crystallography. The analysis of the crystal structures of M-23 and tolcapone in complex with V30M-TTR showed that M-23 establishes more interactions in the binding pocket than tolcapone, opposite to what occurred for V122I-TTR. Contrarily to what was expected from these results, M-23 presents a lower binding affinity for V30M-TTR than tolcapone and a slightly higher affinity for V122I-TTR. Overall, this suggests that the lack of information on protein dynamics in X-ray crystal structures might generate misleading results, decreasing the accuracy and efficiency of structure-based drug design. Noteworthy, M-23 was designed based on the crystal structure of WT-TTR in complex with tolcapone[17]. Therefore, the results obtained herein demonstrate that is not possible to extrapolate the efficiency of TTR kinetic stabilizers between different TTR variants, highlighting the need to use the structure of the specific TTR variant one wants to target for the design of kinetic stabilizers. In this context, the fact that MS-based techniques can identify the changes that underlie the decreased stability of TTR variants offers a clear advantage. Furthermore, these tools require picomole amounts of protein, allow to analyze them under physiological conditions, and are highly practical, which makes them an attractive approach not only for the screening of TTR kinetic stabilizers, but also for the structure-based drug in general.

Materials and Methods

TTR expression and purification. The vectors encoding for V30M- and V122I-TTR were prepared by PCR site-directed mutagenesis using a pet28a vector (Novagen) encoding for the WT protein as a template. WT-TTR and TTR variants were recombinantly expressed and purified as explained before[29]. The fractions eluting from the gel filtration chromatography were analyzed by SDS-PAGE and the ones with higher purity were combined and stored at -20 °C. Protein concentration was determined spectrophotometrically at 280 nm using a molar extinction coefficient of 77 600 M^{-1} cm^{-1}.

Synthesis procedure. M-23 was prepared as previously reported[17]. Tolcapone was purchased from Fisher.

HDX-MS experiments. HDX-MS was carried out on WT-, V122I- and V30M-TTR, with and without tolcapone, and M23. A total of nine states were investigated by HDX-MS, (i) WT-TTR, (ii) V122I-TTR, (iii) V30M-TTR, (iv) WT-TTR + tolcapone, (v) WT-TTR + M-23, (vi) V122I-TTR + tolcapone, (vii) V122I-TTR + M-23, (viii) V30M-TTR + tolcapone, and (ix) V30M-TTR + M-23. For each unbound state, a stock solution of 30 μM TTR was prepared by diluting in PBS (pH 7.4) buffer. HDX was initiated by adding 5 μl of the protein solutions to 95 μl of deuterated PBS buffer and was carried out for 30, 120, 900, 3600, and 14400 s at 37 °C. At these times, HDX was quenched by adding a solution of 4 M guanidine-hydrochloride, 200 mM tris(2-carboxyethyl)phosphine, pH 2.5 at room temperature. After 2 min of incubation, the mixture was flash-frozen in liquid nitrogen and held there until chromatographic separation and mass spectral analysis. Samples were thawed quickly and introduced into the LC/MS system, submitted to 3 min of online digestion using an immobilized fungal XIII column followed by a pepsin column (2 mm × 20 mm). The flow rate was set as 200 μL/min and comprised of 0.1% formic acid aqueous solvent. The peptides from online digestion were trapped

on a ZORBAX Eclipse XDB C8 column (2.1 × 15 mm, Agilent) and desalting was carried out for 3 min. After desalting, the peptides were separated by reversed-phase chromatography using a 2.1 mm × 50 mm C18 column (2.5-μm XSelect CSH C18, Waters Corporation). The acetonitrile content was increased from 5 to 80% acetonitrile in 0.1% formic acid within 15 min of chromatographic separation at a flow rate of 100 μL/min. Except for fungal and pepsin columns, the valves and tubes were placed in an ice slush to minimize deuterium loss (back exchange) during chromatography. The eluted peptides were submitted to a maXis-II HM qTOF mass spectrometer (Bruker Daltonics, Inc.) coupled with an electrospray ionization source for detection. HDX experiments were performed in duplicate. The data analysis was carried out using HDExaminer (version 2.5.0, Sierra Analytics, Inc.). No back exchange correction was applied to the HDX data because each of the HDX comparison was differential. For the bound state, TTR and compounds were mixed in the molar ratio of 1:5 and incubated for 2 h at 37 °C. The subsequent steps were the same as discussed above.

Peptide mapping. Prior to HDX experiments, the peptides generated from double digestion were separated by chromatography and identified by the Bruker Maxis HM Q-TOF. In the MS/MS mode, cycle time was 3 s. The parent and fragment ions were analyzed utilizing Byonic and Byologic (Protein Metrics). A reverse protein sequence was included in the data analysis to exclude false positive confirmations.

Statistical validation. The statistical differences between the two states were calculated by using the global significance limit approach. The global limits were estimated using a two-tailed t-test value ($p < 0.05$ and 0.01). Besides the global limit, the cumulated difference in HDX was compared with 4.3 times of propagated error. The peptide level cumulative differences which exceed both the global limit and calculated propagated error were considered statistically significant[30].

FPOP-MS experiments. FPOP labeling was performed as previously described for other proteins[12,31]. Briefly, a KrF excimer laser (GAM Laser Inc.) generated a laser beam with an excitation wavelength of 248 nM and initiated H_2O_2 photolysis to give hydroxyl radicals. The TTR tetramers in PBS were mixed with 10 mM glutamine (scavenger) and 30 mM H_2O_2 just prior to injection into the flow tubing for FPOP. The flow rate was adjusted according to the width of the laser irradiation window to ensure 10% irradiation-excluded volume and to minimize repeated laser exposure. The total time for one sample to pass through the silica tubing was ~2.5 min. After laser irradiation, the sample was collected in a tube containing 500 nM catalase and 20 mM methionine to decompose leftover H_2O_2 and to prevent oxidation-artifacts during storage. For each sample condition described for HDX, TTR tetramers in the absence or presence of small-molecule stabilizers were incubated independently in triplicate and subjected to FPOP. In addition, control samples of TTR tetramers were handled in the same manner in triplicate, but not laser-irradiated to monitor background oxidation. Each FPOP-labeled sample was transferred into aliquots and digested overnight with trypsin at 37 °C with a protease-to-protein ratio of 1:25 (w/w). The digestion was terminated by acidifying the sample with 1% trifluoroacetic acid.

LC-MS/MS-analysis. For peptide and residue level analysis, 5 μL digested sample was submitted to LC–MS/MS analysis. Samples were preconcentrated on an Acclaim PepMap C18 column (Thermo Scientific, 100 μm × 2 cm, 5 μm, 100 Å) and desalted for 15 min before elution. Separation was performed on a 15 cm custom-packed C18 column (Magic, 75 μm × 15 cm, 5 μm, 200 Å) maintained at 45 °C by using a Nano UltiMate 3000 Rapid Separation system (Dionex, Co.). LC separation was directly coupled to online detection using a Q Exactive Plus hybrid quadrupole

orbitrap mass spectrometer with a Nanospray Flex ion source (Thermo Fisher). The top 15 abundant ions seen in the mass spectrum were subjected to higher energy collision dissociation (HCD) for identification and characterization of possible FPOP modifications. The mass resolving power was 70,000 (at m/z 400) for MS1 and 17,500 (m/z 400) for MS/MS.

Data analysis. Identification of the unmodified peptides and assigned modifications were done by using Byologic (Protein Metrics) and further validated by manual inspection. Modification sites were identified based on MS/MS. Signal intensities of the unmodified peptide (Iu) and its modified species (Iox) were integrated using Byologic (Protein Metrics) from the extracted ion chromatograms (XICs). The FPOP modification level of a peptide was calculated using the following equation: % modified = Iox/(Iox + Iu) × 100. Quantification of the modified species was based on the dominant FPOP products with oxygen addition/substitution(s) (+ 15.9949 Da, + 31.9898 Da, etc.). All the FPOP oxidation levels were corrected by subtracting the background oxidation determined from the un-illuminated FPOP controls. The error of FPOP modification was represented by the standard deviation from the triplicate experiments.

TTR *in vitro* aggregation assays. The anti-aggregational effect of M-23 and tolcapone was assessed using the standard acid-mediated TTR aggregation assay[22,32]. In short, 7 μM TTR samples (in 10 mM sodium phosphate, 100 mM KCl, 1 mM EDTA, 1 mM DTT, pH 7.0) were incubated in the absence or presence of increasing concentrations of M-23 and tolcapone. As the compounds stock solutions were prepared in 100% DMSO, the percentage of DMSO was adjusted to 5% (v/v) in all samples. After a 30 min incubation at 37 °C, the pH of the samples was lowered to 4.2 by diluting them in acidification buffer (100 mM sodium acetate, 100 mM KCl, 1 mM EDTA, 1 mM DTT, pH 4.2). The final protein concentration was 3.6 μM. After an additional incubation period of 72 h at 37 °C, sample turbidity at 340 nm was measured on a Varian Cary Eclipse Fluorescence Spectrophotometer (Agilent Technologies). All measurements were corrected by subtracting the turbidity of a sample containing the same concentration of compound, but no TTR. The values were normalized to the maximum turbidity value (100% aggregation), which corresponds to that of a sample incubated without compound.

TTR tetramer stabilization in the presence of urea. TTR samples (1.8 μM in PBS) were incubated with 3.6 μM M-23 or tolcapone for 30 min at RT and 6 M urea was added to induce denaturation. A control sample containing the same amount of DMSO rather than the compound was prepared. The extent of TTR unfolding was evaluated over time by intrinsic fluorescence spectroscopy on a FP-8200 Spectrofluorometer (Jasco). Trp residues were excited at 295 nm and three accumulations of the emission spectra were recorded from 310 to 410 nm. Trp exposure upon denaturation is accompanied by a change in the wavelength of maximum fluorescence from 335 to 355 nm, approximately. The 355/335 fluorescence intensity ratio was normalized from minimum (folded) to maximum (unfolded) and plotted against time. The ratio of the control sample after 96 h incubation at RT was considered the maximum.

Isothermal titration calorimetry. All ITC measurements were performed with protein and compounds dissolved in the same buffer (PBS buffer pH 7.0, containing 100 mM KCl, 1mM EDTA and 2.5% DMSO), and degassed. The ITC measurements were performed at 25 °C using a Nano ITC calorimeter (TA Instruments). The NanoAnalyze software (TA Instruments) was used to study the

binding isotherms. Titrations were carried out as a set of 20 injections of 100 µM compound into protein (5 µM), programmed as a 2.02 µl injection with 150 s of equilibration period. Fittings were done using the independent binding sites model provided with the system.

Crystallization and structure determination. Cocrystals of V30M-TTR/M-23, V122I-TTR/M-23 and V30M-TTR/tolcapone were obtained as previously reported[29]. In short, purified proteins (140 µM) were mixed with 10-fold molar excess of M-23/tolcapone and co-crystallized at 18 °C by hanging-drop vapor diffusion by mixing equal amounts of complex and reservoir solution. The reservoir solution contained 25-30% PEG 400, 200 mM $CaCl_2$, 100 mM HEPES, pH 7.0-7.5. The crystals were flash-frozen in liquid nitrogen (100 K) and diffraction data were recorded at the BL13-XALOC beamline from the ALBA Synchrotron in Barcelona[33]. Data were integrated and merged using XDS[34] and scaled, reduced, and further analyzed with CCP4[35]. The structures of TTR/M-23 and V30M-TTR/tolcapone complexes were determined by molecular replacement with Phenix (version 1.19.2-4158)[36] using a previous TTR structure (PDB 1F41) as a search model. Model refinement was done using Phenix[36] and model building was performed with Coot[37]. Figures were prepared using Pymol (The PyMOL Molecular Graphics System, Version 2.0, Schrödinger, LLC).

References

1   Hurshman Babbes, A. R., Powers, E. T. & Kelly, J. W. Quantification of the thermodynamically linked quaternary and tertiary structural stabilities of transthyretin and its disease-associated variants: the relationship between stability and amyloidosis. *Biochemistry* **47**, 6969-6984, doi:10.1021/bi800636q (2008).

2   Hammarstrom, P., Jiang, X., Hurshman, A. R., Powers, E. T. & Kelly, J. W. Sequence-dependent denaturation energetics: A major determinant in amyloid disease diversity. *Proceedings of the National Academy of Sciences of the United States of America* **99 Suppl 4**, 16427-16432, doi:10.1073/pnas.202495199 (2002).

3   Palaninathan, S. K. Nearly 200 X-ray crystal structures of transthyretin: what do they tell us about this protein and the design of drugs for TTR amyloidoses? *Current medicinal chemistry* **19**, 2324-2342, doi:10.2174/092986712800269335 (2012).

4   Hornberg, A., Eneqvist, T., Olofsson, A., Lundgren, E. & Sauer-Eriksson, A. E. A comparative analysis of 23 structures of the amyloidogenic protein transthyretin. *Journal of molecular biology* **302**, 649-669, doi:10.1006/jmbi.2000.4078 (2000).

5   Connelly, S., Choi, S., Johnson, S. M., Kelly, J. W. & Wilson, I. A. Structure-based design of kinetic stabilizers that ameliorate the transthyretin amyloidoses. *Current opinion in structural biology* **20**, 54-62, doi:10.1016/j.sbi.2009.12.009 (2010).

6   Johnson, S. M. *et al.* Native state kinetic stabilization as a strategy to ameliorate protein misfolding diseases: a focus on the transthyretin amyloidoses. *Accounts of chemical research* **38**, 911-921, doi:10.1021/ar020073i (2005).

7   Vallejo, D. D. *et al.* Mass Spectrometry Methods for Measuring Protein Stability. *Chemical reviews* **122**, 7690-7719, doi:10.1021/acs.chemrev.1c00857 (2022).

8   Wales, T. E. & Engen, J. R. Hydrogen exchange mass spectrometry for the analysis of protein dynamics. *Mass spectrometry reviews* **25**, 158-170, doi:10.1002/mas.20064 (2006).

9   Konermann, L., Pan, J. & Liu, Y. H. Hydrogen exchange mass spectrometry for studying protein structure and dynamics. *Chemical Society reviews* **40**, 1224-1234, doi:10.1039/c0cs00113a (2011).

10   Li, K. S., Shi, L. & Gross, M. L. Mass Spectrometry-Based Fast Photochemical Oxidation of Proteins (FPOP) for Higher Order Structure Characterization. *Accounts of chemical research* **51**, 736-744, doi:10.1021/acs.accounts.7b00593 (2018).

11   Hambly, D. M. & Gross, M. L. Laser flash photolysis of hydrogen peroxide to oxidize protein solvent-accessible residues on the microsecond timescale. *Journal of the American Society for Mass Spectrometry* **16**, 2057-2063, doi:10.1016/j.jasms.2005.09.008 (2005).

12   Li, K. S. *et al.* Hydrogen-Deuterium Exchange and Hydroxyl Radical Footprinting for Mapping Hydrophobic Interactions of Human Bromodomain with a Small Molecule Inhibitor. *Journal of the American Society for Mass Spectrometry* **30**, 2795-2804, doi:10.1007/s13361-019-02316-1 (2019).

13   Cornwell, O., Radford, S. E., Ashcroft, A. E. & Ault, J. R. Comparing Hydrogen Deuterium Exchange and Fast Photochemical Oxidation of Proteins: a Structural Characterisation of Wild-Type and DeltaN6 beta(2)-Microglobulin. *Journal of the American Society for Mass Spectrometry* **29**, 2413-2426, doi:10.1007/s13361-018-2067-y (2018).

14   Zhang, Y. *et al.* Pulsed hydrogen-deuterium exchange mass spectrometry probes conformational changes in amyloid beta (Abeta) peptide aggregation. *Proceedings of the National Academy of Sciences of the United States of America* **110**, 14604-14609, doi:10.1073/pnas.1309175110 (2013).

15   Ozohanics, O. & Ambrus, A. Hydrogen-Deuterium Exchange Mass Spectrometry: A Novel Structural Biology Approach to Structure, Dynamics and Interactions of Proteins and Their Complexes. *Life* **10**, doi:10.3390/life10110286 (2020).

16   Johnson, D. T., Di Stefano, L. H. & Jones, L. M. Fast photochemical oxidation of proteins (FPOP): A powerful mass spectrometry-based structural proteomics tool. *The Journal of biological chemistry* **294**, 11969-11979, doi:10.1074/jbc.REV119.006218 (2019).

17   Pinheiro, F. *et al.* Development of a Highly Potent Transthyretin Amyloidogenesis Inhibitor: Design, Synthesis, and Evaluation. *Journal of medicinal chemistry* **65**, 14673-14691, doi:10.1021/acs.jmedchem.2c01195 (2022).

18   Sant'Anna, R. *et al.* Repositioning tolcapone as a potent inhibitor of transthyretin amyloidogenesis and associated cellular toxicity. *Nature communications* **7**, 10787, doi:10.1038/ncomms10787 (2016).

19   Cendron, L. *et al.* Amyloidogenic potential of transthyretin variants: insights from structural and computational analyses. *The Journal of biological chemistry* **284**, 25832-25841, doi:10.1074/jbc.M109.017657 (2009).

20   Damas, A. M., Ribeiro, S., Lamzin, V. S., Palha, J. A. & Saraiva, M. J. Structure of the Val122Ile variant transthyretin - a cardiomyopathic mutant. *Acta crystallographica. Section D, Biological crystallography* **52**, 966-972, doi:10.1107/S0907444996003307 (1996).

21   Leach, B. I., Zhang, X., Kelly, J. W., Dyson, H. J. & Wright, P. E. NMR Measurements Reveal the Structural Basis of Transthyretin Destabilization by Pathogenic Mutations. *Biochemistry* **57**, 4421-4430, doi:10.1021/acs.biochem.8b00642 (2018).

22   Jiang, X., Buxbaum, J. N. & Kelly, J. W. The V122I cardiomyopathy variant of transthyretin increases the velocity of rate-limiting tetramer dissociation, resulting in accelerated amyloidosis. *Proceedings of the National Academy of Sciences of the United States of America* **98**, 14943-14948, doi:10.1073/pnas.261419998 (2001).

23   Blake, C. C., Geisow, M. J., Oatley, S. J., Rerat, B. & Rerat, C. Structure of prealbumin: secondary, tertiary and quaternary interactions determined by Fourier refinement at 1.8 A. *Journal of molecular biology* **121**, 339-356, doi:10.1016/0022-2836(78)90368-6 (1978).

24   Palaninathan, S. K., Mohamedmohaideen, N. N., Snee, W. C., Kelly, J. W. & Sacchettini, J. C. Structural insight into pH-induced conformational changes within the native human transthyretin tetramer. *Journal of molecular biology* **382**, 1157-1167, doi:10.1016/j.jmb.2008.07.029 (2008).

25   Ferguson, J. A., Sun, X., Dyson, H. J. & Wright, P. E. Thermodynamic Stability and Aggregation Kinetics of EF Helix and EF Loop Variants of Transthyretin. *Biochemistry* **60**, 756-764, doi:10.1021/acs.biochem.1c00073 (2021).

26   Neto-Silva, R. M. *et al.* X-ray crystallographic studies of two transthyretin variants: further insights into amyloidogenesis. *Acta crystallographica. Section D, Biological crystallography* **61**, 333-339, doi:10.1107/S0907444904034316 (2005).

27   Wang, Y. S. *et al.* A molecular basis for tetramer destabilization and aggregation of transthyretin Ala97Ser. *Protein science : a publication of the Protein Society* **32**, e4610, doi:10.1002/pro.4610 (2023).

28   Saelices, L. *et al.* Uncovering the Mechanism of Aggregation of Human Transthyretin. *The Journal of biological chemistry* **290**, 28932-28943, doi:10.1074/jbc.M115.659912 (2015).

29   Pinheiro, F. *et al.* Tolcapone, a potent aggregation inhibitor for the treatment of familial leptomeningeal amyloidosis. *The FEBS journal* **288**, 310-324, doi:10.1111/febs.15339 (2021).

30   Kailasan, S. *et al.* Antigenic landscapes on Staphylococcus aureus pore-forming toxins reveal insights into specificity and cross-neutralization. *mAbs* **14**, 2083467, doi:10.1080/19420862.2022.2083467 (2022).

31   Li, K. S. *et al.* Orthogonal Mass Spectrometry-Based Footprinting for Epitope Mapping and Structural Characterization: The IL-6 Receptor upon Binding of Protein Therapeutics. *Analytical chemistry* **89**, 7742-7749, doi:10.1021/acs.analchem.7b01748 (2017).

32   Jiang, X. *et al.* An engineered transthyretin monomer that is nonamyloidogenic, unless it is partially denatured. *Biochemistry* **40**, 11442-11452, doi:10.1021/bi011194d (2001).

33   Juanhuix, J. *et al.* Developments in optics and performance at BL13-XALOC, the macromolecular crystallography beamline at the ALBA synchrotron. *Journal of synchrotron radiation* **21**, 679-689, doi:10.1107/S160057751400825X (2014).

34   Kabsch, W. Integration, scaling, space-group assignment and post-refinement. *Acta crystallographica. Section D, Biological crystallography* **66**, 133-144, doi:10.1107/S0907444909047374 (2010).

35   Winn, M. D. *et al.* Overview of the CCP4 suite and current developments. *Acta crystallographica. Section D, Biological crystallography* **67**, 235-242, doi:10.1107/S0907444910045749 (2011).

36   Adams, P. D. *et al.* PHENIX: a comprehensive Python-based system for macromolecular structure solution. *Acta crystallographica. Section D, Biological crystallography* **66**, 213-221, doi:10.1107/S0907444909052925 (2010).

37   Emsley, P., Lohkamp, B., Scott, W. G. & Cowtan, K. Features and development of Coot. *Acta crystallographica. Section D, Biological crystallography* **66**, 486-501, doi:10.1107/S0907444910007493 (2010).

CONCLUDING REMARKS

Chapter 1 – Tolcapone, a potent aggregation inhibitor for the treatment of familial leptomeningeal amyloidosis

- Tolcapone inhibits the aggregation of A25T-, V30G- and Y114C-TTR.
- Tolcapone protects V30G- and Y114C-TTR from urea-induced unfolding. Despite the anti-aggregational effect of tolcapone for A25T-TTR, it does not stabilize this variant in the assayed conditions.
- A25T-TTR tetramer dissociation and monomer unfolding are not significantly linked at the concentration used in these experiments, suggesting that only a fraction of protein is in a native tetrameric form.
- The initial tetramer population for leptomeningeal-associated TTR variants under native conditions, especially A25-TTR, is lower than for WT-TTR, and fairly correlates with tolcapone's antiaggregational activity.
- Tolcapone binds with high affinity to A25T-, V30G- and Y114C-TTR. Independently of the TTR variant, the binding is always enthalpically driven.
- Crystal structures of TTR/tolcapone complexes reveal the formation of hydrophobic and polar interactions, similar to those described for the WT protein, pointing to a canonical mechanism of TTR kinetic stabilization.
- The stabilizing and anti-aggregational activity of tolcapone over leptomeningeal-associated TTR variants, together with its ability to cross the blood-brain barrier, indicate that it might become a first broad-spectrum drug to treat all forms of TTR amyloidosis.

Chapter 2 – Development of a highly potent transthyretin amyloidogenesis inhibitor: Design, synthesis and evaluation

- Molecular dynamics (MD) simulations provide atomic information on TTR-ligand interactions and allow to rank the molecules according to their binding energetics.
- The application of MD simulations to the rational design of tolcapone derivatives led to the discovery of M-23, a novel TTR kinetic stabilizer presenting one of the highest affinities described for TTR so far.
- M-23 binds to TTR with an affinity >5-fold than that of tolcapone and with a higher affinity than tafamidis, especially for the second binding site. The exceptional affinity of M-23 results from its very high binding enthalpy.
- M-23 has a higher stabilizing and anti-aggregational activity *in vitro* than tolcapone.
- M-23 selectively binds TTR in human plasma, displaying a higher TTR stabilizing effect than tolcapone and tafamidis, according to its optimized binding enthalpy.
- The TTR/M-23 crystal structure confirms the existence of new contacts between the ligand and the protein, as predicted by MD simulations, which likely underlain its higher affinity and binding enthalpy.
- M-23 displays no cytotoxicity against HeLa and HepG2 cell lines.
- Incorporating MD simulations to the design of TTR ligands constitutes a time and cost-effective strategy for finding molecules that, as M-23, hold the potential to become potent ATTR disease modifiers.

Chapter 3 – PITB: a high affinity transthyretin aggregation inhibitor with optimal pharmacokinetic properties

- M-23 presents a poor pharmacokinetic profile, compromising its clinical use.
- The 3-*O*-methylation of M-23 *in vivo* generates a metabolite, called PITB, with higher stability.
- PITB inhibits the dissociation of WT-TTR and the two most common TTR variants V30M and V122I, hindering their aggregation.
- PITB binds with nanomolar affinity to WT-, V30M- and V122I-TTR.
- The TTR/PITB crystal structures reveal the formation of new stabilizing contacts, identical to the ones established by M-23.
- PITB presents a high binding selectivity and stabilizing activity in plasma from patients, outperforming tolcapone under the same conditions.
- PITB shows no toxic effects on HeLa and HepG2 cell lines.
- The pharmacokinetic evaluation of PITB in mice demonstrates that it has remarkable pharmacokinetic properties.
- The strong stabilizing effect of PITB in plasma, its apparent lack of toxicity, and its excellent pharmacokinetic profile, turn PITB into a very promising candidate to treat ATTR.

Chapter 4 – Hydrogen deuterium exchange and fast photochemical oxidation of proteins coupled with mass spectrometry in transthyretin therapeutics

- Hydrogen deuterium exchange (HDX) analysis of V30M- and V122I-TTR shows that the V30M mutation induces a large-scale destabilization of TTR structure, while the effect of V122I is centered around the site of the mutation. These differences are not observed in the X-ray crystal structures of TTR variants.
- HDX and fast photochemical oxidation of proteins (FPOP) studies reveal that the stabilization of WT-, V30M- and V122I-TTR upon binding to M-23 and tolcapone results from short range conformational changes, but also long-distance effects that are not detected by X-ray crystallography.
- The results obtained by HDX and FPOP indicate that M-23 causes greater structural effects on WT-TTR than tolcapone, in agreement with its higher binding affinity and stabilization potency.
- M-23 effectively stabilizes and inhibits the aggregation of V30M- and V122I-TTR *in vitro*, exerting a similar effect than tolcapone.
- M-23 presents a lower binding affinity for V30M-TTR than tolcapone, despite its higher binding enthalpy. On the other hand, M-23 has a higher affinity for V122I-TTR relative to tolcapone, but a lower binding enthalpy.
- The crystal structures of M-23 and tolcapone bound to V30M-TTR reveal that M-23 forms a greater number of interactions with the protein than tolcapone, contrarily to what is observed for V122I-TTR. This is in contrast with the binding affinities determined by ITC, suggesting that X-ray crystal structures might generate misleading results.
- HDX and FPOP analysis of the binding of M-23 to V30M- and V122I-TTR indicate that it exerts a similar impact on the structure than tolcapone or slightly inferior, as in the case of V122I-TTR, which largely agrees with the ITC data.

- HDX and FPOP provide key insights into the effect of pathogenic mutations and kinetic stabilizers on TTR structure that together with their ability to analyze proteins in near-native conditions, using minor amounts of protein, and the possibility to implement them routinely, makes them an attractive approach for the screening of variant-specific TTR kinetic stabilizers.

REFERENCES

1   Halling, P. J. Proteins: Structures and molecular properties (2nd edition). by Thomas E. Creighton, W. H. Freeman, New York, 1992, xiii + 512 pp. ISBN 0-7167-7030-X. *Journal of Chemical Technology & Biotechnology* **62**, 105-105, doi:https://doi.org/10.1002/jctb.280620121 (1995).

2   Anfinsen, C. B. Principles that govern the folding of protein chains. *Science* **181**, 223-230, doi:10.1126/science.181.4096.223 (1973).

3   Dobson, C. M. Protein folding and misfolding. *Nature* **426**, 884-890, doi:10.1038/nature02261 (2003).

4   Jahn, T. R. & Radford, S. E. Folding versus aggregation: polypeptide conformations on competing pathways. *Archives of biochemistry and biophysics* **469**, 100-117, doi:10.1016/j.abb.2007.05.015 (2008).

5   Eichner, T. & Radford, S. E. A diversity of assembly mechanisms of a generic amyloid fold. *Molecular cell* **43**, 8-18, doi:10.1016/j.molcel.2011.05.012 (2011).

6   Chiti, F. & Dobson, C. M. Protein Misfolding, Amyloid Formation, and Human Disease: A Summary of Progress Over the Last Decade. *Annual review of biochemistry* **86**, 27-68, doi:10.1146/annurev-biochem-061516-045115 (2017).

7   Anfinsen, C. B., Haber, E., Sela, M. & White, F. H., Jr. The kinetics of formation of native ribonuclease during oxidation of the reduced polypeptide chain. *Proceedings of the National Academy of Sciences of the United States of America* **47**, 1309-1314, doi:10.1073/pnas.47.9.1309 (1961).

8   Redfern, O. C., Dessailly, B. & Orengo, C. A. Exploring the structure and function paradigm. *Current opinion in structural biology* **18**, 394-402, doi:10.1016/j.sbi.2008.05.007 (2008).

9   Levinthal, C. How to fold graciously. *Mossbauer Spectroscopy in Biological Systems Proceedings* **67**, 22-26 (1969).

10   Wetlaufer, D. B. Nucleation, rapid folding, and globular intrachain regions in proteins. *Proceedings of the National Academy of Sciences of the United States of America* **70**, 697-701, doi:10.1073/pnas.70.3.697 (1973).

11   Karplus, M. & Weaver, D. L. Protein-folding dynamics. *Nature* **260**, 404-406, doi:10.1038/260404a0 (1976).

12   Pace, C. N. *et al.* Contribution of hydrophobic interactions to protein stability. *Journal of molecular biology* **408**, 514-528, doi:10.1016/j.jmb.2011.02.053 (2011).

13   Itzhaki, L. S., Otzen, D. E. & Fersht, A. R. The structure of the transition state for folding of chymotrypsin inhibitor 2 analysed by protein engineering methods: evidence for a nucleation-condensation mechanism for protein folding. *Journal of molecular biology* **254**, 260-288, doi:10.1006/jmbi.1995.0616 (1995).

14   Fersht, A. R. Optimization of rates of protein folding: the nucleation-condensation mechanism and its implications. *Proceedings of the National Academy of Sciences of the United States of America* **92**, 10869-10873, doi:10.1073/pnas.92.24.10869 (1995).

15   Wolynes, P. G., Onuchic, J. N. & Thirumalai, D. Navigating the folding routes. *Science* **267**, 1619-1620, doi:10.1126/science.7886447 (1995).

16   Dill, K. A. & Chan, H. S. From Levinthal to pathways to funnels. *Nature structural biology* **4**, 10-19, doi:10.1038/nsb0197-10 (1997).

17   Dill, K. A. & MacCallum, J. L. The protein-folding problem, 50 years on. *Science* **338**, 1042-1046, doi:10.1126/science.1219021 (2012).

18   Dobson, C. M., Sali, A. & Karplus, M. Protein Folding: A Perspective from Theory and Experiment. *Angewandte Chemie* **37**, 868-893, doi:10.1002/(SICI)1521-3773(19980420)37:7<868::AID-ANIE868>3.0.CO;2-H (1998).

19   Ward, J. J., Sodhi, J. S., McGuffin, L. J., Buxton, B. F. & Jones, D. T. Prediction and functional analysis of native disorder in proteins from the three kingdoms of life. *Journal of molecular biology* **337**, 635-645, doi:10.1016/j.jmb.2004.02.002 (2004).

20   Uversky, V. N., Oldfield, C. J. & Dunker, A. K. Intrinsically disordered proteins in human diseases: introducing the D2 concept. *Annual review of biophysics* **37**, 215-246, doi:10.1146/annurev.biophys.37.032807.125924 (2008).

21   Tompa, P. Intrinsically disordered proteins: a 10-year recap. *Trends in biochemical sciences* **37**, 509-516, doi:10.1016/j.tibs.2012.08.004 (2012).

22   Bahramali, G., Goliaei, B., Minuchehr, Z. & Marashi, S. A. A network biology approach to understanding the importance of chameleon proteins in human physiology and pathology. *Amino acids* **49**, 303-315, doi:10.1007/s00726-016-2361-6 (2017).

23   Mezei, M. Chameleon sequences in the PDB. *Protein engineering* **11**, 411-414, doi:10.1093/protein/11.6.411 (1998).

24   Bahramali, G., Goliaei, B., Minuchehr, Z. & Salari, A. Chameleon sequences in neurodegenerative diseases. *Biochemical and biophysical research communications* **472**, 209-216, doi:10.1016/j.bbrc.2016.01.187 (2016).

25   Gendoo, D. M. & Harrison, P. M. Discordant and chameleon sequences: their distribution and implications for amyloidogenicity. *Protein science : a publication of the Protein Society* **20**, 567-579, doi:10.1002/pro.590 (2011).

26   Uversky, V. N. The triple power of D(3): protein intrinsic disorder in degenerative diseases. *Frontiers in bioscience* **19**, 181-258, doi:10.2741/4204 (2014).

27   Chiti, F. & Dobson, C. M. Amyloid formation by globular proteins under native conditions. *Nature chemical biology* **5**, 15-22, doi:10.1038/nchembio.131 (2009).

28   Ke, P. C. *et al.* Half a century of amyloids: past, present and future. *Chemical Society reviews* **49**, 5473-5509, doi:10.1039/c9cs00199a (2020).

29   Fandrich, M. & Dobson, C. M. The behaviour of polyamino acids reveals an inverse side chain effect in amyloid structure formation. *The EMBO journal* **21**, 5682-5690, doi:10.1093/emboj/cdf573 (2002).

30   Adler-Abramovich, L. *et al.* Phenylalanine assembly into toxic fibrils suggests amyloid etiology in phenylketonuria. *Nature chemical biology* **8**, 701-706, doi:10.1038/nchembio.1002 (2012).

31   Adamcik, J. & Mezzenga, R. Amyloid Polymorphism in the Protein Folding and Aggregation Energy Landscape. *Angewandte Chemie* **57**, 8370-8382, doi:10.1002/anie.201713416 (2018).

32   Neudecker, P. *et al.* Structure of an intermediate state in protein folding and aggregation. *Science* **336**, 362-366, doi:10.1126/science.1214203 (2012).

33   Frauenfelder, H., Sligar, S. G. & Wolynes, P. G. The energy landscapes and motions of proteins. *Science* **254**, 1598-1603, doi:10.1126/science.1749933 (1991).

34   Kern, D. & Zuiderweg, E. R. The role of dynamics in allosteric regulation. *Current opinion in structural biology* **13**, 748-757, doi:10.1016/j.sbi.2003.10.008 (2003).

35   Dumoulin, M., Kumita, J. R. & Dobson, C. M. Normal and aberrant biological self-assembly: Insights from studies of human lysozyme and its amyloidogenic variants. *Accounts of chemical research* **39**, 603-610, doi:10.1021/ar050070g (2006).

36   Johnson, R. J. *et al.* Rationalising lysozyme amyloidosis: insights from the structure and solution dynamics of T70N lysozyme. *Journal of molecular biology* **352**, 823-836, doi:10.1016/j.jmb.2005.07.040 (2005).

37   Liu, K., Cho, H. S., Lashuel, H. A., Kelly, J. W. & Wemmer, D. E. A glimpse of a possible amyloidogenic intermediate of transthyretin. *Nature structural biology* **7**, 754-757, doi:10.1038/78980 (2000).

38   Hammarstrom, P., Jiang, X., Hurshman, A. R., Powers, E. T. & Kelly, J. W. Sequence-dependent denaturation energetics: A major determinant in amyloid disease diversity. *Proceedings of the National Academy of Sciences of the United States of America* **99 Suppl 4**, 16427-16432, doi:10.1073/pnas.202495199 (2002).

39   Uversky, V. N. Amyloidogenesis of natively unfolded proteins. *Current Alzheimer research* **5**, 260-287, doi:10.2174/156720508784533312 (2008).

40   Chirita, C. N., Congdon, E. E., Yin, H. & Kuret, J. Triggers of full-length tau aggregation: a role for partially folded intermediates. *Biochemistry* **44**, 5862-5872, doi:10.1021/bi0500123 (2005).

41   Romling, U., Bian, Z., Hammar, M., Sierralta, W. D. & Normark, S. Curli fibers are highly conserved between Salmonella typhimurium and Escherichia coli with respect to operon structure and regulation. *Journal of bacteriology* **180**, 722-731, doi:10.1128/JB.180.3.722-731.1998 (1998).

42   Santos, J. & Ventura, S. Functional Amyloids Germinate in Plants. *Trends in plant science* **26**, 7-10, doi:10.1016/j.tplants.2020.10.001 (2021).

43   Fowler, D. M. *et al.* Functional amyloid formation within mammalian tissue. *PLoS biology* **4**, e6, doi:10.1371/journal.pbio.0040006 (2006).

44   Chapman, M. R. *et al.* Role of Escherichia coli curli operons in directing amyloid fiber formation. *Science* **295**, 851-855, doi:10.1126/science.1067484 (2002).

45   King, C. Y. *et al.* Prion-inducing domain 2-114 of yeast Sup35 protein transforms in vitro into amyloid-like filaments. *Proceedings of the National Academy of Sciences of the United States of America* **94**, 6618-6622, doi:10.1073/pnas.94.13.6618 (1997).

46   Baxa, U. *et al.* Filaments of the Ure2p prion protein have a cross-beta core structure. *Journal of structural biology* **150**, 170-179, doi:10.1016/j.jsb.2005.02.007 (2005).

47   Dos Reis, S. *et al.* The HET-s prion protein of the filamentous fungus Podospora anserina aggregates in vitro into amyloid-like fibrils. *The Journal of biological chemistry* **277**, 5703-5706, doi:10.1074/jbc.M110183200 (2002).

48   Watt, B. *et al.* N-terminal domains elicit formation of functional Pmel17 amyloid fibrils. *The Journal of biological chemistry* **284**, 35543-35555, doi:10.1074/jbc.M109.047449 (2009).

49   Maji, S. K. *et al.* Functional amyloids as natural storage of peptide hormones in pituitary secretory granules. *Science* **325**, 328-332, doi:10.1126/science.1173155 (2009).

50   Knowles, T. P. & Mezzenga, R. Amyloid Fibrils as Building Blocks for Natural and Artificial Functional Materials. *Advanced materials* **28**, 6546-6561, doi:10.1002/adma.201505961 (2016).

51   Diaz-Caballero, M., Fernandez, M. R., Navarro, S. & Ventura, S. Prion-based nanomaterials and their emerging applications. *Prion* **12**, 266-272, doi:10.1080/19336896.2018.1521235 (2018).

52   Sunde, M. & Blake, C. The structure of amyloid fibrils by electron microscopy and X-ray diffraction. *Advances in protein chemistry* **50**, 123-159, doi:10.1016/s0065-3233(08)60320-4 (1997).

53   Sabate, R. & Ventura, S. Cross-beta-sheet supersecondary structure in amyloid folds: techniques for detection and characterization. *Methods in molecular biology* **932**, 237-257, doi:10.1007/978-1-62703-065-6_15 (2013).

54   Petkova, A. T. *et al.* A structural model for Alzheimer's beta -amyloid fibrils based on experimental constraints from solid state NMR. *Proceedings of the National Academy of Sciences of the United States of America* **99**, 16742-16747, doi:10.1073/pnas.262663499 (2002).

55   Fitzpatrick, A. W. *et al.* Atomic structure and hierarchical assembly of a cross-beta amyloid fibril. *Proceedings of the National Academy of Sciences of the United States of America* **110**, 5468-5473, doi:10.1073/pnas.1219476110 (2013).

56   Guerrero-Ferreira, R. *et al.* Cryo-EM structure of alpha-synuclein fibrils. *eLife* **7**, doi:10.7554/eLife.36402 (2018).

57   Weirich, F. *et al.* Structural Characterization of Fibrils from Recombinant Human Islet Amyloid Polypeptide by Solid-State NMR: The Central FGAILS Segment Is Part of the beta-Sheet Core. *PLoS one* **11**, e0161243, doi:10.1371/journal.pone.0161243 (2016).

58   Close, W. *et al.* Physical basis of amyloid fibril polymorphism. *Nature communications* **9**, 699, doi:10.1038/s41467-018-03164-5 (2018).

59   Fitzpatrick, A. W. P. *et al.* Cryo-EM structures of tau filaments from Alzheimer's disease. *Nature* **547**, 185-190, doi:10.1038/nature23002 (2017).

60   Pinheiro, F., Santos, J. & Ventura, S. AlphaFold and the amyloid landscape. *Journal of molecular biology* **433**, 167059, doi:10.1016/j.jmb.2021.167059 (2021).

61   Nilsson, M. R. Techniques to study amyloid fibril formation in vitro. *Methods* **34**, 151-160, doi:10.1016/j.ymeth.2004.03.012 (2004).

62   Monsellier, E. & Chiti, F. Prevention of amyloid-like aggregation as a driving force of protein evolution. *EMBO reports* **8**, 737-742, doi:10.1038/sj.embor.7401034 (2007).

63   Watters, A. L. *et al.* The highly cooperative folding of small naturally occurring proteins is likely the result of natural selection. *Cell* **128**, 613-624, doi:10.1016/j.cell.2006.12.042 (2007).

64   Barral, J. M., Broadley, S. A., Schaffar, G. & Hartl, F. U. Roles of molecular chaperones in protein misfolding diseases. *Seminars in cell & developmental biology* **15**, 17-29, doi:10.1016/j.semcdb.2003.12.010 (2004).

65   Balchin, D., Hayer-Hartl, M. & Hartl, F. U. In vivo aspects of protein folding and quality control. *Science* **353**, aac4354, doi:10.1126/science.aac4354 (2016).

66   Lin, Z. & Rye, H. S. GroEL-mediated protein folding: making the impossible, possible. *Critical reviews in biochemistry and molecular biology* **41**, 211-239, doi:10.1080/10409230600760382 (2006).

67   Schubert, U. *et al.* Rapid degradation of a large fraction of newly synthesized proteins by proteasomes. *Nature* **404**, 770-774, doi:10.1038/35008096 (2000).

68   Komatsu, M. *et al.* Loss of autophagy in the central nervous system causes neurodegeneration in mice. *Nature* **441**, 880-884, doi:10.1038/nature04723 (2006).

69   McKinnon, C. & Tabrizi, S. J. The ubiquitin-proteasome system in neurodegeneration. *Antioxidants & redox signaling* **21**, 2302-2321, doi:10.1089/ars.2013.5802 (2014).

70   Martinez-Lopez, N., Athonvarangkul, D. & Singh, R. Autophagy and aging. *Advances in experimental medicine and biology* **847**, 73-87, doi:10.1007/978-1-4939-2404-2_3 (2015).

71   Olzscha, H. *et al.* Amyloid-like aggregates sequester numerous metastable proteins with essential cellular functions. *Cell* **144**, 67-78, doi:10.1016/j.cell.2010.11.050 (2011).

72   Labbadia, J. & Morimoto, R. I. The biology of proteostasis in aging and disease. *Annual review of biochemistry* **84**, 435-464, doi:10.1146/annurev-biochem-060614-033955 (2015).

73   Steward, A., Adhya, S. & Clarke, J. Sequence conservation in Ig-like domains: the role of highly conserved proline residues in the fibronectin type III superfamily. *Journal of molecular biology* **318**, 935-940, doi:10.1016/S0022-2836(02)00184-5 (2002).

74   Parrini, C. *et al.* Glycine residues appear to be evolutionarily conserved for their ability to inhibit aggregation. *Structure* **13**, 1143-1151, doi:10.1016/j.str.2005.04.022 (2005).

75   Rousseau, F., Serrano, L. & Schymkowitz, J. W. How evolutionary pressure against protein aggregation shaped chaperone specificity. *Journal of molecular biology* **355**, 1037-1047, doi:10.1016/j.jmb.2005.11.035 (2006).

76   Ventura, S. *et al.* Short amino acid stretches can mediate amyloid formation in globular proteins: the Src homology 3 (SH3) case. *Proceedings of the National Academy of Sciences of the United States of America* **101**, 7258-7263, doi:10.1073/pnas.0308249101 (2004).

77   Beerten, J., Schymkowitz, J. & Rousseau, F. Aggregation prone regions and gatekeeping residues in protein sequences. *Current topics in medicinal chemistry* **12**, 2470-2478, doi:10.2174/1568026611212220003 (2012).

78   Schwartz, R., Istrail, S. & King, J. Frequencies of amino acid strings in globular protein sequences indicate suppression of blocks of consecutive hydrophobic residues. *Protein science : a publication of the Protein Society* **10**, 1023-1031, doi:10.1110/ps.33201 (2001).

79   Chiti, F. *et al.* Studies of the aggregation of mutant proteins in vitro provide insights into the genetics of amyloid diseases. *Proceedings of the National Academy of Sciences of the United States of America* **99 Suppl 4**, 16419-16426, doi:10.1073/pnas.212527999 (2002).

80   DuBay, K. F. *et al.* Prediction of the absolute aggregation rates of amyloidogenic polypeptide chains. *Journal of molecular biology* **341**, 1317-1326, doi:10.1016/j.jmb.2004.06.043 (2004).

81   Morel, B., Varela, L., Azuaga, A. I. & Conejero-Lara, F. Environmental conditions affect the kinetics of nucleation of amyloid fibrils and determine their morphology. *Biophysical journal* **99**, 3801-3810, doi:10.1016/j.bpj.2010.10.039 (2010).

82   Uversky, V. N. Natively unfolded proteins: a point where biology waits for physics. *Protein science : a publication of the Protein Society* **11**, 739-756, doi:10.1110/ps.4210102 (2002).

83   Linding, R., Schymkowitz, J., Rousseau, F., Diella, F. & Serrano, L. A comparative study of the relationship between protein structure and beta-aggregation in globular and intrinsically disordered proteins. *Journal of molecular biology* **342**, 345-353, doi:10.1016/j.jmb.2004.06.088 (2004).

84   Tartaglia, G. G., Pechmann, S., Dobson, C. M. & Vendruscolo, M. Life on the edge: a link between gene expression levels and aggregation rates of human proteins. *Trends in biochemical sciences* **32**, 204-206, doi:10.1016/j.tibs.2007.03.005 (2007).

85   Adams, D., Koike, H., Slama, M. & Coelho, T. Hereditary transthyretin amyloidosis: a model of medical progress for a fatal disease. *Nature reviews. Neurology* **15**, 387-404, doi:10.1038/s41582-019-0210-4 (2019).

86   Andrade, C. A peculiar form of peripheral neuropathy; familiar atypical generalized amyloidosis with special involvement of the peripheral nerves. *Brain : a journal of neurology* **75**, 408-427, doi:10.1093/brain/75.3.408 (1952).

87   Araki, S. Type I familial amyloidotic polyneuropathy (Japanese type). *Brain & development* **6**, 128-133, doi:10.1016/s0387-7604(84)80061-3 (1984).

88   Sousa, A., Andersson, R., Drugge, U., Holmgren, G. & Sandgren, O. Familial amyloidotic polyneuropathy in Sweden: geographical distribution, age of onset, and prevalence. *Human heredity* **43**, 288-294, doi:10.1159/000154146 (1993).

89   Cruz, M. W. *et al.* Epidemiological and clinical characteristics of persons with transthyretin hereditary amyloid polyneuropathy: a global synthesis of 532 cases. *Amyloid : the international journal of experimental and clinical investigation : the official journal of the International Society of Amyloidosis* **24**, 109-110, doi:10.1080/13506129.2017.1292902 (2017).

90   Benson, M. D. *et al.* Amyloid nomenclature 2020: update and recommendations by the International Society of Amyloidosis (ISA) nomenclature committee. *Amyloid : the international journal of experimental and clinical investigation : the official journal of the International Society of Amyloidosis* **27**, 217-222, doi:10.1080/13506129.2020.1835263 (2020).

91   Westermark, P., Sletten, K., Johansson, B. & Cornwell, G. G., 3rd. Fibril in senile systemic amyloidosis is derived from normal transthyretin. *Proceedings of the National Academy of Sciences of the United States of America* **87**, 2843-2845, doi:10.1073/pnas.87.7.2843 (1990).

92   Cornwell, G. G., 3rd, Sletten, K., Johansson, B. & Westermark, P. Evidence that the amyloid fibril protein in senile systemic amyloidosis is derived from normal prealbumin. *Biochemical and biophysical research communications* **154**, 648-653, doi:10.1016/0006-291x(88)90188-x (1988).

93   Connors, L. H. *et al.* Heart Failure Resulting From Age-Related Cardiac Amyloid Disease Associated With Wild-Type Transthyretin: A Prospective, Observational Cohort Study. *Circulation* **133**, 282-290, doi:10.1161/CIRCULATIONAHA.115.018852 (2016).

94   Connors, L. H. *et al.* Clinical features and survival in senile systemic amyloidosis: comparison to familial transthyretin cardiomyopathy. *Amyloid : the international journal of experimental and clinical investigation : the official journal of the International Society of Amyloidosis* **18 Suppl 1**, 157-159, doi:10.3109/13506129.2011.574354059 (2011).

95   Grogan, M. *et al.* Natural History of Wild-Type Transthyretin Cardiac Amyloidosis and Risk Stratification Using a Novel Staging System. *Journal of the American College of Cardiology* **68**, 1014-1020, doi:10.1016/j.jacc.2016.06.033 (2016).

96   Nakagawa, M. *et al.* Carpal tunnel syndrome: a common initial symptom of systemic wild-type ATTR (ATTRwt) amyloidosis. *Amyloid : the international journal of experimental and clinical investigation : the official journal of the International Society of Amyloidosis* **23**, 58-63, doi:10.3109/13506129.2015.1135792 (2016).

97   Westermark, P., Westermark, G. T., Suhr, O. B. & Berg, S. Transthyretin-derived amyloidosis: probably a common cause of lumbar spinal stenosis. *Upsala journal of medical sciences* **119**, 223-228, doi:10.3109/03009734.2014.895786 (2014).

98   Geller, H. I., Singh, A., Alexander, K. M., Mirto, T. M. & Falk, R. H. Association Between Ruptured Distal Biceps Tendon and Wild-Type Transthyretin Cardiac Amyloidosis. *Jama* **318**, 962-963, doi:10.1001/jama.2017.9236 (2017).

99   Rowczenio, D. M. *et al.* Online registry for mutations in hereditary amyloidosis including nomenclature recommendations. *Human mutation* **35**, E2403-2412, doi:10.1002/humu.22619 (2014).

100   Sekijima, Y. Transthyretin (ATTR) amyloidosis: clinical spectrum, molecular pathogenesis and disease-modifying treatments. *Journal of neurology, neurosurgery, and psychiatry* **86**, 1036-1043, doi:10.1136/jnnp-2014-308724 (2015).

101   Dispenzieri, A. *et al.* Clinical and genetic profile of patients enrolled in the Transthyretin Amyloidosis Outcomes Survey (THAOS): 14-year update. *Orphanet journal of rare diseases* **17**, 236, doi:10.1186/s13023-022-02359-w (2022).

102   Parman, Y. *et al.* Sixty years of transthyretin familial amyloid polyneuropathy (TTR-FAP) in Europe: where are we now? A European network approach to defining the epidemiology and management patterns for TTR-FAP. *Current opinion in neurology* **29 Suppl 1**, S3-S13, doi:10.1097/WCO.0000000000000288 (2016).

103   Yamashita, T. *et al.* Genetic and clinical characteristics of hereditary transthyretin amyloidosis in endemic and non-endemic areas: experience from a single-referral center in Japan. *Journal of neurology* **265**, 134-140, doi:10.1007/s00415-017-8640-7 (2018).

104   Mariani, L. L. *et al.* Genotype-phenotype correlation and course of transthyretin familial amyloid polyneuropathies in France. *Annals of neurology* **78**, 901-916, doi:10.1002/ana.24519 (2015).

105   Koike, H. *et al.* Natural history of transthyretin Val30Met familial amyloid polyneuropathy: analysis of late-onset cases from non-endemic areas. *Journal of neurology, neurosurgery, and psychiatry* **83**, 152-158, doi:10.1136/jnnp-2011-301299 (2012).

106   Conceicao, I. & De Carvalho, M. Clinical variability in type I familial amyloid polyneuropathy (Val30Met): comparison between late- and early-onset cases in Portugal. *Muscle & nerve* **35**, 116-118, doi:10.1002/mus.20644 (2007).

107   Gonzalez-Duarte, A. Autonomic involvement in hereditary transthyretin amyloidosis (hATTR amyloidosis). *Clinical autonomic research : official journal of the Clinical Autonomic Research Society* **29**, 245-251, doi:10.1007/s10286-018-0514-2 (2019).

108   Waddington-Cruz, M. *et al.* Characteristics of Patients with Late- vs. Early-Onset Val30Met Transthyretin Amyloidosis from the Transthyretin Amyloidosis Outcomes Survey (THAOS). *Neurology and therapy* **10**, 753-766, doi:10.1007/s40120-021-00258-z (2021).

109   Samoes, R. *et al.* Amyloid detection in the transverse carpal ligament of patients with hereditary ATTR V30M amyloidosis and carpal tunnel syndrome. *Amyloid : the*

international journal of experimental and clinical investigation : the official journal of the International Society of Amyloidosis **24**, 73-77, doi:10.1080/13506129.2017.1313222 (2017).

110   Beirao, J. M. *et al.* Ophthalmological manifestations in hereditary transthyretin (ATTR V30M) carriers: a review of 513 cases. *Amyloid : the international journal of experimental and clinical investigation : the official journal of the International Society of Amyloidosis* **22**, 117-122, doi:10.3109/13506129.2015.1015678 (2015).

111   Maia, L. F. *et al.* CNS involvement in V30M transthyretin amyloidosis: clinical, neuropathological and biochemical findings. *Journal of neurology, neurosurgery, and psychiatry* **86**, 159-167, doi:10.1136/jnnp-2014-308107 (2015).

112   Cakar, A., Durmus-Tekce, H. & Parman, Y. Familial Amyloid Polyneuropathy. *Noro psikiyatri arsivi* **56**, 150-156, doi:10.29399/npa.23502 (2019).

113   Ranlov, I. *et al.* A Danish kindred with familial amyloid cardiomyopathy revisited: identification of a mutant transthyretin-methionine111 variant in serum from patients and carriers. *The American journal of medicine* **93**, 3-8, doi:10.1016/0002-9343(92)90672-x (1992).

114   Maurer, M. S. *et al.* Genotype and Phenotype of Transthyretin Cardiac Amyloidosis: THAOS (Transthyretin Amyloid Outcome Survey). *Journal of the American College of Cardiology* **68**, 161-172, doi:10.1016/j.jacc.2016.03.596 (2016).

115   Damy, T. *et al.* Prevalence and clinical phenotype of hereditary transthyretin amyloid cardiomyopathy in patients with increased left ventricular wall thickness. *European heart journal* **37**, 1826-1834, doi:10.1093/eurheartj/ehv583 (2016).

116   Damy, T. *et al.* Transthyretin cardiac amyloidosis in continental Western Europe: an insight through the Transthyretin Amyloidosis Outcomes Survey (THAOS). *European heart journal* **43**, 391-400, doi:10.1093/eurheartj/ehz173 (2019).

117   Maurer, M. S. *et al.* Expert Consensus Recommendations for the Suspicion and Diagnosis of Transthyretin Cardiac Amyloidosis. *Circulation. Heart failure* **12**, e006075, doi:10.1161/CIRCHEARTFAILURE.119.006075 (2019).

118   Finsterer, J. *et al.* Hereditary transthyretin-related amyloidosis. *Acta neurologica Scandinavica* **139**, 92-105, doi:10.1111/ane.13035 (2019).

119   Goren, H., Steinberg, M. C. & Farboody, G. H. Familial oculoleptomeningeal amyloidosis. *Brain : a journal of neurology* **103**, 473-495, doi:10.1093/brain/103.3.473 (1980).

120   Qin, Q. *et al.* Current Review of Leptomeningeal Amyloidosis Associated With Transthyretin Mutations. *The neurologist* **26**, 189-195, doi:10.1097/NRL.0000000000000337 (2021).

121   McColgan, P. *et al.* Oculoleptomeningeal Amyloidosis associated with transthyretin Leu12Pro in an African patient. *Journal of neurology* **262**, 228-234, doi:10.1007/s00415-014-7594-2 (2015).

122   Holmgren, G. *et al.* Homozygosity for the transthyretin-Met30-gene in seven individuals with familial amyloidosis with polyneuropathy detected by restriction enzyme analysis of amplified genomic DNA sequences. *Clinical genetics* **41**, 39-41, doi:10.1111/j.1399-0004.1992.tb03627.x (1992).

123   Nichols, W. C., Liepnieks, J. J., Snyder, E. L. & Benson, M. D. Senile cardiac amyloidosis associated with homozygosity for a transthyretin variant (ILE-122). *The Journal of laboratory and clinical medicine* **117**, 175-180 (1991).

124   Jacobson, D. R. & Buxbaum, J. N. A double-variant transthyretin allele (Ser 6, Ile 33) in the Israeli patient "SKO" with familial amyloidotic polyneuropathy. *Human mutation* **3**, 254-260, doi:10.1002/humu.1380030313 (1994).

125   Hammarstrom, P., Schneider, F. & Kelly, J. W. Trans-suppression of misfolding in an amyloid disease. *Science* **293**, 2459-2462, doi:10.1126/science.1062245 (2001).

126   Saraiva, M. J., Birken, S., Costa, P. P. & Goodman, D. S. Amyloid fibril protein in familial amyloidotic polyneuropathy, Portuguese type. Definition of molecular abnormality in

transthyretin (prealbumin). *The Journal of clinical investigation* **74**, 104-119, doi:10.1172/JCI111390 (1984).

127   Reines, J. B. *et al.* Epidemiology of transthyretin-associated familial amyloid polyneuropathy in the Majorcan area: Son Llatzer Hospital descriptive study. *Orphanet journal of rare diseases* **9**, 29, doi:10.1186/1750-1172-9-29 (2014).

128   Dardiotis, E. *et al.* Epidemiological, clinical and genetic study of familial amyloidotic polyneuropathy in Cyprus. *Amyloid : the international journal of experimental and clinical investigation : the official journal of the International Society of Amyloidosis* **16**, 32-37, doi:10.1080/13506120802676948 (2009).

129   Rapezzi, C. *et al.* Transthyretin-related amyloidoses and the heart: a clinical overview. *Nature reviews. Cardiology* **7**, 398-408, doi:10.1038/nrcardio.2010.67 (2010).

130   Gorevic, P. D., Prelli, F. C., Wright, J., Pras, M. & Frangione, B. Systemic senile amyloidosis. Identification of a new prealbumin (transthyretin) variant in cardiac tissue: immunologic and biochemical similarity to one form of familial amyloidotic polyneuropathy. *The Journal of clinical investigation* **83**, 836-843, doi:10.1172/JCI113966 (1989).

131   Buxbaum, J. N. & Ruberg, F. L. Transthyretin V122I (pV142I)* cardiac amyloidosis: an age-dependent autosomal dominant cardiomyopathy too common to be overlooked as a cause of significant heart disease in elderly African Americans. *Genetics in medicine : official journal of the American College of Medical Genetics* **19**, 733-742, doi:10.1038/gim.2016.200 (2017).

132   Jacobson, D. R. *et al.* Variant-sequence transthyretin (isoleucine 122) in late-onset cardiac amyloidosis in black Americans. *The New England journal of medicine* **336**, 466-473, doi:10.1056/NEJM199702133360703 (1997).

133   Connors, L. H. *et al.* Cardiac amyloidosis in African Americans: comparison of clinical and laboratory features of transthyretin V122I amyloidosis and immunoglobulin light chain amyloidosis. *American heart journal* **158**, 607-614, doi:10.1016/j.ahj.2009.08.006 (2009).

134   Buxbaum, J. *et al.* Transthyretin V122I in African Americans with congestive heart failure. *Journal of the American College of Cardiology* **47**, 1724-1725, doi:10.1016/j.jacc.2006.01.042 (2006).

135   Carroll, A. *et al.* Novel approaches to diagnosis and management of hereditary transthyretin amyloidosis. *Journal of neurology, neurosurgery, and psychiatry* **93**, 668-678, doi:10.1136/jnnp-2021-327909 (2022).

136   Ando, Y. *et al.* Guideline of transthyretin-related hereditary amyloidosis for clinicians. *Orphanet journal of rare diseases* **8**, 31, doi:10.1186/1750-1172-8-31 (2013).

137   Lemos, C. *et al.* Overcoming artefact: anticipation in 284 Portuguese kindreds with familial amyloid polyneuropathy (FAP) ATTRV30M. *Journal of neurology, neurosurgery, and psychiatry* **85**, 326-330, doi:10.1136/jnnp-2013-305383 (2014).

138   Alves-Ferreira, M. *et al.* A Trans-acting Factor May Modify Age at Onset in Familial Amyloid Polyneuropathy ATTRV30M in Portugal. *Molecular neurobiology* **55**, 3676-3683, doi:10.1007/s12035-017-0593-4 (2018).

139   Santos, D. *et al.* Variants in RBP4 and AR genes modulate age at onset in familial amyloid polyneuropathy (FAP ATTRV30M). *European journal of human genetics : EJHG* **24**, 756-760, doi:10.1038/ejhg.2015.180 (2016).

140   Santos, D. *et al.* mtDNA copy number associated with age of onset in familial amyloid polyneuropathy. *Journal of neurology, neurosurgery, and psychiatry* **89**, 300-304, doi:10.1136/jnnp-2017-316657 (2018).

141   Plante-Bordeneuve, V. *et al.* Genetic study of transthyretin amyloid neuropathies: carrier risks among French and Portuguese families. *Journal of medical genetics* **40**, e120, doi:10.1136/jmg.40.11.e120 (2003).

142   Hellman, U. *et al.* Heterogeneity of penetrance in familial amyloid polyneuropathy, ATTR Val30Met, in the Swedish population. *Amyloid : the international journal of experimental and clinical investigation : the official journal of the International Society of Amyloidosis* **15**, 181-186, doi:10.1080/13506120802193720 (2008).

143   Buxbaum, J. *et al.* Significance of the amyloidogenic transthyretin Val 122 Ile allele in African Americans in the Arteriosclerosis Risk in Communities (ARIC) and Cardiovascular Health (CHS) Studies. *American heart journal* **159**, 864-870, doi:10.1016/j.ahj.2010.02.006 (2010).

144   Plante-Bordeneuve, V. *et al.* The Transthyretin Amyloidosis Outcomes Survey (THAOS) registry: design and methodology. *Current medical research and opinion* **29**, 77-84, doi:10.1185/03007995.2012.754349 (2013).

145   Gonzalez-Moreno, J. *et al.* A Descriptive Analysis of ATTR Amyloidosis in Spain from the Transthyretin Amyloidosis Outcomes Survey. *Neurology and therapy* **10**, 833-845, doi:10.1007/s40120-021-00267-y (2021).

146   Adams, D. *et al.* Regional difference and similarity of familial amyloidosis with polyneuropathy in France. *Amyloid : the international journal of experimental and clinical investigation : the official journal of the International Society of Amyloidosis* **19 Suppl 1**, 61-64, doi:10.3109/13506129.2012.685665 (2012).

147   (!!! INVALID CITATION !!!).

148   Carr, A. S. *et al.* A study of the neuropathy associated with transthyretin amyloidosis (ATTR) in the UK. *Journal of neurology, neurosurgery, and psychiatry* **87**, 620-627, doi:10.1136/jnnp-2015-310907 (2016).

149   Reilly, M. M., Staunton, H. & Harding, A. E. Familial amyloid polyneuropathy (TTR ala 60) in north west Ireland: a clinical, genetic, and epidemiological study. *Journal of neurology, neurosurgery, and psychiatry* **59**, 45-49, doi:10.1136/jnnp.59.1.45 (1995).

150   Ines, M. *et al.* Epidemiology of Transthyretin Familial Amyloid Polyneuropathy in Portugal: A Nationwide Study. *Neuroepidemiology* **51**, 177-182, doi:10.1159/000490553 (2018).

151   Schmidt, H. H. *et al.* Estimating the global prevalence of transthyretin familial amyloid polyneuropathy. *Muscle & nerve* **57**, 829-837, doi:10.1002/mus.26034 (2018).

152   Dvorak, A. M., Letourneau, L., Login, G. R., Weller, P. F. & Ackerman, S. J. Ultrastructural localization of the Charcot-Leyden crystal protein (lysophospholipase) to a distinct crystalloid-free granule population in mature human eosinophils. *Blood* **72**, 150-158 (1988).

153   Munar-Ques, M., Costa, P. P., Saraiva, M. J., Viader-Farre, C. & Munar-Bernat, C. [Familial type I (Portuguese form) amyloidotic polyneuropathy in Majorca. Study using the TTR (Met30) genetic marker]. *Medicina clinica* **91**, 441-444 (1988).

154   Tanskanen, M. *et al.* Senile systemic amyloidosis affects 25% of the very aged and associates with genetic variation in alpha2-macroglobulin and tau: a population-based autopsy study. *Annals of medicine* **40**, 232-239, doi:10.1080/07853890701842988 (2008).

155   Shiozaki, T., Sato, N., Hayashi, T., Kobayashi, K. & Asamura, H. Wild-type ATTR amyloidosis may be associated with unexpected death among the elderly. *Legal medicine* **41**, 101634, doi:10.1016/j.legalmed.2019.101634 (2019).

156   Jacobsson, B. *et al.* Transthyretin immunoreactivity in human and porcine liver, choroid plexus, and pancreatic islets. *The journal of histochemistry and cytochemistry : official journal of the Histochemistry Society* **37**, 31-37, doi:10.1177/37.1.2642294 (1989).

157   Herbert, J. *et al.* Transthyretin: a choroid plexus-specific transport protein in human brain. The 1986 S. Weir Mitchell award. *Neurology* **36**, 900-911, doi:10.1212/wnl.36.7.900 (1986).

158   Benvenga, S. *et al.* Radioimmunoassay for human thyroxine-binding prealbumin. *Annals of clinical and laboratory science* **16**, 231-240 (1986).

159   Stabilini, R., Vergani, C., Agostoni, A. & Agostoni, R. P. Influence of age and sex on prealbumin levels. *Clinica chimica acta; international journal of clinical chemistry* **20**, 358-359, doi:10.1016/0009-8981(68)90173-3 (1968).

160   Vatassery, G. T., Quach, H. T., Smith, W. E., Benson, B. A. & Eckfeldt, J. H. A sensitive assay of transthyretin (prealbumin) in human cerebrospinal fluid in nanogram amounts by ELISA. *Clinica chimica acta; international journal of clinical chemistry* **197**, 19-25, doi:10.1016/0009-8981(91)90344-c (1991).

161   Aldred, A. R., Brack, C. M. & Schreiber, G. The cerebral expression of plasma protein genes in different species. *Comparative biochemistry and physiology. Part B, Biochemistry & molecular biology* **111**, 1-15, doi:10.1016/0305-0491(94)00229-n (1995).

162   Magalhaes, J., Eira, J. & Liz, M. A. The role of transthyretin in cell biology: impact on human pathophysiology. *Cellular and molecular life sciences : CMLS* **78**, 6105-6117, doi:10.1007/s00018-021-03899-3 (2021).

163   Pfeffer, B. A., Becerra, S. P., Borst, D. E. & Wong, P. Expression of transthyretin and retinol binding protein mRNAs and secretion of transthyretin by cultured monkey retinal pigment epithelium. *Molecular vision* **10**, 23-30 (2004).

164   Vieira, M. & Saraiva, M. J. Transthyretin: a multifaceted protein. *Biomolecular concepts* **5**, 45-54, doi:10.1515/bmc-2013-0038 (2014).

165   Schreiber, G. & Richardson, S. J. The evolution of gene expression, structure and function of transthyretin. *Comparative biochemistry and physiology. Part B, Biochemistry & molecular biology* **116**, 137-160, doi:10.1016/s0305-0491(96)00212-x (1997).

166   Chanoine, J. P. & Braverman, L. E. The role of transthyretin in the transport of thyroid hormone to cerebrospinal fluid and brain. *Acta medica Austriaca* **19 Suppl 1**, 25-28 (1992).

167   Goodman, D. S. Vitamin A and retinoids in health and disease. *The New England journal of medicine* **310**, 1023-1031, doi:10.1056/NEJM198404193101605 (1984).

168   Noy, N. & Xu, Z. J. Interactions of retinol with binding proteins: implications for the mechanism of uptake by cells. *Biochemistry* **29**, 3878-3883, doi:10.1021/bi00468a012 (1990).

169   Raz, A. & Goodman, D. S. The interaction of thyroxine with human plasma prealbumin and with the prealbumin-retinol-binding protein complex. *The Journal of biological chemistry* **244**, 3230-3237 (1969).

170   Episkopou, V. *et al.* Disruption of the transthyretin gene results in mice with depressed levels of plasma retinol and thyroid hormone. *Proceedings of the National Academy of Sciences of the United States of America* **90**, 2375-2379, doi:10.1073/pnas.90.6.2375 (1993).

171   Palha, J. A. *et al.* Thyroid hormone metabolism in a transthyretin-null mouse strain. *The Journal of biological chemistry* **269**, 33135-33139 (1994).

172   van Bennekum, A. M. *et al.* Biochemical basis for depressed serum retinol levels in transthyretin-deficient mice. *The Journal of biological chemistry* **276**, 1107-1113, doi:10.1074/jbc.M008091200 (2001).

173   Monk, J. A. *et al.* Delayed development of specific thyroid hormone-regulated events in transthyretin null mice. *American journal of physiology. Endocrinology and metabolism* **304**, E23-31, doi:10.1152/ajpendo.00216.2012 (2013).

174   Liz, M. A., Gomes, C. M., Saraiva, M. J. & Sousa, M. M. ApoA-I cleaved by transthyretin has reduced ability to promote cholesterol efflux and increased amyloidogenicity. *Journal of lipid research* **48**, 2385-2395, doi:10.1194/jlr.M700158-JLR200 (2007).

175   Costa, R., Ferreira-da-Silva, F., Saraiva, M. J. & Cardoso, I. Transthyretin protects against A-beta peptide toxicity by proteolytic cleavage of the peptide: a mechanism sensitive to the Kunitz protease inhibitor. *PloS one* **3**, e2899, doi:10.1371/journal.pone.0002899 (2008).

176   Liz, M. A. *et al.* Substrate specificity of transthyretin: identification of natural substrates in the nervous system. *The Biochemical journal* **419**, 467-474, doi:10.1042/BJ20082090 (2009).

177   Schwarzman, A. L. *et al.* Transthyretin sequesters amyloid beta protein and prevents amyloid formation. *Proceedings of the National Academy of Sciences of the United States of America* **91**, 8368-8372, doi:10.1073/pnas.91.18.8368 (1994).

178   Gloeckner, S. F. *et al.* Quantitative analysis of transthyretin, tau and amyloid-beta in patients with dementia. *Journal of Alzheimer's disease : JAD* **14**, 17-25, doi:10.3233/jad-2008-14102 (2008).

179   Buxbaum, J. N. *et al.* Transthyretin protects Alzheimer's mice from the behavioral and biochemical effects of Abeta toxicity. *Proceedings of the National Academy of Sciences of the United States of America* **105**, 2681-2686, doi:10.1073/pnas.0712197105 (2008).

180   Ribeiro, C. A. *et al.* Transthyretin stabilization by iododiflunisal promotes amyloid-beta peptide clearance, decreases its deposition, and ameliorates cognitive deficits in an Alzheimer's disease mouse model. *Journal of Alzheimer's disease : JAD* **39**, 357-370, doi:10.3233/JAD-131355 (2014).

181   Gomes, J. R. *et al.* Transthyretin provides trophic support via megalin by promoting neurite outgrowth and neuroprotection in cerebral ischemia. *Cell death and differentiation* **23**, 1749-1764, doi:10.1038/cdd.2016.64 (2016).

182   Sousa, J. C. *et al.* Transthyretin influences spatial reference memory. *Neurobiology of learning and memory* **88**, 381-385, doi:10.1016/j.nlm.2007.07.006 (2007).

183   Fleming, C. E., Saraiva, M. J. & Sousa, M. M. Transthyretin enhances nerve regeneration. *Journal of neurochemistry* **103**, 831-839, doi:10.1111/j.1471-4159.2007.04828.x (2007).

184   Blake, C. C. *et al.* An x-ray study of the subunit structure of prealbumin. *Journal of molecular biology* **61**, 217-224, doi:10.1016/0022-2836(71)90218-x (1971).

185   Blake, C. C., Geisow, M. J., Oatley, S. J., Rerat, B. & Rerat, C. Structure of prealbumin: secondary, tertiary and quaternary interactions determined by Fourier refinement at 1.8 A. *Journal of molecular biology* **121**, 339-356, doi:10.1016/0022-2836(78)90368-6 (1978).

186   Blake, C. C., Geisow, M. J., Swan, I. D., Rerat, C. & Rerat, B. Structure of human plasma prealbumin at 2-5 A resolution. A preliminary report on the polypeptide chain conformation, quaternary structure and thyroxine binding. *Journal of molecular biology* **88**, 1-12, doi:10.1016/0022-2836(74)90291-5 (1974).

187   Blake, C. C. & Oatley, S. J. Protein-DNA and protein-hormone interactions in prealbumin: a model of the thyroid hormone nuclear receptor? *Nature* **268**, 115-120, doi:10.1038/268115a0 (1977).

188   Wojtczak, A., Cody, V., Luft, J. R. & Pangborn, W. Structures of human transthyretin complexed with thyroxine at 2.0 A resolution and 3',5'-dinitro-N-acetyl-L-thyronine at 2.2 A resolution. *Acta crystallographica. Section D, Biological crystallography* **52**, 758-765, doi:10.1107/S0907444996003046 (1996).

189   Colon, W. & Kelly, J. W. Partial denaturation of transthyretin is sufficient for amyloid fibril formation in vitro. *Biochemistry* **31**, 8654-8660, doi:10.1021/bi00151a036 (1992).

190   Lai, Z., Colon, W. & Kelly, J. W. The acid-mediated denaturation pathway of transthyretin yields a conformational intermediate that can self-assemble into amyloid. *Biochemistry* **35**, 6470-6482, doi:10.1021/bi952501g (1996).

191   Jiang, X. *et al.* An engineered transthyretin monomer that is nonamyloidogenic, unless it is partially denatured. *Biochemistry* **40**, 11442-11452, doi:10.1021/bi011194d (2001).

192   Foss, T. R., Wiseman, R. L. & Kelly, J. W. The pathway by which the tetrameric protein transthyretin dissociates. *Biochemistry* **44**, 15525-15533, doi:10.1021/bi051608t (2005).

193   Hurshman, A. R., White, J. T., Powers, E. T. & Kelly, J. W. Transthyretin aggregation under partially denaturing conditions is a downhill polymerization. *Biochemistry* **43**, 7365-7381, doi:10.1021/bi049621l (2004).

194 Jarrett, J. T. & Lansbury, P. T., Jr. Seeding "one-dimensional crystallization" of amyloid: a pathogenic mechanism in Alzheimer's disease and scrapie? *Cell* **73**, 1055-1058, doi:10.1016/0092-8674(93)90635-4 (1993).

195 Harper, J. D. & Lansbury, P. T., Jr. Models of amyloid seeding in Alzheimer's disease and scrapie: mechanistic truths and physiological consequences of the time-dependent solubility of amyloid proteins. *Annual review of biochemistry* **66**, 385-407, doi:10.1146/annurev.biochem.66.1.385 (1997).

196 Kelly, J. W. & Lansbury, P. T. A chemical approach to elucidate the mechanism of transthyretin and β-protein amyloid fibril formation. *Amyloid : the international journal of experimental and clinical investigation : the official journal of the International Society of Amyloidosis* **1**, 186-205, doi:10.3109/13506129409148451 (1994).

197 Quintas, A., Saraiva, M. J. & Brito, R. M. The amyloidogenic potential of transthyretin variants correlates with their tendency to aggregate in solution. *FEBS letters* **418**, 297-300, doi:10.1016/s0014-5793(97)01398-7 (1997).

198 Marcoux, J. *et al.* A novel mechano-enzymatic cleavage mechanism underlies transthyretin amyloidogenesis. *EMBO molecular medicine* **7**, 1337-1349, doi:10.15252/emmm.201505357 (2015).

199 Ihse, E. *et al.* Amyloid fibrils containing fragmented ATTR may be the standard fibril composition in ATTR amyloidosis. *Amyloid : the international journal of experimental and clinical investigation : the official journal of the International Society of Amyloidosis* **20**, 142-150, doi:10.3109/13506129.2013.797890 (2013).

200 Ihse, E. *et al.* Amyloid fibril composition is related to the phenotype of hereditary transthyretin V30M amyloidosis. *The Journal of pathology* **216**, 253-261, doi:10.1002/path.2411 (2008).

201 Gustafsson, S. *et al.* Amyloid fibril composition as a predictor of development of cardiomyopathy after liver transplantation for hereditary transthyretin amyloidosis. *Transplantation* **93**, 1017-1023, doi:10.1097/TP.0b013e31824b3749 (2012).

202 Mangione, P. P. *et al.* Proteolytic cleavage of Ser52Pro variant transthyretin triggers its amyloid fibrillogenesis. *Proceedings of the National Academy of Sciences of the United States of America* **111**, 1539-1544, doi:10.1073/pnas.1317488111 (2014).

203 Mangione, P. P. *et al.* Plasminogen activation triggers transthyretin amyloidogenesis in vitro. *The Journal of biological chemistry* **293**, 14192-14199, doi:10.1074/jbc.RA118.003990 (2018).

204 Slamova, I. *et al.* Plasmin activity promotes amyloid deposition in a transgenic model of human transthyretin amyloidosis. *Nature communications* **12**, 7112, doi:10.1038/s41467-021-27416-z (2021).

205 McCutchen, S. L., Lai, Z., Miroy, G. J., Kelly, J. W. & Colon, W. Comparison of lethal and nonlethal transthyretin variants and their relationship to amyloid disease. *Biochemistry* **34**, 13527-13536, doi:10.1021/bi00041a032 (1995).

206 Niraula, T. N. *et al.* Decreased thermodynamic stability as a crucial factor for familial amyloidotic polyneuropathy. *Journal of molecular biology* **320**, 333-342, doi:10.1016/S0022-2836(02)00425-4 (2002).

207 Jiang, X., Buxbaum, J. N. & Kelly, J. W. The V122I cardiomyopathy variant of transthyretin increases the velocity of rate-limiting tetramer dissociation, resulting in accelerated amyloidosis. *Proceedings of the National Academy of Sciences of the United States of America* **98**, 14943-14948, doi:10.1073/pnas.261419998 (2001).

208 Hurshman Babbes, A. R., Powers, E. T. & Kelly, J. W. Quantification of the thermodynamically linked quaternary and tertiary structural stabilities of transthyretin and its disease-associated variants: the relationship between stability and amyloidosis. *Biochemistry* **47**, 6969-6984, doi:10.1021/bi800636q (2008).

209   Lashuel, H. A., Wurth, C., Woo, L. & Kelly, J. W. The most pathogenic transthyretin variant, L55P, forms amyloid fibrils under acidic conditions and protofilaments under physiological conditions. *Biochemistry* **38**, 13560-13573, doi:10.1021/bi991021c (1999).

210   Sekijima, Y. *et al.* The biological and chemical basis for tissue-selective amyloid disease. *Cell* **121**, 73-85, doi:10.1016/j.cell.2005.01.018 (2005).

211   Sekijima, Y. *et al.* Energetic characteristics of the new transthyretin variant A25T may explain its atypical central nervous system pathology. *Laboratory investigation; a journal of technical methods and pathology* **83**, 409-417, doi:10.1097/01.lab.0000059937.11023.1f (2003).

212   Hammarstrom, P. *et al.* D18G transthyretin is monomeric, aggregation prone, and not detectable in plasma and cerebrospinal fluid: a prescription for central nervous system amyloidosis? *Biochemistry* **42**, 6656-6663, doi:10.1021/bi027319b (2003).

213   Palaninathan, S. K. Nearly 200 X-ray crystal structures of transthyretin: what do they tell us about this protein and the design of drugs for TTR amyloidoses? *Current medicinal chemistry* **19**, 2324-2342, doi:10.2174/092986712800269335 (2012).

214   Sebastiao, M. P., Saraiva, M. J. & Damas, A. M. The crystal structure of amyloidogenic Leu55 --> Pro transthyretin variant reveals a possible pathway for transthyretin polymerization into amyloid fibrils. *The Journal of biological chemistry* **273**, 24715-24722, doi:10.1074/jbc.273.38.24715 (1998).

215   Pasquato, N. *et al.* Acidic pH-induced conformational changes in amyloidogenic mutant transthyretin. *Journal of molecular biology* **366**, 711-719, doi:10.1016/j.jmb.2006.11.076 (2007).

216   Cendron, L. *et al.* Amyloidogenic potential of transthyretin variants: insights from structural and computational analyses. *The Journal of biological chemistry* **284**, 25832-25841, doi:10.1074/jbc.M109.017657 (2009).

217   Leach, B. I., Zhang, X., Kelly, J. W., Dyson, H. J. & Wright, P. E. NMR Measurements Reveal the Structural Basis of Transthyretin Destabilization by Pathogenic Mutations. *Biochemistry* **57**, 4421-4430, doi:10.1021/acs.biochem.8b00642 (2018).

218   Liu, K., Kelly, J. W. & Wemmer, D. E. Native state hydrogen exchange study of suppressor and pathogenic variants of transthyretin. *Journal of molecular biology* **320**, 821-832, doi:10.1016/s0022-2836(02)00471-0 (2002).

219   Childers, M. C. & Daggett, V. Edge Strand Dissociation and Conformational Changes in Transthyretin under Amyloidogenic Conditions. *Biophysical journal* **119**, 1995-2009, doi:10.1016/j.bpj.2020.08.043 (2020).

220   Koike, H. *et al.* The morphology of amyloid fibrils and their impact on tissue damage in hereditary transthyretin amyloidosis: An ultrastructural study. *Journal of the neurological sciences* **394**, 99-106, doi:10.1016/j.jns.2018.09.011 (2018).

221   Reixach, N., Deechongkit, S., Jiang, X., Kelly, J. W. & Buxbaum, J. N. Tissue damage in the amyloidoses: Transthyretin monomers and nonnative oligomers are the major cytotoxic species in tissue culture. *Proceedings of the National Academy of Sciences of the United States of America* **101**, 2817-2822, doi:10.1073/pnas.0400062101 (2004).

222   Hou, X. *et al.* Transthyretin oligomers induce calcium influx via voltage-gated calcium channels. *Journal of neurochemistry* **100**, 446-457, doi:10.1111/j.1471-4159.2006.04210.x (2007).

223   Sousa, M. M., Cardoso, I., Fernandes, R., Guimaraes, A. & Saraiva, M. J. Deposition of transthyretin in early stages of familial amyloidotic polyneuropathy: evidence for toxicity of nonfibrillar aggregates. *The American journal of pathology* **159**, 1993-2000, doi:10.1016/s0002-9440(10)63050-7 (2001).

224   Roberts, H. L. & Brown, D. R. Seeking a mechanism for the toxicity of oligomeric alpha-synuclein. *Biomolecules* **5**, 282-305, doi:10.3390/biom5020282 (2015).

225   Benilova, I., Karran, E. & De Strooper, B. The toxic Abeta oligomer and Alzheimer's disease: an emperor in need of clothes. *Nature neuroscience* **15**, 349-357, doi:10.1038/nn.3028 (2012).

226   Zhao, L., Buxbaum, J. N. & Reixach, N. Age-related oxidative modifications of transthyretin modulate its amyloidogenicity. *Biochemistry* **52**, 1913-1926, doi:10.1021/bi301313b (2013).

227   Teixeira, P. F., Cerca, F., Santos, S. D. & Saraiva, M. J. Endoplasmic reticulum stress associated with extracellular aggregates. Evidence from transthyretin deposition in familial amyloid polyneuropathy. *The Journal of biological chemistry* **281**, 21998-22003, doi:10.1074/jbc.M602302200 (2006).

228   Sousa, M. M. *et al.* Familial amyloid polyneuropathy: receptor for advanced glycation end products-dependent triggering of neuronal inflammatory and apoptotic pathways. *The Journal of neuroscience : the official journal of the Society for Neuroscience* **21**, 7576-7586, doi:10.1523/JNEUROSCI.21-19-07576.2001 (2001).

229   Monteiro, F. A. *et al.* Activation of ERK1/2 MAP kinases in familial amyloidotic polyneuropathy. *Journal of neurochemistry* **97**, 151-161, doi:10.1111/j.1471-4159.2006.03716.x (2006).

230   Bezerra, F., Saraiva, M. J. & Almeida, M. R. Modulation of the Mechanisms Driving Transthyretin Amyloidosis. *Frontiers in molecular neuroscience* **13**, 592644, doi:10.3389/fnmol.2020.592644 (2020).

231   Holmgren, G. *et al.* Biochemical effect of liver transplantation in two Swedish patients with familial amyloidotic polyneuropathy (FAP-met30). *Clinical genetics* **40**, 242-246, doi:10.1111/j.1399-0004.1991.tb03085.x (1991).

232   Holmgren, G. *et al.* Clinical improvement and amyloid regression after liver transplantation in hereditary transthyretin amyloidosis. *Lancet* **341**, 1113-1116, doi:10.1016/0140-6736(93)93127-m (1993).

233   Ericzon, B. G. *et al.* Liver Transplantation for Hereditary Transthyretin Amyloidosis: After 20 Years Still the Best Therapeutic Alternative? *Transplantation* **99**, 1847-1854, doi:10.1097/TP.0000000000000574 (2015).

234   Olofsson, B. O., Backman, C., Karp, K. & Suhr, O. B. Progression of cardiomyopathy after liver transplantation in patients with familial amyloidotic polyneuropathy, Portuguese type. *Transplantation* **73**, 745-751, doi:10.1097/00007890-200203150-00015 (2002).

235   Liepnieks, J. J., Zhang, L. Q. & Benson, M. D. Progression of transthyretin amyloid neuropathy after liver transplantation. *Neurology* **75**, 324-327, doi:10.1212/WNL.0b013e3181ea15d4 (2010).

236   Munar-Ques, M. *et al.* Vitreous amyloidosis after liver transplantation in patients with familial amyloid polyneuropathy: ocular synthesis of mutant transthyretin. *Amyloid : the international journal of experimental and clinical investigation : the official journal of the International Society of Amyloidosis* **7**, 266-269, doi:10.3109/13506120009146440 (2000).

237   Sekijima, Y. *et al.* Cerebral amyloid angiopathy in posttransplant patients with hereditary ATTR amyloidosis. *Neurology* **87**, 773-781, doi:10.1212/WNL.0000000000003001 (2016).

238   Yazaki, M. *et al.* Cardiac amyloid in patients with familial amyloid polyneuropathy consists of abundant wild-type transthyretin. *Biochemical and biophysical research communications* **274**, 702-706, doi:10.1006/bbrc.2000.3203 (2000).

239   Stangou, A. J. *et al.* Progressive cardiac amyloidosis following liver transplantation for familial amyloid polyneuropathy: implications for amyloid fibrillogenesis. *Transplantation* **66**, 229-233, doi:10.1097/00007890-199807270-00016 (1998).

240   Saelices, L. *et al.* Amyloid seeding of transthyretin by ex vivo cardiac fibrils and its inhibition. *Proceedings of the National Academy of Sciences of the United States of America* **115**, E6741-E6750, doi:10.1073/pnas.1805131115 (2018).

241   Urits, I. *et al.* A Review of Patisiran (ONPATTRO(R)) for the Treatment of Polyneuropathy in People with Hereditary Transthyretin Amyloidosis. *Neurology and therapy* **9**, 301-315, doi:10.1007/s40120-020-00208-1 (2020).

242   Kristen, A. V. *et al.* Patisiran, an RNAi therapeutic for the treatment of hereditary transthyretin-mediated amyloidosis. *Neurodegenerative disease management* **9**, 5-23, doi:10.2217/nmt-2018-0033 (2019).

243   Adams, D. *et al.* Efficacy and safety of vutrisiran for patients with hereditary transthyretin-mediated amyloidosis with polyneuropathy: a randomized clinical trial. *Amyloid : the international journal of experimental and clinical investigation : the official journal of the International Society of Amyloidosis* **30**, 1-9, doi:10.1080/13506129.2022.2091985 (2023).

244   Benson, M. D. *et al.* Inotersen Treatment for Patients with Hereditary Transthyretin Amyloidosis. *The New England journal of medicine* **379**, 22-31, doi:10.1056/NEJMoa1716793 (2018).

245   Gales, L. Tegsedi (Inotersen): An Antisense Oligonucleotide Approved for the Treatment of Adult Patients with Hereditary Transthyretin Amyloidosis. *Pharmaceuticals* **12**, doi:10.3390/ph12020078 (2019).

246   Benson, M. D., Dasgupta, N. R., Rissing, S. M., Smith, J. & Feigenbaum, H. Safety and efficacy of a TTR specific antisense oligonucleotide in patients with transthyretin amyloid cardiomyopathy. *Amyloid : the international journal of experimental and clinical investigation : the official journal of the International Society of Amyloidosis* **24**, 219-225, doi:10.1080/13506129.2017.1374946 (2017).

247   Viney, N. J. *et al.* Ligand conjugated antisense oligonucleotide for the treatment of transthyretin amyloidosis: preclinical and phase 1 data. *ESC heart failure* **8**, 652-661, doi:10.1002/ehf2.13154 (2021).

248   Yokoyama, T. & Mizuguchi, M. Transthyretin Amyloidogenesis Inhibitors: From Discovery to Current Developments. *Journal of medicinal chemistry* **63**, 14228-14242, doi:10.1021/acs.jmedchem.0c00934 (2020).

249   Sebastiao, M. P., Lamzin, V., Saraiva, M. J. & Damas, A. M. Transthyretin stability as a key factor in amyloidogenesis: X-ray analysis at atomic resolution. *Journal of molecular biology* **306**, 733-744, doi:10.1006/jmbi.2000.4415 (2001).

250   Johnson, S. M., Connelly, S., Fearns, C., Powers, E. T. & Kelly, J. W. The transthyretin amyloidoses: from delineating the molecular mechanism of aggregation linked to pathology to a regulatory-agency-approved drug. *Journal of molecular biology* **421**, 185-203, doi:10.1016/j.jmb.2011.12.060 (2012).

251   Miroy, G. J. *et al.* Inhibiting transthyretin amyloid fibril formation via protein stabilization. *Proceedings of the National Academy of Sciences of the United States of America* **93**, 15051-15056, doi:10.1073/pnas.93.26.15051 (1996).

252   Dolado, I. *et al.* Kinetic assay for high-throughput screening of in vitro transthyretin amyloid fibrillogenesis inhibitors. *Journal of combinatorial chemistry* **7**, 246-252, doi:10.1021/cc049849s (2005).

253   Reixach, N., Adamski-Werner, S. L., Kelly, J. W., Koziol, J. & Buxbaum, J. N. Cell based screening of inhibitors of transthyretin aggregation. *Biochemical and biophysical research communications* **348**, 889-897, doi:10.1016/j.bbrc.2006.07.109 (2006).

254   McCammon, M. G. *et al.* Screening transthyretin amyloid fibril inhibitors: characterization of novel multiprotein, multiligand complexes by mass spectrometry. *Structure* **10**, 851-863, doi:10.1016/s0969-2126(02)00771-2 (2002).

255   Klabunde, T. *et al.* Rational design of potent human transthyretin amyloid disease inhibitors. *Nature structural biology* **7**, 312-321, doi:10.1038/74082 (2000).

256   Dessi, A. *et al.* Rational Design, Synthesis, Characterization and Evaluation of Iodinated 4,4'-Bipyridines as New Transthyretin Fibrillogenesis Inhibitors. *Molecules* **25**, doi:10.3390/molecules25092213 (2020).

257   Pinheiro, F. *et al.* Development of a Highly Potent Transthyretin Amyloidogenesis Inhibitor: Design, Synthesis, and Evaluation. *Journal of medicinal chemistry* **65**, 14673-14691, doi:10.1021/acs.jmedchem.2c01195 (2022).

258   Johnson, S. M. *et al.* Native state kinetic stabilization as a strategy to ameliorate protein misfolding diseases: a focus on the transthyretin amyloidoses. *Accounts of chemical research* **38**, 911-921, doi:10.1021/ar020073i (2005).

259   Ferguson, R. N., Edelhoch, H., Saroff, H. A., Robbins, J. & Cahnmann, H. J. Negative cooperativity in the binding of thyroxine to human serum prealbumin. Preparation of tritium-labeled 8-anilino-1-naphthalenesulfonic acid. *Biochemistry* **14**, 282-289, doi:10.1021/bi00673a014 (1975).

260   Neumann, P., Cody, V. & Wojtczak, A. Structural basis of negative cooperativity in transthyretin. *Acta biochimica Polonica* **48**, 867-875 (2001).

261   Adamski-Werner, S. L., Palaninathan, S. K., Sacchettini, J. C. & Kelly, J. W. Diflunisal analogues stabilize the native state of transthyretin. Potent inhibition of amyloidogenesis. *Journal of medicinal chemistry* **47**, 355-374, doi:10.1021/jm030347n (2004).

262   Tojo, K., Sekijima, Y., Kelly, J. W. & Ikeda, S. Diflunisal stabilizes familial amyloid polyneuropathy-associated transthyretin variant tetramers in serum against dissociation required for amyloidogenesis. *Neuroscience research* **56**, 441-449, doi:10.1016/j.neures.2006.08.014 (2006).

263   Sekijima, Y., Dendle, M. A. & Kelly, J. W. Orally administered diflunisal stabilizes transthyretin against dissociation required for amyloidogenesis. *Amyloid : the international journal of experimental and clinical investigation : the official journal of the International Society of Amyloidosis* **13**, 236-249, doi:10.1080/13506120600960882 (2006).

264   Berk, J. L. *et al.* Repurposing diflunisal for familial amyloid polyneuropathy: a randomized clinical trial. *Jama* **310**, 2658-2667, doi:10.1001/jama.2013.283815 (2013).

265   Sekijima, Y., Tojo, K., Morita, H., Koyama, J. & Ikeda, S. Safety and efficacy of long-term diflunisal administration in hereditary transthyretin (ATTR) amyloidosis. *Amyloid : the international journal of experimental and clinical investigation : the official journal of the International Society of Amyloidosis* **22**, 79-83, doi:10.3109/13506129.2014.997872 (2015).

266   Ibrahim, M. *et al.* The use of diflunisal for transthyretin cardiac amyloidosis: a review. *Heart failure reviews* **27**, 517-524, doi:10.1007/s10741-021-10143-4 (2022).

267   Takahashi, R. *et al.* Efficacy of diflunisal on autonomic dysfunction of late-onset familial amyloid polyneuropathy (TTR Val30Met) in a Japanese endemic area. *Journal of the neurological sciences* **345**, 231-235, doi:10.1016/j.jns.2014.07.017 (2014).

268   Bulawa, C. E. *et al.* Tafamidis, a potent and selective transthyretin kinetic stabilizer that inhibits the amyloid cascade. *Proceedings of the National Academy of Sciences of the United States of America* **109**, 9629-9634, doi:10.1073/pnas.1121005109 (2012).

269   Coelho, T. *et al.* Tafamidis for transthyretin familial amyloid polyneuropathy: a randomized, controlled trial. *Neurology* **79**, 785-792, doi:10.1212/WNL.0b013e3182661eb1 (2012).

270   Barroso, F. A. *et al.* Long-term safety and efficacy of tafamidis for the treatment of hereditary transthyretin amyloid polyneuropathy: results up to 6 years. *Amyloid : the international journal of experimental and clinical investigation : the official journal of the International Society of Amyloidosis* **24**, 194-204, doi:10.1080/13506129.2017.1357545 (2017).

271   Coelho, T. *et al.* Long-term effects of tafamidis for the treatment of transthyretin familial amyloid polyneuropathy. *Journal of neurology* **260**, 2802-2814, doi:10.1007/s00415-013-7051-7 (2013).

272   Merlini, G. *et al.* Effects of tafamidis on transthyretin stabilization and clinical outcomes in patients with non-Val30Met transthyretin amyloidosis. *Journal of cardiovascular translational research* **6**, 1011-1020, doi:10.1007/s12265-013-9512-x (2013).

273   Cortese, A. *et al.* Monitoring effectiveness and safety of Tafamidis in transthyretin amyloidosis in Italy: a longitudinal multicenter study in a non-endemic area. *Journal of neurology* **263**, 916-924, doi:10.1007/s00415-016-8064-9 (2016).

274   Plante-Bordeneuve, V. *et al.* Long-term treatment of transthyretin familial amyloid polyneuropathy with tafamidis: a clinical and neurophysiological study. *Journal of neurology* **264**, 268-276, doi:10.1007/s00415-016-8337-3 (2017).

275   Maurer, M. S. *et al.* Tafamidis Treatment for Patients with Transthyretin Amyloid Cardiomyopathy. *The New England journal of medicine* **379**, 1007-1016, doi:10.1056/NEJMoa1805689 (2018).

276   Sant'Anna, R. *et al.* Repositioning tolcapone as a potent inhibitor of transthyretin amyloidogenesis and associated cellular toxicity. *Nature communications* **7**, 10787, doi:10.1038/ncomms10787 (2016).

277   Gamez, J. *et al.* Transthyretin stabilization activity of the catechol-O-methyltransferase inhibitor tolcapone (SOM0226) in hereditary ATTR amyloidosis patients and asymptomatic carriers: proof-of-concept study(). *Amyloid : the international journal of experimental and clinical investigation : the official journal of the International Society of Amyloidosis* **26**, 74-84, doi:10.1080/13506129.2019.1597702 (2019).

278   Russ, H. *et al.* Detection of tolcapone in the cerebrospinal fluid of parkinsonian subjects. *Naunyn-Schmiedeberg's archives of pharmacology* **360**, 719-720, doi:10.1007/s002109900168 (1999).

279   Alhamadsheh, M. M. *et al.* Potent kinetic stabilizers that prevent transthyretin-mediated cardiomyocyte proteotoxicity. *Science translational medicine* **3**, 97ra81, doi:10.1126/scitranslmed.3002473 (2011).

280   Penchala, S. C. *et al.* AG10 inhibits amyloidogenesis and cellular toxicity of the familial amyloid cardiomyopathy-associated V122I transthyretin. *Proceedings of the National Academy of Sciences of the United States of America* **110**, 9992-9997, doi:10.1073/pnas.1300761110 (2013).

281   Iakovleva, I. *et al.* Enthalpic Forces Correlate with the Selectivity of Transthyretin-Stabilizing Ligands in Human Plasma. *Journal of medicinal chemistry* **58**, 6507-6515, doi:10.1021/acs.jmedchem.5b00544 (2015).

282   Miller, M. *et al.* Enthalpy-Driven Stabilization of Transthyretin by AG10 Mimics a Naturally Occurring Genetic Variant That Protects from Transthyretin Amyloidosis. *Journal of medicinal chemistry* **61**, 7862-7876, doi:10.1021/acs.jmedchem.8b00817 (2018).

283   Judge, D. P. *et al.* Transthyretin Stabilization by AG10 in Symptomatic Transthyretin Amyloid Cardiomyopathy. *Journal of the American College of Cardiology* **74**, 285-295, doi:10.1016/j.jacc.2019.03.012 (2019).

284   Cardoso, I., Martins, D., Ribeiro, T., Merlini, G. & Saraiva, M. J. Synergy of combined doxycycline/TUDCA treatment in lowering Transthyretin deposition and associated biomarkers: studies in FAP mouse models. *Journal of translational medicine* **8**, 74, doi:10.1186/1479-5876-8-74 (2010).

285   Obici, L. *et al.* Doxycycline plus tauroursodeoxycholic acid for transthyretin amyloidosis: a phase II study. *Amyloid : the international journal of experimental and clinical investigation : the official journal of the International Society of Amyloidosis* **19 Suppl 1**, 34-36, doi:10.3109/13506129.2012.678508 (2012).

286   Galant, N. J. *et al.* Substoichiometric inhibition of transthyretin misfolding by immune-targeting sparsely populated misfolding intermediates: a potential diagnostic and therapeutic for TTR amyloidoses. *Scientific reports* **6**, 25080, doi:10.1038/srep25080 (2016).

287   Capustin, M. & Frishman, W. H. Transthyretin Cardiac Amyloidosis and Novel Therapies to Treat This Not-so-rare Cause of Cardiomyopathy. *Cardiology in review* **29**, 263-273, doi:10.1097/CRD.0000000000000387 (2021).

APPENDIX 1

Supplementary information of chapter 2

Table S1. Hydrogen bond contacts, frequency (in %), and average and shortest H-bond distances (in Å) for WT-TTR in complex with tolcapone and halogenated tolcapone analogues.

Compound	Ligand	L-TTR contacts	Frequency	Average distance	Shortest distance
Tolcapone	L1	C=O-THR119	10.7	2.83	2.63
M-14	L1	NO2-THR106	7.1	2.84	2.62
M-14	L2	C=O-LYS15	12.9	2.84	2.68
M-17	L1	C=O-THR119	35.7	2.82	2.63
M-17	L2	C=O-THR119	62.1	2.82	2.55
M-17	L1	F-SER117A	17.1	2.84	2.65
M-17	L1	F-THR119	33.6	2.86	2.68
M-17	L2	F-SER117B	23.6	2.88	2.68
M-17	L2	F-THR118	18.2	2.91	2.73

Table S2. Hydrogen bond contacts, frequency (in %), and average and shortest H-bond distances (in Å) for WT-TTR in complex with demethylated 3,5-disubstituted and halogenated tolcapone analogues.

Compound	Ligand	L-TTR Contacts	Frequency	Average distance	Shortest distance
M-20	L1	Cl-THR119	59.3	3.28	2.95
M-20	L2	Cl-THR119	44.3	3.28	2.93
M-21	L1	C=O-THR119	21.4	2.86	2.68
M-21	L2	C=O-THR119	12.2	2.85	2.63
M-21	L1	F-SER117A	7.1	2.88	2.69
M-21	L2	F-SER117B	17.9	2.86	2.64
M-21	L2	F-SER117D	9.3	2.90	2.79
M-23	L1	C=O-THR119	48.6	2.83	2.59
M-23	L2	C=O-THR119	37.1	2.84	2.63
M-23	L1	F-SER117A	87.1	2.81	2.59
M-23	L1	OH-SER117B	22.1	2.77	2.59
M-23	L2	OH-SER117A	90.7	2.79	2.52
M-23	L2	OH-SER117C	15.0	2.79	2.60

Table S3. Ser117···Ser17 hydrogen bond contacts, frequency (in %) and average and shortest H-bond distances (in Å) for WT-TTR in the absence or presence of tolcapone and its analogs.

Ligand	Hydrogen bond	Frequency	Average distance	Shortest distance
TTR	SER117A-SER117B	25	2.79	2.53
TTR	SER117C-SER117D	17	2.79	2.56
Tolcapone	SER117A-SER117B	86	2.77	2.54
Tolcapone	SER117C-SER117D	83	2.78	2.58
M-14	SER117A-SER117B	76	2.78	2.51
M-14	SER117C-SER117D	76	2.79	2.53
M-17	SER117A-SER117B	91	2.76	2.49
M-17	SER117C-SER117D	61	2.81	2.56
M-20	SER117A-SER117B	81	2.79	2.52
M-20	SER117C-SER117D	84	2.79	2.54
M-21	SER117A-SER117B	68	2.75	2.51
M-21	SER117C-SER117D	69	2.79	2.59
M-23	SER117A-SER117B	90	2.74	2.48
M-23	SER117C-SER117D	77	2.77	2.57

Table S4. Ser117···Ser117 interdimer average and shortest distances (in Å) for WT-TTR in the absence or presence of tolcapone and its analogs.

Ligand	Hydrogen bond	Average distance	Shortest distance
TTR	SER117A-SER117C	5.18	4.19
TTR	SER117B-SER117D	5.49	4.70
Tolcapone	SER117A-SER117C	4.85	4.15
Tolcapone	SER117B-SER117D	5.73	4.26
M-14	SER117A-SER117C	4.98	3.85
M-14	SER117B-SER117D	5.39	4.37
M-17	SER117A-SER117C	4.88	4.01
M-17	SER117B-SER117D	5.48	4.35
M-20	SER117A-SER117C	5.12	3.70
M-20	SER117B-SER117D	5.42	4.53
M-21	SER117A-SER117C	5.03	3.92
M-21	SER117B-SER117D	5.66	4.82
M-23	SER117A-SER117C	5.01	4.33
M-23	SER117B-SER117D	5.03	4.18

Table S5. Data collection and refinement statistics. Values in parentheses are for the last shell.

	WT-TTR/M-23
Data collection	
Beamline	ALBA-XALOC
Space group	$P2_12_12$
Wavelength (nm)	0.9791
Resolution range (Å)	38.89 – 1.20
a, b, c (Å)	84.37, 43.82, 65.47
α, β, γ (°)	α = β = γ = 90
Unique reflections	76,526
Data redundancy	5.4(5.4)
R_{merge}	0.038(0.65)
$CC_{1/2}$	0.999(0.83)
$(I/\sigma(I))$	17.8(2.4)
Completeness (%)	99.9(99.9)
Structure refinement	
Resolution range (Å)	38.89 – 1.20
Non-anomalous reflections	76,460
R_{work}/R_{free} (%)	16.0/17.3
Number of all atoms	2,144
RMSD bond (Å)/Angle (°)	0.012/1.254
Ramachandran plot	
Favored (%)	97.81
Allowed (%)	2.19
Disallowed (%)	0
Overall B factors (Å^2)	15.4
PDB code	7QC5

A
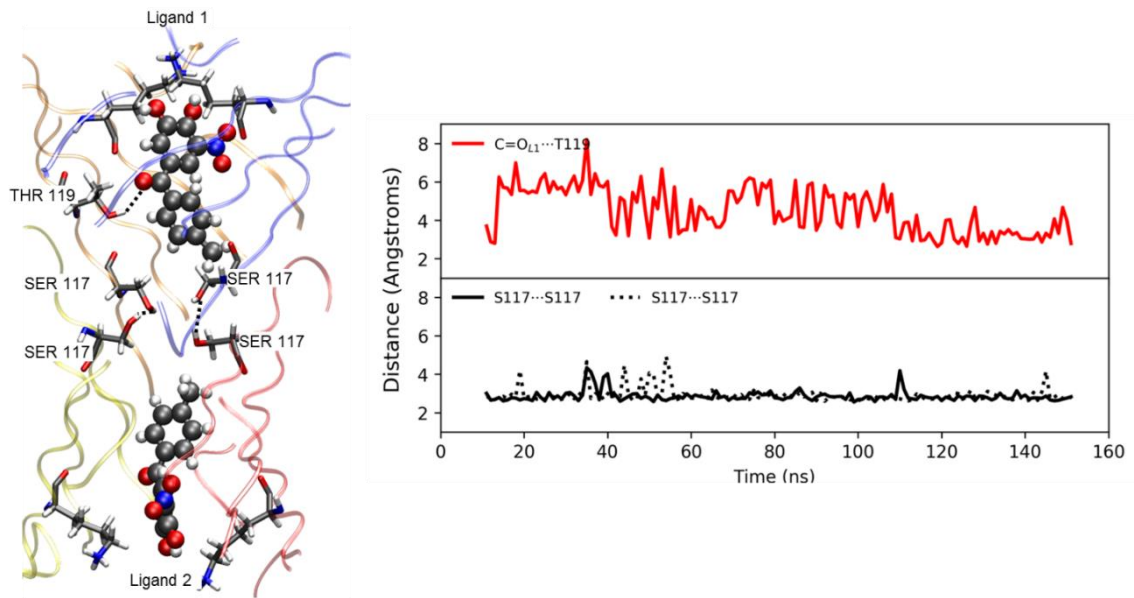
B
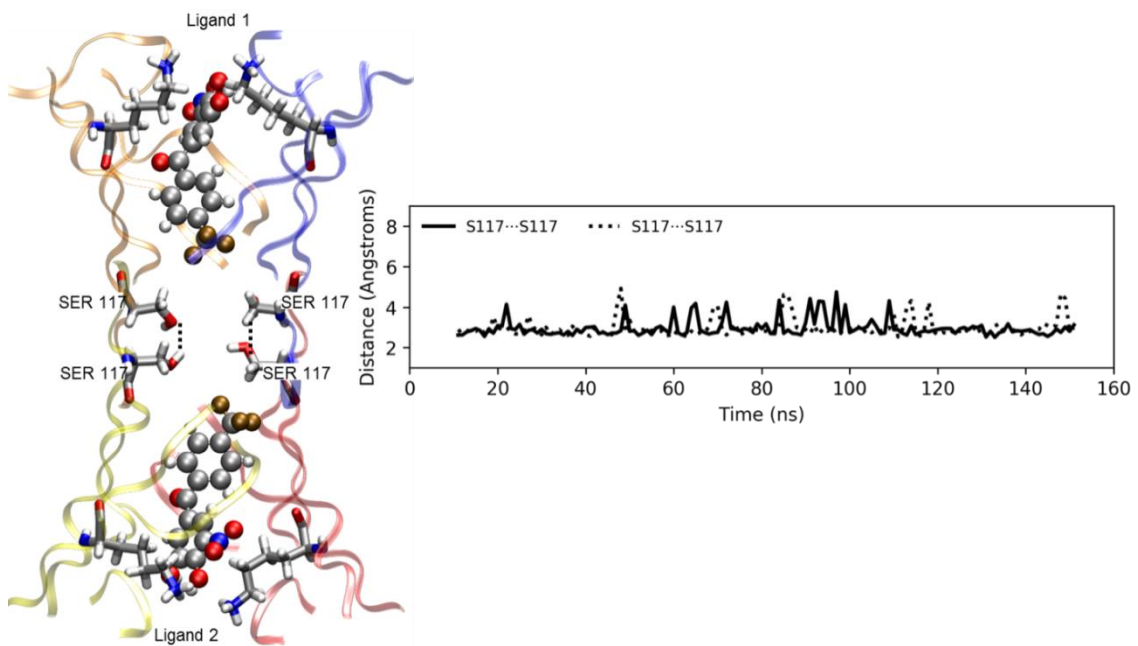
C
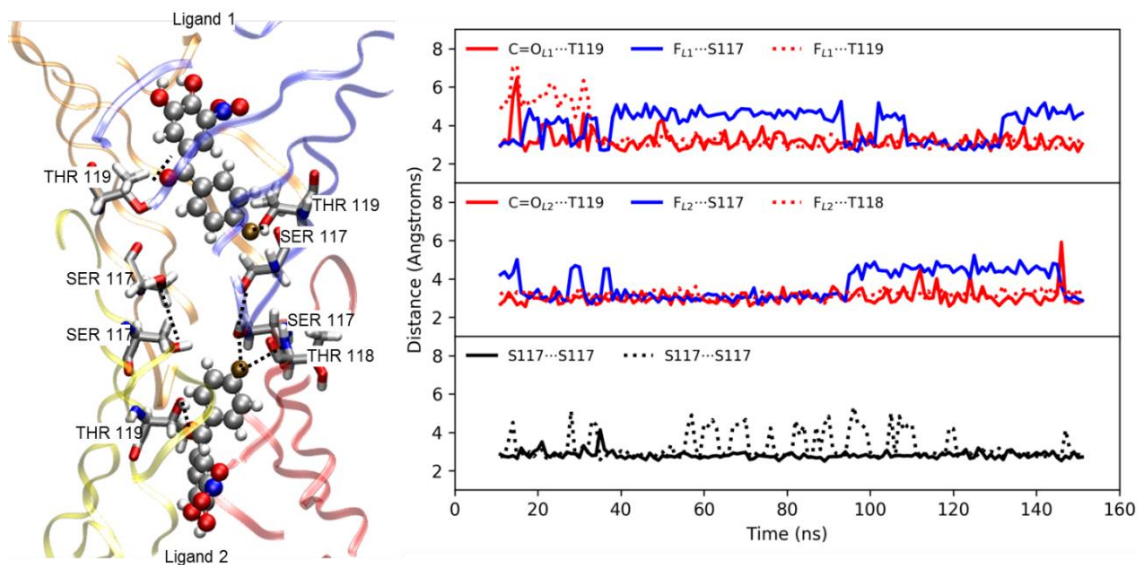
Figure S1. Tolcapone – TTR (A), **M-14** – TTR (B) and **M-17** – TTR (C) binding site and main contacts evolution along the 150 ns trajectory.

A
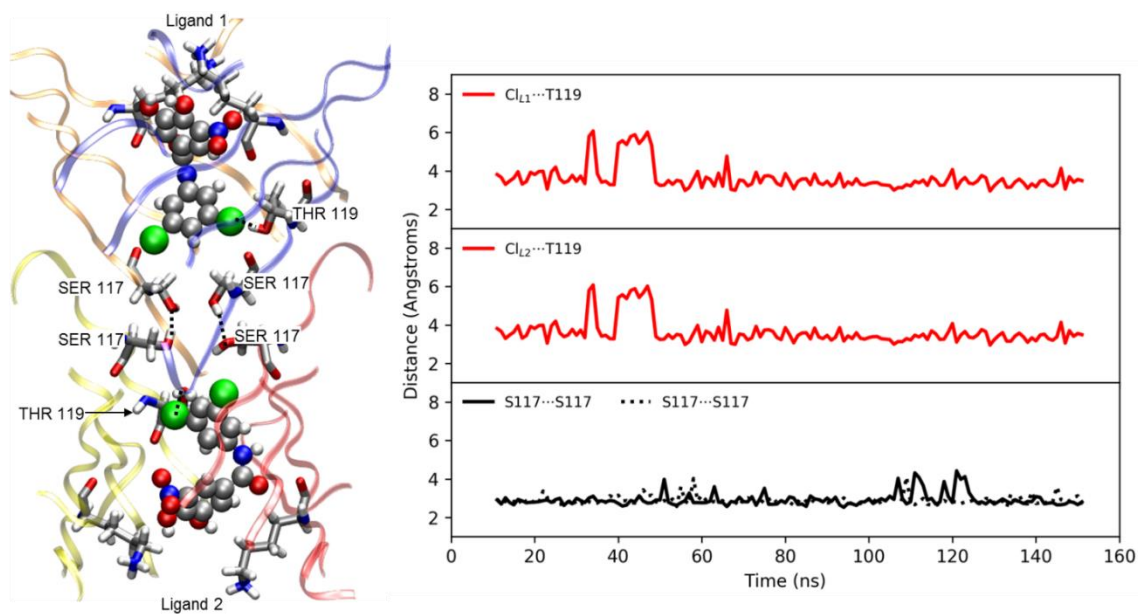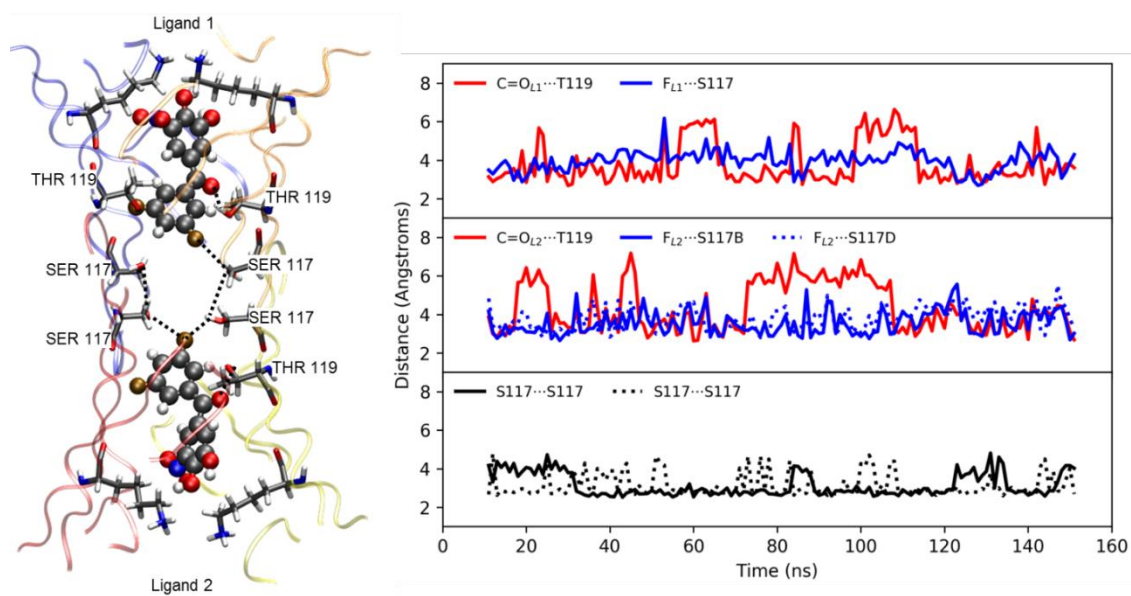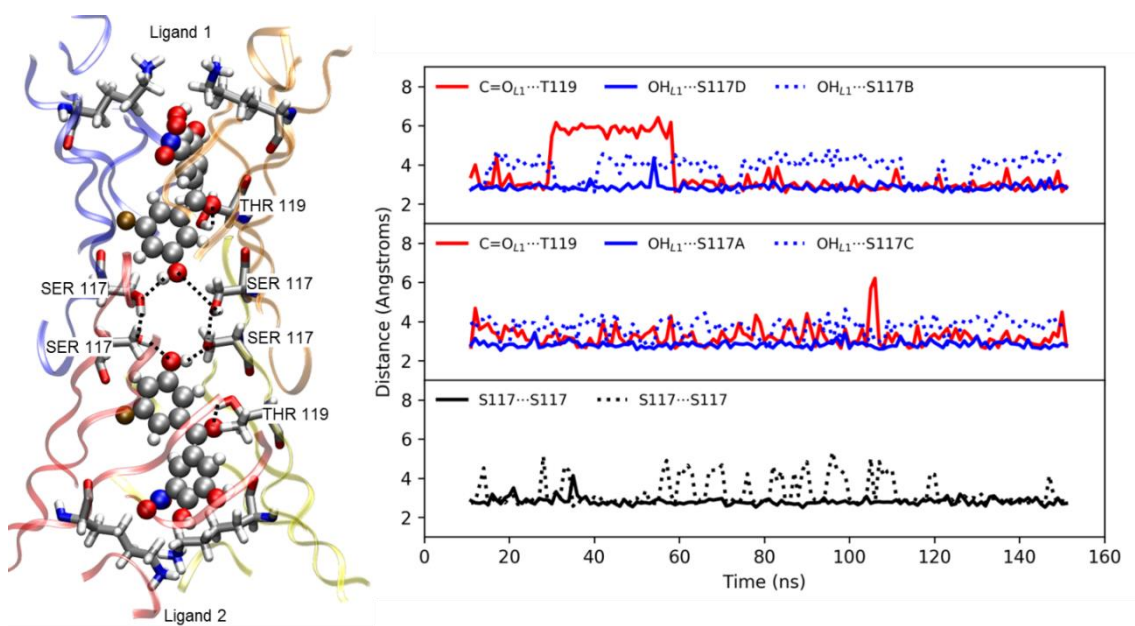
Figure S2. **M-20** – TTR (A), **M-21** – TTR (B) and **M-23** – TTR (C) binding site and main contacts evolution along the 150 ns trajectory.
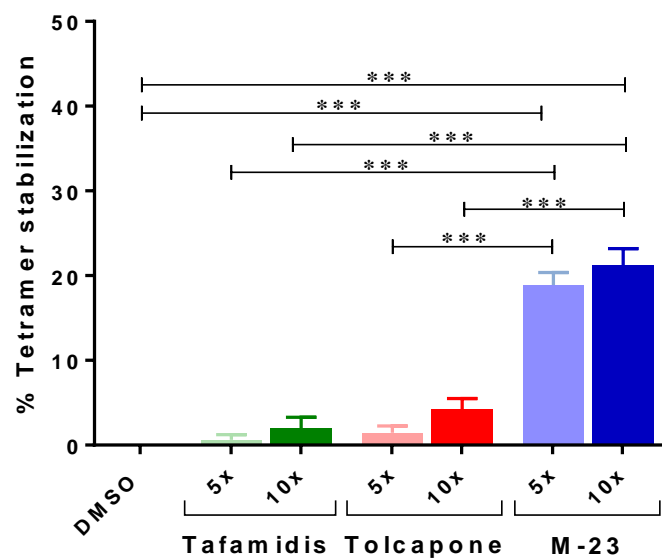
Figure S3. TTR tetramer stabilization effect of tafamidis, tolcapone and **M-23** in human plasma as assessed by IEF under semi-denaturing conditions. The test compounds were five (5x) or ten (10x) times more concentrated than WT-TTR. The values represent mean $\pm$ SEM (n=6); ***$p < 0.001$.
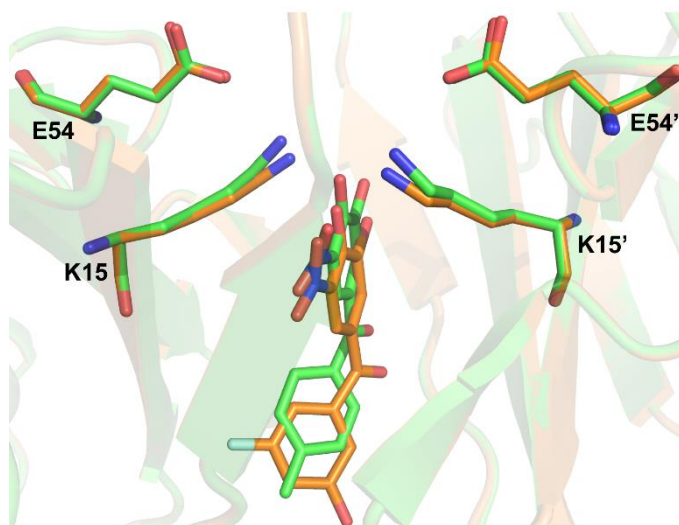
Figure S4. Overlay of one of the WT-TTR T_4-binding sites when bound to **M-23** (PDB: 7QC5) and tolcapone (PDB: 4D7B)[1], highlighting the inward movement of Lys15 from both chains when the protein is bound to **M-23**. WT-TTR/**M-23** and WT-TTR/tolcapone structures are colored in orange and green, respectively. Ligands and residues Lys15 and Glu54 are shown in sticks.

154
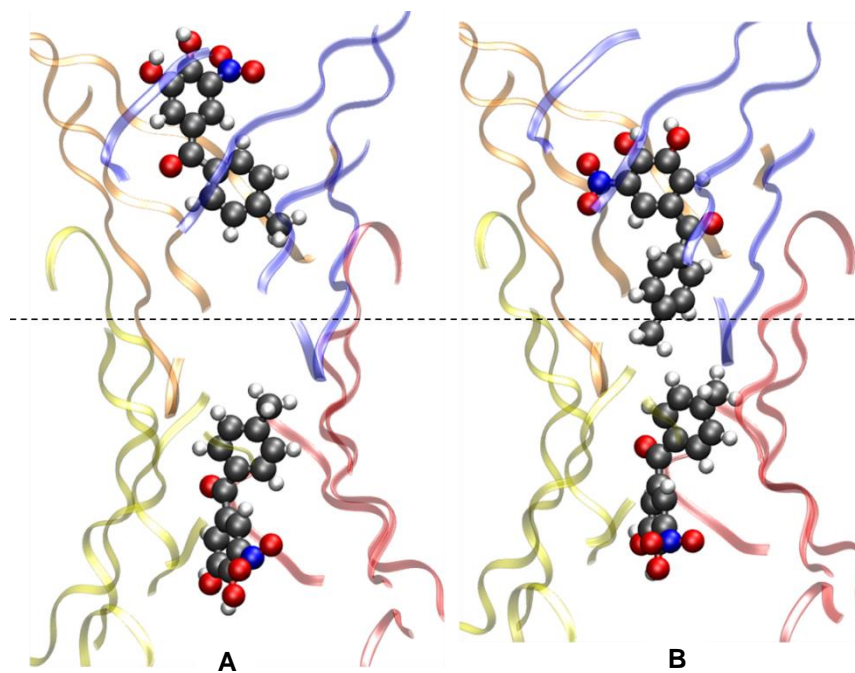
Figure S5. Tolcapone-TTR binding-poses from MD simulations in the absence of backbone constraints. Starting (A) and final (B) geometries are shown.

¹H and ¹³C NMR spectra of new compounds
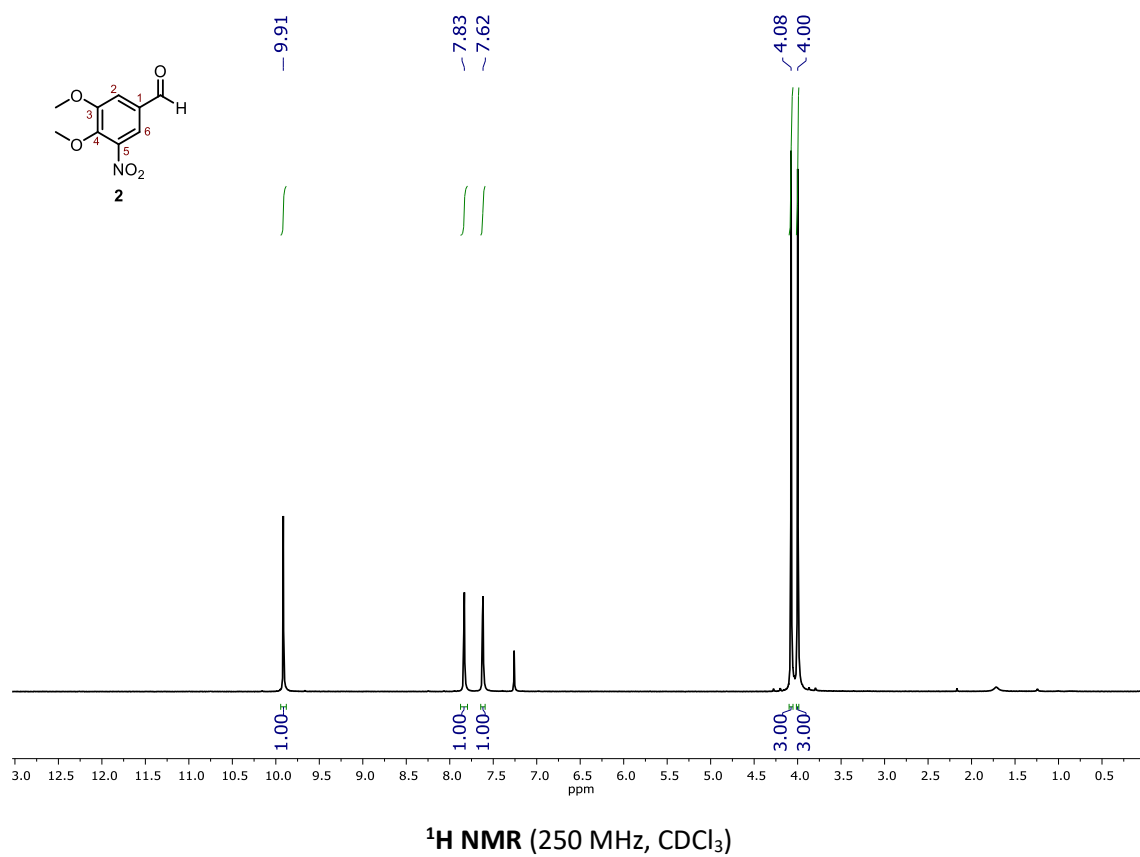
¹H NMR (250 MHz, CDCl₃)

Figure S6. ¹H NMR spectrum of compound **2**.

1e

7.05
7.02
6.58
3.78

2.00
1.00
3.00

9.5 9.0 8.5 8.0 7.5 7.0 6.5 6.0 5.5 5.0 4.5 4.0 3.5 3.0 2.5 2.0 1.5 1.0 0.5
f1 (ppm)

^{1}H NMR (400 MHz, CDCl$_3$)

163.2
161.4
119.5
117.4
102.0
93.3
55.9

190 180 170 160 150 140 130 120 110 100 90 80 70 60 50 40 30 20 10 0
ppm
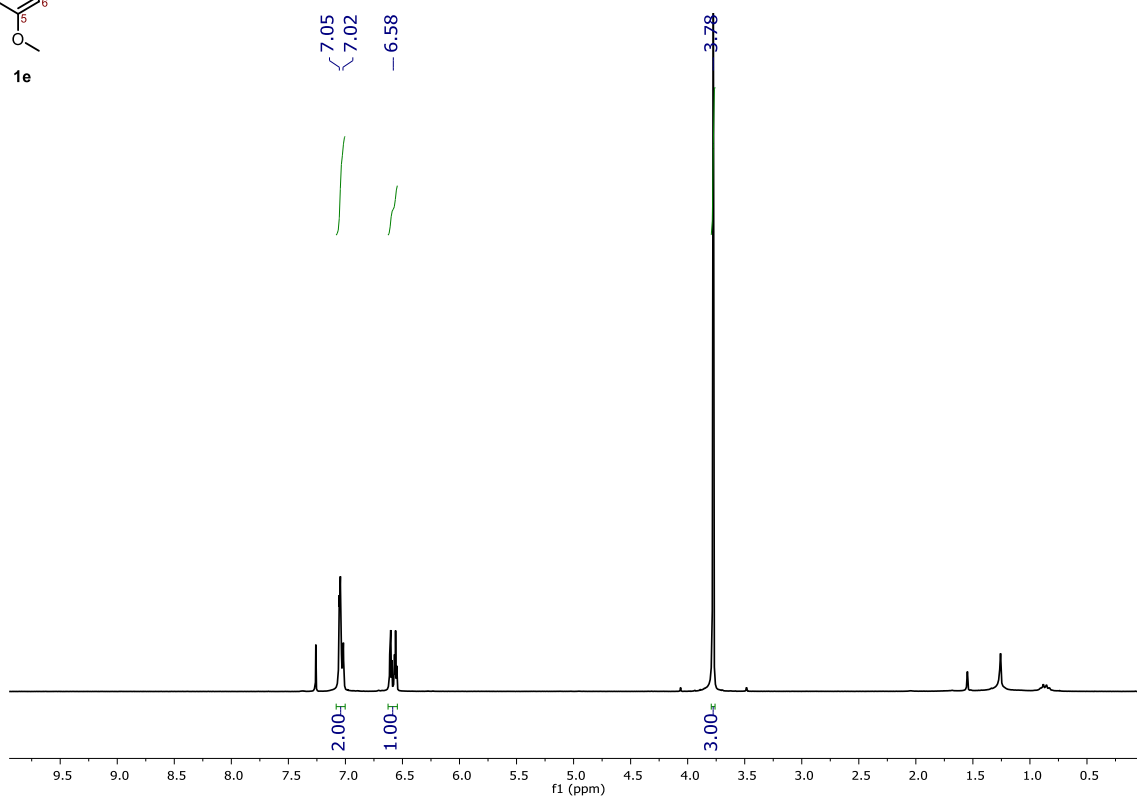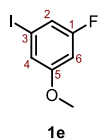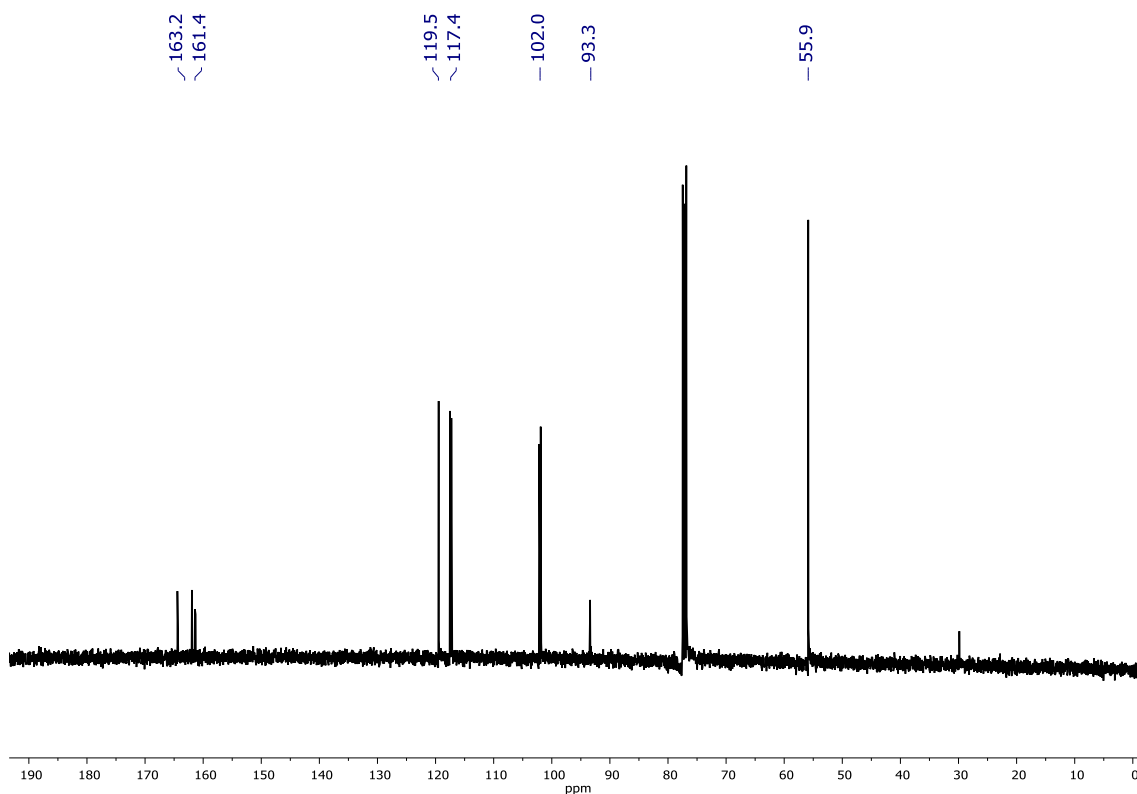
^{13}C NMR (100 MHz, CDCl$_3$)

Figure S7. ^{1}H and ^{13}C NMR spectra of compound **1e**.

¹H NMR (400 MHz, CDCl₃)

¹³C NMR (100 MHz, CDCl₃)
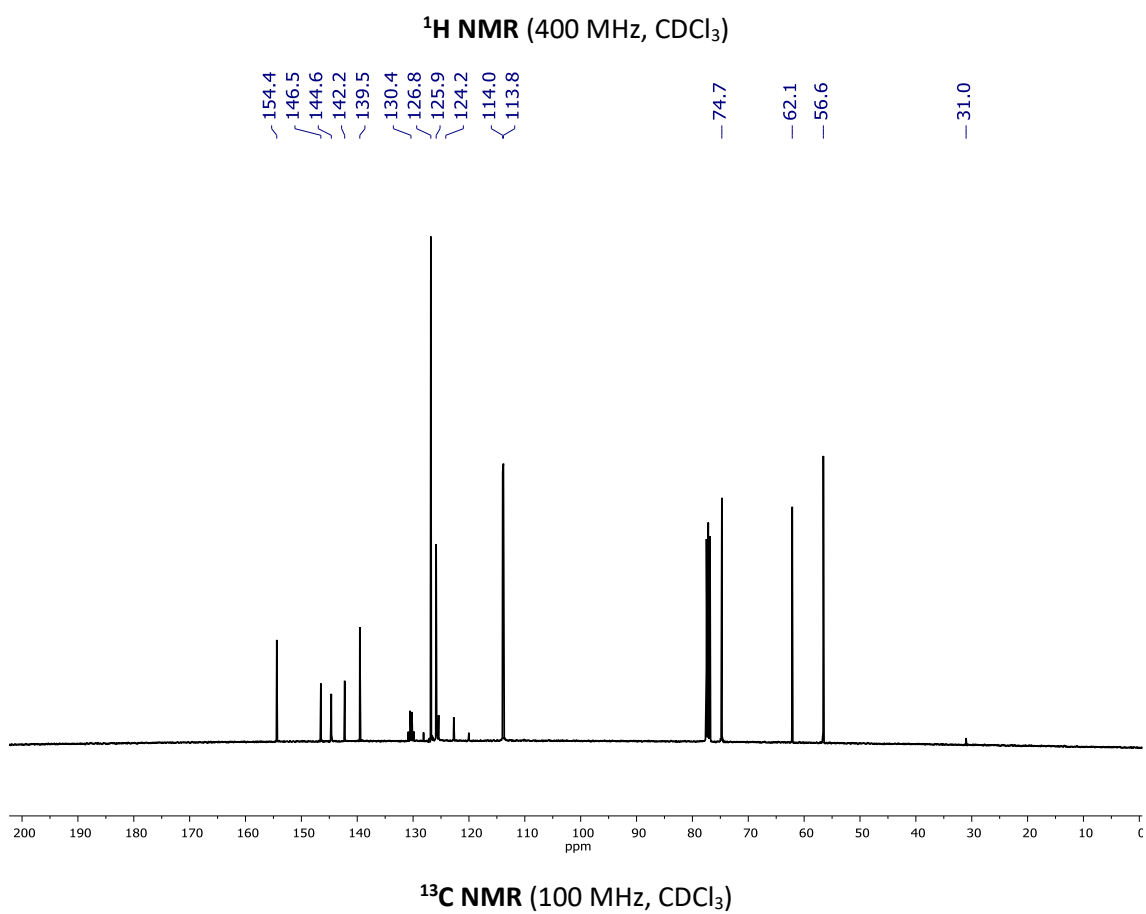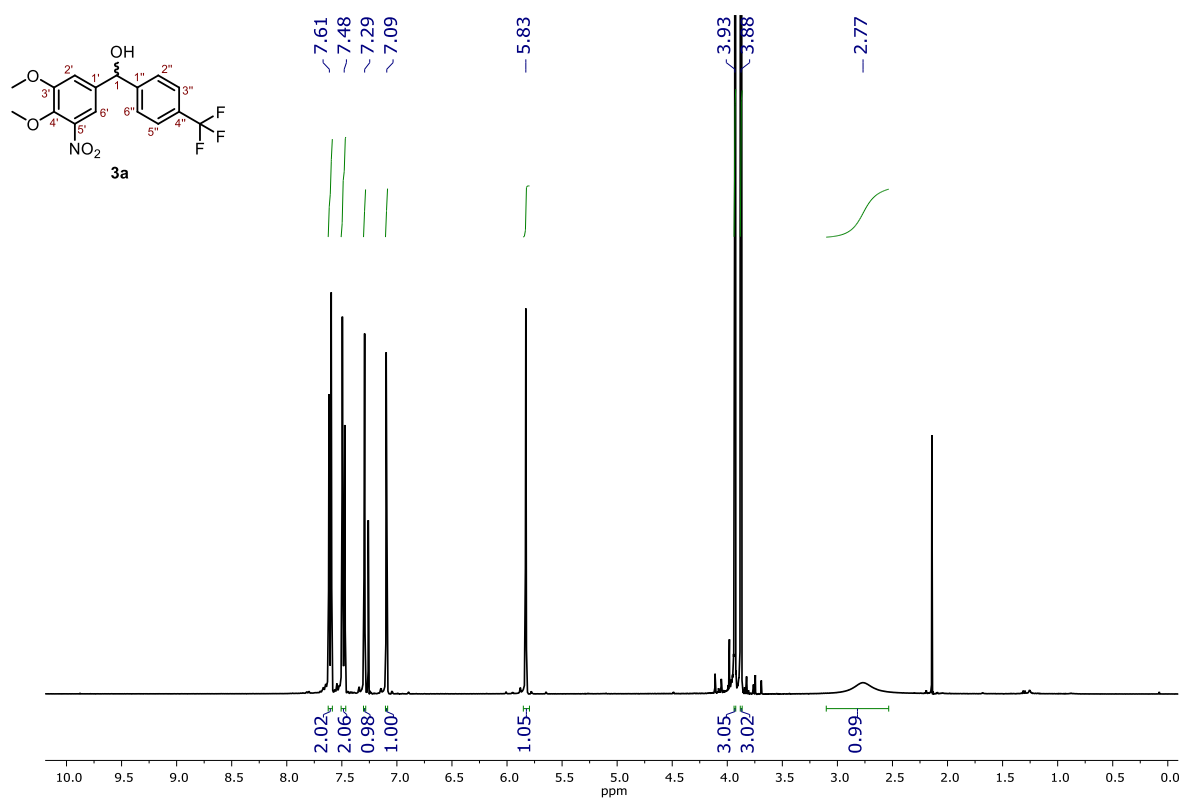
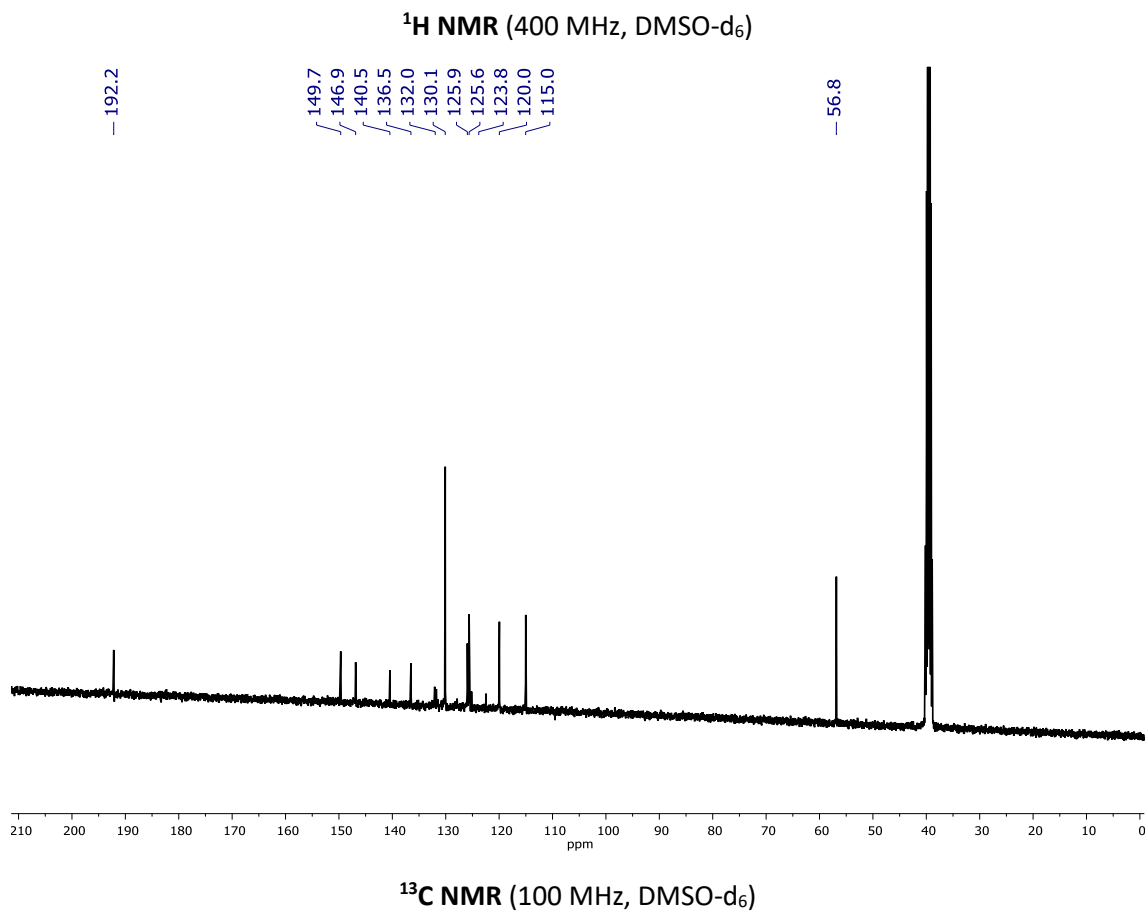**Figure S8.** ¹H and ¹³C NMR spectra of compound **3a**.
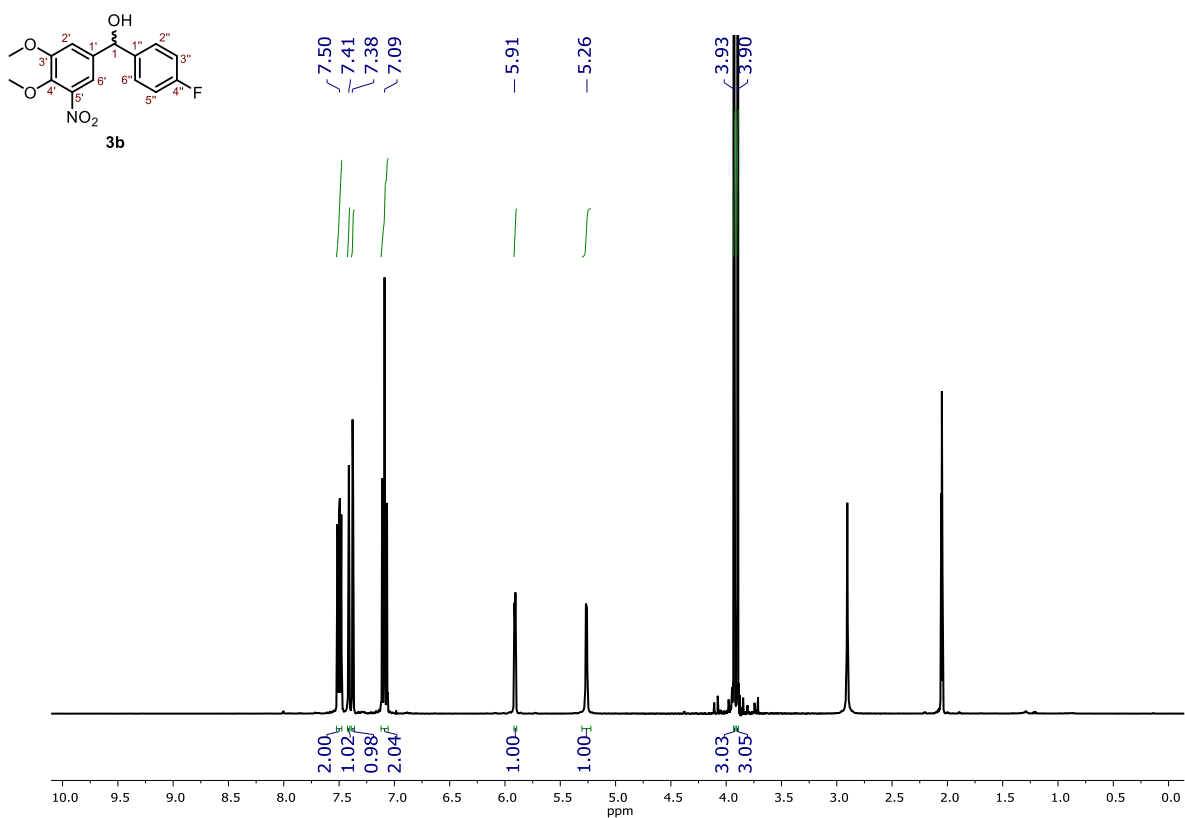
¹H NMR (400 MHz, acetone-d₆)
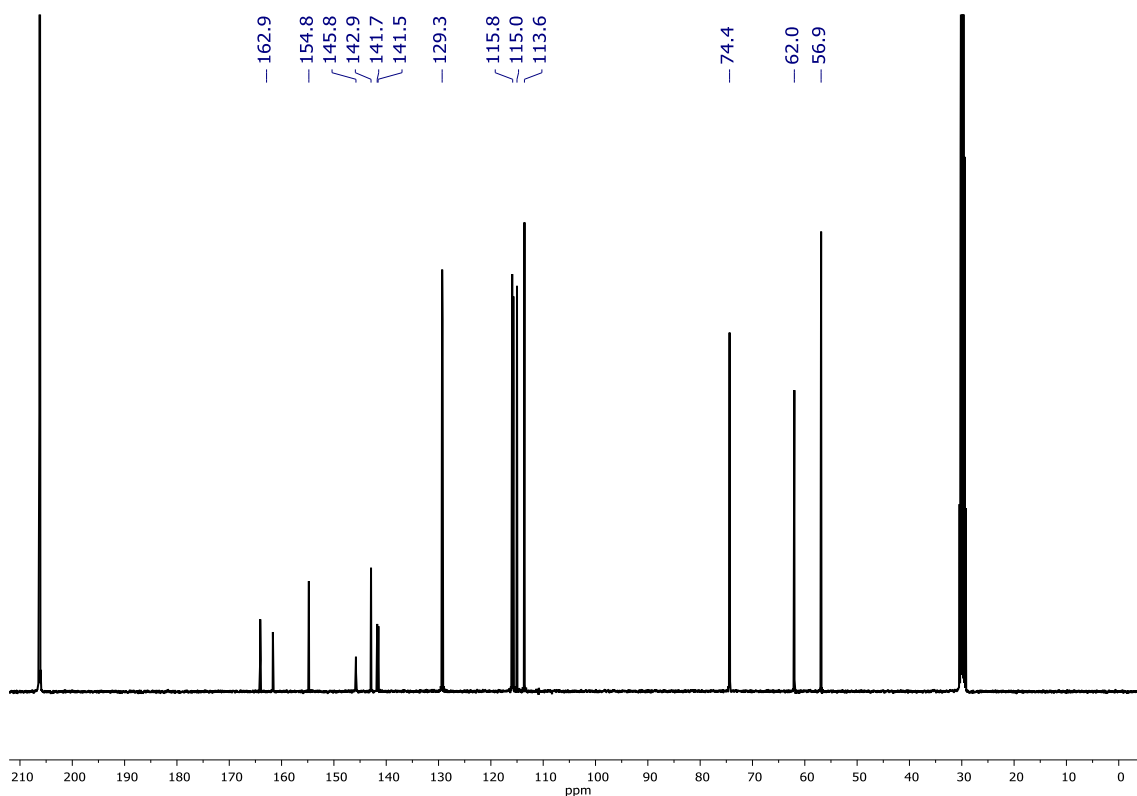
¹³C NMR (100 MHz, acetone-d₆)

Figure S9. ¹H and ¹³C NMR spectra of compound **3b**.
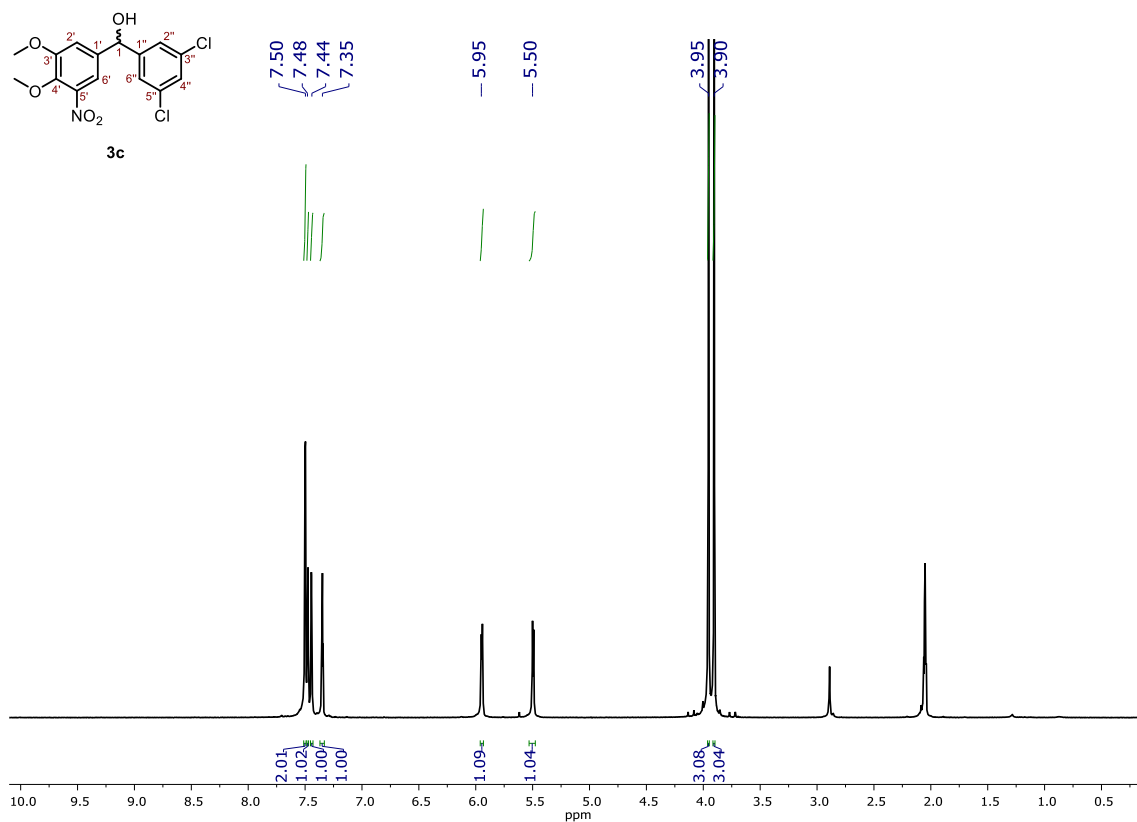
¹H NMR (400 MHz, acetone-d₆)
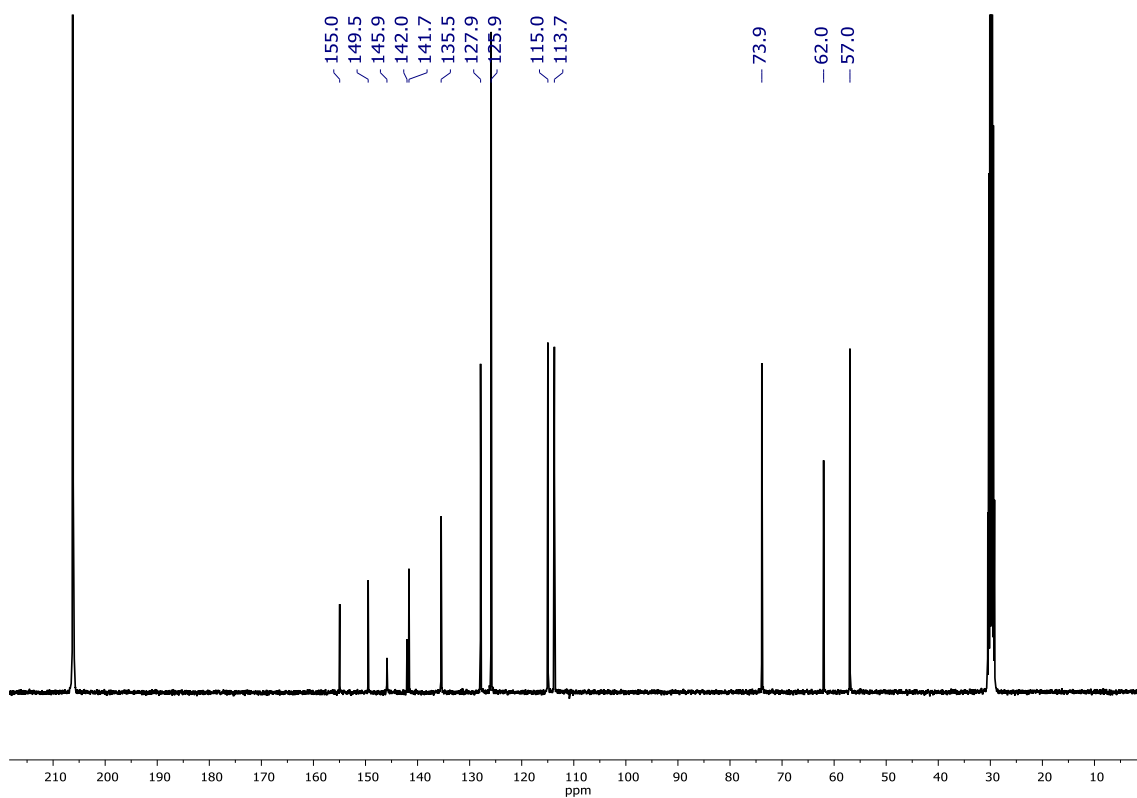
¹³C NMR (90 MHz, acetone-d₆)

Figure S10. ¹H and ¹³C NMR spectra of compound **3c**.
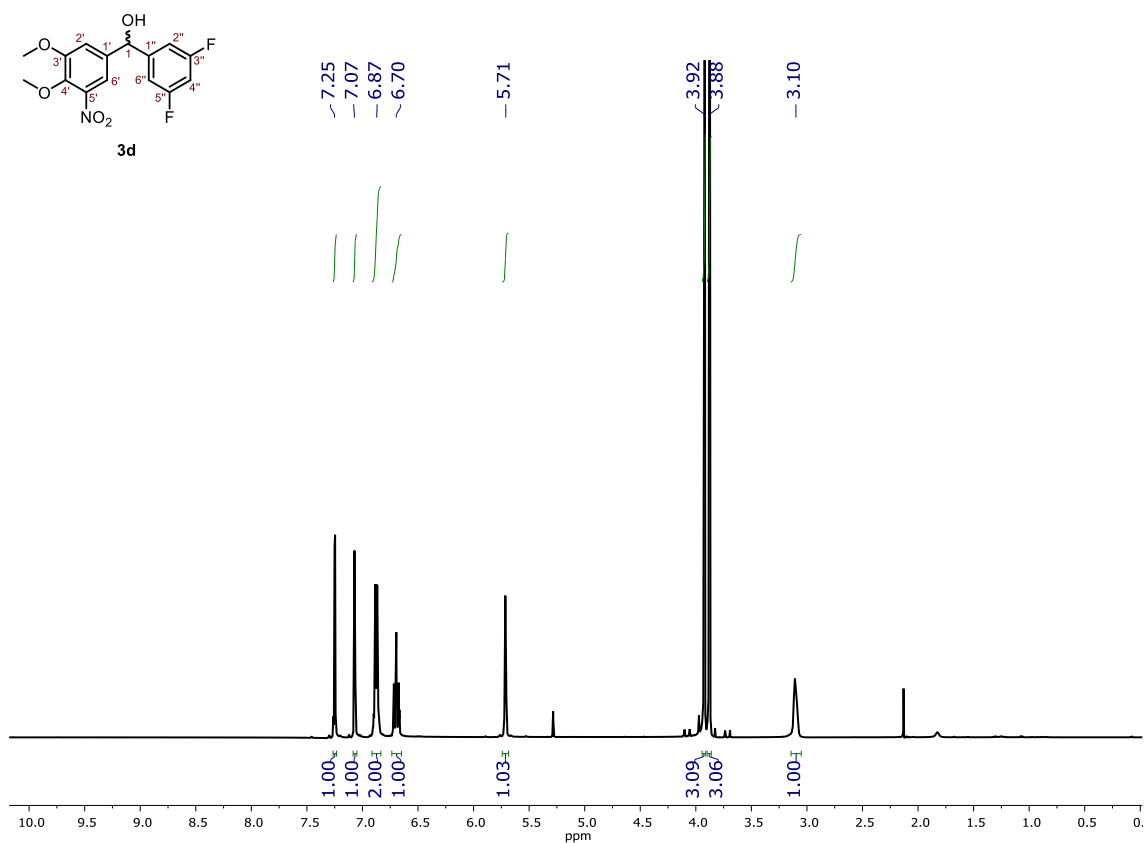
1H NMR (400 MHz, CDCl₃)
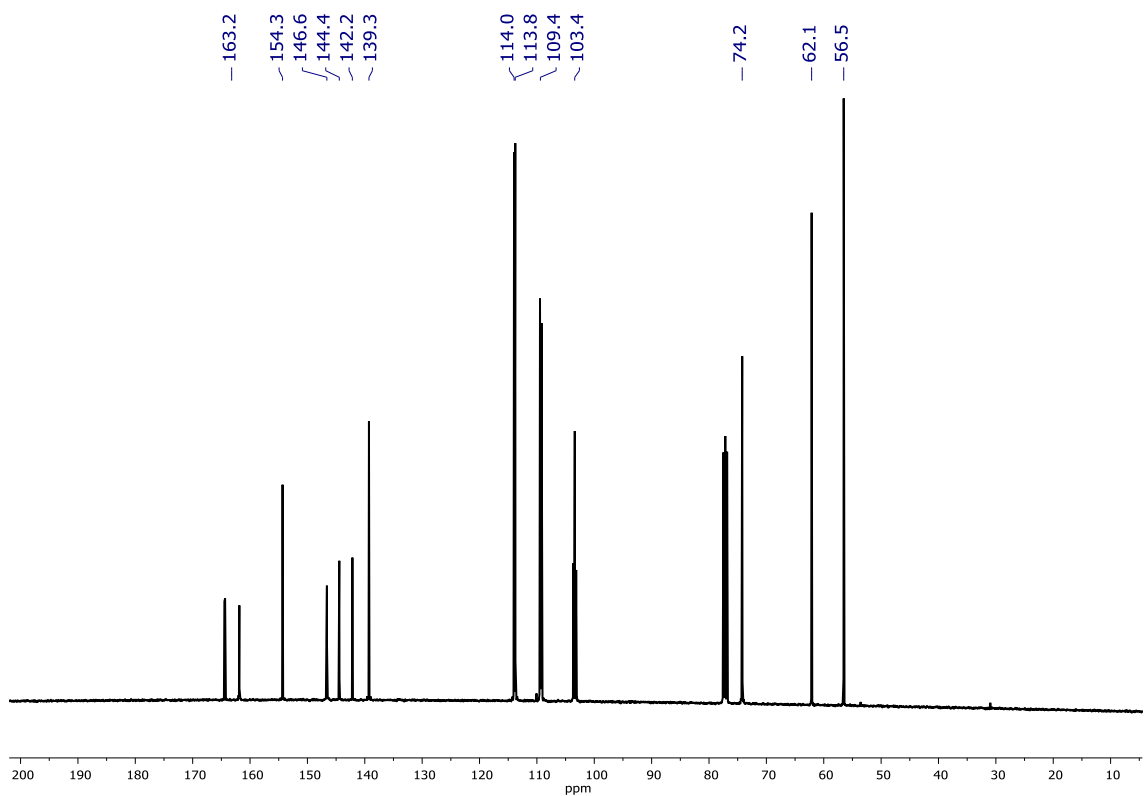
13C NMR (100 MHz, CDCl₃)

Figure S11. ¹H and ¹³C NMR spectra of compound **3d**.

¹H NMR (400 MHz, CDCl₃)

¹³C NMR (100 MHz, CDCl₃)
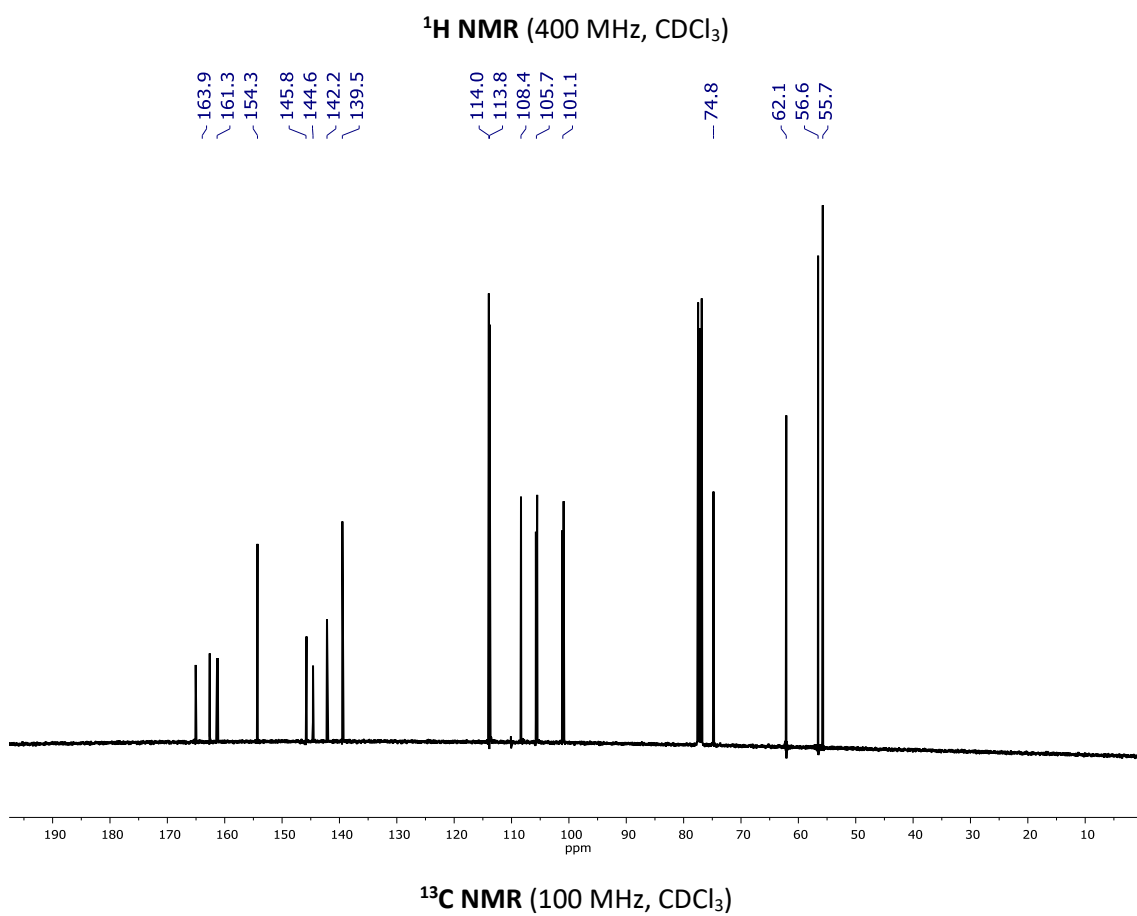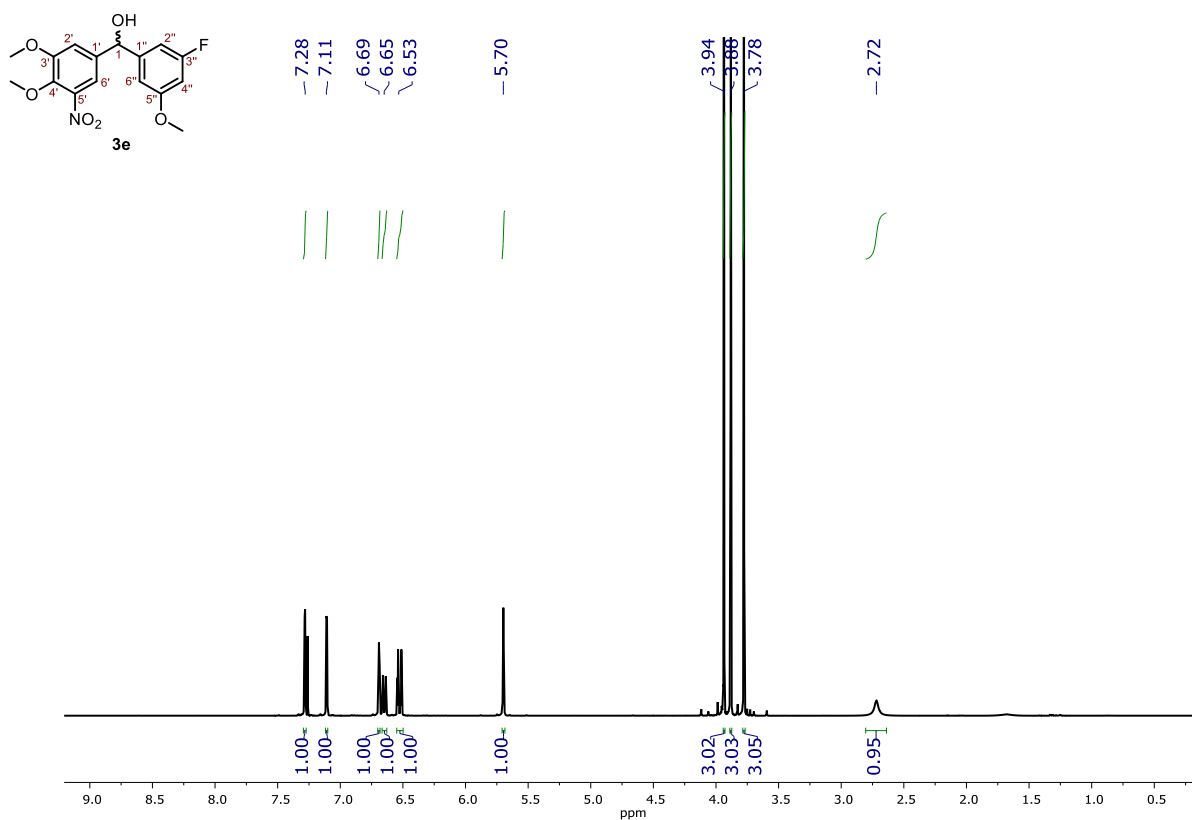
Figure S12. ¹H and ¹³C NMR spectra of compound **3e**.
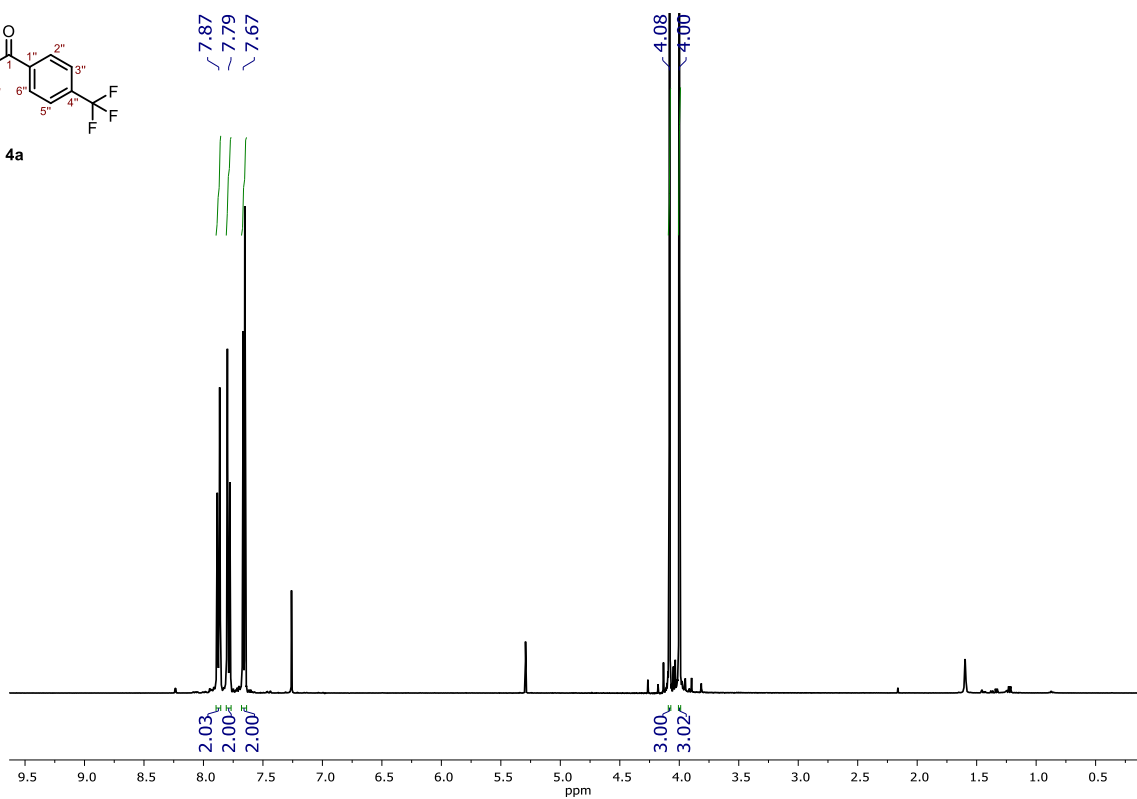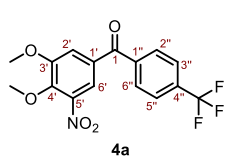
¹H NMR (400 MHz, CDCl₃)
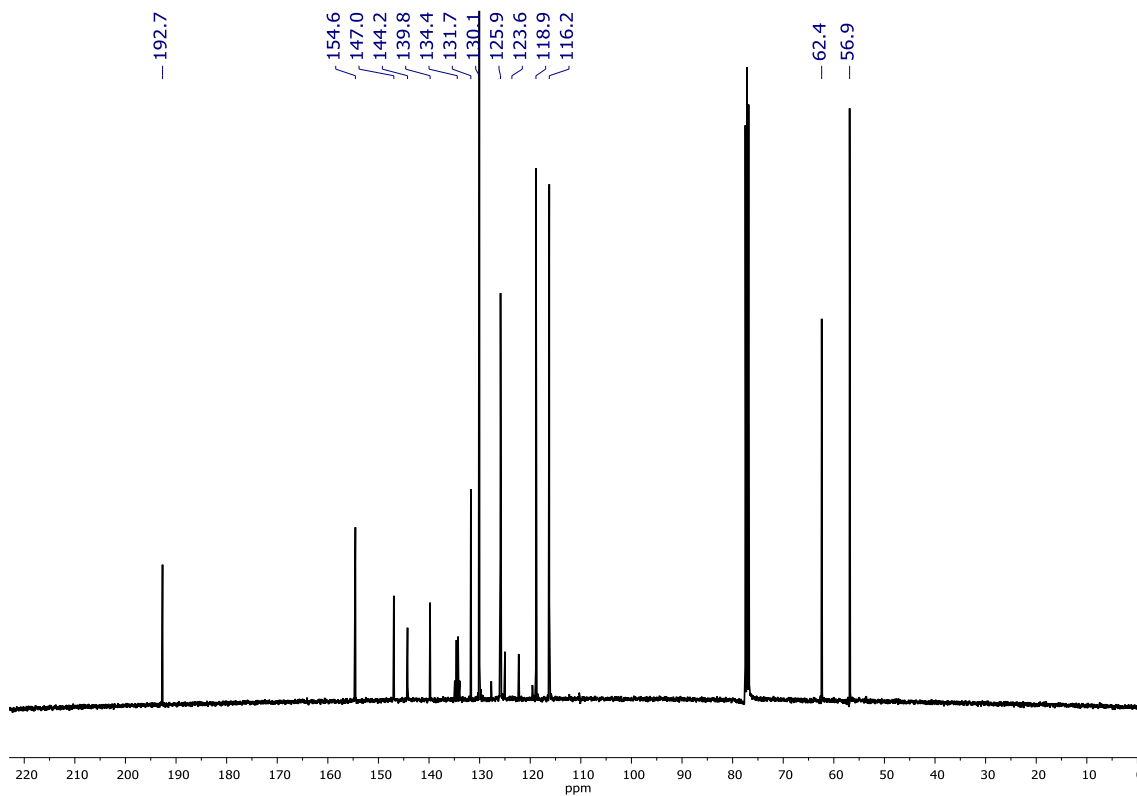
¹³C NMR (100 MHz, CDCl₃)
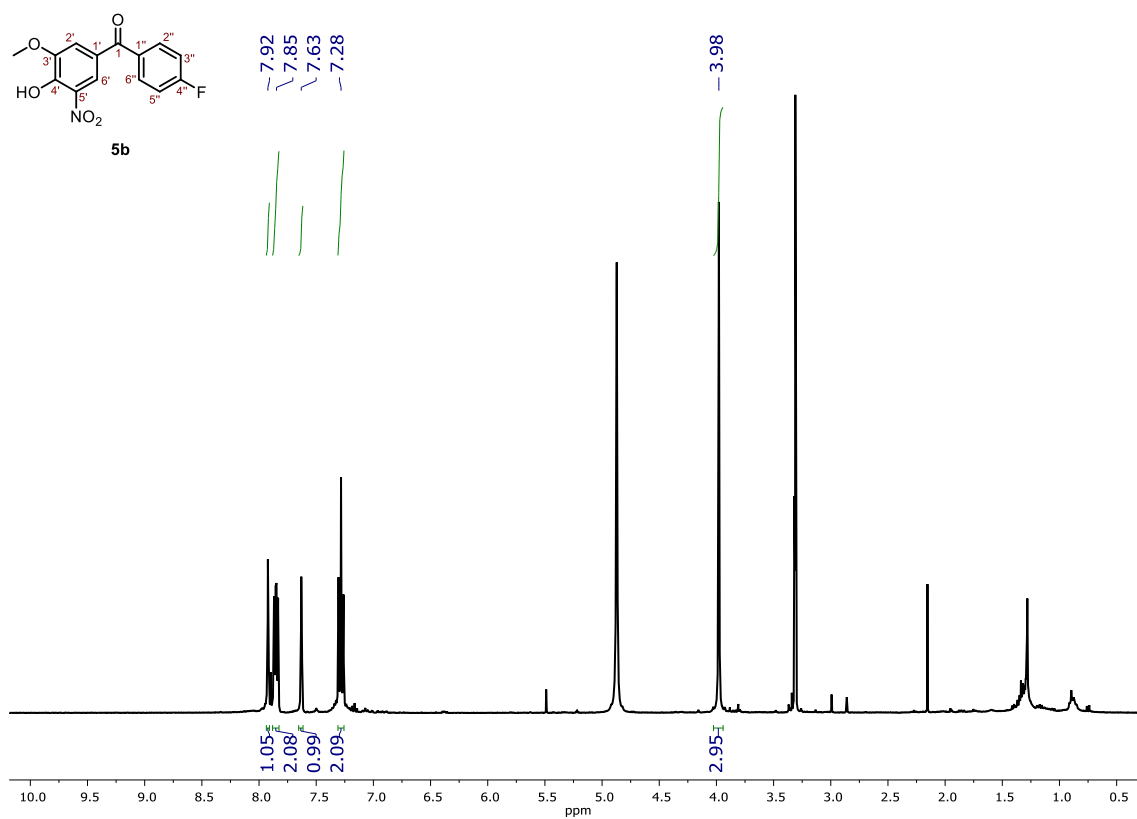
Figure S13. ¹H and ¹³C NMR spectra of compound **4a**.

163
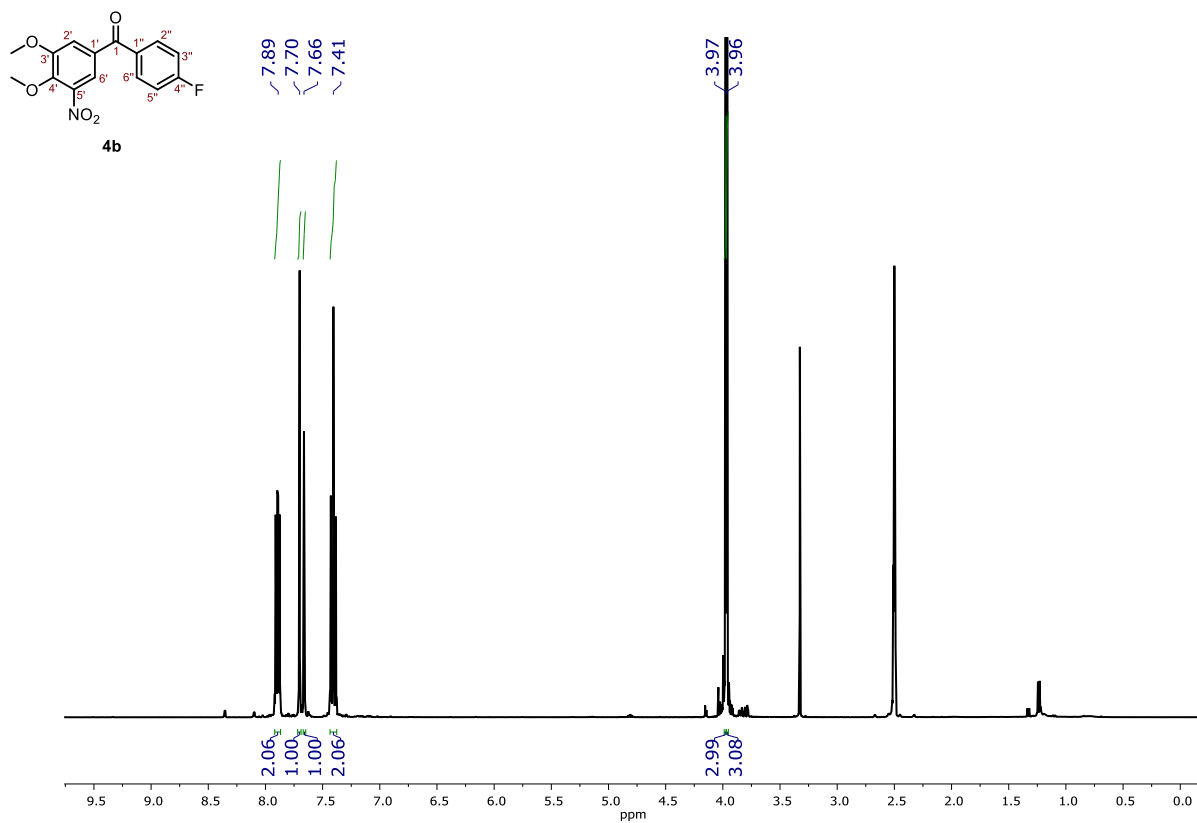
^{1}H NMR (400 MHz, DMSO-d$_6$)
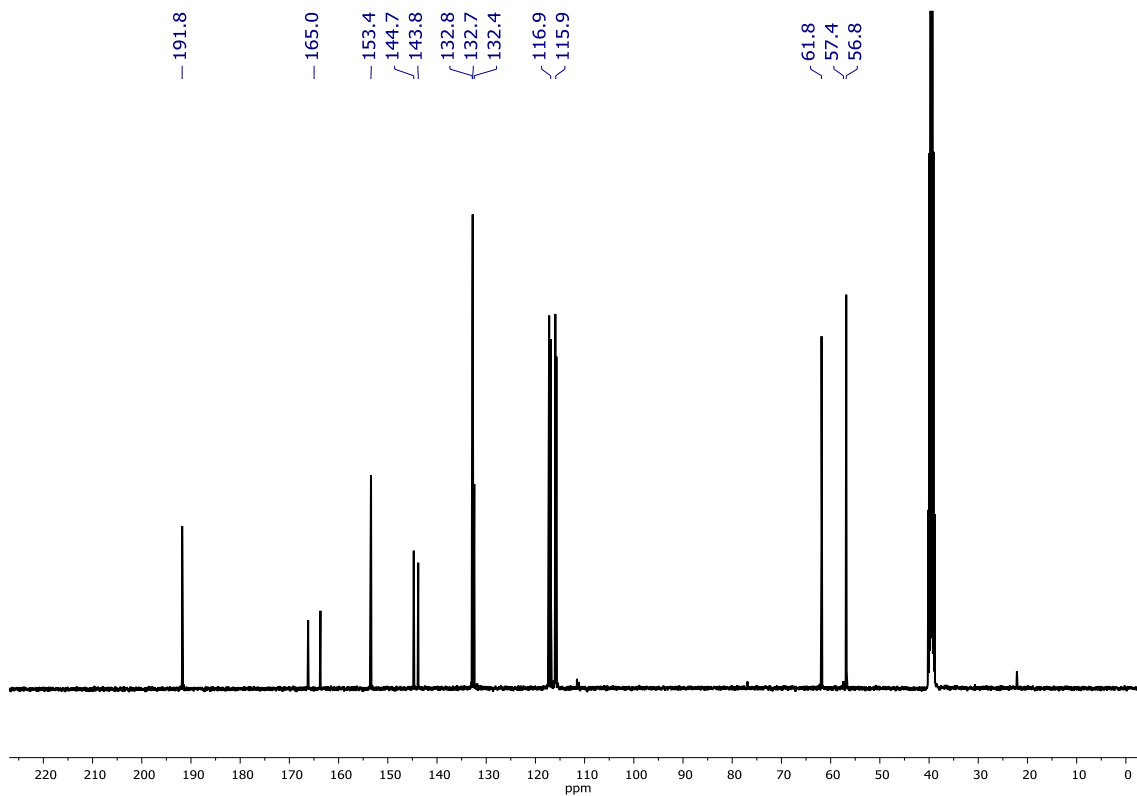
^{13}C NMR (100 MHz, DMSO-d$_6$)

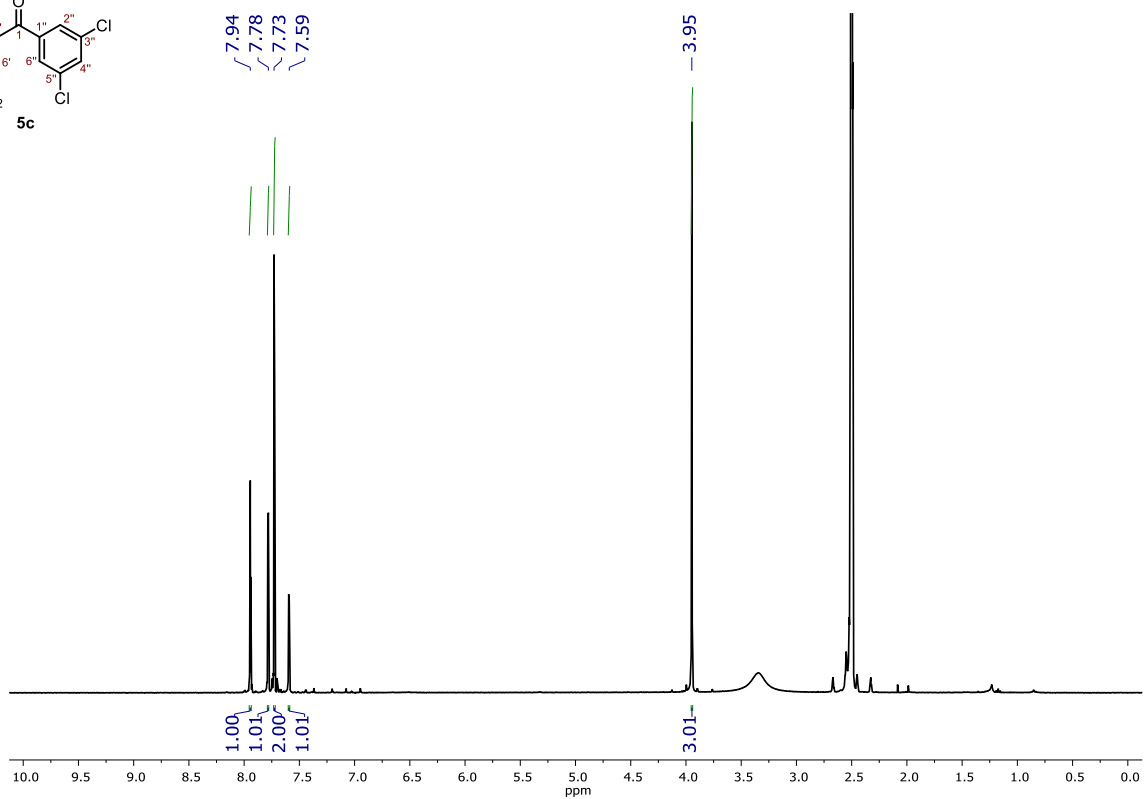**Figure S14.** ^{1}H and ^{13}C NMR spectra of compound **4b**.

¹H NMR (400 MHz, DMSO-d₆)

¹³C NMR (100 MHz, DMSO-d₆)
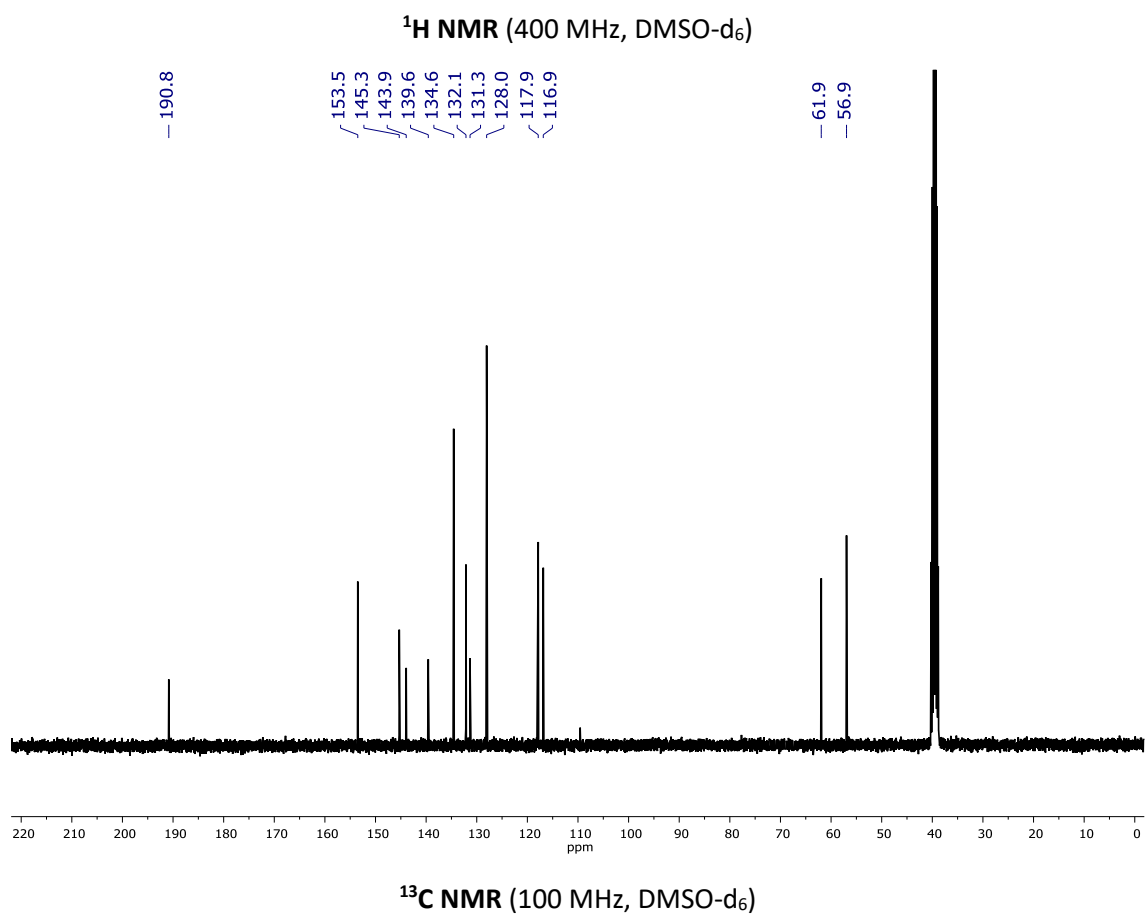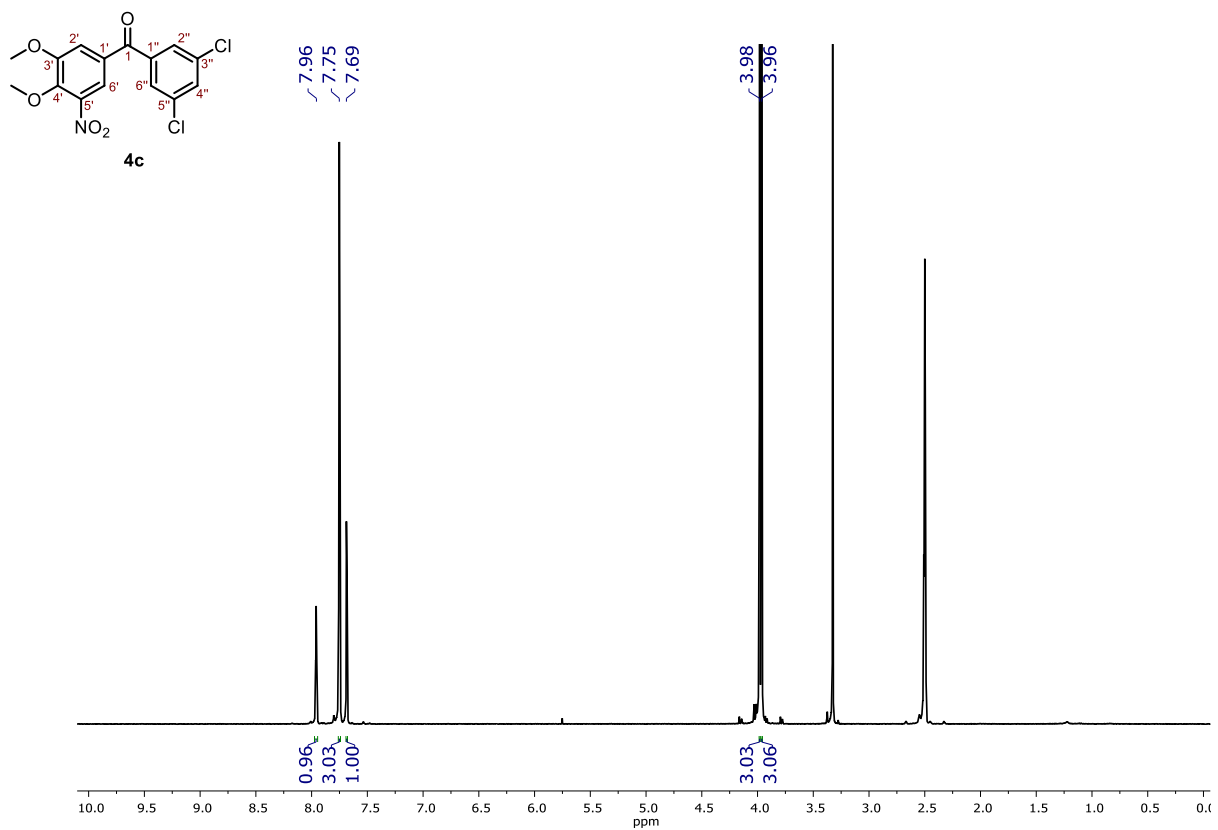
Figure S15. ¹H and ¹³C NMR spectra of compound **4c**.

¹H NMR (360 MHz, CDCl₃)
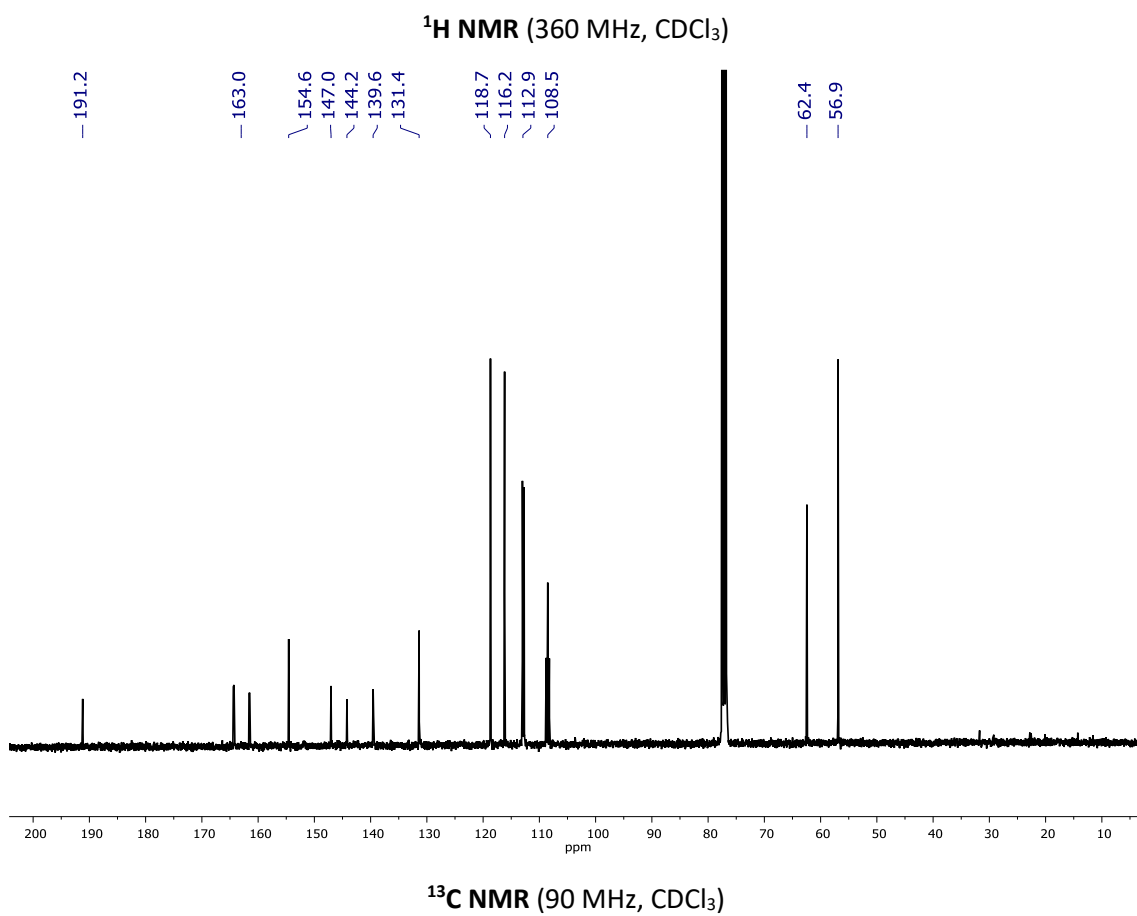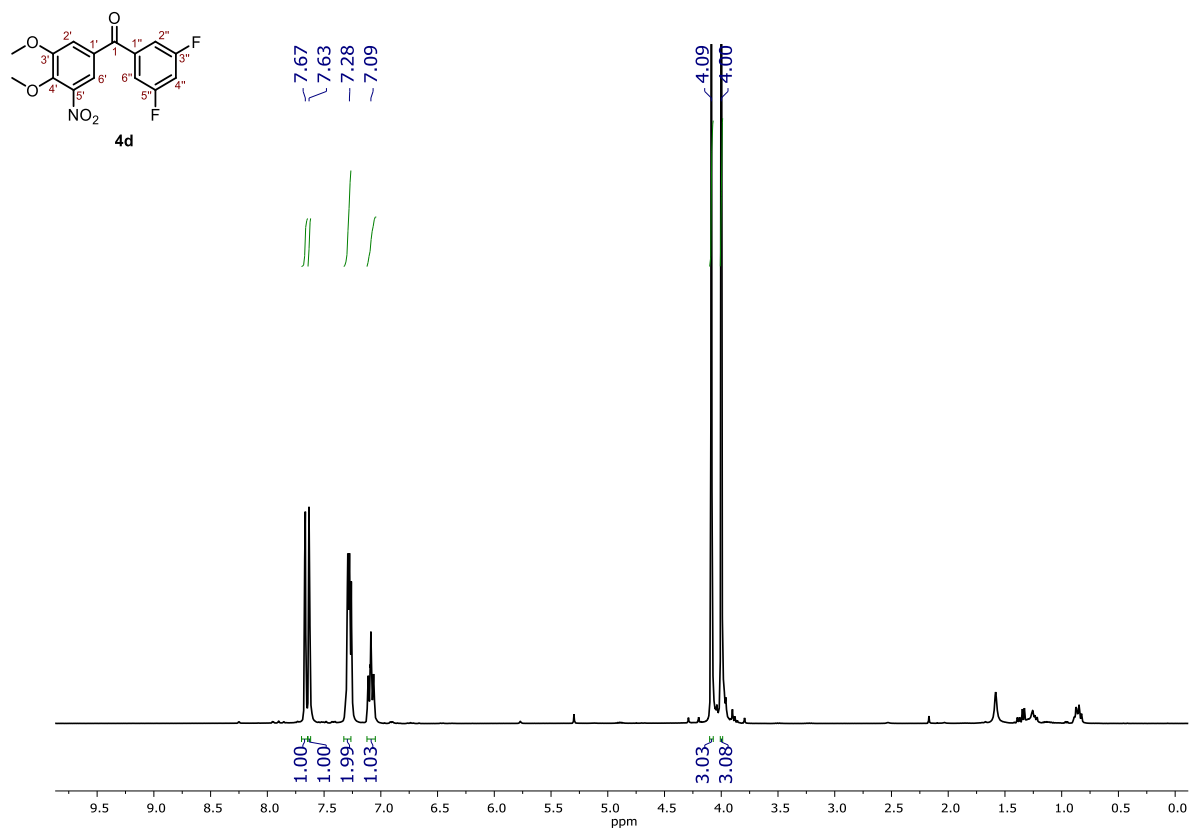
¹³C NMR (90 MHz, CDCl₃)

Figure S16. ¹H and ¹³C NMR spectra of compound **4d**.
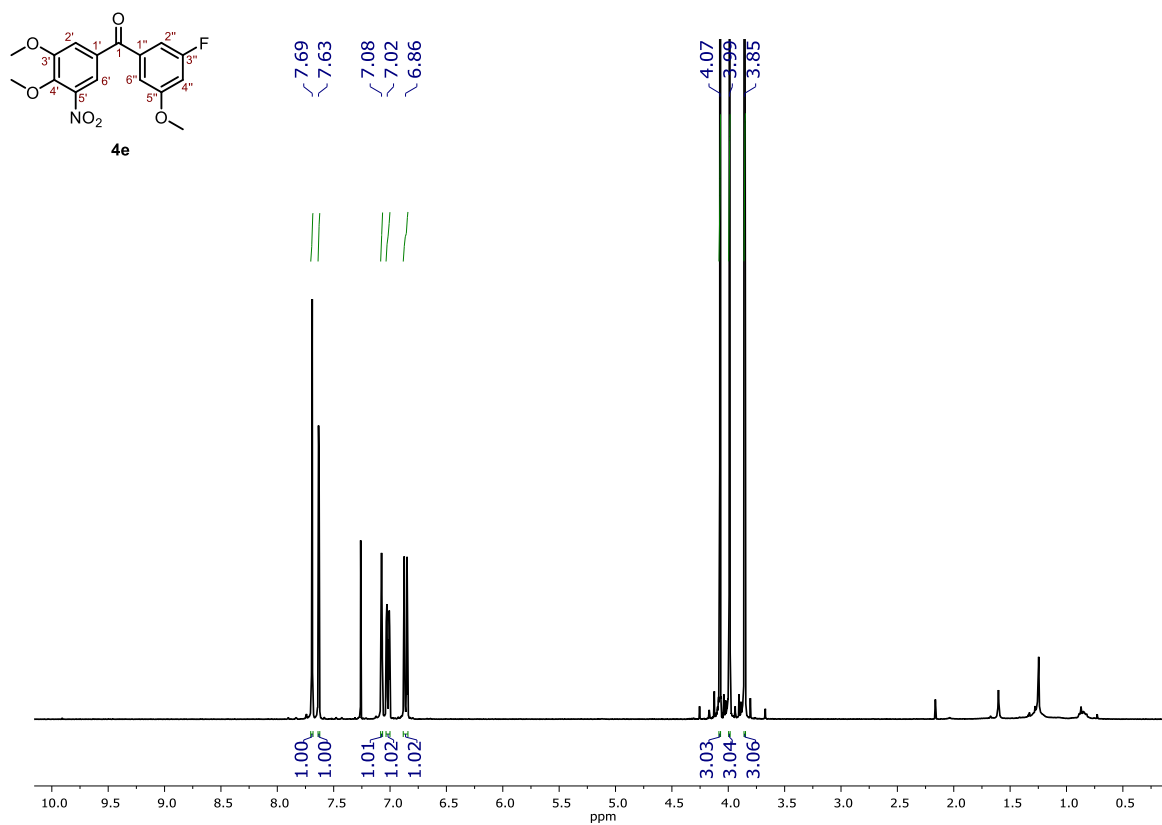
¹H NMR (400 MHz, CDCl₃)
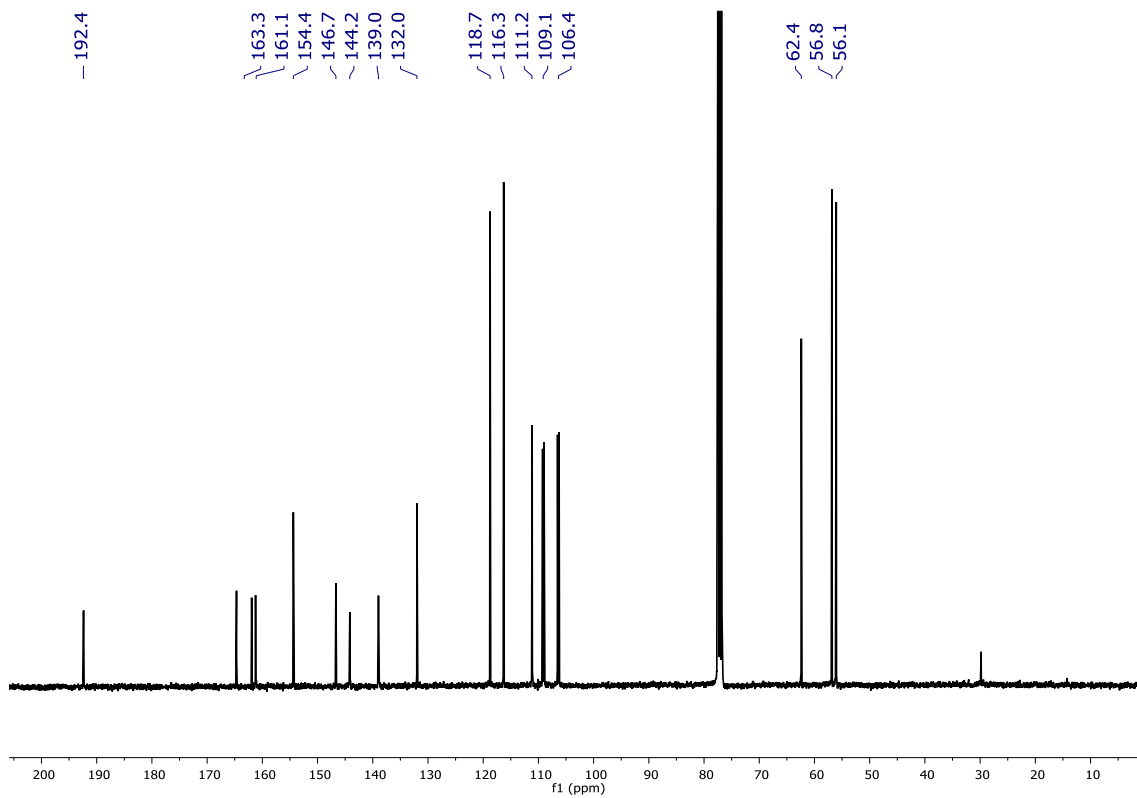
¹³C NMR (90 MHz, CDCl₃)

Figure S17. ¹H and ¹³C NMR spectra of compound **4e**.

¹H NMR (400 MHz, DMSO-d₆)

¹³C NMR (100 MHz, DMSO-d₆)
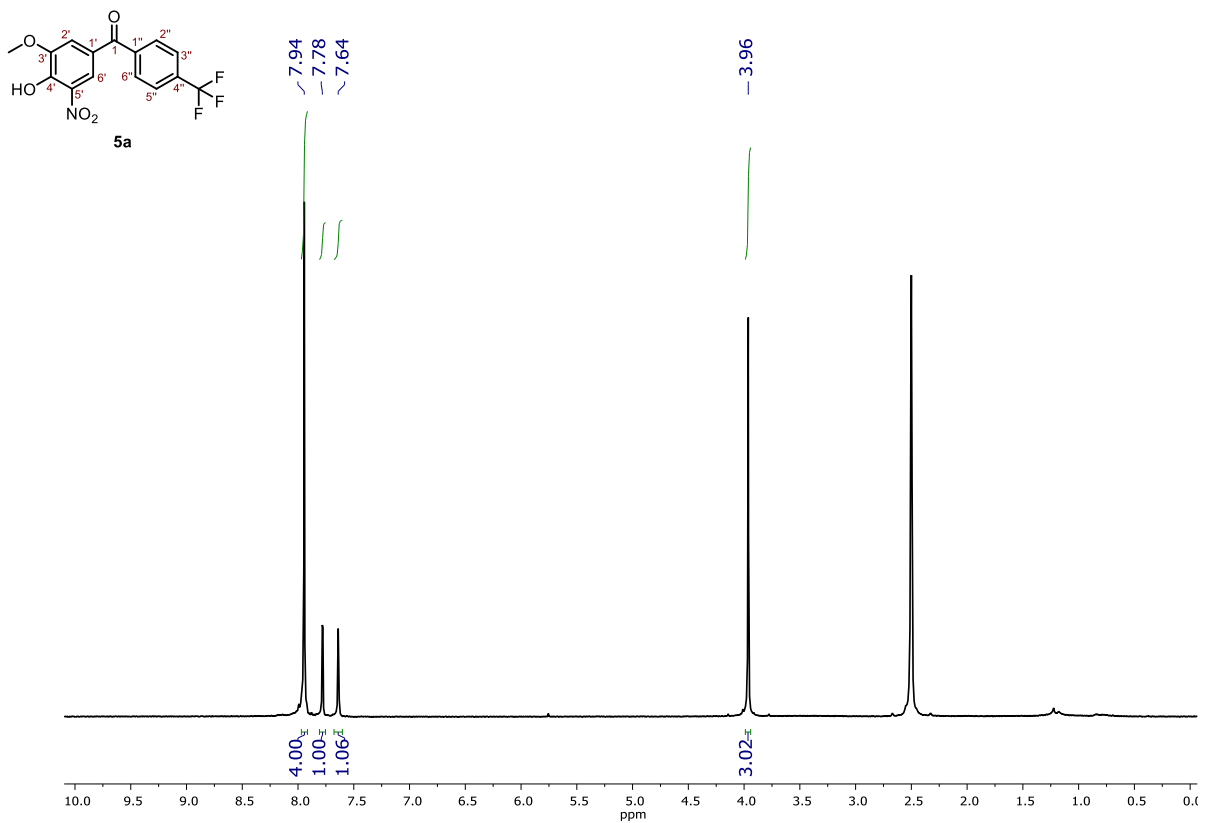
Figure S18. ¹H and ¹³C NMR and spectra of compound **5a**.

¹H NMR (400 MHz, methanol-d₄)

¹³C NMR (100 MHz, methanol-d₄)
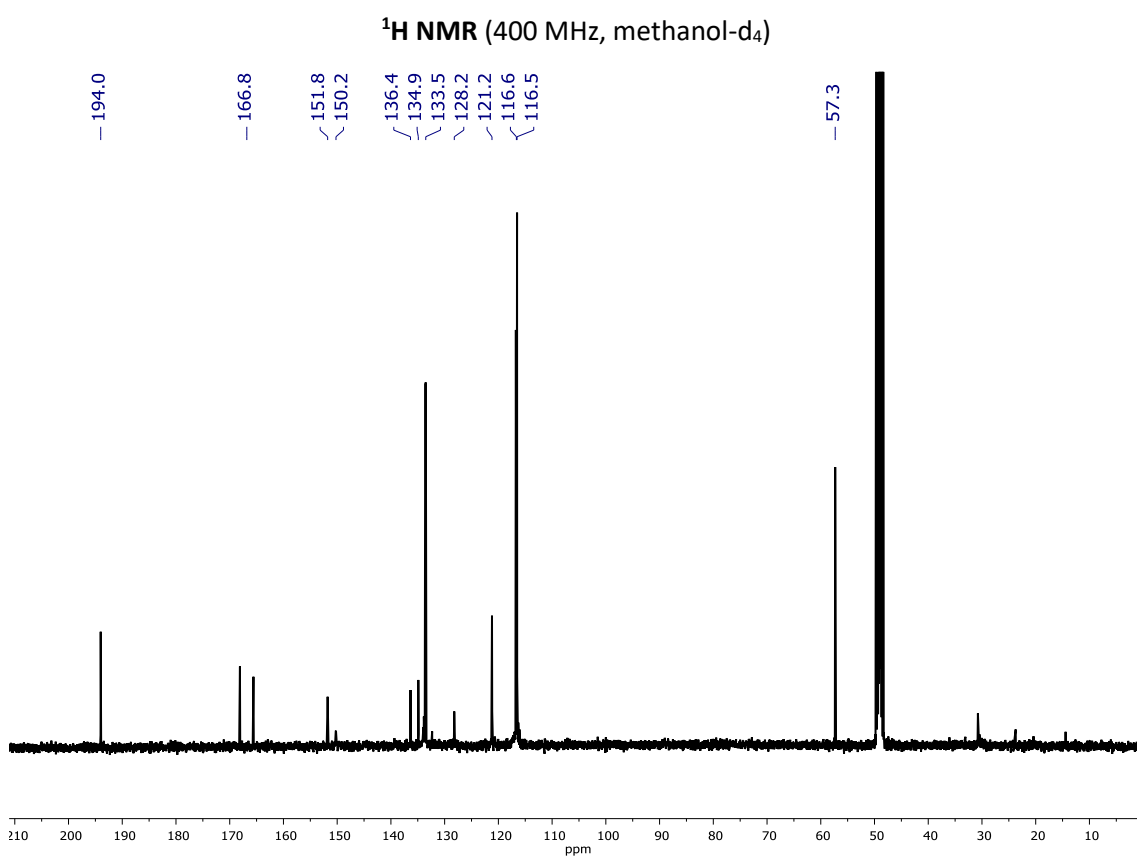
Figure S19. ¹H and ¹³C NMR spectra of compound **5b**.

^{1}H NMR (400 MHz, DMSO-d$_6$)

^{13}C NMR (100 MHz, DMSO-d$_6$)
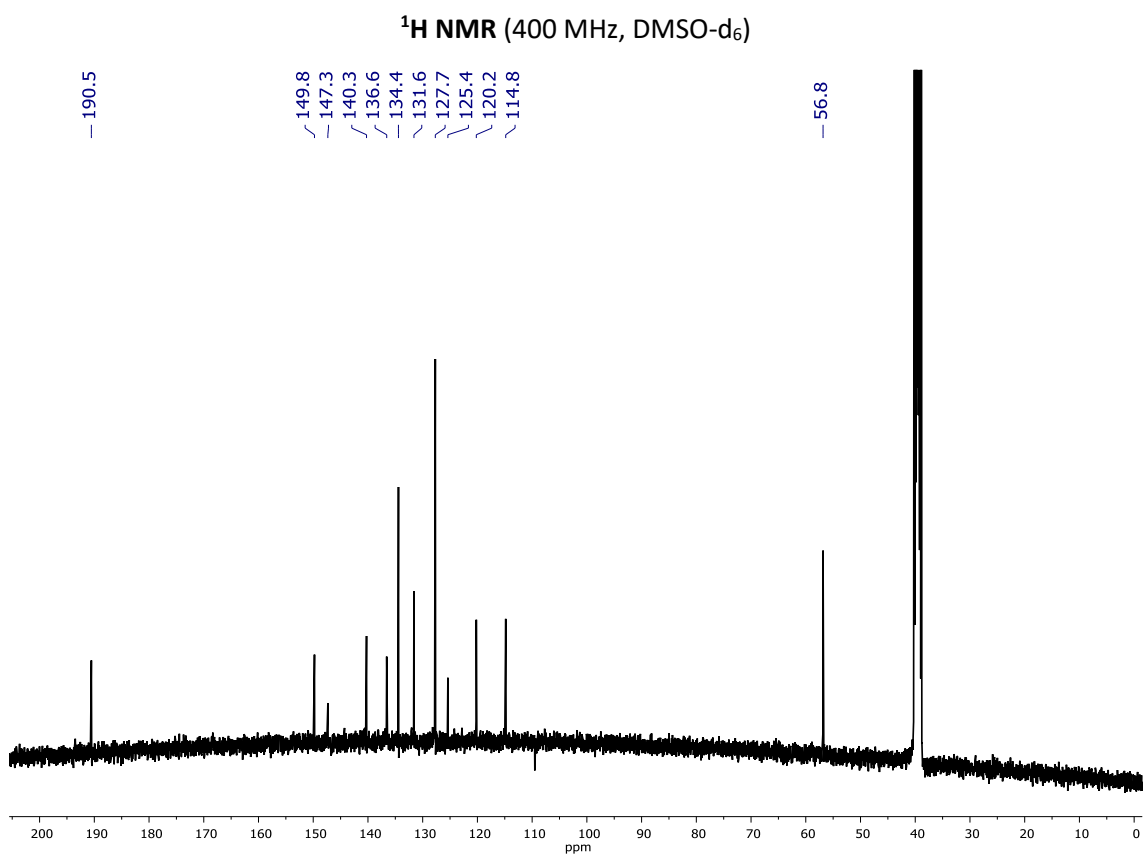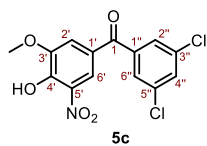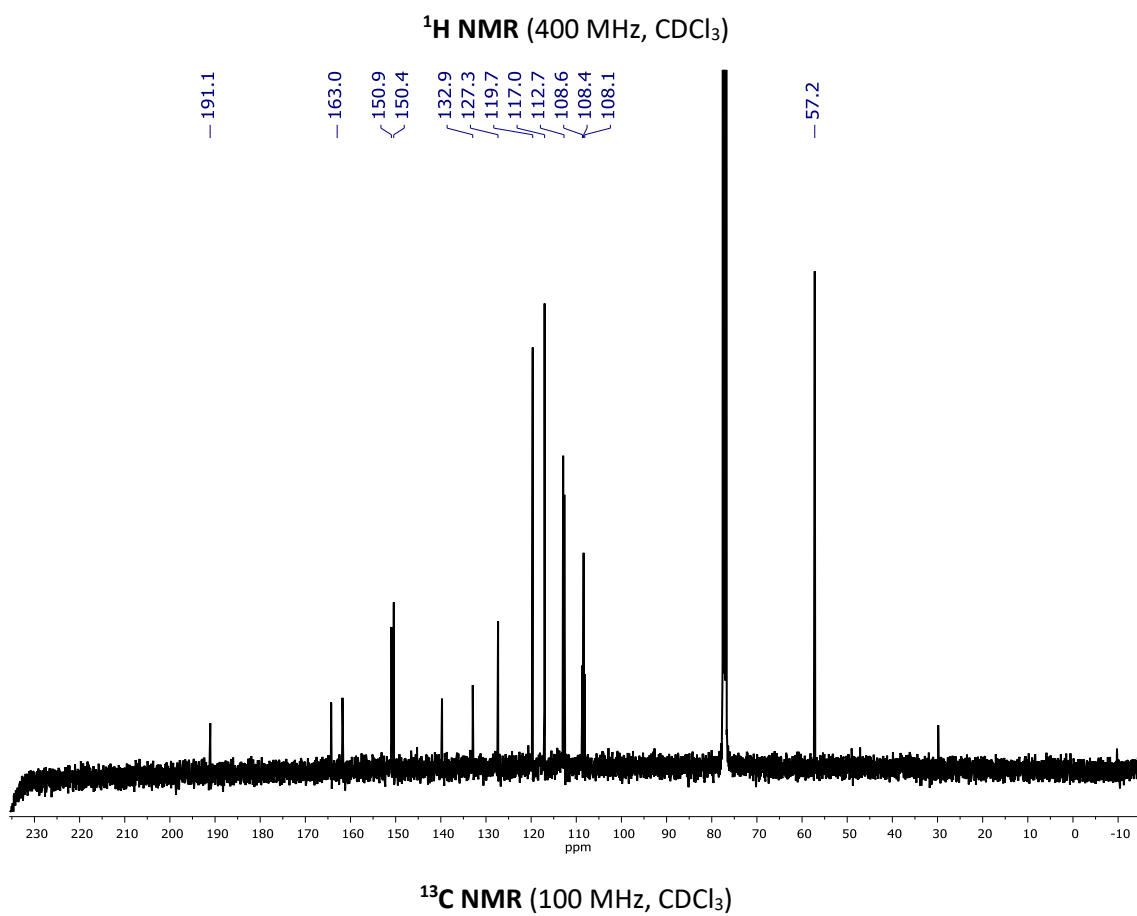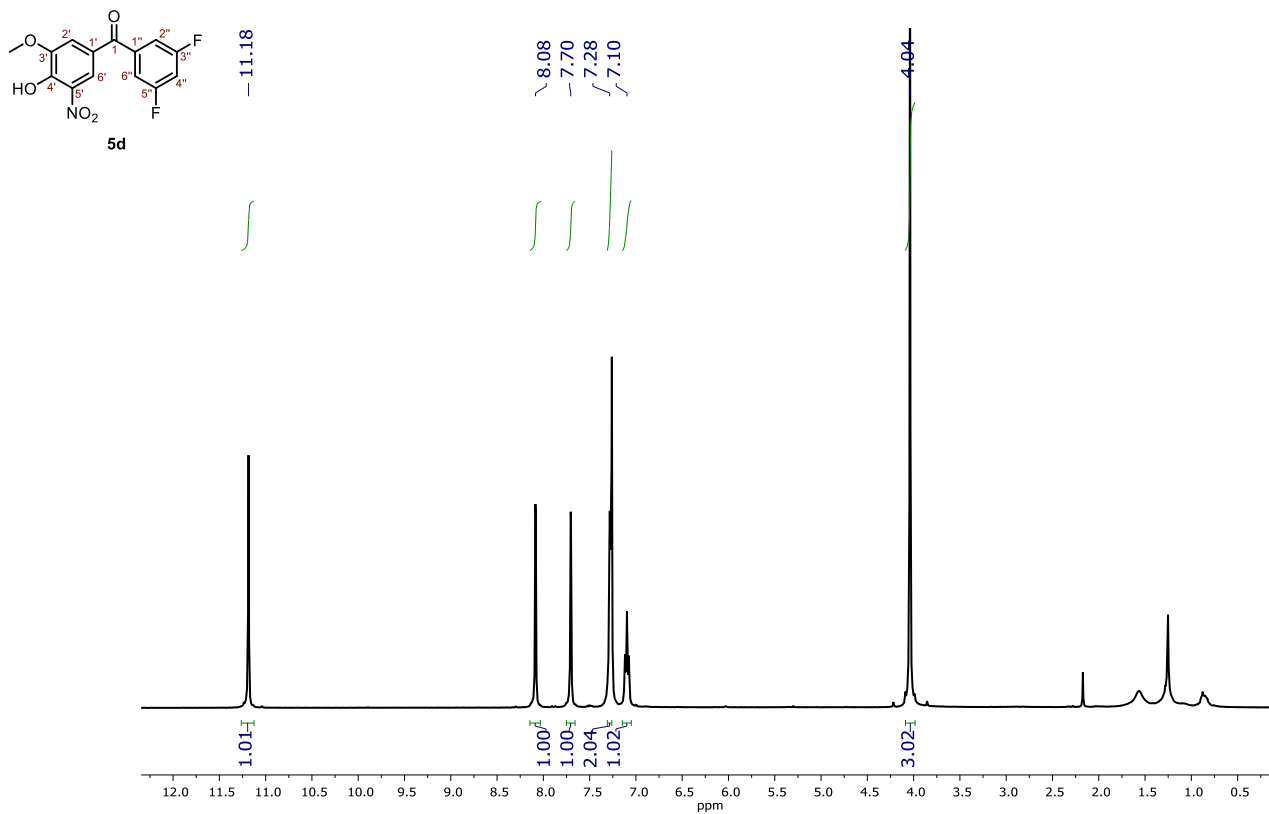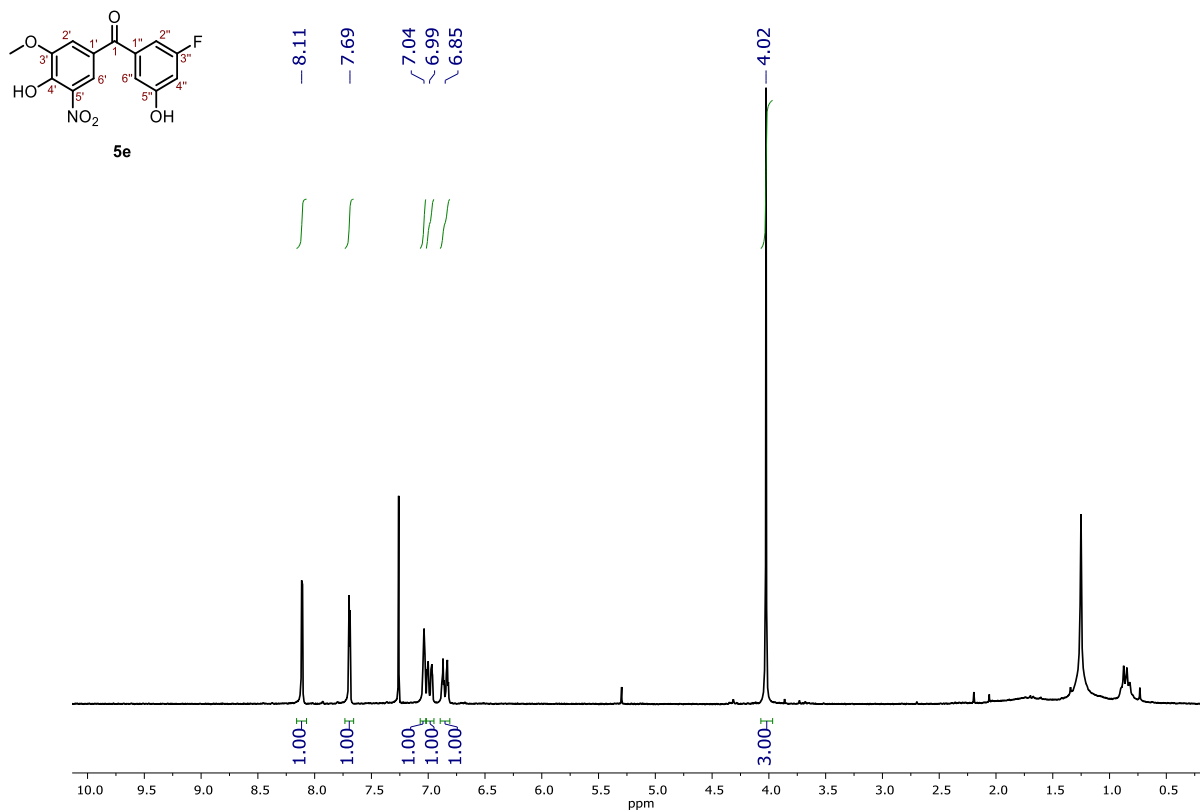
Figure S20. ^{1}H and ^{13}C NMR spectra of compound **5c**.

^{1}**H NMR** (400 MHz, CDCl$_3$)

^{13}**C NMR** (100 MHz, CDCl$_3$)

Figure S21. ^{1}H and ^{13}C NMR spectra of compound **5d**.

^{1}H NMR (250 MHz, CDCl$_3$)
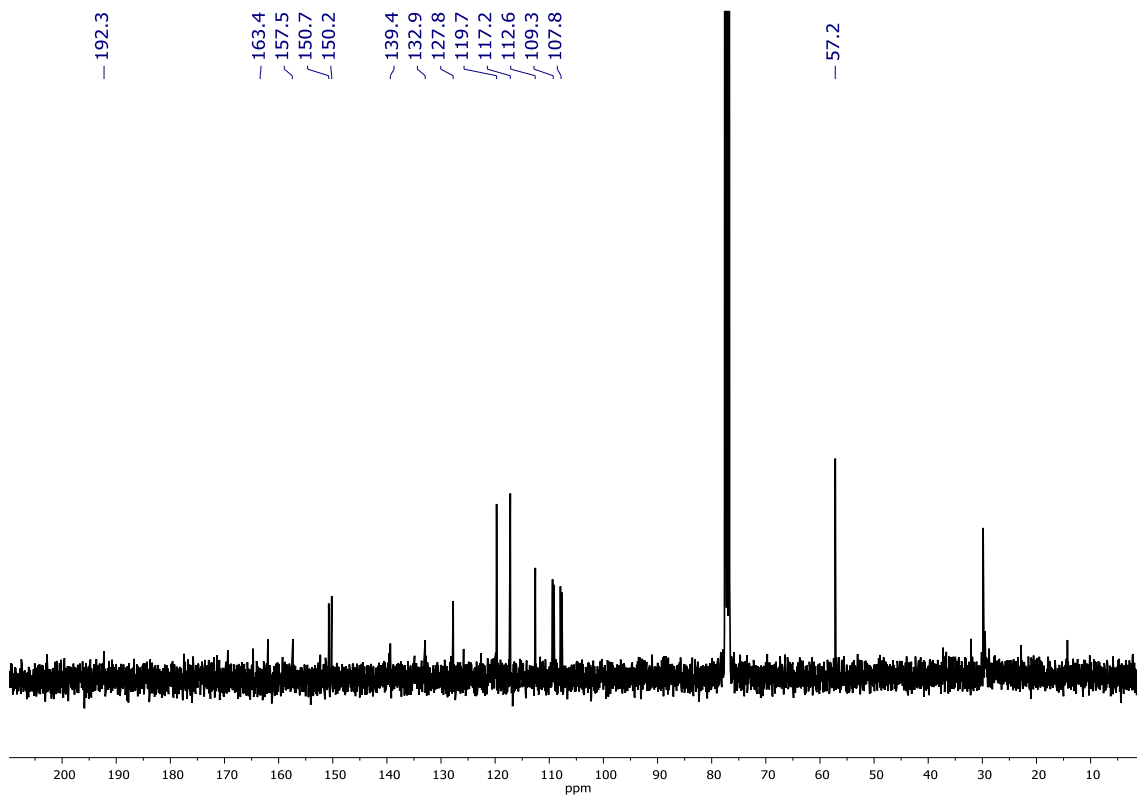
^{13}C NMR (90 MHz, CDCl$_3$)

Figure S22. ^{1}H and ^{13}C NMR spectra of compound **5e**.

¹H NMR (360 MHz, acetone-d₆)

¹³C NMR (90 MHz, acetone-d₆)
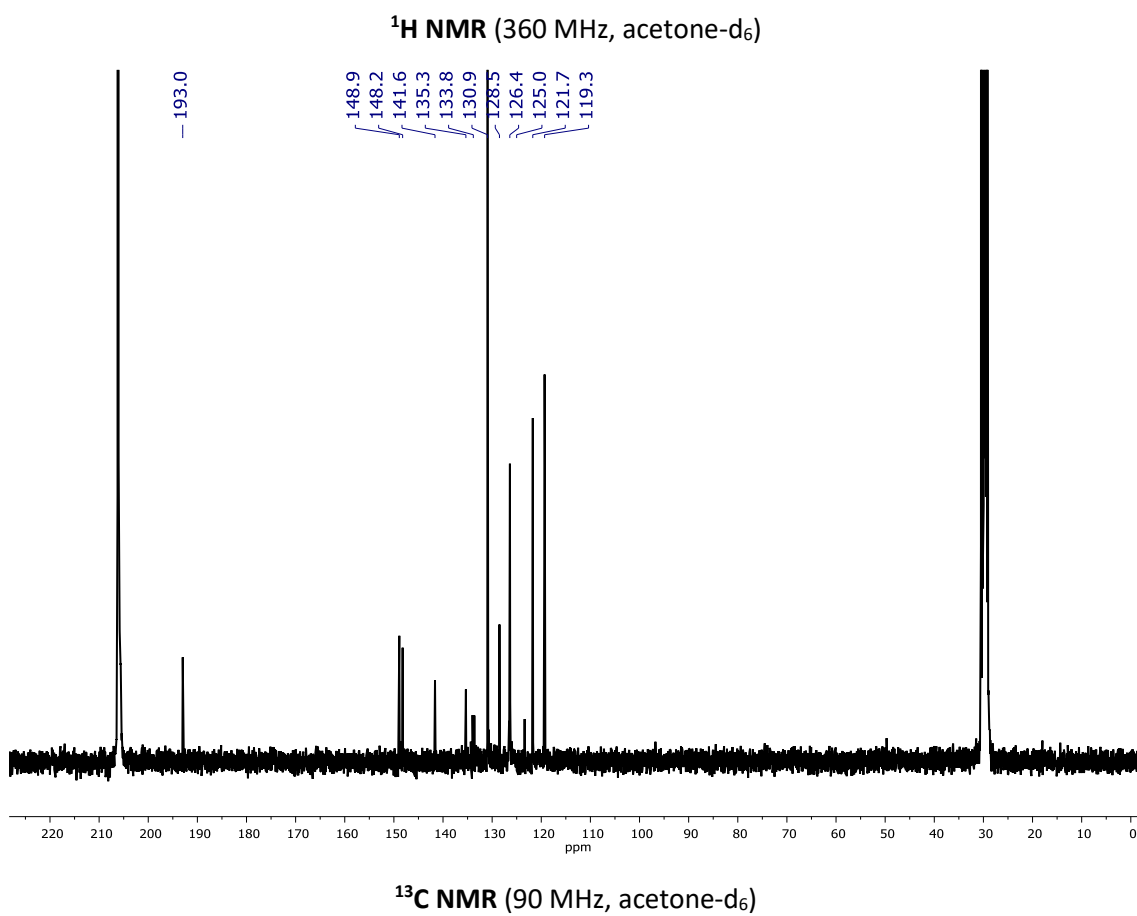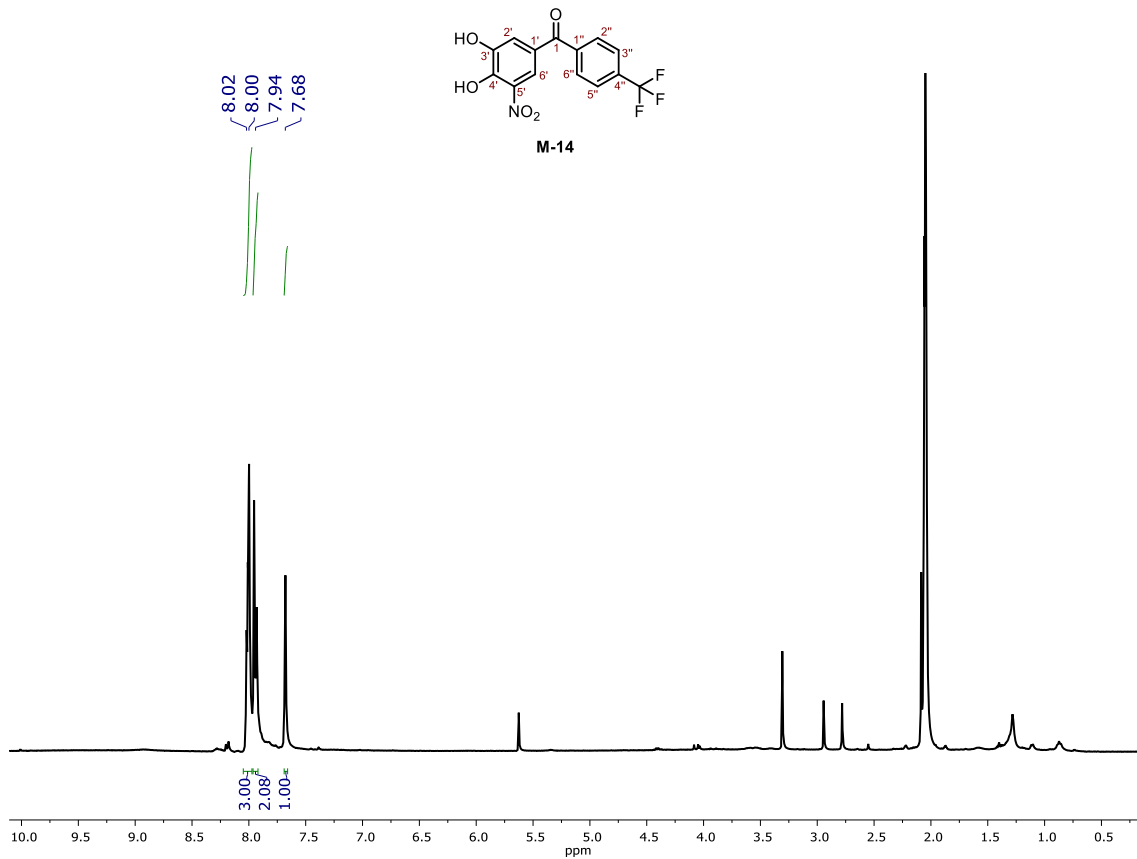
Figure S23. ¹H and ¹³C NMR spectra of compound **M-14**.

¹H NMR (360 MHz, acetone-d₆)

¹³C NMR (90 MHz, acetone-d₆)
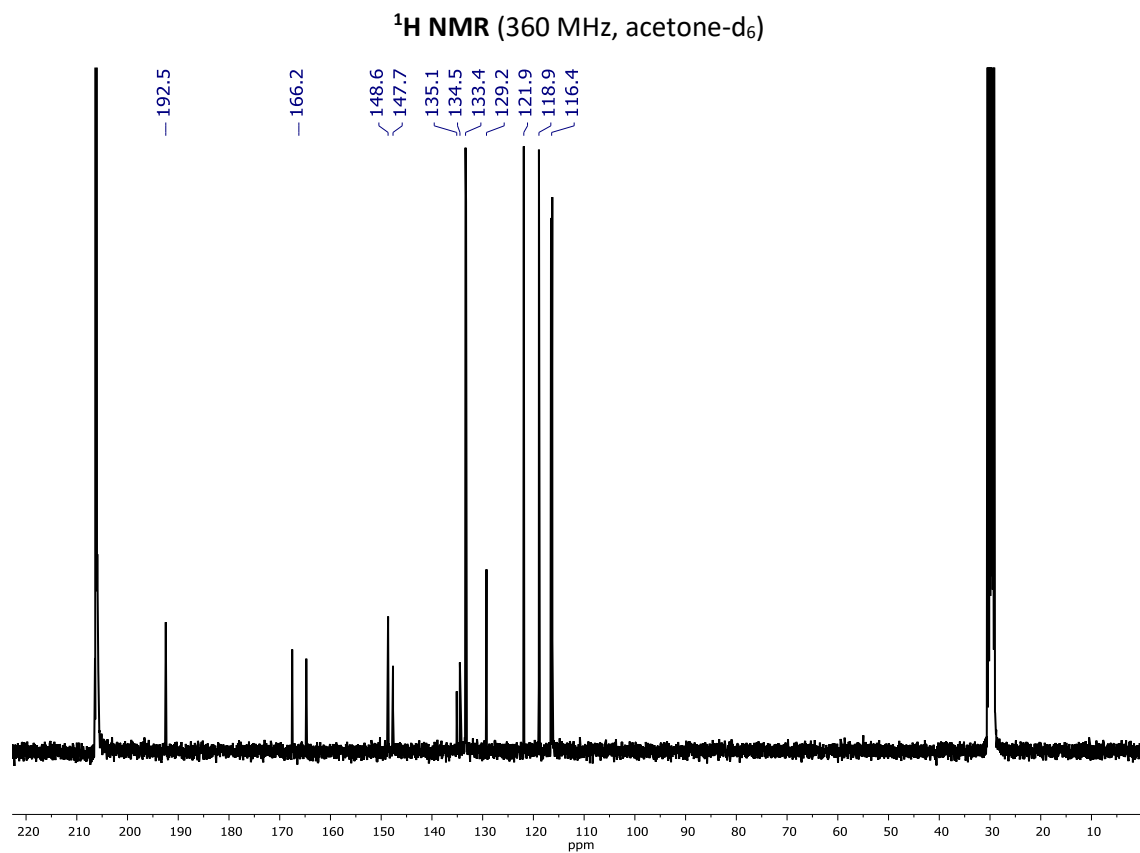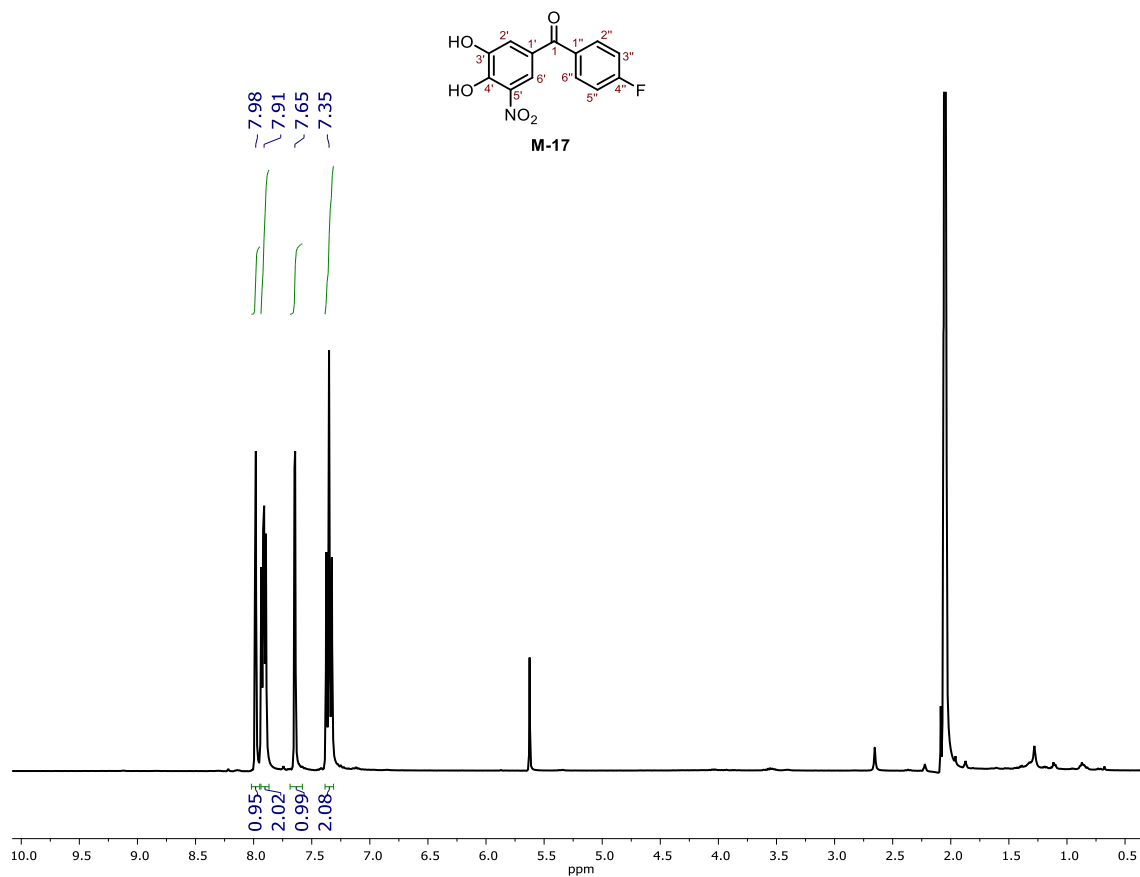
Figure S24. ¹H and ¹³C NMR spectra of compound **M-17**.

¹H NMR (250 MHz, acetone-d₆)

¹³C NMR (100 MHz, acetone-d₆)

Figure S25. ¹H and ¹³C NMR spectra of compound **M-20**.

¹H NMR (360 MHz, DMSO-d₆)

¹³C NMR (90 MHz, DMSO-d₆)
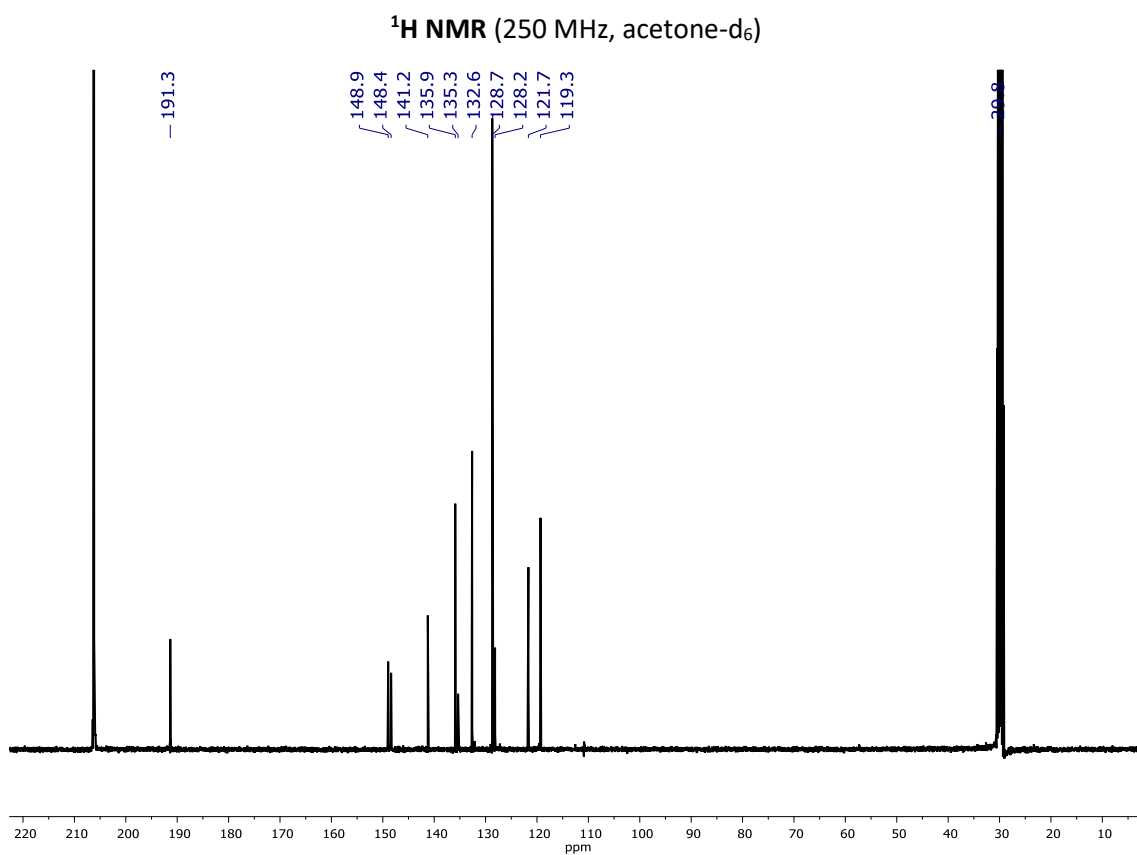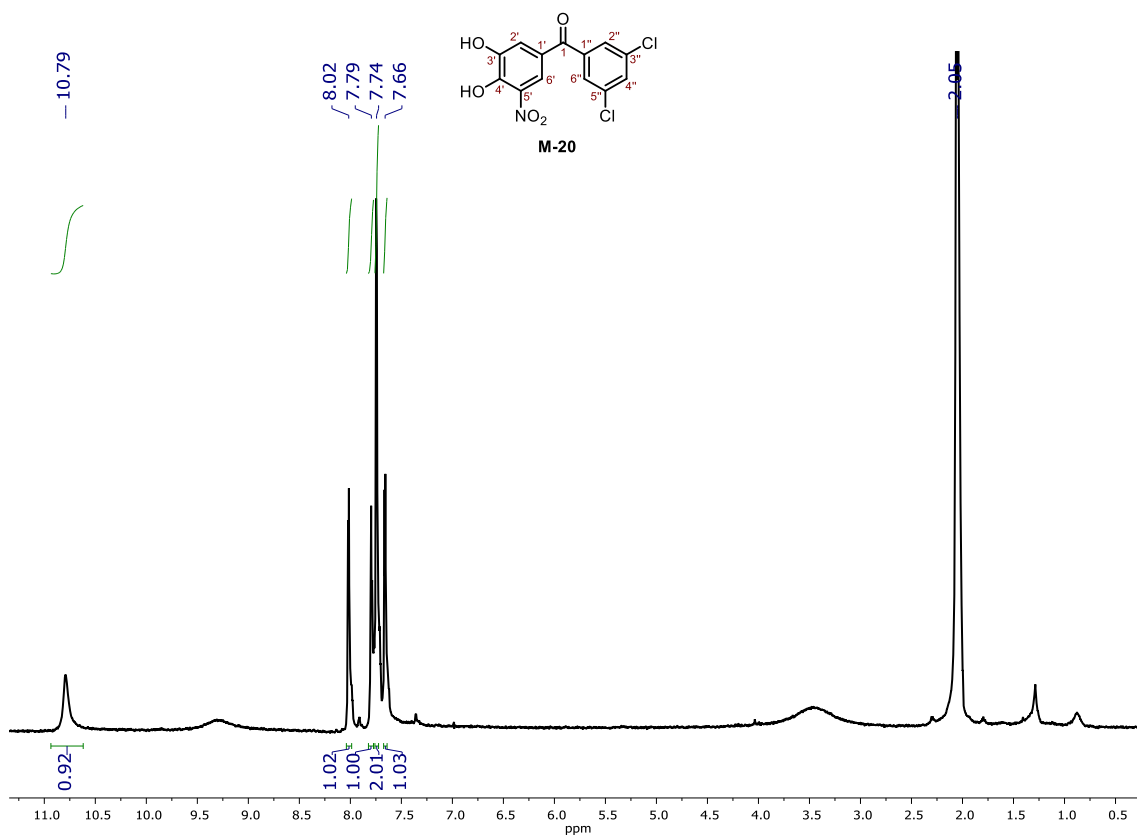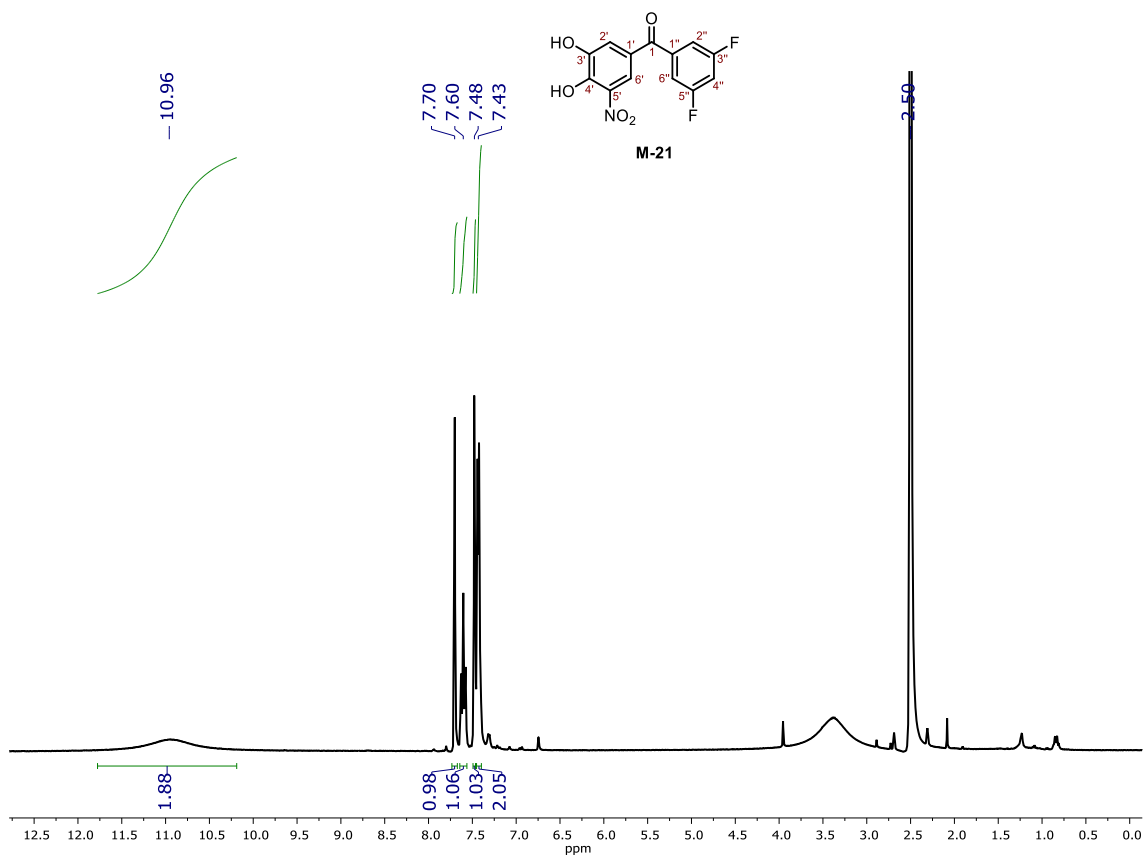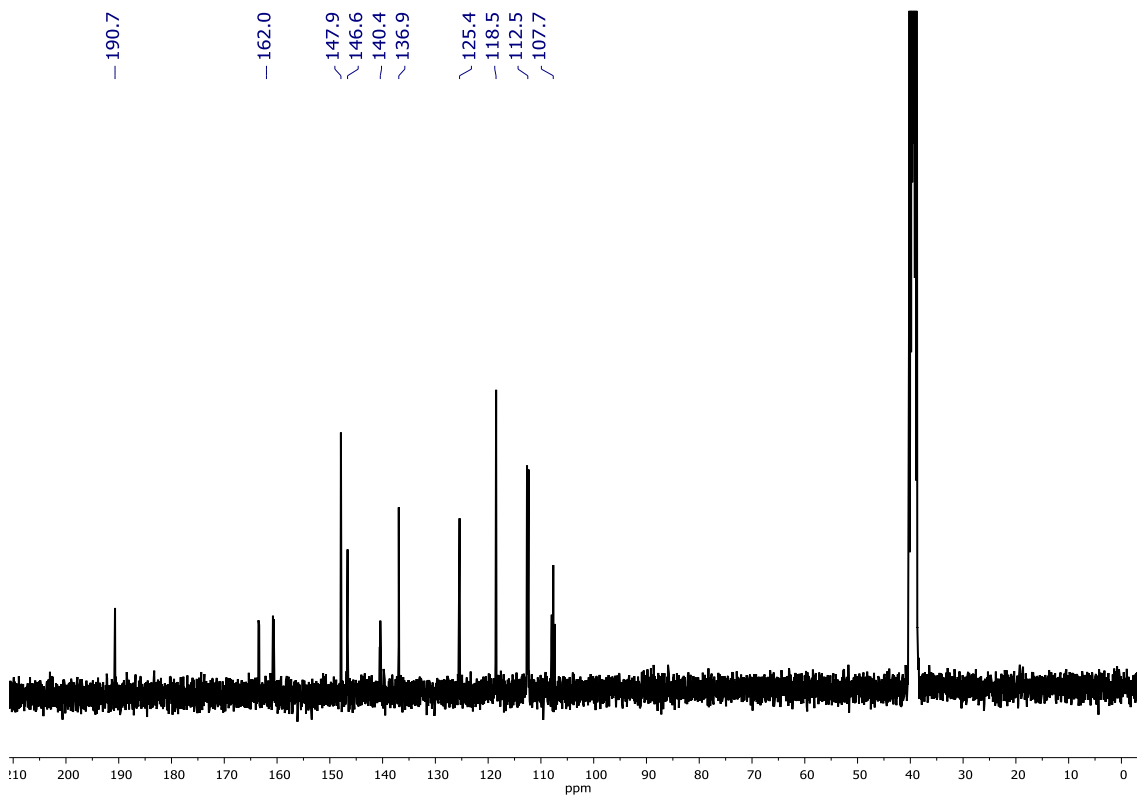
Figure S26. ¹H and ¹³C NMR spectra of compound **M-21**.

¹H NMR (360 MHz, acetone-d₆)
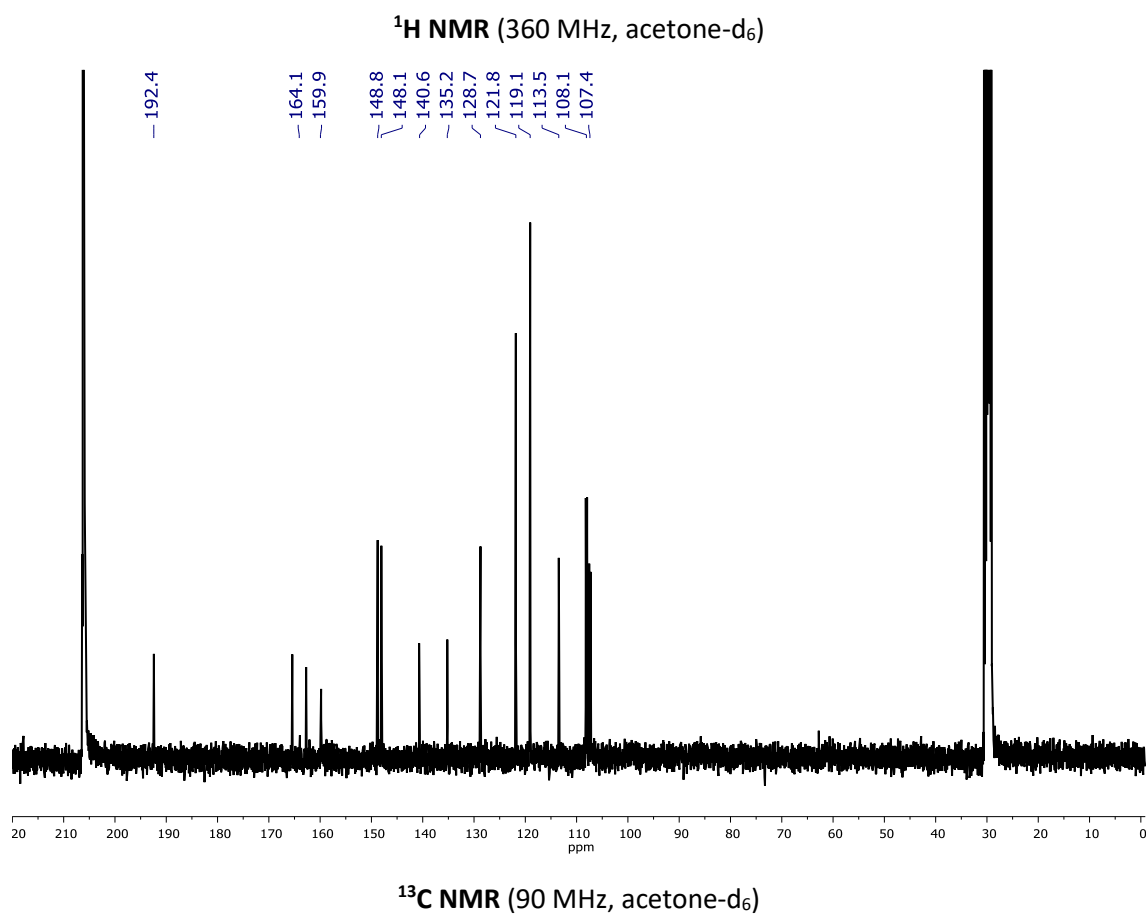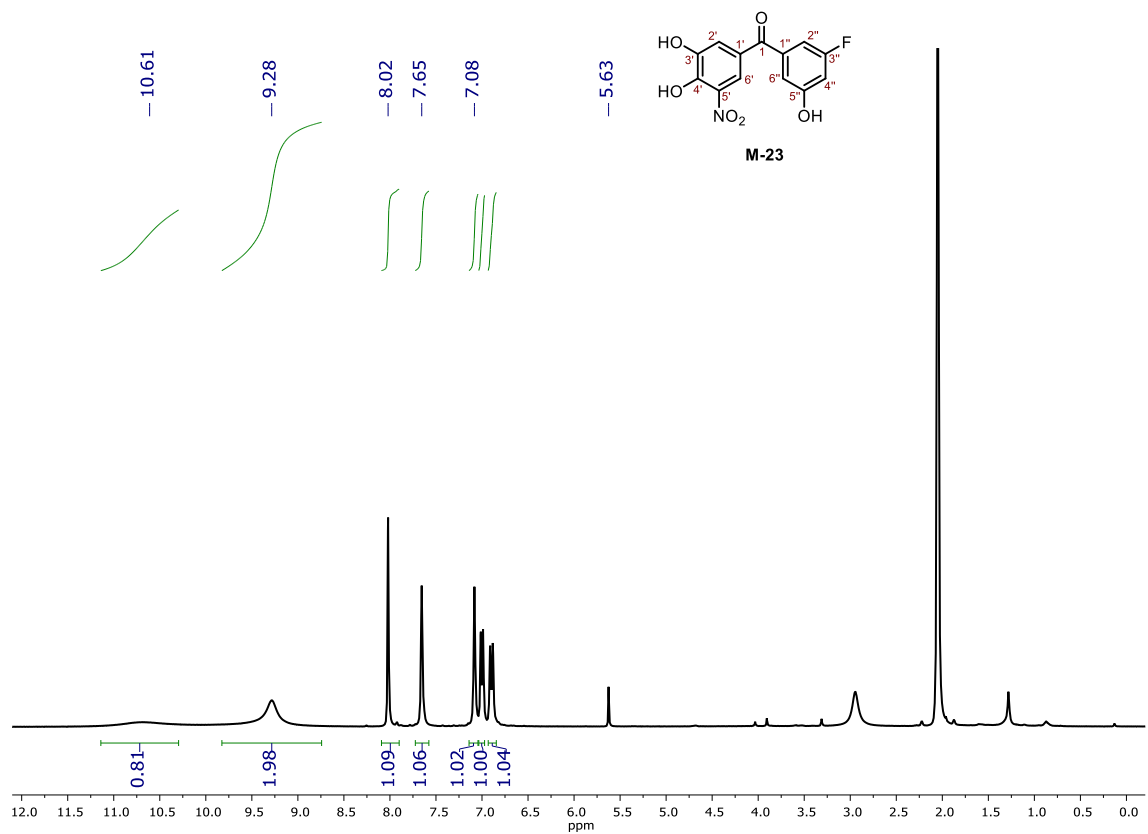

¹³C NMR (90 MHz, acetone-d₆)

Figure S27. ¹H and ¹³C NMR spectra of compound **M-23**.

HPLC traces for the final compounds

HPLC analysis of all final compounds was performed on Agilent-1200 HPLC with a binary pump and photodiode array detector (DAD), using a Phenomenex Luna Omega C18 column (150 mm × 4.6 mm, 5 μm). Gradient elution at a flow rate of 1 mL min^{-1} was performed by mixing 0.1% HCOOH in Water / 0.1% HCOOH in CAN.

(3,4-Dihydroxy-5-nitrophenyl)-[4-(trifluoromethyl)phenyl]methanone, **M-14**
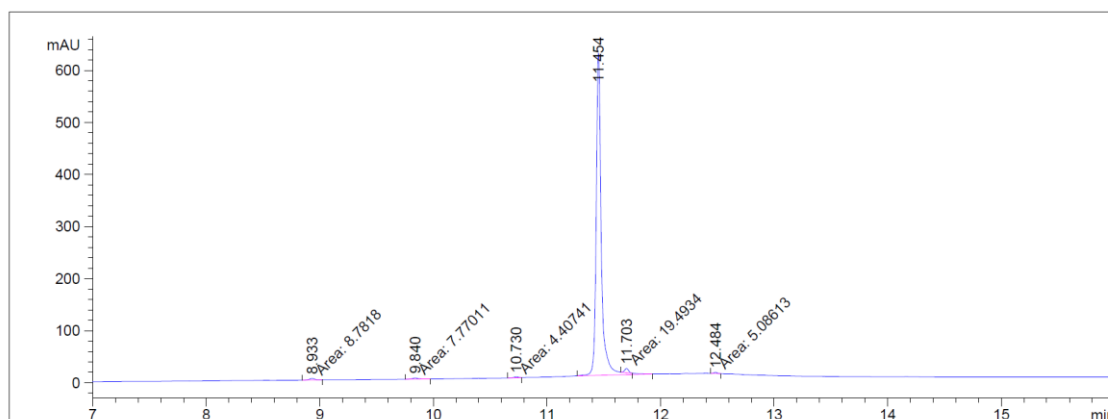

```
=====================================================================
                        Area Percent Report
=====================================================================

Signal 1: DAD1 C, Sig=254,4 Ref=850,100

Peak RetTime Type  Width     Area       Height     Area
 #    [min]        [min]   [mAU*s]      [mAU]       %
----|-------|----|-------|----------|-----------|--------|
  1   8.933 MM    0.0503     8.78180    2.90987   0.4427
  2   9.840 MM    0.0607     7.77011    2.13294   0.3917
  3  10.730 MM    0.0456     4.40741    1.61013   0.2222
  4  11.454 MM R  0.0521  1938.04407  620.13800  97.7042
  5  11.703 MM T  0.0398    19.49343    8.17263   0.9827
  6  12.484 MM    0.0362     5.08613    2.34038   0.2564

Totals :                  1983.58294  637.30395


=====================================================================
                       *** End of Report ***
```

(3,4-Dihydroxy-5-nitrophenyl)-(4-fluorophenyl)methanone, **M-17**
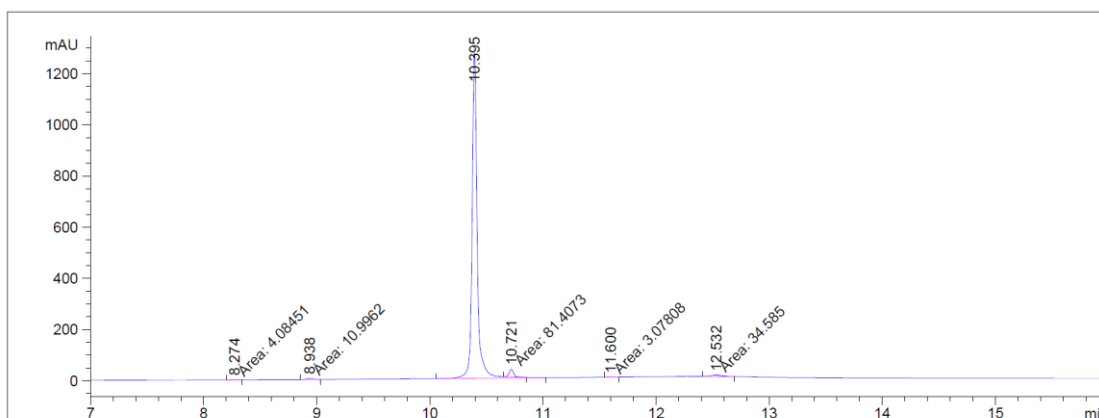

```
=====================================================================
                       Area Percent Report
=====================================================================



Signal 1: DAD1 C, Sig=254,4 Ref=850,100

Peak RetTime Type  Width     Area        Height     Area
  #   [min]        [min]   [mAU*s]        [mAU]       %
----|-------|----|-------|----------|----------|--------|
   1   8.274 MM    0.0507    4.08451    1.34252   0.0983
   2   8.938 MM    0.0518   10.99619    3.53849   0.2647
   3  10.395 MM R  0.0527 4020.18896 1272.45691  96.7708
   4  10.721 MM T  0.0453   81.40733   29.96630   1.9596
   5  11.600 MM    0.0498    3.07808    1.02924   0.0741
   6  12.532 MM    0.1162   34.58496    4.96011   0.8325

Totals :                  4154.34004 1313.29357



                  *** End of Report ***


=====================================================================
```

(3,5-Dichlorophenyl)-(3,4-dihydroxy-5-nitrophenyl)methanone, **M-20**
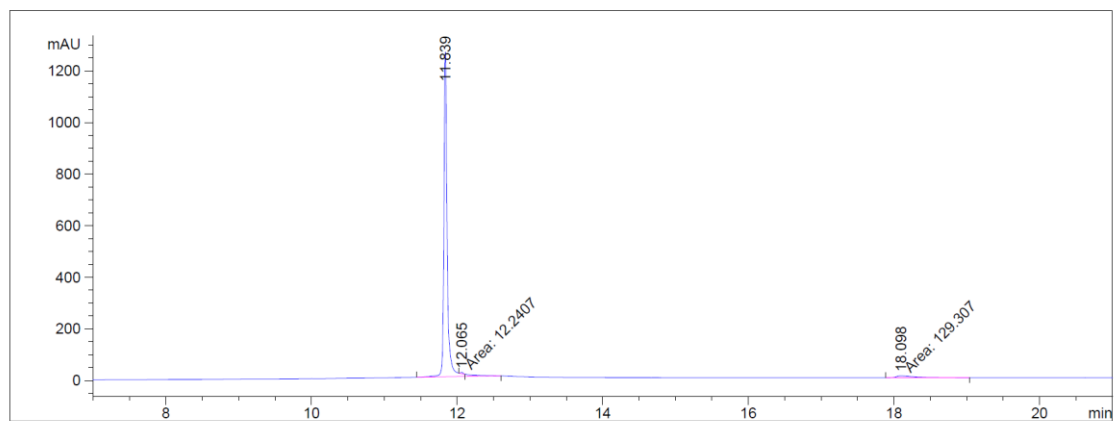

```
========================================================================
                          Area Percent Report
= ======================================================================

Signal 1: DAD1 C, Sig=254,4 Ref=850,100

Peak RetTime Type  Width     Area       Height     Area
 #    [min]        [min]    [mAU*s]      [mAU]       %
----|-------|----|-------|----------|----------|--------|
  1  11.839 MM R  0.0533 4037.51025 1261.70142  96.6129
  2  12.065 MM T  0.0373   12.24067    5.46862   0.2929
  3  18.098 MM    0.3013  129.30652    7.15321   3.0942

Totals :                 4179.05744 1274.32324


========================================================================
                        *** End of Report ***
```

(3,5-Difluorophenyl)-(3,4-dihydroxy-5-nitrophenyl)methanone, **M-21**
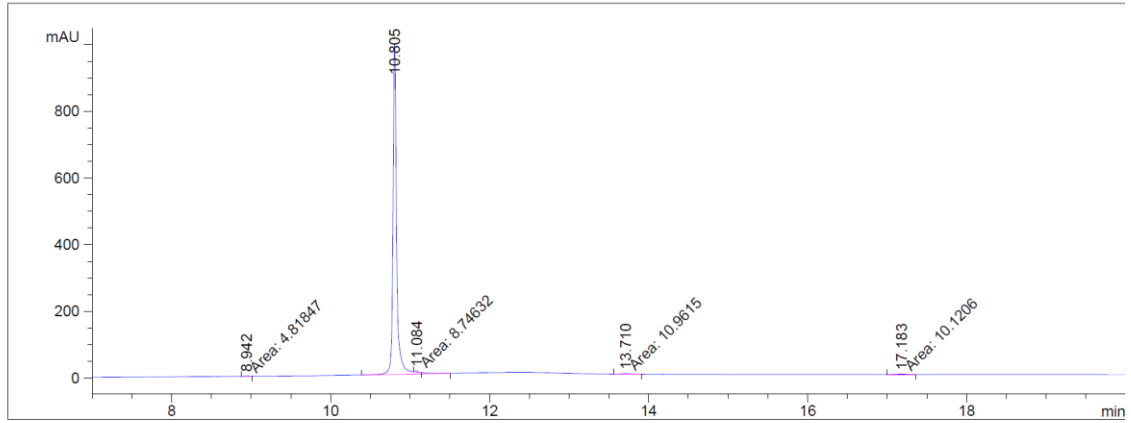

```
===================================================================
                        Area Percent Report
===================================================================

Signal 1: DAD1 C, Sig=254,4 Ref=850,100

Peak RetTime Type  Width     Area       Height     Area
  #   [min]        [min]    [mAU*s]      [mAU]       %
----|-------|----|-------|----------|----------|--------|
  1   8.942 MM    0.0508     4.81847    1.58075   0.1492
  2  10.805 MM R  0.0538  3194.64185  989.05627  98.9271
  3  11.084 MM T  0.0399     8.74632    3.65545   0.2708
  4  13.710 MM    0.1271    10.96149    1.43683   0.3394
  5  17.183 MM    0.1415    10.12057    1.19178   0.3134

Totals :                  3229.28871  996.92109


===================================================================
                      *** End of Report ***
```

181

(3,4-dihydroxy-5-nitrophenyl)-(3-fluoro-5-hydroxyphenyl)methanone, **M-23**


```
========================================================================
                          Area Percent Report
========================================================================


Signal 1: DAD1 C, Sig=254,4 Ref=850,100

Peak RetTime Type  Width     Area       Height     Area
 #    [min]        [min]   [mAU*s]      [mAU]       %
----|-------|----|-------|----------|----------|--------|
  1   8.897 MF    0.0803    5.32038    1.10473   0.1368
  2   8.977 FM    0.0770    4.98687    1.07999   0.1282
  3   9.100 FM    0.0652   11.76150    3.00604   0.3024
  4   9.247 FM    0.0938    8.72693    1.55105   0.2244
  5   9.929 MM R  0.0548 3799.80054 1154.64966  97.7122
  6  10.233 MF T  0.0685   28.44840    8.40367   0.7316
  7  10.309 FM T  0.0450   16.18774    5.99999   0.4163
  8  10.753 MM    0.0806    5.97613    1.23617   0.1537
  9  11.524 MM    0.0619    7.55914    2.03585   0.1944

Totals :                 3888.76762 1179.06714


========================================================================
                         *** End of Report ***
```

References

Sant'Anna, R.; Gallego, P.; Robinson, L. Z.; Pereira-Henriques, A.; Ferreira, N.; Pinheiro, F.; Esperante, S.; Pallares, I.; Huertas, O.; Almeida, M. R.; Reixach, N.; Insa, R.; Velazquez-Campoy, A.; Reverter, D.; Reig, N.; Ventura, S. Repositioning tolcapone as a potent inhibitor of transthyretin amyloidogenesis and associated cellular toxicity. *Nat. Commun.* **2016**, 7, 10787.

APPENDIX 2

Supplementary information of chapter 3

Table S1. PK parameters for M-23 following IV (1 mg/Kg) and PO (10 mg/Kg) administration in mice.

	M-23 IV (1 mg/Kg)	M-23 PO (10 mg/Kg)
T_{max} (h)	-	< 0.25
C_{max} (ng/mL)	1363.0	743.7
AUC_{0-24h} (h·ng/mL)	761.0	866.4
$t_{1/2}$ (h)	1.5	0.9
k_e (h^{-1})	0.468	0.802
Vd (L/Kg)	2.8	14.3
Cl (L/h·Kg)	1.3	11.4
F (%)	-	5.5%

Table S2. Data collection and refinement statistics. Values in parentheses are for the last shell.

|	PITB:WT-TTR	PITB:V30M-TTR	PITB:V122I-TTR	Tolca:V30M-TTR
Data collection				
Beamline	ALBA-XALOC	ALBA-XALOC	ALBA-XALOC	ALBA-XALOC
Space group	$P2_122_1$	$P2_122_1$	$P2_12_12$	$P2_122_1$
Wavelength (nm)	0.9792	0.9792	0.9792	0.9794
Resolution range (Å)	43.50(1.85)	44.06(1.20)	66.04 – 1.24	42.80 – 1.57
a, b, c (Å)	43.50, 64.09, 84.78	44.06, 65.34, 85.21	83.40, 43.78, 66.04	42.80, 64.13, 85.00
α, β, γ (°)	$\alpha = \beta = \gamma = 90$	$\alpha = \beta = \gamma = 90$	$\alpha = \beta = \gamma = 90$	$\alpha = \beta = \gamma = 90$
Unique reflections	20,915	76,676	68,808	33,424
Data redundancy	6.3(6.5)	12.8(12.8)	6.4(5.3)	5.9(3.4)
R_{merge}	0.05(1.23)	0.03(1.53)	0.05(1.27)	0.05(1.06)
$CC_{1/2}$	0.99(0.69)	1.0(0.77)	0.99(0.56)	0.99(0.50)
$(I/\sigma(I))$	14.8(1.6)	28.3(1.8)	14.6(1.2)	11.8(0.9)
Completeness (%)	99.9(100)	98.7(100)	100(100)	99.9(99.0)
Structure refinement				
Resolution range (Å)	42.39-1.85	39.14-1.20	66.05-1.24	65.41-1.60
Non-anomalous reflections	20,863	76,541	68,782	31,214
R_{work}/R_{free} (%)	21.4/23.3	17.6/19.8	18.3/21.5	16.0/20.4
Number of all atoms	1,966	2,164	2,153	2,011
RMSD bond (Å)/Angle (°)	0.006/0.915	0.013/1.341	0.008/0.962	0.02/1.77
Ramachandran plot				
Favored (%)	96.93	97.81	97.37	4
Allowed (%)	2.63	2.19	2.63	98
Disallowed (%)	0.44	0	0	0
Overall B factors (Å^2)	33.23	17.48	18.06	26.49
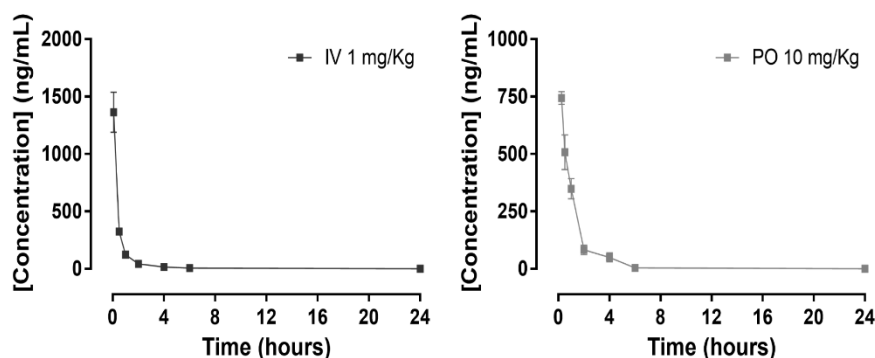
Figure S1. Plasma concentration-time profiles for M-23 after IV (1 mg/Kg) and PO (10 mg/Kg) administration in CD-1 mice. Data represents mean ± SEM (n = 3). No M-23 was detected after 24 h.
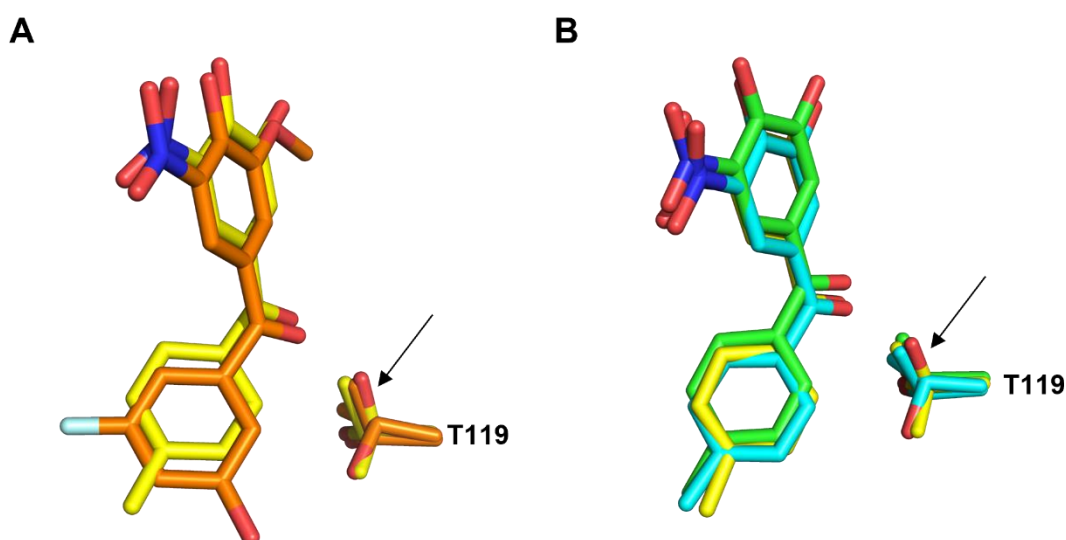

Figure S2. Position of the hydroxy side chain of T119 in the different TTR:ligand structures. (A) Overlay of one of WT-TTR binding sites when bound to **PITB** (in orange) and tolcapone (in yellow). The arrow highlights the different orientation of T119 side chain in the WT-TTR:tolcapone. (B) Superposition of tolcapone when bound to WT-TTR (in yellow), V30M-TTR (in cyan) and V122I-TTR (in green). The arrow indicates the different orientation of T119 side chain in the WT-TTR:tolcapone structure. Ligands and residue T119 are shown as sticks. PDB files 4D7B and 5A6I were used for WT-TTR:tolcapone and V122I-TTR:tolcapone, respectively.
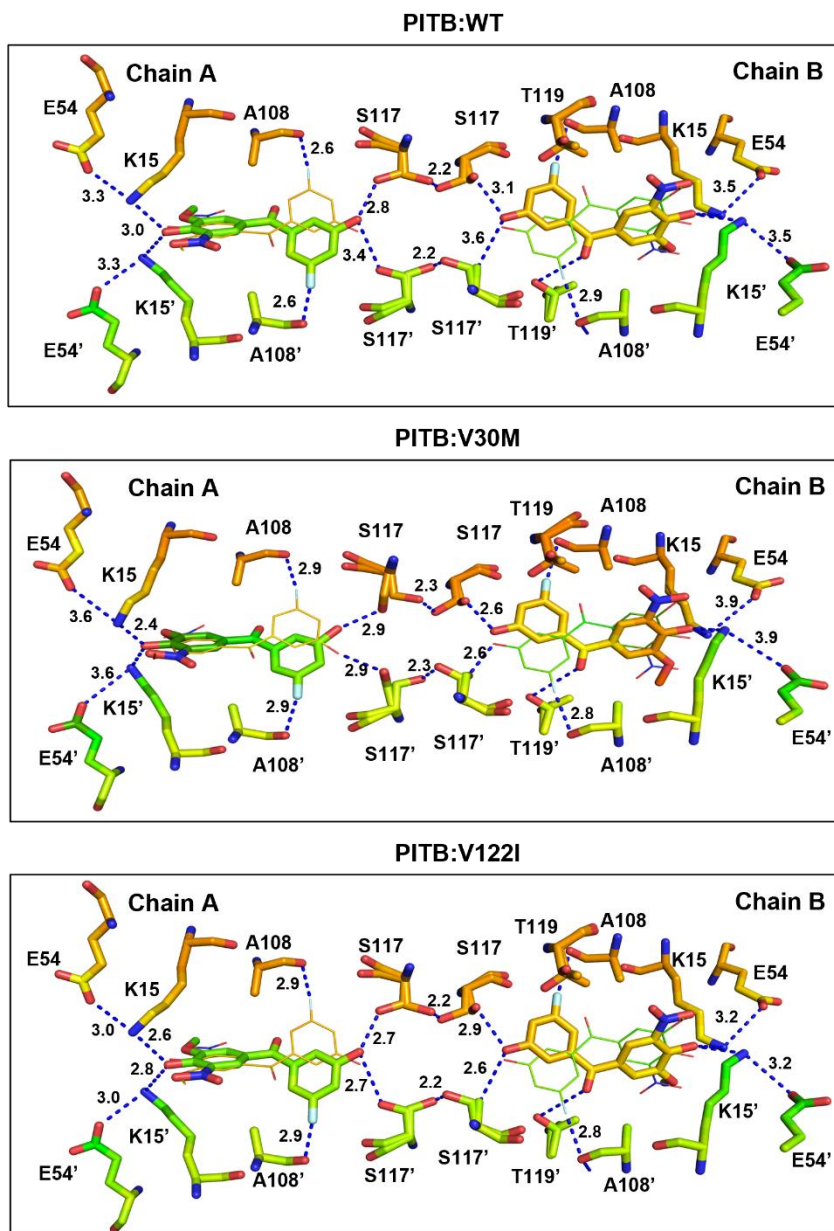
Figure S3. PITB binding at the WT-, V30M- and V122I-TTR dimer-dimer interface. PITB and some of the TTR residues interacting with the ligand are depicted by sticks. Dashed lines indicate relevant contacts between **PITB** and TTR and between the hydroxyl groups of S117/S117′.